Universidad del País Vasco
Euskal Herriko Unibertsitatea

UNIVERSITY OF THE BASQUE COUNTRY

MATERIALS PHYSICS CENTER

DOCTORAL THESIS

Theoretical description of low-energy excitations in nanostructures as probed by fast electrons

Author:
Andrea KONEČNÁ

Supervisors:
Dr. Javier AIZPURUA
Dr. Rainer HILLENBRAND

A thesis submitted for the degree of
Doctor of Philosophy in Physics

Donostia-San Sebastián, April 2019

Laburpena

Ikusmena da gutako gehienontzat mundua hautemateko zentzumen nagusia. Gure ikusmenak mugatua izan arren, antzinarotik gaur egundaino eginiko aurkikuntza ugari begiei esker egin dira. Giza begiak, edozein leiarrek bezala, zenbait aberrazio optiko ditu eta uhin-luzera tarte jakin batean soilik funtziona dezake, espektro ikusgaia deritzon horretan (VIS ingelesezko sigletan). Hala ere, berez begi hutsez bereiztezinak liratekeen gauzak ikusteko nahiak, lupa, teleskopio eta lehen mikroskopio optikoen asmakuntzak eragin zituen 16. eta 17. mendeetan. Mikroskopio optikoek biologia eta medikuntzaren garapenak azkartzea ahalbidetu zuten, gaur egun oinarrizko tresnak direlarik oraindik ere laborategi askotan. Hori, 1873an Ernst Abbek formulatu zuen bezala, sistema optiko tradizionalek gertu diren bi puntu bereizteko duten ahalmena difrakzioak mugatua den arren. Alegia, erabilitako argiaren uhin-luzerarekiko proportzionala da tresna hauon bereizmen ahalmena [1]. Hortaz, ezinezkoa da ohiko teknika optikoak erabiliz argi ikusgaiarekin ehun(daka) nanometro baino tamaina txikiagoa duten xehetasun eta objektuak bereiztea.

Nanoeskalako objetuak edota, are gehiago, atomoak ikusteko aukeretako bat argiaren erabilera alde batera uztea litzateke. Luis de Broglie-k 1925. urtean postulatu zuen hipotesiaren arabera, partikula guztiek uhinen-izaera ere erakusten dute. Beranduago etorri zen honen baieztapena elektroi-difrakzio esperimentuen bidez, zeinean elektroien uhin gisako portaera erakusten zuten [2]. Ez zen luzaro igaro mikroskopio elektronikoaren ideia garatu zen arte, katodotik erauzitako eta boltai altuaz (ehundaka kilovoltetakoa normalean) azeleratutako elektroiak kontrolatu eta bideratuko lituzkeena. Ernst Ruska eta Max Knoll-ek leiar elektromagnetikoak zerabiltzan transmisioko mikroskopio elektronikoaren (TEM ingelesezko sigletan) [3, 4] lehen prototipoa 1931. urtean aurkeztu zutenetik elektroi mikroskopioa zientzia modernoaren tresna garrantzitsuenetako bat bilakatu da, XX. mendean fisika, kimika eta biologian eginiko aurkikuntza askotan ezinbestekoa izan delarik [5, 6]. Horrez gain, mikroskopio elektronikoak analisirako zein tresnak sortzeko erabiltzen dira nanoteknologia bezalako arlo berrietan, eta, besteak beste, elektronika modernoan eginiko zenbait aurrerapen ahalbidetu ditu.

TEMaren bidez lorturiko bereizmen handiko lehen irudiak kristal-laginak elektroi-sorta zabalekin argiztatuz lortu ziren, plano atomikoekin difraktaturiko elektroi-sortekin, hain zuzen ere. Hala ere, elektronikan eginiko aurrerapenei esker, gaur egun posible da irudiak lortzea oso enfokatutako elektroi sortekin, atomo baten tamainaren zabalera duten elektroi sortekin, laginaren ekorketa azkarrak eginez. Gaur egun punta-puntakoak diren eta aberrazio zuzenketak dituzten ekorketa eta transmisioko mikroskopio elektronikoek nanometro azpiko bereizmena dute [7, 8]. Are garrantzitsuagoa dena, mikroskopioari erantsitako zenbait detektagailu gai dira elektroi azkarren eta materiaren elkarrekintzatik sorturiko seinale anitzak (adibidez, erradiazio elektromagnetikoa, Auger elektroien eta elektroi sekundarioen igorpena) zehaztasunez kontrolatutako elektroi-sortaren posizioarekin korrelazionatuta neurtzeko. Ekorketa eta

transmisioko mikroskopio elektronikoak (STEM ingelesezko sigletan), beraz, materialak espazio-bereizmenarekin eskala atomikoan aztertzeko teknika malgu bat eskaintzen du.

Horrez gain, bereizmen handiko irudiak osatzen dituzten elektroiek hasierako energiaren zati txiki bat gal dezakete laginean zehar edo laginetik gertu igarotzean. Elektroien energia-galera probabilitatea elektroiek lagineko kitzikapenekin duten elkarrekintzaren araberakoa da. Energia tarte zabaleko kitzikapenak identifika litezke, transmititutako elektroiak mikroskopioaren zutabeari erantsitako elektroien energia-galerako espektrometroarekin analizatuko balira. Energia altuetan (50 eV ingurutik keV batzuetara) nukleo-galerak agertzen dira, atomoen barne-geruzetako elektroien kitzikapenetatik datozenak [9, 10]. Egitura kimikoari buruzko informazioa ematen dute nukleo-galerek, eta eskala atomikoko irudiekin korrelaziona daitezke [11–13], elektroien energia-galerako espektroskopia (EELS ingelesezko sigletan) teknika analitiko garrantzitsua bihurtuz STEMaren barruan.

Energia baxuetan (normalean 50 eV-ren azpitik) elektroi azkarrek balentzia bandako elektroien kitzikapenekin, banden arteko trantsizio elektronikoekin, edo bibrazio molekularrekin izan dezakete elkarrekintza. Galera txikiko kitzikapen hauetako asko espektroskopia optikoarekin azter daitezke, garrantzitsuak izanik materialak identifikatzeko (adibidez, bibrazio molekularrek "hatz-marka" bereizgarriak dituzte espektro infragorrian (IR ingelesezko sigletan) [14]) eta beraien propietateak karakterizatzeko. Tesi honetan erakutsiko dugun bezala, argian oinarritutako urruneko eremuko espektroskopiarekiko osagarria den informazioa eman dezake maiz energia baxuko EELS teknikak. Horrez gain, STEM-EELSak aztertzen ari garen laginean tokian tokiko kitzikapenak sortzeko aukera ematen digu, eta argi-espektroskopiako teknika konbentzionalekin "ilunak" liratekeen, alegia, agertuko ez liratekeen kitzikapenak aztertzeko aukera ematen digu. Lerro zuzenean higitzen den elektroiak (hurbilketa ona dena STEMko elektroi-sortentzat) banda zabaleko eremu desagerkorra dakar berarekin batera. Beraz, gertuko eremuaren bidez modu naturalean akoplatzen da kitzikapenekin, kitzikapen optikoak aztertzeko argia erabiltzen duten teknikekiko desberdintasunetako bat izanik hau.

Elektroi-sorten gertuko eremu izaera dela eta, galera txikiko STEM-EELS teknika bereziki interesgarria da nanofotonikaren arloan [15]. Nanofotonikak edo nanooptikak material ezberdinen propietate optikoak aztertzen ditu nanoeskalan, eta desiragarriak liratekeen erantzun eta funtzionalitateak izan ditzaketen nanoegiturak garatzea du helburu [16]. Nanofotonika maiz materiaren energia baxuko kitzikapen kolektiboetan oinarritzen da, hala nola, plasmoietan (kargadentsitatearen kuantu bezala definituak) eta fonoietan (kristal-sareko bibrazioen kuantuak) zeinak [17], kasu batzuetan, fotoiekin akopla daitezkeen, polaritoi deritzen uhin elektromagnetiko (EM) bereziak osatuz. Nanoegituren gertutasunean, gertuko eremuan, erradiazio elektromagnetikoa nabarmen konfinatzeko gaitasuna dute polaritoi-kitzikapenek. Honek urruneko eremuko erradiazio elektromagnetikoa gertuko eremu, eta alderantziz, bihurtzeko aukera ematen digu,

nanofotonikaren printzipioetako bat ezarriz. Nanoegitura fotonikoen funtzionalitatea eta portaera ulertzeko maiz ezinbestekoa izaten da gertuko eremua ezaugarritzea, eta hau era naturalean egin daiteke elektroi-sorten bidez.

Dauden polaritoi-kitzikapenen artetik, plasmoi- eta fonoi-polaritoiak aztertu ditugu batez ere tesi honetan. Alde batetik, plasmoi polaritoiak (PP), metaletan edo balentzia-elektroi askeak dituzten materialetan (besteak beste, dopatutako erdieroaleetan) kitzika daitezke [18]; bestetik, fonoi-polaritoiak (PhP ingelesezko sigletan) kristal ionikoetan kitzika daitezke [19]. Horrez gain, polaritoien eremu elektromagnetikoaren propietateek mendekotasun handia dute kitzikatzen den nanoegituraren geometriarekiko. Gainazaleko polaritoiak muga-gainazal lauetan heda daitezke, edo partikula txikien kasuan, gainazalean lokalizatutako kitzikapenak eragin daitezke, gainazaleko polaritoiak bezalako uhin geldikorrak sorturik. Hauen artean, lokalizatutako gainazaleko plasmoiak edo fonoiak oso ustiatuak dira, eremu elektromagnetikoen lokalizazioa eta handitzea ahalbidetzen baitituzte "nanoantena" fotonikoetan [20, 21]. Dena den, plasmoi/fonoi polaritoiak izan ditzaketen beste zenbait egitura aztertu dira, beste beste, patroi espezifikoak dituzten metalezko xafla meheak [22], 2D material berriak [23–25], edo metamaterialak [26].

Gaur egun nanooptikak optoelektronikan [27], (bio)detekzio-espektroskopian [28, 29], eguzki-panelen eraginkortasunaren hobekuntzan [30] edota difrakzio limitea gainditzen duten mikroskopioetan eta irudien lorpenean [31–33] ditu aplikazioak. Gaur egun, polaritoien kitzikapenaren eta egitura nanofotonikoen ikerketan EELS teknikaren erabilera oso hedatua dago. Gainera, EELSa erabiliz elektroi-sorta zabalekin xafla eta gainazal metalikoetan eginiko lehen esperimentuak [34, 35] ezinbestekoak izan ziren bolumeneko plasmoien [36, 37] identifikaziorako eta gainazaleko plasmoi-polaritoien (SPP ingelesezko sigletan) aurkikuntzarako 50eko eta 60ko hamarkadetan [38]. Ikerketa ugari egin dira momentuz-bereizitako EELSa garatzeko, normalean sorta zabal bat (enfokatu gabekoa) erabiliz, neurketak kitzikatutako modoen dispertsioarekin erlazionatu baitaitezke.

XX. mendearen erdialdetik, gainazal lauetan hedatzen diren SPPak karakterizatzen laguntzeaz gain, antena fotonikoetako gainazalean lokalizatutako kitzikapenen mapaketarako [39] ere izan da garrantzitsua EELS teknika. Adibidez, banako nanotriangelu [40], nanoesfera [41, 42], nanokubo [43], nanodisko [44], eta nanoorratz [45, 46] metalikoetan lokalizatutako gainazaleko plasmoiak (LSP ingelesezko sigletan), edota partikula ugaritan kitzikatutako LSP modo akoplatuak [42, 45, 47–52] aztertzeko erabili da STEM-EELSa. Praktikan, 3-Dko data-kubo bat sortzeko erabil daiteke espazio-bereizmena duen espektroa, nanoegituraren energian filtratutako mapak lortzeko. Mapa hauek elektroien energia-galera (EEL ingelesezko sigletan) probabilitatea irudikatzen dute energia jakin baterako fokuplanoan elektroi-sortak duen posizioaren arabera, eta kitzikaturiko hurbileko eremuarekin erlaziona daitezke (sakontasun gehiagoz eztabaidatuko da EEL espektrua 1.2 sekzioan.

Duela gutxi arte, EELS teknika STEMaren baitan gai izan da kitzikapenak infragorri hurbilaren (NIR ingelesezko sigletan) espektro-tartera arte ($\sim$ 1 eV) aztertzeko. Hala ere, intrumentazioan eginiko aurrerapenek ikaragarri hobetu dute espektro-bereizmena [53, 54], eta oso energia baxuko galerako espektro-tartea aztertzea ahalbidetu dute, infragorri ertaineko (MIR ingelesezko sigletan) bibrazioak esploratzeko bidea emanez [10]. Gainera, STEM-EELS teknikaren bereizmenean eta energia tarte detektagarrian eginiko aurrerapenek hainbat konposatu organiko eta ez-organikoaren nanoeskalako erantzun bibrazionalaren ikerketa teorikoa eta esperimentala bultzatu dituzte. Aztertutako konposatu organikoen artean, guanina [55, 56], hidroxilo-taldeak [57] edo karbono nitruro adsorbatuak [58] leudeke, eta material ez-organikoen artean h-BN konposatua [10, 59–61], magnesio oxidoa [62], silizio karburoa [10], silizio dioxidoa [63–65] eta urari buruzko hainbat ikerketa [66].

Bereizmen espazialeko galera (ultra)baxuko EEL espektroen interpretazio eta aurreikuspen teorikoa dira tesi honen muina. Lehen hiru kapituluetan sakontasunez eztabaidatuko ditugu bibrazio-EELS teknikaren zenbait alderdi eta goimailako gailuekin eginiko zenbait esperimentuk bultzatutako hainbat kalkulu erakutsiko ditugu. Nanofotonikaren ikuspegitik abiatuta, bereziki bibrazio-EEL espektroan zentratuko gara eta elektroi-sortaren eta fonoi optikoen arteko akoplamendua aztertuko dugu. Ondoren, kitzikapen ezberdinen arteko elkarrekintza teorikoki aztertuko dugu eta gainazalek hobetutako EELSaren kontzeptua proposatuko dugu, gainazalek hobetutako espektrokopia optikoen teknikekin parekatuz. Azken atalean, momentu angeluarra daramaten zurrunbilodun elektroi-sortekin eginiko EELSa hartuko dugu kontuan. Errefakzio-indize altua duten noanoantenek dielektrikoen nanofotonikan duten interesa haintzat hartuta, nanoantena hauen zurrunbilodun EELSa aztertuko dugu teorikoki.

Infragorri ertaineko fonoiak STEM-EELSa erabiliz kitzikatzeko aukera eta fonoi-polaritoien nanofotonikak gaur egun duen interesa [19] tesi honen lehen atalerako motibazio garrantzitsuak dira. Kristal ionikoetan (adibidez, SiC, MgO edo h-BN) kitzika daitezkeen moteltze txikiko fonoi-polaritoi modoak duela gutxi aztertu ziren ekorketako hurbileko eremuko mikroskopio optikoarekin (SNOM ingelesezko sigletan) [67–69] eta hautagai gisa proposatu izan dira superleiar modura [70], IR erradiazioaren nanofokuratzerako [71] edota detekziorako [72], aplikazio gutxi batzuk aipatzearren. Sakabanaketa hiperbolikoa duten fonoi-polaritoi bereziak aurkeztuko ditugu 2. kapituluan, h-BN materialaren egiturak eta lotura atomikoek duten anisotropia dela eta existitzen direnak. Esperimentuetako emaitzak behar bezala interpretatzeko, erantzun dielektrikoa barne hartzen duen elektrodinamika klasikoan oinarritutako eredu teorikoa erabiliko dugu, xafla infinituen eta ebakitako xafla mehen EEL espektroa lortzeko. Frogatzen dugu, eta esperimentuen emaitzek horrela baieztatzen dute, PhP hiperbolikoak (hPhP ingelesezko sigletan) modu eraginkorrean kitzika daitezkeela elektroi azkarrekin. Horrez gain, ebakitako h-BN xaflarekiko elektroi-sortak duen posizioaren arabera, bolumen motako edo gainazal motako hPhP modo gidatuen kitzikapenak beha ditzakegu.

3. kapituluak ere ebakitako xaflen bibrazio-EEL espektroskopia kontuan duen arren, aurreko kapituluarekin alderatuta, honako honek gehiago sakontzen du modo bakoitzarekiko EEL seinaleak espazioarekiko duen galeran, zeina induzitutako eremu elektromagnetikoaren hedadurarekin erlazionatuta dagoen. Espazio-bereizmena duen EEL espektroa kalkulatu dugu, besteak beste, silizezko xafla isotropo baten ebakiduratik gertu, eta silize eta silizioaren arteko juntura batetik gertu, ondoren emaitza teorikoak [63] erreferentziatik lorturiko datu esperimentalekin konparatzeko. Argi ikusgaiaren tarteko uhin-luzerako SPP kitzikapen kolektiboekin bezala [73], silize xaflak gainazalari akoplatutako fonoi-polaritoi (SPhP ingelesezko sigletan) modoak, eta baita ertzei akoplatutako SPhP modoak, ditu ebakiduran, silizioaren presentziak (errefrakzio-indize altua dela eta) hauek desagarrerazten dituelarik. Beraz, emaitza hauek STEM-EELSaren komunitatearen baitan gaur egun bibrazio-EEL espektroskopiaren espazio-bereizmenaren ezaugarri eta mugei buruz dagoen eztabaidari ekarpena egiten diete [59, 74]. Gehienetan, energian iragazitako EEL seinalean fonoi optikoen kitzikapenek materialen arteko gainazalak bereizi ahal izatea eragozten dute. Tesi honetan lorturiko emaitzetan oinarrituta, aldiz, EELSak kitzikatutako gertuko eremu elektromagnetikoei buruzko informazio baliotsua ematen duela argudia daiteke. Ekarpen hau garrantzitsua izango litzateke nanofotonikaren aplikazioentzat.

Bestalde, elektroi azkarrek energia galtzeaz gain, irabazi ere egin dezakete lagina dagoeneko kitzikatua baldin badago eta bere energiaren zati bat elektroi-sortari transferitzen badio [75, 76]. Egoera hau beti betetzen da, bai mikroskopioek eta baita laginaren euskarriek ere tenperatura finitua dutelako, ondorioz laginean termikoki kitzikatutako egoerak induzituz [77]. Tenperatura finituak EEL espektroan duen eraginarekin batera, k_BT-rekiko konparagarriak diren energietan (k_B Boltzmann-en konstantea eta T laginaren tenperatura izanik) detektagarria den elektroien energia-irabaziaren (EEG ingelesezko sigletan) espektroa eztabaidatu da 4. kapituluan. Espektro osoak tenperaturarekiko duen mendekotasunaren deskribapen teorikoa aurkeztu dugu, energia-galerarik edo irabazirik gabe transmititutako elektroiei dagokien zero galerako gailurra (ZLP ingelesezko sigletan) deritzona barne. Tenperaturaren menpeko EEL espektroskopiaren teoria hau erabiliz, elektroi-sorta berotutako laginetik gertu dagoen kasuetarako, esperimentuetan behatzen den "ZLP" gailurraren zabaltzea azal daiteke. STEM-EELS teknikaren espektro-bereizmenaren oinarrizko mugen ondorioak ere eztabaidatu ditugu.

Punta-puntako STEM-EEL espektroskopiak molekulak aztertzeko duen gaitasuna eta bibrazio-EEL espektroaren interpretazioa dira 5 kapituluaren lehen atalaren oinarria. Zehazki, kitzikapen ez-polaritonikoentzat, adibidez molekulen bibrazioentzat, EEL espektroa interpretatzeko orduan molekularen forma kontuan hartu behar dela frogatu dugu, karbonozko oinarri batean ezarritako urburbuiletam egindako espazioan bereizitako EEL espektroetan ikusi bezala [66]. Hala, materialaren propietateak eta, are garrantzitsuagoa dena, konfigurazio geometrikoa aintzat hartzen dituen eredua erabiltzea da gakoa, laginean dagoen

molekula kopuruari eta beraien orientazioari buruzko informazioa lortzeko.

Espektro-bereizmenaren hobekuntzek, teknikaren zenbait eragozpenekin batera, hala nola erradiazioaren bidez molekuletan eragindako kalteek [55], motibatu dute 5 kapituluaren bigarren atala. Bertan, espektroskopia optikotik ezaguna den plasmoien eta molekulen kitzikapenen akoplamendu elektromagnetikoaren kontzeptua aurkeztu dugu, ondoren EELS teknikan aplikatzeko. "Plasmoiek handitutako EELS" kontzeptua proposatu dugu bertan, eta eV gutxi batzutako energia tartean (VIS ingelesezko sigletan) elektroien bidez aztertutako nanoantena metalikoetako plasmoien eta molekuletako eszitoien arteko akoplamendu elektromagnetikoa ikertu dugu. Kontzeptuaren oinarria frogatzeaz bat erakutsi dugu, kasu berezietan, akoplamendua horren eraginkorra izanik, "akoplamendu indartsuko erregimenera" iritsi daitekeela, eta elektroi bidez aztertua izan daitekeela. Funtsean, antena plasmonikoaren eta molekulen arteko elkarrekintzaren erritmoa akoplatu gabeko kitzikapenen moteltzea baino azkarragoa izatea da "akoplamendu indartsuko erregimenera" iristeko baldintza. Akoplatutako plasmoi eta bibrazio molekularrez osatutako sistemen EEL espektroa ere aztertu dugu meV-etako tartean (IR ingelesezko sigletan), gainazalak handitutako IR espektroskopia optikoarekin parekatuz. Gehienetan, akoplamenduaren mekanismoa IR tartean molekula kopuru txikien detekzio-limiteak hobetzeko erabili ohi da [28], baina akoplamendu indartsuko erregimenera ere era berean iritsi daiteke [72, 78].

Gehienetan urruneko eremuko teknika optikoen bidez ikertzen diren aukera hauek guztiak aztertu ditugu elektroi-sortak erabiliz, eta elektroiaren eta akoplatutako laginaren arteko gertuko eremuaren elkarrekintza dela eta sorturiko ezberdintasunak eztabaidatu ditugu. Elektroi-sorten bidezko tokian-tokiko azterketak antena-molekula akoplamenduaren indarra kontrolatzeko aukera eskaintzen du, eta akoplamendu-erregimen ezberdinen oinarrizko ikerketa (akoplamendu ahula vs. indartsua) egiteko erabil daiteke. Horrez gain, "gainazalak handitutako EELS" teknikak molekula-laginak urrunetik ikertzeko aukera dakar, erradiazioak eragindako kalteak murriztuz, eta gainerako ohiko EELS teknikek duten sentikortasuna gaindituz.

Materia aztertzeko beste aukera batzuk sortu dira elektroi-sortaren hedatzenorabidearekiko zeharkako planoan ondo egituratutako fase-egitura duten izpiak erabiliz [79–81]. Bereziki, momentu angeluar orbitala daramaten zurrunbilodun elektroi-sortetan (VEB ingelesezko sigletan) jarri dugu arreta. Zurrunbilorik gabeko elektroi-sorta bat bereziki diseinatutako irekidura batean difraktatuz, monopolo magnetiko batek sortutako eremu batekin elkarreraginez, edo baita ere fase-xafla batetik pasaaraziz, sor daitezke elektroi-sorta berezi hauek. Ohiko sorten ordez VEB sortak erabiliz EELSa neurtzeko aukera aztertu dugu 6 kapituluan. Galera baxuko EEL espektroskopiaren trataera elektrodinamiko klasikoaren baitan VEBak inplementatuz, forma arbitrarioa duten egitura fotonikoekin VEBek duten elkarrekintza ikertzeko esparrua garatu dugu. Gure hurbilketa teorikoa aplikatu diegu silizioz eginiko antena dielektrikoei, VEB-EELSa aztertzeko eta

erakusteko nola ustia daitezkeen (zurrunbilodun) elektroi-sortak izaera elektrikoa eta magnetikoa duten modoak EEL espektroan bereizteko. Erantzun dikroikoa erakusten duten nanoegiturak ere aztertu ditugu, espektro-erantzunean ezberdintasunak ageri dituztelarik VEBak erabiltzean. Hortaz, VEBa noanoeskalan kiralitate espezifikoko espektroskopia izatez egiteko gai dela erakutsi dugu.

Acknowledgements

In the first place, I thank my supervisors, **Prof. Javier Aizpurua** and **Prof. Rainer Hillenbrand**, for helping me get to this point. Javier and Rainer, you both were always ready for a brainstorming or discussion when I needed an advice or inspiration, you supported me, and guided my first steps in the world of science. I learned different things from each of you, and I am very grateful that I could work with such great scientists and people as you both are.

I thank **Prof. Philip Batson** who hosted me at Rutgers University during the first year of my PhD studies and introduced me to high-resolution STEM-EELS. Phil, the visit at Rutgers and discussions with you opened to me new perspectives, and I am thankful that I can work with you.

Prof. Peter Rez and **Prof. Peter Crozier** made possible my second stay in the USA at Arizona State University. I thank you for hosting me and sharing with me your results and thoughts on vibrational EELS. I really enjoyed the interaction with you and other members of the group. I also appreciated discussions and coffees I had with **Prof. Christian Dwyer**.

One year ago, I was having a great time at Oak Ridge National Laboratory with **Dr. Juan Carlos Idrobo** and **Dr. Jordan Hachtel**. I am still astonished by your passion for science, and patience with challenging and often very difficult experiments. You both taught me not to give up. Juan Carlos, I thank you for encouraging and motivating me. If something like "enthusiasm spectroscopy" existed, there would always be intense gain peaks after talking with you.

Many words of thanks go to **Dr. Tomáš Neuman**. You were always around when I needed any kind of support. There are not so many people like you, and I think I was lucky that I could share with you this exciting, although sometimes difficult, part of our lives. I will never forget our hiking trips across the Basque Country as well as all those hours we spent talking about science and many other topics.

I thank all members of the "Theory of Nanophotonics" group who I had a chance to meet during my PhD: **Prof. Alberto Rivacoba**, **Dr. Nerea Zabala**, **Dr. Rubén Esteban**, **Dr. Aitzol García-Etxarri**, **Dr. Yao Zhang**, **Dr. Angela Demetriadou**, **Dr. Mario Zapata**, **Dr. Luca Bergamini**, **Dr. Yuan Zhang**, **Dr. Mikołaj Schmidt**, **Dr. Garikoitz Aguirregabiria**, **Mattin Urbieta**, **Alvaro Nodar**, **Antton Babaze**, **Jon Lasa**, **Unai Muniain** and **Carlos Maciel**. Some of you helped me to resolve several scientific doubts that I was dealing with, and you all have been contributing to the great atmosphere in CFM and DIPC. I am very grateful that I was surrounded with such great colleagues/friends.

I was also often coming to NanoGUNE, and had a chance to work there with many excellent scientists. My special thanks go to **Dr. Alexander Govyadinov** who spent many months working with me and from whom I learned a lot! Sasha, thank you for all those hours of discussions over results that helped me so much and motivated me in the first months of my PhD. **Prof. Andrey Chuvilin** has

provided us with fantastic experimental results and made a substantial contribution to this thesis. I participated in some activities of the "Nanooptics" group. I would like to thank all "Nano-opticians" for tolerating presentations on EELS occasionally penetrating in their group meetings, and for feedback that I have received from them: **Dr. Alexey Nikitin**, **Dr. Marta Autore**, **Dr. Peining Li**, **Dr. Shu Chen**, **Dr. Iban Amenabar**, **Dr. Martin Schnell**, **Dr. Elizaveta Nikulina**, **Dr. Curdin Maissen**, **Dr. Stefan Mastel**, **Dr. Paulo Sarriugarte**, **Javier Alfaro**, **Divya Virmani**, **Lars Mester**, **Irene Dolado**, **Andrei Bylinkin** and **Dr. Monika Goikoetxea**.

I shared many coffees, pizza/pintxo-potes, and some hiking trips with PhD students (some of them became doctors meanwhile) from CFM and DIPC. I always enjoyed talking with you and had a lot of fun! Thank you, **Dr. Moritz Müller**, **Dr. Bernhard Kretz**, **Dr. Miguel Borinaga**, **Dr. Federico Marchesin**, **Mikel Rouco**, **Alba Pascual**, **Unai Aseguinolaza**, **Iker Gallardo**, **José Reina**, **Joseba Goikoetxea**, **Donaldi Mancelli**, **Francesco Belli**, **Antonella Mennino**.

Dr. Vladimír Zobač deserves special mention. Láď o, díky, že jsi mi byl zvláště v posledních měsících tak skvělým kamarádem.

Some of the free-time activities I shared with several short-term Czecho-Slovak visitors and friends from Brno University of Technology. **Lukáš Kormoš**, **Martin Hrtoň**, **Gabča Schánilcová**, **Vladimír Biolek**, **Pavel Gallina** and **Katarína Rovenská**, thank you all! I díky vám mi na dobu doktorátu zůstanou ty nejlepší vzpomínky!

Milí **rodiče, prarodiče a strýčku**, vám všem děkuji za podporu na dálku. I když to je se mnou někdy těžké, díky, že to tolerujete.

Stando, závěrečné poděkování patří Tobě. Děkuji, že jsi se mnou sdílel nejenom úspěchy, ale že jsi mě dokázal povzbudit v okamžicích zklamání a nejistoty. Nevím, jestli bych bez Tvé každodenní podpory a lásky zvládla dojít až sem.

Contents

List of Abbreviations

BEM	**B**oundary **E**lement **M**ethod
CD	**C**ircular **D**ichroism
CL	**C**athodo**L**uminescence
DDA	**D**iscrete **D**ipole **A**pproximation
ED	**E**lectric **D**ipole
EEG	**E**lectron **E**nergy **G**ain
EEL(S)	**E**lectron **E**nergy **L**oss (**S**pectroscopy)
EM	**E**lectro**M**agnetic
FDTD	**F**inite-**D**ifference **T**ime-**D**omain
FEM	**F**inite **E**lement **M**ethod
FWHM	**F**ull **W**idth at **H**alf **M**aximum
HAADF	**H**igh-**A**ngle **A**nnular **D**ark-**F**ield
HPhP	**H**yperbolic **Ph**onon **P**olariton
HREELS	**High R**esolution **EELS**
IR	**I**nfra**R**ed
LCP	**L**eft-handed **C**ircularly **P**olarized
LDOS	**L**ocal **D**ensity **O**f **S**tates
LO	**L**ongitudinal **O**ptical
LSP	**L**ocalized **S**urface **P**lasmon
LSPh	**L**ocalized **S**urface **Ph**onon
NIR	**N**ear **I**nfra**R**ed
NR	**N**on-**R**etarded
MD	**M**agnetic **D**ipole
MIR	**M**id **I**nfra**R**ed
NR	**N**on-**R**etarded
OAM	**O**rbital **A**ngular **M**omentum
PP	**P**lasmon **P**olariton
PhP	**Ph**onon **P**olariton
PML	**P**efectly **M**atched **L**ayers
PMMA	**P**oly(**M**ethyl **M**eth**A**crylate)
PSF	**P**oint **S**pread **F**unction
QEP	**Q**uasi-**E**lastic **P**eak
RB	**R**eststrahlen **B**and
RCP	**R**ight-handed **C**ircularly **P**olarized
SEIRA	**S**urface-**E**nhanced **IR A**bsorption
SNOM	**S**canning **N**ear-field **O**ptical **M**icroscopy

SP(P)	**S**urface **P**lasmon (**P**olariton)
SPh(P)	**S**urface **Ph**onon (**P**olariton)
STEM	**S**canning **T**ransmission **E**lectron **M**icroscopy
TEM	**T**ransmission **E**lectron **M**icroscope/y
TM	**T**ransverse **M**agnetic
TO	**T**ransverse **O**ptical
VEB	**V**ortex **E**lectron **B**eam
VIS	**VIS**ible (spectrum)
ZLP	**Z**ero **L**oss **P**eak

List of Symbols

a	radius of a sphere
b	impact parameter
$\mathbf{B}$	magnetic B-field
c	speed of light in vacuum
d	slab thickness/distance along an interface
e	elementary charge
E	energy
$\mathbf{E}$	electric field
$\mathbf{F}$	force
F_i	oscillator strength
g	interaction coupling strength
$\mathbf{G}$	Green's dyadic function
$\mathbf{H}$	magnetic H-field
$\hat{H}_I$	interaction Hamiltonian
$\hbar$	reduced Planck's constant
$\mathbf{I}$	unit dyadic
$\mathbf{J}_e$	electric current density
$\mathbf{J}_m$	magnetic current density
k_B	Boltzmann's constant
l	topological charge (winding number)
L	length
$\mathbf{m}$	magnetic dipole
m_e	electron mass
n	(mode) index
N	complex refractive index
n_e	density of free electrons
$\mathbf{p}$	dipole moment
P	differential loss probability
$\mathbf{q}$	wavevector
Q	wavevector component perpendicular to the electron trajectory
q_0	magnitude of wavevector of light in vacuum
$\mathbf{r}$	position vector
R_0	radius of a cylinder
t	time
T	temperature

$t_n^{E/M}$	Mie coefficients
$\mathbf{v}$	velocity (vectorial) of the electron
Z	impedance
$\boldsymbol{\alpha}$	polarizability
ε	relative dielectric permittivity
ε_0	vacuum permittivity
γ	damping
γ_L	Lorentz contraction factor
γ^{NR}	non-retarded transition rate
Γ	electron energy loss/gain probability
κ	in-plane wavevector of surface plasmon polariton
κ_i	oscillator damping
λ	wavelength
μ_0	vacuum permeability
μ_B	Bohr's magneton
$\widehat{\rho}$	charge-density operator
ρ	photonic local density of states
ρ_F	free charge density
σ	surface charge density
Φ	electrostatic potential
ϕ	angle between an interface and electron's trajectory/azimuthal angle
ϕ_{coll}	spectrometer collection semi-angle
ϕ_r	reflection phase
ψ	wavefunction
ω	angular frequency (energy in Hartree atomic units)
Ω_i	oscillator frequency

Introduction: Nanophotonics and electron energy loss spectroscopy

Vision is for most of us the dominant sense responsible for perception of world. Many discoveries have been made since ancient times only thanks to our eyes, despite substantial limits in resolution that our vision has. The human eye, as any lens, also suffers from a number of optical aberrations and works only in a restricted range of wavelengths, in the visible (VIS) spectrum. Nevertheless, curiosity to see things, otherwise unresolvable with naked eyes, has brought up the discovery of magnifying glasses, telescopes and the first optical microscopes in the 16^{th} and 17^{th} century. Optical microscopes boosted rapid advances in biology and medicine and still remain the essential equipment in many scientific laboratories, although, as formulated in 1873 by Ernst Abbe, the ability of traditional optical systems to resolve two close points is diffraction-limited and thus proportional to the wavelength of light [1]. Hence, it is impossible to resolve details and objects smaller than hundred(s) of nanometers with visible light using conventional optical techniques.

One of the possibilities to see objects at the nanoscale or to even resolve atoms is to depart from the use of light for imaging. In 1925, Luis de Broglie postulated the hypothesis that all particles also show a wave nature, which was later confirmed by electron-diffraction experiments showing the wave-like behavior of electrons [2]. The idea of an electron microscope, controlling and focusing electrons extracted from a cathode and accelerated by high voltage (typically hundreds of kilovolts), was developed soon after. Since 1931 when the first prototype of a transmission electron microscope (TEM) using electro-magnetic lenses was demonstrated by Ernst Ruska and Max Knoll [3, 4], electron microscopes have become one of the most important tools in modern science and played a crucial role in many discoveries made in physics, chemistry and biology during the 20^{th} century [5, 6]. Electron microscopes are also used as both analytical and manufacturing tools in the emerging field of nanotechnology and are responsible, e.g., for advances in modern electronics.

The first high-resolution TEM images were generated by illuminating crystalline samples with an extended electron beam diffracting at atomic planes. However, thanks to improvements in electronics, it is nowadays possible to record

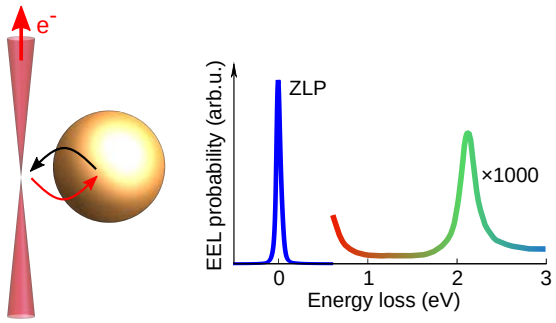

FIGURE 1: Schematics of an electron beam interacting with a sample (a nanoparticle) in aloof geometry and electron energy loss (EEL) spectrum showing an intense zero loss peak (ZLP) and an additional peak corresponding to a collective excitation in the nanoparticle in the low-loss spectral range.

images with a tightly focused, atom-sized electron beam which is scanned at high rates across the sample. The current state-of-art aberration-corrected scanning transmission electron microscopes are routinely capable of sub-Ångstrom resolution in imaging [7, 8] and importantly, various detectors attached to the microscope facilitate to capture diverse signals emerging from the interaction of the fast electrons with matter (e.g., electromagnetic radiation, secondary and Auger electron emission) correlated with the well-controlled position of the electron beam. Scanning transmission electron microscopy (STEM) thus represents a versatile technique for spatially-resolved analysis of materials at the atomic scale.

Importantly, the electrons transmitted through or near the sample (see Fig. 1), which form the high-resolution images, can lose a small fraction of their initial energy. The electron energy loss probability is related to excitations in the sample which they interact with. If the transmitted electrons are analyzed by an electron energy loss spectrometer connected with the microscope column, one can identify excitations in a broad energy range.

At high energies (from approximately 50 eV up to keVs), core losses coming from excitations of electrons in inner atomic shells appear [9, 10]. The core losses providing chemical information can be correlated with atomic-scale imaging [11–13], which makes electron energy loss spectroscopy (EELS) an important analytical technique in STEM.

On the other hand, valence electronic excitations, interband electronic transitions and lattice or molecular vibrations appear at low energies (typically below 50 eV). Many of these low-loss excitations can be probed by optical spectroscopy, where they are important for identifying materials (e.g., molecular vibrations lead to characteristic "fingerprints" in the infrared (IR) spectra [14]) and characterizing their properties. As we will show thorough this thesis, fast electrons

can also couple to the low-energy excitations and the low-loss EELS can provide in many cases complementary spectral information to light-based far-field spectroscopy. Moreover, STEM-EELS brings the possibility of a local excitation of the sample under investigation and accesses some of the excitations that would be "dark" (are not probed) if one used the conventional light-spectroscopy techniques, which is possible due to evanescent nature of a broadband electromagnetic field accompanying the fast electron.

Due to the near-field nature of the fast electron beam probes, the low-loss STEM-EELS is particularly interesting in connection with the field of nanophotonics [15]. Nanophotonics or nano-optics deals with optical properties of various materials at the nanoscale and aims at designing nanostructures with desired optical response and functionalities [16]. Nanophotonics often relies on low-energy collective excitations in matter, such as plasmons (defined as quanta of oscillations of the charge density) or phonons (quanta of lattice vibrations) [17], which can, in certain cases, strongly couple with photons and form a special type of electromagnetic (EM) waves, the so-called polaritons. Polaritonic excitations enable to strongly confine the EM radiation in the near-field region close to the nanostructures, which opens the possibility to convert the propagating EM radiation from the far field into the near-field and vice versa, setting one of the basic principles in nanophotonics [1]. Characterizing the near-field, which is naturally accessible by the fast electron probes [15], is often crucial for understanding the functionality and behavior of photonic nanostructures.

From the various polaritonic excitations, in this thesis we mainly address plasmon and phonon polaritons, respectively. Plasmon polaritons (PPs) can be excited, e.g., in metals (or other materials with free valence electrons such as highly doped semiconductors) [18], whereas phonon polaritons (PhPs) are supported for instance by ionic crystals [19]. Furthermore, the properties of the polaritonic EM field strongly depend on geometry of the nanostructures where they are excited. Surface polaritons can propagate along flat interfaces, or in the case of small particles, one can excite localized surface excitations formed as standing surface-polariton waves. Localized surface plasmons or phonons are commonly exploited as the material excitations allowing EM field localization and enhancement in photonic "nanoantennas" [20, 21], however, patterned thin films made of metals [22], novel 2D materials [23–25] or metamaterials [26] supporting various types of plasmon/phonon polaritons have been also explored as such. Nano-optics nowadays finds applications in optoelectronics [27], spectroscopic (bio)sensing [28, 29], in improving efficiency of solar cells [30], or imaging and microscopy below the diffraction limit [31–33].

The possibility of using EELS for investigation of polaritonic excitations and nanophotonics structures is nowadays well established. Interestingly, early EELS experiments with broad electron beams interacting with metallic foils and interfaces [34, 35] were crucial in identifying bulk plasmons [36, 37] and in the discovery of surface plasmon polaritons (SPPs) in the 1950s and 1960s [38]. Many studies were devoted to momentum-resolved EELS, typically performed with a broad

(unfocused) beam, as such measurements can be related to the dispersion of the excited modes. In Fig. 2(a) we show an example of momentum-resolved EELS adapted from Ref. [82] where the beam probes bulk plasmons and SPP modes coupled across a thin aluminum film.

Since the mid 20th century, EELS has not only contributed to the characterization of SPPs propagating along flat surfaces, but has been also important in mapping localized surface excitations in photonic nanoantennas [39]. For instance, STEM-EELS has been used to analyze localized surface plasmons (LSPs) in individual metallic nanotriangles [40], nanospheres [41, 42], nanocubes [43], nanodiscs [44], nanorods [45, 46] or coupled LSPs in multiple nanoparticles [42, 45, 47–52]. In practice, the spatially resolved spectra, such as those obtained for a beam scanned across a silver nanotriangle (reproduced from Ref. [40]) as shown in Fig. 2(b), can produce a 3-D datacube, used to obtain energy-filtered maps of the nanostructure. These maps visualize the electron energy loss (EEL) probability for a selected energy depending on the beam position in the focal plane and can be linked to the excited near-field (the interpretation of EEL spectra will be discussed more rigorously in Section 1.2). For instance, the maps in Fig. 2(b) extracted for the energies of the observed peaks correspond to the "corner" (dipole) mode (black frame), "edge" (hexapole) mode (blue frame) and breathing mode (red frame) of the silver nanotriangle [83].

Until recently, EELS in STEM has been capable of probing excitations down to the near-infrared (NIR) spectral range (~ 1 eV). However, advances in instrumentation have dramatically improved the spectral resolution [53, 54], and opened access to the very low-energy loss range, where mid-IR (MIR) vibrations can be explored [10]. In Fig. 2(c) we show the first demonstration of vibrational STEM-EELS on a thin slab of hexagonal boron nitride (h-BN) from Ref. [10]. Fig. 2(d) reproduces a measurement of EEL spectra in a magnesium oxide nanocube supporting localized phononic excitations of surface and bulk-like character from Ref. [62]. The nature of these excitation can be revealed in the energy-filtered maps shown in the lower right corner, similarly to the case of the silver nanoprism. The energy-filtered maps at energies 50 meV and 90 meV in the black frame visualize the excitation probability of bulk modes as a function of the electron beam position. As can be observed, these modes are highly localized within the nanocube and can be probed only when the beam directly penetrates the material. On the other hand, the excitation of the localized surface modes is possible even in "aloof" beam incidence which is demonstrated by the energy-filtered maps in the colored frames. We note that besides the selected examples in the right panels of Fig. 2 [10, 62], the improvements in the spectral resolution and detectable energy range of STEM-EELS have stimulated the experimental and theoretical investigation of the nanoscale-resolved vibrational response of organic compounds such as guanine [55, 56], alanine isotopes [84], hydroxyl groups [57] or carbon nitride adsorbates [58], and inorganic materials including several studies of h-BN [10, 59–61], silicon carbide [10], silicon dioxide [63–65] and water [66].

The theoretical interpretation and prediction of the spatially-resolved (ultra)

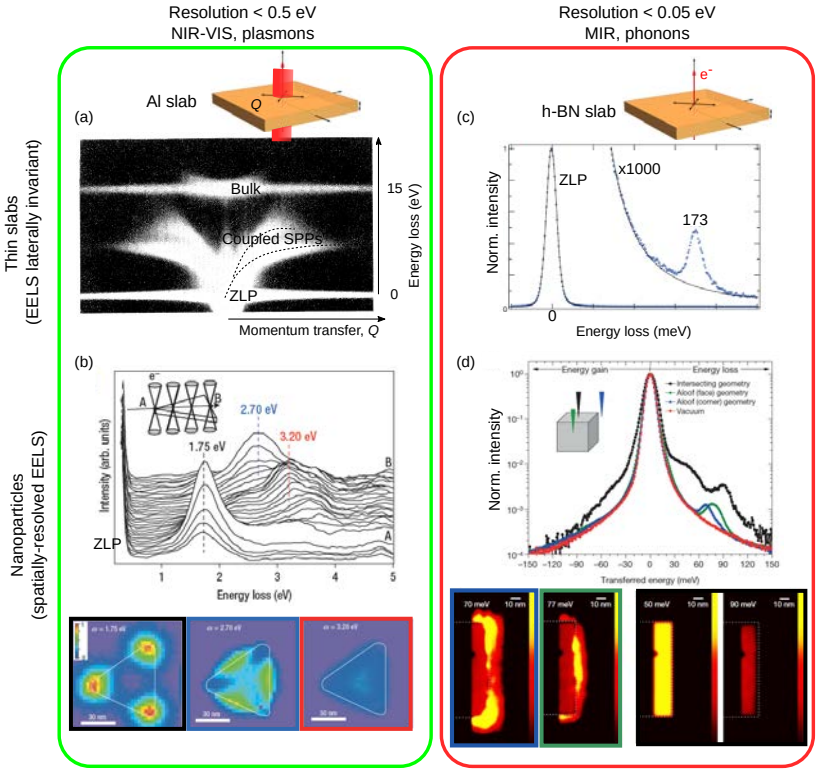

FIGURE 2: Left panel: EELS measurements of plasmonic nanostructures. (a) Momentum-resolved spectrum acquired for a broad beam penetrating a slab made of aluminum. The beam excites SPPs coupled across the slab (schematically shown by the dashed curves) and bulk plasmons. Reprinted with permission from Ref. [82]. ©1973 by the American Physical Society. (b) Spatially-resolved EELS measurement of a silver nanotriangle supporting various localized plasmon modes that are excitable with different efficiency depending on the beam position. Adapted by permission from Springer Customer Service Center GmbH: Springer Nature, Nature Physics [40], ©Nature Publishing group (2007). Right panel: measurements of phononic excitations. (c) EEL spectrum (integrated over scattering momenta) for a focused beam passing through a thin h-BN slab. Adapted by permission from Springer Customer Service Center GmbH: Springer Nature, Nature [10], ©Macmillan Publishers Limited (2014). EEL spectra in (d) correspond to selected beam positions close to a 100-nm MgO cube supporting localized phonon modes. Adapted by permission from Springer Customer Service Center GmbH: Springer Nature, Nature [62], ©Macmillan Publishers Limited (2017). The images below the spectra in (b,d) are energy-filtered maps at energies selected according to the observed peaks and correspond to surface-like or bulk-like plasmonic (left) and phononic (right) modes. In all spectra we denote the zero loss peaks (ZLPs).

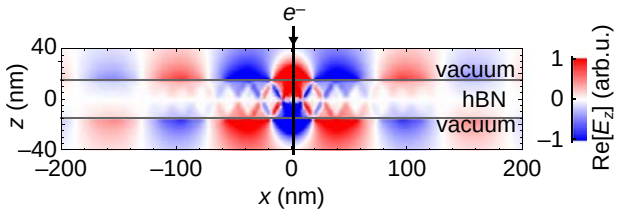

FIGURE 3: Real part of the z component of the total electric field arising in the interaction of an electron beam with energy 60 keV penetrating a 30-nm slab made of h-BN. The characteristic zig-zag pattern and oscillatory field propagating along the slab is caused by the excitation of hyperbolic phonon polariton modes.

low-loss EEL spectra is at the core of this thesis. After going through a basic theoretical background in Chapter 1, in Chapters 2-4 we will discuss various aspects of vibrational EELS and show calculations stimulated by recent experiments with the use of state-of-art instruments. Particularly, we focus on the vibrational EEL spectra from the perspective of nanophotonics and analyze the coupling of the electron beam with optical phonons. In Chapter 5 we theoretically study coupling between different types of excitations and suggest a concept of surface-enhanced EELS in analogy to surface-enhanced optical spectroscopic techniques. In the last Chapter 6, we will consider EELS with the use of special vortex electron beams which carry angular momentum. We will theoretically study the vortex EELS of high-refractive index nanoantennas due to their interest in dielectric nanophotonics.

The possibility of probing the excitation of mid-IR phonons by STEM-EELS together with the current interest in phonon-polariton nanophotonics [19] is a strong the motivation for the first part of this thesis. The low-damped phonon polariton modes excitable in ionic crystals (e.g., SiC, MgO or h-BN) were recently studied by scanning near-field optical microscopy (SNOM) [67–69] and were suggested as candidates for superlensing [70], nanofocusing the IR radiation [71] or sensing [72] to name a few promising applications. In Chapter 2 we introduce special PhPs exhibiting hyperbolic dispersion, which exist in h-BN due to the pronounced anisotropy of its lattice structure and atomic bonding. To correctly interpret experimental results, we apply a theoretical framework based on the dielectric response within classical electrodynamics and obtain EEL spectra of infinite and truncated thin slabs made of h-BN. We show that hyperbolic PhPs (HPhPs) are indeed efficiently excited by the fast electrons (see Fig. 3 showing the calculated electric field arising in the interaction of the electron beam and a h-BN slab), as confirmed by experimental results. Furthermore, depending on the electron beam position with respect to a truncation of the h-BN slab, one can observe excitation of either volume-like or surface guided HPhP modes.

Chapter 3 also deals with vibrational EELS in truncated slabs, but compared

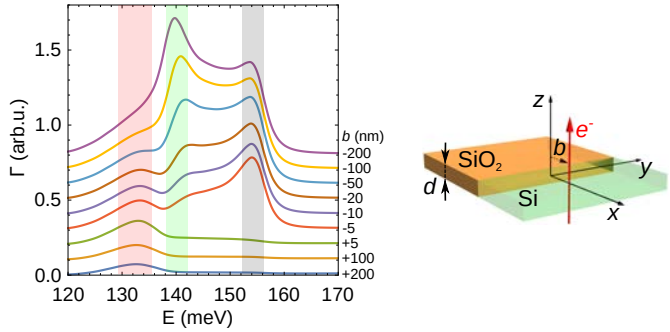

FIGURE 4: EEL spectra calculated for an electron beam positioned close to a junction of silica and silicon slab of thickness d = 30 nm. By changing the impact parameter b as denoted in the schematics, the beam excites different types of excitations. Bulk losses (gray region) and coupled-surface losses (green region) are dominant when the beam penetrates silica whereas the excitation of silica-silicon interface (red region) becomes more intense when the beam approaches the junction and is moved into silicon.

to the analysis in the preceding chapter, this chapter is more focused on understanding the spatial decay of the EEL signal for different modes, which is related to the extent of their induced EM field. In particular, we calculate spatially-resolved EEL spectra close to the truncation of an isotropic slab made of silica and a junction between silica and silicon (see Fig. 4), and compare the theoretical results with experimental data from Ref. [63]. Analogous to the collective SPP excitations in the VIS [73], the silica slab supports coupled-surface phonon polariton (SPhP) modes as well as coupled-edge SPhP modes at the truncation, which are suppressed when (high-refractive-index) silicon is present. These results contribute to the discussion in the STEM-EELS community on the properties and limits of the spatial resolution in vibrational EELS [59, 74]. The excitation of optical phonons typically prevents one from resolving the material interfaces in energy-filtered EEL signal, but it is possible to argue, in light of the results of this thesis, that EEL signal provides valuable information on the excited EM near-field, which is important for nanophotonics applications.

Fast electrons do not only lose energy, they can also gain energy if the sample is already excited and transfers part of that energy to the beam [75, 76]. This situation always occurs as the microscope and the sample holder sits at a finite temperature, which induces thermally excited states in the sample [77]. Chapter 4 discusses finite-temperature effects in EEL and electron energy gain (EEG) spectra detectable at energies comparable with k_BT (k_B being the Boltzmann's constant and T the sample temperature). We introduce a theoretical description for the temperature dependence of the complete spectrum, including the so-called zero

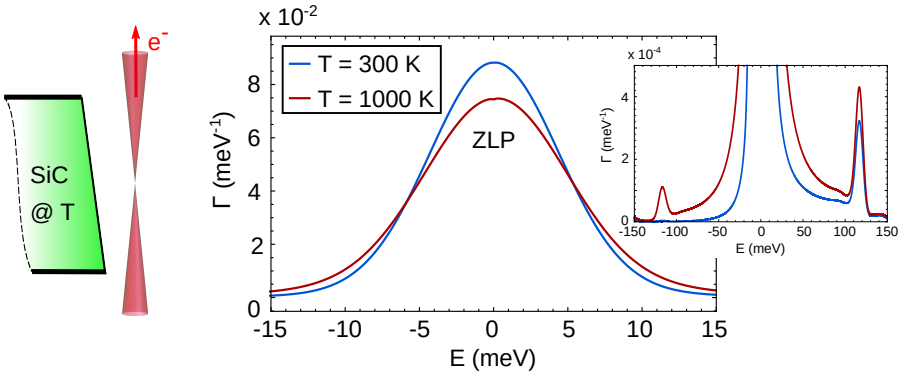

FIGURE 5: EEL spectra theoretically calculated for a 60-keV electron beam passing close to SiC surface under a small tilt angle (as schematically sketched). We consider a finite temperature T of the sample which causes the broadening of the ZLP for T = 1000 K, together with an increase of the intensity of the loss and gain peaks corresponding to the excitation of SPhP in SiC around 120 meV.

loss peak (ZLP) corresponding to the electrons that are transmitted without experiencing any energy loss or gain (see ZLP denoted in the spectrum shown in Fig. 1). Using this theory of temperature-dependent EEL, one can explain experimental observations of a substantial broadening of the "ZLP" when the beam is close to a heated sample as illustrated in Fig. 5.

The capability of probing molecules by state-of-art STEM-EELS and the interpretation of vibrational EEL spectra is the focus of the first part of Chapter 5. In particular, we show that even for non-polaritonic excitations such as molecular vibrations, the shape of the molecular samples needs to be considered in the interpretation of EEL spectra, as we show in the case of spatially-resolved EEL spectra of water bubbles placed on a carbon substrate [66]. The use of a good model description which accounts for the properties of the materials and, very importantly, their geometrical configuration is found to be key for acquiring information on the particular amount of molecules and their orientation.

The improved spectral resolution as well as some of the technique's drawbacks, such as the radiation damage of the molecules [55], motivated the second part of Chapter 5, where we introduce the concept of EM coupling between plasmons and molecular excitations known from optical spectroscopy and apply it to EELS. We suggest "plasmon-enhanced EELS", schematically depicted in Fig. 6, and study the EM coupling of plasmons in metallic nanoantennas and molecular excitons probed by electrons in the eV range (VIS). We demonstrate the working principle of this concept and show that in special cases, the coupling is so efficient that the "strong coupling regime" can be reached and probed by electrons when the interaction rate of the plasmonic antenna and the molecules is faster than respective decay rates of the uncoupled excitations. We also study EEL spectra for

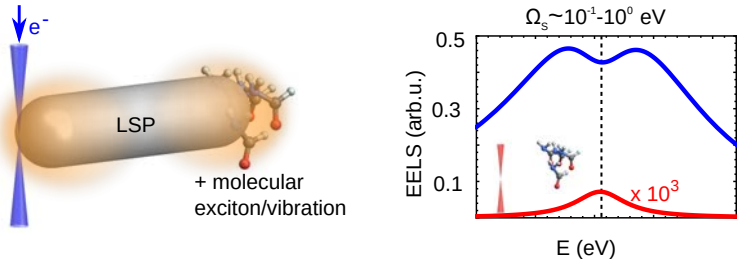

FIGURE 6: Schematics of the suggested surface-enhanced EELS: the electron beam excites a localized surface plasmon (LSP) in the rod which couples via the induced EM field with molecular excitations (either molecular excitons or vibrations). The spectrum of the coupled system (blue) exhibits a broad plasmonic peak with a dip arising due to the coupling. The signal contrast (dip depth) in the coupled scenario is much larger than if the beam probes only the molecules (the peak in the red spectrum).

the system of coupled plasmons and molecular vibrations in the meV range (IR), with similarities to optical surface-enhanced IR spectroscopy. In the IR, the coupling mechanism is usually employed to improve the detection limits of small molecular amounts [28], but the strong coupling regime can be equally reached [72, 78].

We explore all these possibilities, usually studied by far-field optical techniques, with the electron beam as a probe and discuss the differences arising due to the near-field interaction of the electron and the coupled sample. Interestingly, the local probing by the electron beam offers the advantage to control the antenna-molecule coupling strength on demand, so this capability might be used for fundamental studies of different coupling regimes (weak vs. strong coupling). Also, "surface-enhanced EELS" opens the possibility to study molecular samples remotely, thus reducing the radiation damage, and with increased sensitivity compared to conventional EELS.

Other novel options to probe matter have been opened by introducing shaped electron beams with a well-defined phase structure in the plane transverse to the beam propagation [79–81]. In particular, here we focus on vortex electron beams (VEBs) carrying orbital angular momentum (OAM), which can be created, e.g., if a non-vortex beam diffracts on a specially designed aperture, or if it interacts with a magnetic monopole-like field or if it passes through a phase plate. In Chapter 6 we explore the possibility of measuring EELS with VEB instead of the conventional beam. We develop a framework for the interaction of VEBs with arbitrarily shaped photonic nanostructures implementing VEBs within a classical electrodynamics treatment of the low-loss EELS. We apply our theoretical approach to address VEB-EELS of dielectric antennas made of silicon (see schematics in Fig. 7). We show how to exploit the use of (vortex) electron beams to distinguish modes of electric and magnetic nature from the EEL spectra. We also analyze

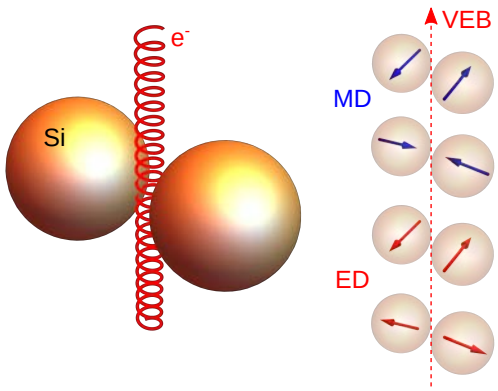

FIGURE 7: VEB represented as a spiralling electric current interacting with a dimer consisting of two silicon spheres, which support modes of both electric and magnetic nature. VEB can excite a set of bonding and anti-bonding modes of the dimer as schematically depicted for the case of coupled electric and magnetic dipoles (ED and MD, respectively).

nanostructures exhibiting optical dichroism, which also yield differences in the spectral response when probed by VEBs with OAM of opposite signs. We thus show that VEBs are naturally capable of performing chiral-specific spectroscopy at the nanoscale.

Chapter 1

Theoretical background

Before we start the thorough discussion of the topics mentioned in the introduction, in the following sections we provide information on basic concepts and methods exploited in this thesis. In Section 1.1 we introduce plasmon and phonon polaritons in the context of optical properties of solids. In Section 1.2 we present a common theoretical background which allows for calculations of low-loss EEL spectra in the framework of classical electrodynamics, showing how polaritonic excitations can be probed by fast electrons. We also briefly discuss the link between the classical description and (semi)-quantum formalisms. Finally, we present some practical aspects of the STEM-EELS technique in Section 1.3, which will be important for theoretical modeling of experiments.

1.1 Low-energy collective excitations in matter

Low-energy collective excitations in matter, namely phonons and plasmons, will play a crucial role in many parts of this thesis. As both phononic and plasmonic excitations arise due to the oscillation of charges in matter, they are expressed as such in the optical response of the materials where they are induced. In the following sections, we thus introduce simple models to describe the optical properties of plasmonic and phononic materials and we also show how polaritons can emerge in different geometrical arrangements, in particular in the bulk, at interfaces and in finite nanostructures.

1.1.1 Optical properties of metals and insulators

It is illustrative to start by discussing the propagation of EM waves in bulk materials. If we consider a linear, homogeneous and isotropic material, its optical properties can be characterized by a relative permittivity (dielectric function) ε. The propagation of an electromagnetic wave in a such medium can be expressed by the wave equation. The wave equation for the electric field $\mathbf{E}(\mathbf{r}, t)$ in absence of free currents is [85]:

$$\nabla(\nabla \cdot \mathbf{E}) - \nabla^2 \mathbf{E} + \varepsilon\mu_0\varepsilon_0 \frac{\partial^2 \mathbf{E}}{\partial t^2} = \mathbf{0}, \tag{1.1}$$

where ε_0 and μ_0 are the permittivity and the permeability of vacuum, respectively, related to the speed of light in vacuum as $c = 1/\sqrt{\varepsilon_0\mu_0}$. We now substitute the Gauss's law

$$\nabla \cdot \mathbf{E} = \frac{\rho_F}{\varepsilon_0\varepsilon} \tag{1.2}$$

in Eq. (1.1), consider zero free charge density, $\rho_F = 0$, and perform the Fourier transform[1] to obtain

$$(-q^2 + \varepsilon\omega^2/c^2)\mathcal{E} = \mathbf{0}, \tag{1.5}$$

where ω is angular frequency, $\mathbf{q}$ is wavevector and $\mathcal{E}$ is the Fourier-transformed electric field. If we discard the trivial solution $\mathcal{E}(\mathbf{q}, \omega) = \mathbf{0}$, the transformed wave equation (1.5) sets a condition for the wavevector q:

$$q = \frac{\omega\sqrt{\varepsilon}}{c} = q_0\sqrt{\varepsilon}, \tag{1.6}$$

where $q_0 = \omega/c$ is the wavevector in free space (vacuum). The wave propagation will be governed by the dielectric permittivity, which is related to the (complex) refractive index of the material $N(\omega) = \sqrt{\varepsilon(\omega)}$. Interestingly, the propagation of waves is forbidden for frequencies at which the permittivity becomes negative [for $\varepsilon < 0$, q is imaginary, see Eq. (1.6)]. Such a scenario can arise, as we show below, e.g. in metals or in ionic crystals.

When an external field is applied, metals are able to screen the field due to the presence of free valence electrons, the so-called free electron gas. The dielectric response of metals can be in some cases well described by the Drude model [86]:

$$\varepsilon_D(\omega) = \varepsilon(\infty) - \frac{\omega_p^2}{\omega^2 + i\gamma\omega}, \tag{1.7}$$

where $\varepsilon(\infty)$ is a contribution of an ionic background and interband transitions, γ is the damping, and we defined the bulk plasma frequency

[1] Thorough the thesis we assume the following form of the Fourier transform of a function $F(\mathbf{r}, t)$:

$$\mathcal{F}(\mathbf{q}, \omega) = \mathrm{FT}\{F(\mathbf{r}, t)\} = \int d\mathbf{r}\, dt\, F(\mathbf{r}, t) \exp[-i(\mathbf{q}\cdot\mathbf{r} - \omega t)], \tag{1.3}$$

and the inverse Fourier transform

$$F(\mathbf{r}, t) = \mathrm{FT}^{-1}\{\mathcal{F}(\mathbf{q}, \omega)\} = \frac{1}{(2\pi)^4} \int d\mathbf{q}\, d\omega\, \mathcal{F}(\mathbf{q}, \omega) \exp[i(\mathbf{q}\cdot\mathbf{r} - \omega t)]. \tag{1.4}$$

$$\omega_p = \sqrt{\frac{n_e e^2}{m_e \varepsilon_0}}, \tag{1.8}$$

where n_e is density of free electrons, e is the elementary charge and m_e is the (effective) mass of the electron. By analyzing the Drude dielectric function in Eq. (1.7) we find that that $\varepsilon_D < 0$ for $\omega < \omega_p/\sqrt{\varepsilon(\infty)}$ (considering $\gamma \to 0$). Below the frequency threshold $\omega_p/\sqrt{\varepsilon(\infty)}$, the free electrons can oscillate in counterphase with respect to the applied field and thus compensate for it, which leads to the high reflectivity of metals as EM waves do not propagate through the metallic bulk.

In Fig. 1.1(a) we plot the dielectric function of Eq. (1.7) considering $\varepsilon(\infty) = 1$, $\hbar\omega_p = 15.1$ eV ($\hbar$ is the reduced Planck's constant) with zero damping ($\gamma = 0$), which becomes negative for $\hbar\omega < 15.1$ eV. These parameters approximately mimic the response of aluminum. We note that the simple Drude model typically works well at IR frequencies, but it fails to describe the optical response of some noble metals in the visible. For instance, interband transitions appearing in gold above 2 eV or in silver above 3.5 eV require to complete this model if one wants to describe the optical response in this spectral region accurately.

Similarly, the dielectric response in insulating polar materials can become negative if the material contains highly polarizable ions, typically arranged in a well-defined lattice supporting phononic modes. The possibility of excitation of optical phonons in the crystal can be described by the dielectric response as [17]:

$$\varepsilon(\omega) = \varepsilon(\infty) + \frac{\varepsilon(\infty) - \varepsilon(0)}{\omega^2/\omega_{TO}^2 - 1}, \tag{1.9}$$

where $\varepsilon(0)$ is the static dielectric constant and ω_{TO} is the transverse optical mode frequency for which the polarization density would be perpendicular to the propagation of the wave in the crystal. On the other hand, the polarization of the lattice can be along the wave propagation, which is possible if $\varepsilon(\omega) = 0$. After combining this condition with Eq. (1.9), the longitudinal optical (LO) mode frequency can be expressed as [17]:

$$\omega_{LO}^2 = \frac{\varepsilon(0)}{\varepsilon(\infty)}\omega_{TO}^2, \tag{1.10}$$

which is known as the Lyddane-Sachs-Teller relationship. The dielectric function in Eq. (1.9) can be then rewritten in the commonly expressed Lorentz-Drude formula (including the damping γ) as:

$$\varepsilon_{LD}(\omega) = \varepsilon_\infty \left(1 + \frac{\omega_{LO}^2 - \omega_{TO}^2}{\omega_{TO}^2 - \omega^2 - i\gamma\omega}\right). \tag{1.11}$$

We note that $\mathrm{Re}\,[\varepsilon_{LD}]$ becomes negative for $\omega_{TO} < \omega < \omega_{LO}$ (exactly valid for $\gamma = 0$, otherwise the condition is approximate). This frequency region is often

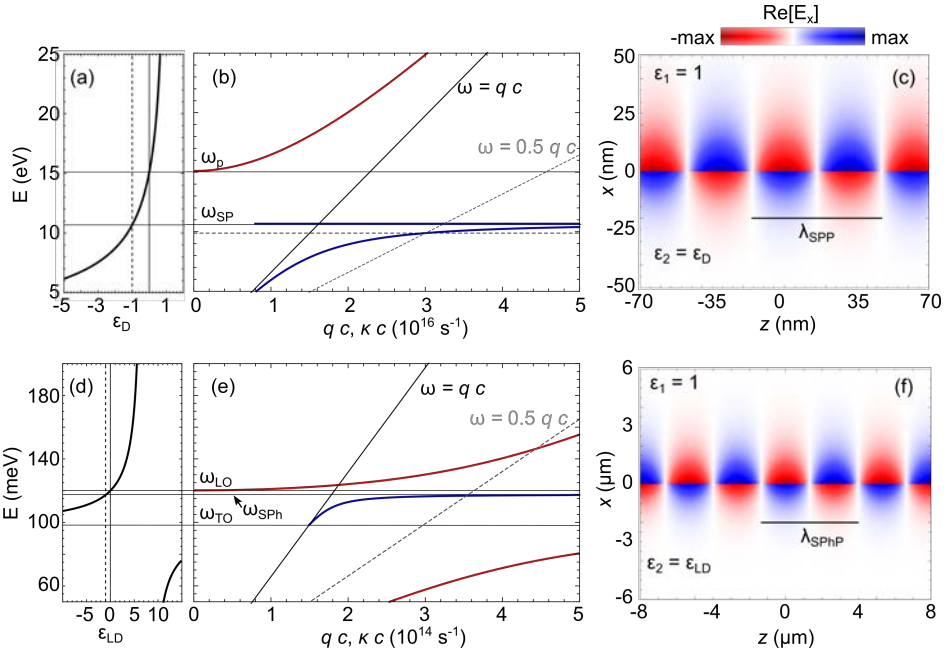

FIGURE 1.1: (a) Drude dielectric function [Eq. (1.7)] with the bulk plasmon energy $\hbar\omega_p = 15.1$ eV, $\varepsilon(\infty) = 1$ and $\gamma = 0$. (b) Dispersion of the bulk plasmon polariton according to Eq. (1.6) (red) and dispersion of the surface plasmon polariton from Eq. (1.16) (blue) considering $\varepsilon_1 = 1$ and $\varepsilon_2 = \varepsilon_D$ taken from (a). The bulk plasmon energy at ω_p and the surface plasmon limit given by Eq. (1.17a) are plotted with horizontal black lines. The dispersion for a photon in vacuum given by $\omega = qc$ is also plotted. (c) Real part of the x component of the electric field, $\mathrm{Re}[E_x]$, of a surface plasmon polariton at the interface of vacuum and metal characterized by the dielectric response from (a) at energy of $\hbar\omega = 9.89$ eV [marked by the dashed horizontal line line (b)]. (d) Lorentz-Drude dielectric function [Eq. (1.11)] with parameters $\hbar\omega_{TO} = 98$ meV, $\hbar\omega_{LO} = 120$ meV, $\varepsilon(\infty) = 6.7$ and $\gamma = 0$. (e) Bulk (red) and surface (blue) phonon polariton dispersions obtained from Eq. (1.6) and Eq. (1.16), respectively, considering $\varepsilon_1 = 1$ and $\varepsilon_2 = \varepsilon_{LD}$ taken from (d). The horizontal lines denote the transverse and longitudinal optical phonon energies (LO corresponds to the bulk phonon excitation) and the surface phonon energy given by Eq. (1.17b). We note that the horizontal axis of the dispersion plots correspond to either qc for the bulk dispersion, or κc for the surface polariton dispersion. (f) $\mathrm{Re}[E_x]$ of a surface phonon polariton at the interface of vacuum and the ionic crystal characterized by the dielectric response plotted in (d) at en energy of $\hbar\omega = 116.8$ meV. Notice different length scale with respect to (c).

denoted as "Reststrahlen band" due to the forbidden propagation of the electromagnetic waves inside the material. In Fig. 1.1(d) we consider a material featuring optical phonons in the mid-IR characterized by the parameters $\varepsilon(\infty) = 6.7$, $\hbar\omega_{TO} = 98$ meV, and $\hbar\omega_{TO} = 120$ meV, which characterize the properties of SiC. However, for illustrative purpose of the remaining parts of the plot, we neglect the damping and set $\gamma = 0$.

1.1.2 Surface and bulk polaritons

Although electromagnetic waves can hardly propagate inside materials characterized by the Drude model [Eq. (1.7)] below $\omega_p/\sqrt{\varepsilon(\infty)}$, and in the Reststrahlen band ($\omega_{TO} < \omega < \omega_{TO}$) arising from the Lorentz-Drude dielectric function [Eq. (1.11)], we now discuss a special type of EM waves that can exist at the boundaries of such media.

If we consider an infinite interface at $x = 0$ between materials characterized by dielectric functions ε_1 (for $x > 0$) and ε_2 ($x < 0$), the condition for the existence of surface waves can be derived by rigorously solving Maxwell's equations for two half-spaces and imposing the boundary conditions for the fields at the interface. The resulting electromagnetic field associated to a surface wave exponentially decaying in the direction transverse to the interface has transverse magnetic (TM) character. Assuming a geometrical arrangement as the one defined in Fig. 1.1(c,f), the components of the electric field (E_x, E_z) and the out-of-plane magnetic field H_y are expressed as [87, 88]:

$$E_{x,1} = -e_0 \frac{\kappa}{\omega\varepsilon_0\varepsilon_1} e^{i\kappa z} e^{-k_1 x}, \quad (1.12a) \qquad E_{x,2} = -e_0 \frac{\kappa}{\omega\varepsilon_0\varepsilon_2} e^{i\kappa z} e^{k_2 x}, \quad (1.13a)$$

$$E_{z,1} = e_0 \frac{ik_1}{\omega\varepsilon_0\varepsilon_1} e^{i\kappa z} e^{-k_1 x}, \quad (1.12b) \qquad E_{z,2} = -e_0 \frac{ik_2}{\omega\varepsilon_0\varepsilon_2} e^{i\kappa z} e^{k_2 x}, \quad (1.13b)$$

$$H_{y,1} = e_0 e^{i\kappa z} e^{-k_1 x}, \quad (1.12c) \qquad H_{y,2} = e_0 e^{i\kappa z} e^{k_2 x}, \quad (1.13c)$$

where the subscripts $1, 2$ denote the field components in environment characterized by ε_1 and ε_2, respectively, e_0 is the amplitude of the electric field, κ is the propagation wavevector along the interface and we defined

$$k_1^2 = \kappa^2 - q_0^2\varepsilon_1, \quad (1.14a)$$

$$k_2^2 = \kappa^2 - q_0^2\varepsilon_2. \quad (1.14b)$$

Importantly, the boundary conditions at the interface yield

$$\frac{k_1}{k_2} = \frac{-\varepsilon_1}{\varepsilon_2}, \quad (1.15)$$

which can be for positive and real $k_{1/2}$ (so that the wave's amplitude decays with increasing distance from the interface $|x|$) fulfilled only when the dielectric functions ε_1 and ε_2 have opposite signs. Such a situation can arise at an interface between a polaritonic material characterized by Eq. (1.7) or Eq. (1.11) (assuming that the damping γ is small) and a dielectric material or vacuum where $\mathrm{Re}[\varepsilon] > 0$. Combining Eqs. (1.14) and Eq. (1.15), one obtains the dispersion of the surface wave, i.e., the relationship between its propagation wavevector and frequency:

$$\kappa = q_0 \sqrt{\frac{\varepsilon_1(\omega)\varepsilon_2(\omega)}{\varepsilon_1(\omega) + \varepsilon_2(\omega)}}. \tag{1.16}$$

In Fig. 1.1(b,e) we analyze the surface polariton and bulk polariton dispersions corresponding to an interface between vacuum and a plasmonic material characterized by Drude dielectric function [Eq. (1.7)] and a material featuring optical phonon modes characterized by Lorentz-Drude response [Eq. (1.11)] shown in Fig. 1.1(a,d), respectively. The surface polariton dispersions plotted with blue lines, appear below ω_p for the plasmon polariton in Fig. 1.1(b) and between ω_{TO} and ω_{LO} for the phonon polariton in Fig. 1.1(e). Both cases show the same asymptotes: for high wavevectors, the curves approach the surface plasmon given by $\varepsilon_D(\omega_{SP}) = -1$ or the surface phonon limit, given by the condition $\varepsilon_{LD}(\omega_{SPh}) = -1$, which yield the frequencies

$$\omega_{SP} = \frac{\omega_p}{\sqrt{1 + \varepsilon(\infty)}}, \tag{1.17a}$$

$$\omega_{SPh} = \frac{\sqrt{\varepsilon(\infty)\omega_{LO}^2 + \omega_{TO}^2}}{\sqrt{1 + \varepsilon(\infty)}}, \tag{1.17b}$$

respectively, arising from the poles of Eq. (1.16), i.e. the condition $\varepsilon_1 + \varepsilon_2 = 0$. On the other hand, for low wavevectors, both surface polariton dispersions approach the free-space photon dispersion given by $q_0 = \omega/c$, but do not intersect it which has practical consequences: surface plasmon and surface phonon polaritons at a perfectly semi-infinite interface cannot be excited by optical plane waves.

The red curves in graphs 1.1(b,e) show the bulk dispersions given by Eq. (1.6) which appear in the frequency ranges for which the dielectric function (its real part) is positive. In both the plasmonic and phononic case we observe the upper branch starting at frequencies ω_p or ω_{LO}, respectively, asymptotically approaching $\omega = qc/\sqrt{\varepsilon(\infty)}$ for higher wavevectors. The phononic material further exhibits the lower bulk polaritonic branch between the asymptotes $\omega = qc/\sqrt{\varepsilon(0)}$ for low q and ω_{TO} for high q.

Finally, in Fig. 1.1(c) we plot the electric field [the real part of its x component, Eqs. (1.12a) and (1.13a)] corresponding to excitation of the polaritonic surface-plasmon wave at an energy 9.55 eV, considering the interface of vacuum and the

material characterized by ε_D shown in Fig. 1.1(a). We denote the SPP wavelength obtained as $\lambda_{SPP} = 2\pi/\kappa$. Similarly, we show the field associated to the surface-phonon polariton at energy 115 meV for the interface between vacuum and the material described by ε_{LD} as plotted in Fig. 1.1(d). Notice the difference between typical wavelengths of the plasmonic and phononic surface waves ($\lambda_{SPP} = 63$ nm vs. $\lambda_{SPhP} = 5308$ nm) stemming from the typical frequencies of oscillations of free electrons compared to those of the crystal lattice, which typically emerge in the VIS and IR, respectively.

1.1.3 Plasmon and phonon polaritons in confined geometries

Let us continue now from the description of EM fields in bulk materials and their infinite interfaces to qualitative discussion on EM modes supported by finite nanostructures. In particles of sizes comparable to the wavelength of the driving EM field, we can sometimes excite confined, standing EM waves. For instance, the so-called localized surface plasmons or phonons (LSP or LSPh) are typically excitable in nanostructures made of materials supporting plasmon or phonon polaritons.

An illustrative example to describe formation of resonances in a confined geometry is a long wire of length L representing a 1-D EM cavity. Such geometry gives rise to the appearance of Fabry-Perot resonances along the wire. The resonance condition of the modes is [89–93]:

$$2q_{1D}L + 2\phi_r = 2\pi n, \tag{1.18}$$

where q_{1D} is the wavevector of a polariton propagating along the wire, ϕ_r is the reflection phase at the ends of the wire and $n \in \mathbb{N}$, $n > 0$ is the resonance order. Both the parameters q_{1D} and ϕ_r depend on geometry of the wire. For a cylindrical wire of radius R_0 with hemispherical apexes of the same radius, analytical expressions are provided, e.g., in Ref. [92]. The wavevector of a fundamental TM mode of an infinite cylinder with dielectric function ε ($\mathrm{Re}[\varepsilon] < 0$)[2] is given by the transcendental equation:

$$q_1 \frac{H_0^{(1)}(q_1 R)}{H_1^{(1)}(q_1 R)} = \frac{q_2}{\varepsilon} \frac{J_0(q_2 R)}{J_1(q_2 R)}, \tag{1.19}$$

where J_m are the Bessel functions of the first kind and order m, $H_m^{(1)}$ are the Hankel functions of the first kind and order m, and

$$q_1 = \sqrt{q_0^2 - q_{1D}^2}, \qquad q_2 = \sqrt{q_0^2 \varepsilon - q_{1D}^2}. \tag{1.20}$$

[2] We note that higher-order modes can be also excited, but we consider their excitation probability to be much smaller than that of the fundamental mode [94, 95].

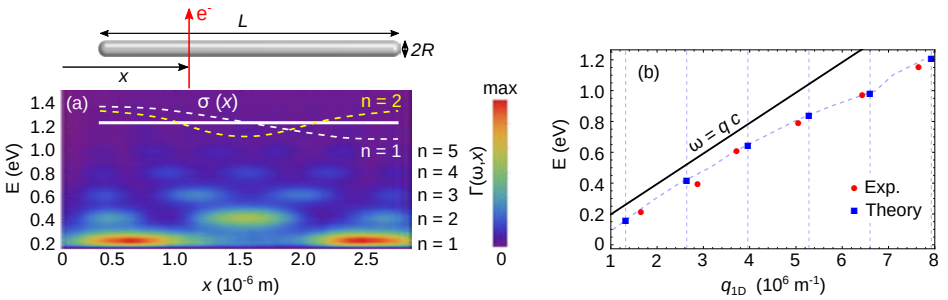

FIGURE 1.2: (a) Measured electron energy loss probability Γ for an electron beam with energy 60 keV scanned close to a silver wire of length $L = 3.2\,\mu m$ and radius $R_0 = 30$ nm (as denoted in schematics). x is parallel to the long axis of the wire. The inset shows a schematic representation of surface charge density $\sigma(x)$ (and field maxima) excited along the rod, the white bar is in the same scale and positioned in x according to the experimental measurement. The data are integrated over a scanning direction parallel to the short rod axis and smoothed. (b) Extracted experimental (red circles) and theoretical (blue squares) dispersion of the discrete modes excited in the wire. The theoretical prediction was obtained with dielectric data of Ag from Ref. [96]. The black line is the dispersion of a photon in vacuum. The experimental data are acquired and preliminary post-processed from EELS measurements by Prof. Andrey Chuvilin in NanoGUNE (San Sebastián).

The reflection phase (considering $R_0 \ll 2\pi/q_{1D}$) can be expressed as [92]

$$\phi_r = -i \ln\left(\frac{i/R_0 - q_{1D}/\omega}{i/R_0 + q_{1D}/\omega}\right). \tag{1.21}$$

We test the analytical expressions providing the energies and wavevectors of the discrete EM cavity modes by comparing theory with experimental results. In Fig. 1.2(a) we plot spatially resolved spectra recorded with an electron beam placed at different positions along a silver wire of length $L = 3.2\,\mu m$ and radius $R_0 = 30$ nm (x is parallel to the long rod axis). In this example, the maxima of the excitation probability appear approximately for the positions x where the maxima of EM density of states (and also the excited EM field) occur [93, 97]. We can observe that for a discrete set of energies, a different number of local maxima of the EEL signal appear, related to the maxima of surface charge density induced at the wire, which can be assigned to a set of modes of order $n = 1, 2, ...$ The first-order resonance arises from a dipole-like arrangement of surface charges along the wire with a node in the middle of the wire, as schematically sketched in the inset of Fig. 1.2(a) (white dashed line denoted as $n = 1$). Similarly, for $n = 2$, two nodes and three positions of the maxima (anti-nodes) of the surface charge are evident. Hence, the quantized wavevectors can be obtained as $q_{1D} = \pi/\Delta x$,

where Δx is distance between tha maxima (see similar analysis in Ref. [98]). We plot the resulting discrete dispersion in Fig. 1.2(b) by red circles.

The experimentally obtained data based on the position of the maxima from EELS measurements (red dots) agree very well with the theoretical prediction (blue squares) in Fig. 1.2(b). In the theoretical description, we modeled the dielectric response of silver by tabulated data from Ref. [96] and considered the experimentally measured dimensions of the wire. The small differences between the theoretical and experimental data arise probably due to geometrical imperfections and a presence of a substrate which is not included in the theory. In Chapter 5 we further discuss the EM modes emerging in metallic rods and wires and discuss them in the context of surface-enhanced spectroscopy.

Similarly to the long wires, localized EM modes in differently shaped nanoparticles made of plasmonic or phononic materials have been thoroughly analyzed, for instance in spheres [99, 100], in ellipsoids [101] or in cubes [43, 102]. We will deal with some of the well-defined modes in confined geometries excited by electron beams in the following chapters.

1.2 Theoretical description of low-energy EELS

In the previous section we described that the surface polaritons, evanescent waves that can propagate along interfaces of polaritonic media and dielectrics, cannot be at a perfectly semi-infinite interface excited by plane waves due to the momentum mismatch of the polariton and a free-space photon [see the corresponding dispersions in Fig. 1.1(b,e)]. Hence, alternative ways for the excitation of surface polaritons are needed. For instance, the missing momentum can be supplied via diffraction gratings [103, 104] or discontinuities at the metal-dielectric interface which provide the necessary momentum [105]. Another option is to use localized probes such as sharp tips in SNOM, or fast electrons.

One of the most direct manners of experimentally probing polaritonic as well as other excitations in matter is by obtaining EEL spectra. Therefore we develop in the following a theoretical framework that addresses the energy loss experienced by the fast probing electrons within the classical dielectric formalism. We will also briefly address non-classical approaches to describe EELS in the end of the chapter.

1.2.1 Electron beam as a source of EM field

Within the framework of classical electrodynamics a fast electron beam can be approximated as a charge localized at position $\mathbf{r}_b = \mathbf{v}t$, where $\mathbf{v}$ is the electron's velocity and t time. The electron produces a current density which can be expressed in the real and in the Fourier $(\mathbf{q}, \omega)$ space as:

$$\mathbf{J}_e(\mathbf{r}, t) = -e\mathbf{v}\delta(\mathbf{r} - \mathbf{r}_b(t)), \tag{1.22a}$$

$$\mathcal{J}_e(\mathbf{q}, \omega) = \mathrm{FT}\{\mathbf{J}_e(\mathbf{r}, t)\} = -2\pi e\mathbf{v}\,\delta(\omega - \mathbf{q}\cdot\mathbf{v}), \tag{1.22b}$$

where $\delta(x)$ is the Dirac delta function.

Now we can reconsider the wave equation transformed in the $(\mathbf{q}, \omega)$ space [Eq. (1.5)] and the Gauss's law with the electron as a source of free charge $\rho_F(\mathbf{q}, \omega) = \mathbf{J}_e(\mathbf{q}, \omega)/\mathbf{v}$. The electric field $\mathcal{E}(\mathbf{q}, \omega)$ produced in the medium [characterized by dielectric response $\varepsilon(\omega)$] by the fast electron is given by:

$$\mathcal{E}(\mathbf{q}, \omega) = \frac{2\pi i e}{\varepsilon_0}\delta(\omega - \mathbf{q}\cdot\mathbf{v})\frac{\mathbf{q}/\varepsilon - \mathbf{v}q_0/c}{q^2 - q_0^2\varepsilon}. \tag{1.23}$$

The delta function is related to conservation of energy and sets the condition for wavevectors that can be provided by the electron at a certain energy [15]. Importantly, at a certain energy, the electron beam can couple with wavevectors that are larger than those of a free-space photon as $\omega/v > \omega/c$. For instance, the fast electrons can excite polaritons in the energy-momentum region given by the condition $\omega/v \lesssim \kappa$ with κ given by Eq. (1.16). In Figs. 1.1(b,e) we plot this

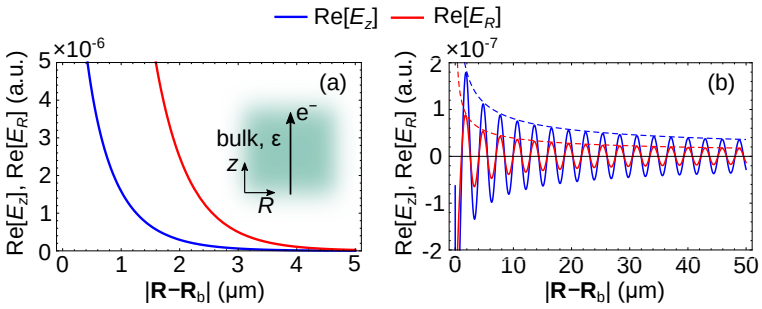

FIGURE 1.3: Real parts of components of the electric field [as from Eq. (1.24)] produced by an electron with energy 60 keV (moving at velocity $v = 0.446\,c$) in a fixed transverse plane $z = 100$ nm. The electron is moving in an unbounded medium as sketched in the inset characterized by the dielectric function from Fig. 1.1(d) mimicking SiC. The field is evaluated at energies (a) $\hbar\omega = 120$ meV and (b) at $\hbar\omega = 90$ meV. For the latter energy, the electrons produce Čerenkov radiation which yields the oscillatory character of the field with an envelope decaying as $\propto 1/\sqrt{R}$ [dashed lines in (b)].

threshold for electrons moving at the speed $v = 0.5\,c$ (typical speeds of electrons in TEM are in range of $0.3 - 0.8\,c$). We can see that the slower the electron is, the closer the resulting excitation gets to the static surface plasmon or surface phonon limit [Eqs. (1.17)].

To have a better intuition about the field accompanying a fast electron moving in bulk medium, we transform the field in Eq. (1.23) to the real space. Considering the electron moving parallel to the z axis along the trajectory $\mathbf{r}_b(t) = (x_b, y_b, z = vt) = (\mathbf{R}_b, z = vt)$ one obtains:

$$\mathbf{E}_{el}(\mathbf{r},\omega) = \frac{2e\omega\, e^{i\omega z/v}}{4\pi\varepsilon_0\gamma_L v^2}\left[-K_1\left(\frac{\omega|\mathbf{R}-\mathbf{R}_b|}{\gamma_L v}\right)\frac{\mathbf{R}-\mathbf{R}_b}{|\mathbf{R}-\mathbf{R}_b|} + \frac{i}{\gamma_L}K_0\left(\frac{\omega|\mathbf{R}-\mathbf{R}_b|}{\gamma_L v}\right)\hat{\mathbf{z}}\right], \tag{1.24}$$

where $\gamma_L = 1/\sqrt{1-\varepsilon v^2/c^2}$ is the Lorentz contraction factor, and $K_m(x)$ are the modified Bessel functions of the second kind of order m. The field produced by the electron moving in a medium characterized by ε given by Eq. (1.24) with $v^2 < c^2/\varepsilon$ (so that the argument of the Bessel functions is real) has an evanescent character and monotonously decays with distance from the electron's trajectory in the transverse plane. On the other hand, if the electron's velocity exceeds the phase speed of light in the medium ($v > c/\sqrt{\varepsilon}$), the so-called Čerenkov photons are emitted and the field exhibits oscillatory behavior. In Fig. 1.3(a,b) we illustrate these two regimes by plotting the dependence of the field components on the radial coordinate (from the electron trajectory in a fixed z plane) considering the electron moving in a phononic material characterized by the dielectric response as that shown in Fig. 1.1(d).

1.2.2 Classical theory of electron energy loss

The field of the fast electron acting on a (nanostructured) material gives rise to an induced EM field, $\mathbf{E}^{\mathrm{ind}}(\mathbf{r},t)$, $\mathbf{B}^{\mathrm{ind}}(\mathbf{r},t)$, which acts back on the electron. From this classical perspective, the resulting EM force $\mathbf{F}(\mathbf{r},t) = -e(\mathbf{E}^{\mathrm{ind}}(\mathbf{r},t) + \mathbf{v}\times\mathbf{B}^{\mathrm{ind}}(\mathbf{r},t))$ is responsible for the energy loss of the fast electron, which can be evaluated by integrating the force along the trajectory of the electron [38, 106]. If we assume that the recoil of the fast electron due to the perpendicular force is negligible (which is a reasonable assumption for highly energetic electrons [107]), we can express the energy loss ΔE as:

$$\Delta E = e\int dt\, v E_z^{\mathrm{ind}}(\mathbf{r}_b(t),t) = -\int dt \int d\mathbf{r}\, E_z^{\mathrm{ind}}(\mathbf{r}(t),t) J_{e,z}(r,t), \tag{1.25}$$

where we considered the electron is moving parallel to the z axis, E_z^{ind} is the z component of the induced electric field of an arbitrary sample, and we used Eq. (1.22a) for the expression of the current. After applying properties of the Fourier transform of real functions,[3] the above equation can be rewritten as:

$$\begin{aligned}\Delta E &= -\frac{1}{\pi}\int_0^\infty d\omega \int d\mathbf{r}\, \mathrm{Re}\left[E_z^{\mathrm{ind}}(\mathbf{r}(t),\omega)\, J_{e,z}^*(\mathbf{r},\omega)\right] \\ &= \frac{e}{\pi}\int_0^\infty d\omega \int dz\, \mathrm{Re}\left[E_z^{\mathrm{ind}}(x_b,y_b,z;\omega)\exp\left(-\frac{i\omega z}{v}\right)\right].\end{aligned} \tag{1.26}$$

We next define the probability $\Gamma(\omega)$ that the electron loses energy $\hbar\omega$ (the so-called electron energy loss probability) according to [38]

$$\Delta E = \int_0^\infty d\omega\, \hbar\omega\, \Gamma(\omega). \tag{1.27}$$

After combining Eqs. (1.27) and (1.26), we obtain the relationship:

$$\Gamma(\omega) = \frac{e}{\pi\hbar\omega}\int_{-\infty}^{\infty} dz\, \mathrm{Re}\left[E_z^{\mathrm{ind}}(x_b,y_b,z;\omega)\exp\left(-\frac{i\omega z}{v}\right)\right]. \tag{1.28}$$

The z component of the induced field in a non-magnetic environment can be expressed in terms of the Green's dyadic function $\mathbf{G}$ as

$$E_z^{\mathrm{ind}}(\mathbf{r},\omega) = ie\mu_0\omega\int_{-\infty}^{\infty} dz' G_{zz}(\mathbf{r},\mathbf{r}_b',\omega)\exp\left(\frac{i\omega z'}{v}\right), \tag{1.29}$$

where G_{zz} is the zz component of the complete dyadic which we define as

[3] For real functions $f_1(t)$, $f_2(t)$, it holds: $\int_{-\infty}^{\infty} dt\, f_1(t) f_2(t) = \frac{1}{\pi}\int_0^\infty d\omega\, \mathrm{Re}\left[F_1(\omega)F_2^*(\omega)\right]$.

$$\nabla \times \nabla \times \mathbf{G}(\mathbf{r}, \mathbf{r}', \omega) - \frac{\omega^2 \varepsilon(\mathbf{r}, \omega)}{c^2} \mathbf{G}(\mathbf{r}, \mathbf{r}', \omega) = -\frac{\omega^2}{c^2} \mathbf{I} \delta(\mathbf{r} - \mathbf{r}'), \tag{1.30}$$

where $\mathbf{I}$ is the unit dyadic. Eq. (1.29) can be inserted in Eq. (1.28), which yields the loss probability in terms of the Green's function:

$$\Gamma(\omega) = -\frac{e^2 \mu_0}{\pi \hbar} \mathrm{Im} \left[\int dz \int dz' G_{zz}(x_b, y_b, z, z', \omega) \exp\left(-\frac{i\omega(z - z')}{v} \right) \right]. \tag{1.31}$$

The EEL spectrum (corresponding to the loss probability) can be thus calculated if the Green's function is known in a system or if one solves directly for the induced field produced in the interaction of the sample with the electron beam.

The solution is readily found for the beam moving inside an unbounded medium (bulk) characterized by the dielectric function $\varepsilon(\omega)$. After inserting the field produced by the electron in the medium [e.g., the inverse Fourier transform of Eq. (1.23) in the corresponding coordinates] in Eq. (1.28) we can obtain the loss probability per unit length along the trajectory that the electron follows through the material:

$$\frac{d\Gamma_{bulk}(\omega)}{dz} = -\frac{e^2}{\hbar \omega 2\pi^2 \varepsilon_0 v} \mathrm{Im} \left[\int_0^{Q_c} Q \, dQ \frac{\omega/(v\varepsilon) - v q_0/c}{Q^2 + (\omega/v)^2 - q_0^2 \varepsilon} \right] \tag{1.32}$$

$$= \frac{e^2}{\hbar 4\pi^2 \varepsilon_0 v^2} \mathrm{Im} \left[\left(\frac{v^2}{c^2} - \frac{1}{\varepsilon} \right) \ln \left(\frac{Q_c^2 - \omega^2 \varepsilon / c^2 + \omega^2 / v^2}{\omega^2 / v^2 - \omega^2 \varepsilon / c^2} \right) \right], \tag{1.33}$$

where we considered a momentum cutoff, $\hbar Q_c$, determined by the collection semi-angle of the spectrometer ϕ_{coll} [15]:

$$\hbar Q_c \approx \sqrt{(m_e v \phi_{coll})^2 + (\hbar \omega / v)^2}. \tag{1.34}$$

Importantly, the cutoff prevents the divergence of the classical bulk loss probability [Eq. (1.33)]. We can see that the bulk loss will strongly depend on $\mathrm{Im}[1/\varepsilon]$. If we describe the sample's response by Drude or Lorentz-Drude dielectric functions (Eqs. (1.7) and (1.11), respectively), one obtains a peak close to energy $\hbar \omega_p$ or $\hbar \omega_{LO}$ for plasmonic and phononic materials, respectively, which corresponds to the poles of the loss function. Interestingly, for $v > c/\sqrt{\varepsilon}$ when the Čerenkov condition is fulfilled, radiation losses arise. They become the only source of energy loss of the electron if $\mathrm{Re}[\varepsilon(\omega)] > 1$ and $\mathrm{Im}[\varepsilon(\omega)] = 0$. In such a case, one can express the cutoff-independent probability of the Čerenkov loss [acquired from Eq. (1.33)] as

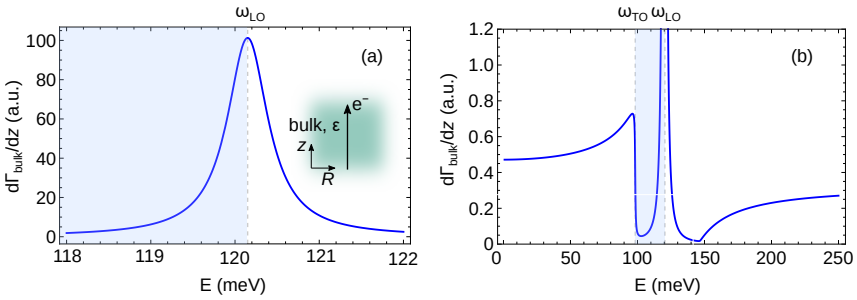

FIGURE 1.4: The bulk loss probability [Eq. (1.33)] evaluated for a material characterized by the Lorentz-Drude dielectric response (1.11) with parameters $\hbar\omega_{TO} = 98$ meV, $\hbar\omega_{LO} = 120$ meV, $\gamma = 0.59$ meV and $\varepsilon(\infty) = 6.7$ probed by an electron beam with speed $v = 0.5\,c$ and for cutoff $Q_c = 0.19\,nm^{-1}$. The light blue area highlights the Reststrahlen band between TO and LO. (a) Shows the bulk-loss peak at $\hbar\omega_{LO}$, whereas in (b) we plot the spectrum over a broader energy region and focus on less intense Čerenkov losses appearing below TO and above ~ 145 meV for which the condition $v > c/\sqrt{\varepsilon}$ is fulfilled [see also Fig. 1.1(e)].

$$\frac{d\Gamma_{\check{C}}(\omega)}{dz} = \frac{e^2}{\hbar 4\pi\varepsilon_0 v^2}\left(\frac{v^2}{c^2} - \frac{1}{\varepsilon}\right). \tag{1.35}$$

In Fig. 1.4 we evaluate Eq. (1.33) for an electron beam moving at speed $v = 0.5\,c$ in SiC characterized by the Lorentz-Drude function [Eq. (1.11)] with parameters $\hbar\omega_{TO} = 98$ meV, $\hbar\omega_{LO} = 120$ meV, $\gamma = 0.59$ meV and $\varepsilon(\infty) = 6.7$. The spectra show both the dominant bulk loss peak at $\hbar\omega_{LO}$ as well as the Čerenkov losses that arise in this case below TO and above ~ 145 meV. The threshold for the Čerenkov radiation can be also seen in Fig. 1.1(e) from the intersection of the "electron line" given by $\omega = vq$ (dashed gray line) and the bulk dispersion.

We have reported EEL in unbounded media, but as we will see thorough this thesis, addressing the exact sample geometry is often crucial to accurately model and understand EEL spectra, especially when materials supporting polaritonic excitations are involved. For that, we need to describe the geometry, usually in terms of boundary conditions, which can be done either by numerically solving Maxwell's equations for complicated geometries (see an overview in Appendix B) or analytically. Besides the situation of the beam interacting with bulk media, the analytical expressions for the EEL probability can be found for several geometries, including fast electron passing close to infinite interfaces [108] [see Fig. 1.5(a)], penetrating slabs [109–111] [see Fig. 1.5(b)], interacting with a dielectric sphere [112, 113] [see Fig. 1.5(c)] or cylinders and cylindrical holes [92, 114–

116]. In the following chapters, we will deal with some of the analytically solvable cases, together with numerical solutions of the induced fields when analytical ones are not possible to obtain.

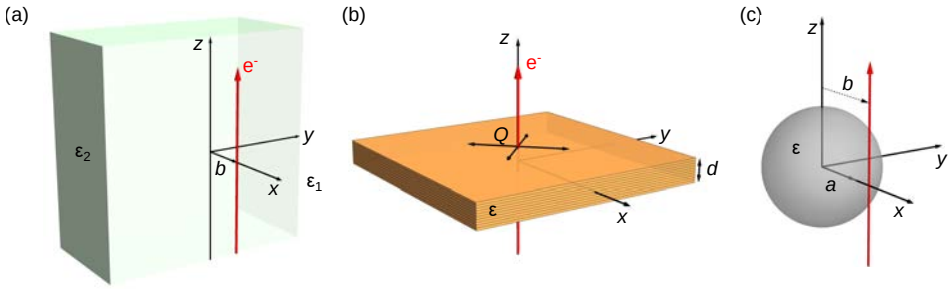

FIGURE 1.5: Some of the analytically solvable geometries to obtain EEL probability [Eq. (1.28)]. (a) An electron beam moving in the z direction parallel to an infinite interface (in the plane $x = 0$) at an impact parameter b. The electron is moving in an environment characterized by the dielectric function ε_1, the neighboring environment has the dielectric function ε_2. (b) Electron beam passing through a thin film of thickness d with dielectric properties given by ε. (c) Electron moving along a trajectory $(b, 0, z)$ interacting with a dielectric sphere of radius a and dielectric function ε.

1.2.3 Quantum description of the electron-sample interaction

So far, we have been dealing with a classical description of the EEL mechanism, treating the electron as a localized charged particle interacting with its surrounding environment via the EM field, within the framework of classical electrodynamics. However, different approaches within quantum-mechanical treatments have been applied to model EEL spectra. A (partially) quantum-mechanical description was employed for low-loss EELS, e.g., to describe excitation of phonon modes and vibrations in boron nitride [59, 117, 118], graphene nanoflakes [119] and molecules [120]. Also, ab-initio calculated response of the samples been used as an input for the classical dielectric formalism outlined in the previous section [56].

We now introduce a quantum description of the electron energy loss process. We express the probability of an electron to go from a state $|i\rangle = \psi_i$ and energy $\mathcal{E}_i = \hbar\omega_i$ to a state $|f\rangle = \psi_f$ and energy $\mathcal{E}_f = \hbar\omega_f$ via the interaction with a target sample. We consider electronic excitations in the sample, which during the interaction undergoes a transition from its ground state $|0\rangle$ with energy $E_0 = \hbar\omega_0$ to excited states $|n\rangle$ of energy $E_n = \hbar\omega_n$. Within the first-order perturbation theory, the non-retarded (NR) probability rate that the initial state of the electron-sample system $|i\rangle|0\rangle$ evolves into the final state $|f\rangle|n\rangle$ (considering that before and

after the scattering event, the interaction between the target and the fast electron can be neglected) can be expressed by Fermi's golden rule as [15, 118, 121]:

$$\frac{d\gamma_{i\to f}^{NR}}{dt} = \frac{2\pi}{\hbar}\sum_{f,n}\left|\langle n|\langle f|\widehat{H}_I|i\rangle|0\rangle\right|^2 \delta(E_n - E_0 + \mathcal{E}_f - \mathcal{E}_i), \tag{1.36}$$

where we omit finite-temperature effects, with $\widehat{H}_I$ the interaction Hamiltonian causing the perturbation in the system. The Hamiltonian can be expressed as (neglecting retardation):

$$\widehat{H}_I = \frac{1}{4\pi\varepsilon_0}\sum_{j=1}^{N}\frac{e^2}{|\mathbf{r}_j - \mathbf{r}_b|} = \frac{1}{4\pi\varepsilon_0}\int d^3\mathbf{r}\frac{e^2\widehat{\rho}(\mathbf{r})}{|\mathbf{r}-\mathbf{r}_b|}, \tag{1.37}$$

where $\widehat{\rho}(\mathbf{r}) = \sum_j \delta(\mathbf{r}-\mathbf{r}_j)$ is the target charge-density operator.

In many situations, the initial and final states of the fast electrons can be described by plane waves as:

$$|i\rangle = \psi_i = e^{i\mathbf{q}_i\cdot\mathbf{r}}, \tag{1.38a}$$

$$|f\rangle = \psi_f = e^{i\mathbf{q}_f\cdot\mathbf{r}}, \tag{1.38b}$$

which we consider to be normalized to unit volume. Then one can write Eq. (1.36) as [107, 121, 122]:

$$\frac{d\gamma_{i\to f}^{NR}}{dt} = \frac{2\pi e^4}{\varepsilon_0^2\hbar^2}\sum_n \frac{1}{q^4}|\langle n|\widehat{\rho}(\mathbf{q})|0\rangle|^2\,\delta(\hbar q^2/(2m_e) - \boldsymbol{\nu}\cdot\mathbf{q} + \omega_n - \omega_0), \tag{1.39}$$

where we denoted $\mathbf{q} = \mathbf{q}_i - \mathbf{q}_f$ and $\widehat{\rho}(\mathbf{q}) = \sum_j e^{-i\mathbf{q}\cdot\mathbf{r}_j}$ represents fluctuations around the average charge density. The expression $|\langle n|\widehat{\rho}(\mathbf{q})|0\rangle|^2$ is the Fourier transform of the density-density correlation function [123] and can be related to macroscopic dielectric function [124].

If we introduce the non-retarded loss probability $\Gamma^{NR}(\omega)$ per unit energy as:

$$\gamma_{i\to f}^{NR} = \int_0^\infty d\omega\,\Gamma^{NR}(\omega), \tag{1.40}$$

and use Eq. (1.39), we can express the loss probability of an electron beam interacting with a bulk dielectric material in terms of the macroscopic dielectric function, dependent on $(\mathbf{q},\omega)$:

$$\frac{\Gamma^{NR}(\omega)}{dL} = \int d^3\mathbf{q}\, \frac{dP^{NR}(\mathbf{q},\omega)}{dL} = \int d^3\mathbf{q}\, \frac{e^2}{4\pi^3\varepsilon_0\hbar v}\frac{1}{q^2}\,\mathrm{Im}\left[\frac{-1}{\varepsilon(\mathbf{q},\omega)}\right]\delta(\omega-\boldsymbol{v}\cdot\mathbf{q}), \tag{1.41}$$

where L is a typical interaction length and P^{NR} is the differential $(\mathbf{q},\omega)$-dependent non-retarded loss probability. We neglected here the recoil of the fast electron which is possible due to its high incident momentum, so that

$$\hbar q^2/(2m_e) - \boldsymbol{v}\cdot\mathbf{q} \approx -\boldsymbol{v}\cdot\mathbf{q}. \tag{1.42}$$

Importantly, Eq. (1.41) corresponds to an expression that can be derived from the classical formalism [by combining Eq. (1.23) for $c \to \infty$ with the definition of the classical loss probability in Eq. (1.28)] considering that the electron interacts with a bulk material described by $\varepsilon(\mathbf{q},\omega)$ [121]. However, we note that the above derivation assumed an "averaged" interaction of the sample with the initial and final electron beam states described by plane waves. Such an approximation breaks down when a probe focused on individual atomic columns is employed and large convergence and collections angles are used [117, 125]. We further discuss some situations where a proper quantum-mechanical treatment is necessary in connection with some of the results of this thesis, however, we also note that in many cases, the dielectric theory is very accurate and precise for capturing the main features of EEL spectra.

1.3 Practical aspects of spatially-resolved EELS

A scanning transmission electron microscope is a rather sophisticated tool and due to its complexity, we are going to focus only on the substantial aspects for understanding the experimental results and theoretical modeling in the following chapters of this thesis. A simplified scheme of an STEM-EELS system with a brief description is plotted in Fig. 1.6(a). Fast electrons are first extracted from an electron gun and accelerated by a voltage typically varying from 30 kV to 300 kV. For state-of-the-art low-loss EELS experiments, it is very important to set a well-defined energy of the primary electron beam and hence, a small energy spread of the electron beam extracted from the gun is desirable. To better define the initial energy, monochromators of different designs have been implemented. The scheme in Fig. 1.6(a) shows an "alpha-type" monochromator [126] with two magnetic prisms and an energy-selecting slit in between.

The electron beam is controlled by sets of electro-magnetic lenses which suffer from aberrations similarly to optical lenses. To that end, aberration correctors consisting of lenses with multipole fields have been developed to compensate for the aberrations of various parts of the microscope system as shown in Fig. 1.6(a). After the beam passes through the corrector, it should not exhibit any distortions in its spatial profile up to a certain aberration order.

The sample, for instance a gold nanorod on a membrane, as shown in our scheme, is usually placed between the pole pieces of an objective lens. The transmitted beam can be imaged after going through a post-specimen electron optics, e.g. on a high-angle annular dark-field (HAADF) detector, and analyzed by an EEL spectrometer. The spectrometer consists of a magnetic prism dispersing the entering electrons according to their energy, a set of post-spectrometer lenses (used for magnification and to reduce aberrations), and a camera to record the spectrum [9].

The raw EEL spectrum is a 2D image with one axis denoting the energy dispersion and the perpendicular axis corresponding to the momentum (or scattering-angle) dispersion [82, 127, 128]. The resulting spectrum is typically acquired by integrating along the axis of the momentum dispersion. For the example of a small gold rod, the integrated spectrum acquired with the beam close to one of the rod tips is shown in Fig. 1.6(b). As observed, the dominant contribution to the spectrum comes from the electrons that have not lost any (or negligible) energy and form the ZLP. The ZLP width is given by the level of monochromation of the beam. Quasi-elastic losses at very small energies can be also responsible for an additional ZLP broadening as will be shown in Chapter 4.

After zooming in the low-loss region of the spectrum for a beam positioned close to the tip of the gold rod sample, we can observe a peak around 2 eV which corresponds to the excitation of a localized surface plasmon mode. An important capability that we already mentioned in the Introduction is the possibility of correlating the beam position with the spectral response. This is demonstrated in Fig. 1.6(c) which shows a spectral linescan along the longer axis of the rod. The

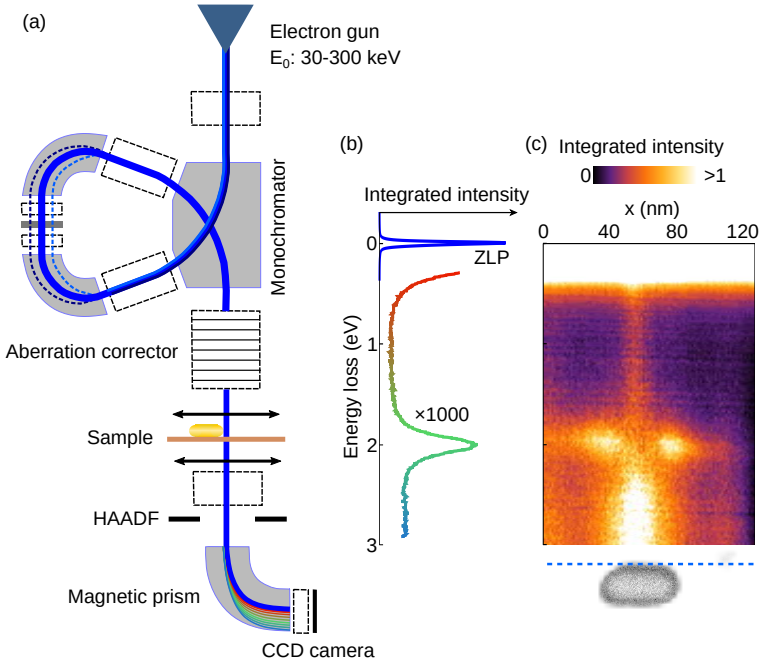

FIGURE 1.6: (a) Schematics of a scanning transmission electron microscope equipped with an electron energy loss spectrometer, and the parts of the system discussed in the main text marked. (b) A representative experimental electron energy loss spectrum recorded with the beam positioned at the tip of a gold nanorod sample as shown in the schematics of (a). The ZLP is the most intense part of the spectrum. The spectrum is plotted as recorded without any post-processing. (c) A smoothed spectral linescan obtained for the electron beam scanned close to the nanorod denoted by the blue dashed line in HAADF image shown below (the x axis is aligned); the energy axis corresponds to (b). The experimental spectra were measured by Dr. Jordan Hachtel at the Oak Ridge National Laboratory in the US, and the sample fabricated by Dr. Thomas Hendel at the Materials Physics Center in Donostia, the Basque Country.

beam position is denoted by the blue dashed line in the HAADF image shown below. We emphasize that the EEL spectrum changes substantially as the electron beam is scanned and excites different plasmonic modes supported by the metallic rod (see Section 1.1.3) with different probabilities. We will further discuss EELS of metallic nanorods in Chapter 5 so for now we will skip a more detailed explanation of the origin of the spectral peaks.

Constantly improving performance of STEM-EELS systems together with additional analytical capabilities go hand-in-hand with theoretical efforts to address various physical phenomena. This thesis is not an exception and all the following chapters are directly related to latest experimental results of to new paths and possibilities in STEM-EELS.

Chapter 2

EELS of hyperbolic phonon polaritons in hexagonal boron nitride

The elemental composition together with the crystallographic arrangement of atoms determine the characteristic properties of materials, including their optical behaviour. Strong anisotropy in the strength of bonds forming the lattice can also give rise to an anisotropic vibrational response, as for instance in hexagonal boron nitride (h-BN). h-BN is a van der Waals crystal, where two-dimensional hexagonal lattice planes are bonded by weak van der Waals forces, which yields a strongly anisotropic dielectric function in the mid-infrared (MIR) spectral range.

Interestingly, the anisotropic optical response provides a possibility to excite hyperbolic phonon polaritons showing subwavelength electromagnetic field confinement [68, 69, 129], thus turning h-BN into a very promising material for applications in hyperlensing [130], nanofocusing [71] or sensing [72]. The detailed characterization and understanding of the phononic behaviour at the micro- or nanoscale is therefore highly desirable. Several spectral studies of h-BN nanostructures have been performed with use of nano-probes which localize light below the diffraction limit, such as sharp tips in scanning near-field optical microscopy [68, 69, 131, 132] or in atomic force microscopy [133, 134]. Complementary information to these near-field optical studies can be retrieved by using a fast electron beam as a probe. In this chapter we show theoretically that the hyperbolic phonon polaritons can indeed be excited by a fast electron beam and use the classical dielectric theory to interpret the experimental EEL mapping of a h-BN flake.

2.1 Experimental mapping of EEL in a h-BN flake

The theoretical analysis presented in this chapter is stimulated by experimental results from spatially-resolved EELS of a thin h-BN flake as shown in Fig. 2.1(a). The electron beam accelerated by a 60 kV voltage is scanned across the sample to acquire a 3D spectral datacube. After subtraction of the ZLP at each pixel

[see Fig. 2.1(b,c)], a clear phononic signal in the spectral region above 170 meV is present for the beam positioned on the flake or close to it.

Interestingly, the color map of Fig. 2.1(d) showing the energy of the measured peak extracted by fitting a Gaussian function to the phononic signal at each beam position, revealed significant variations of the peak energy with respect to (i) the sample thickness (compare with Fig. 2.1(a) where the brighter areas correspond to a larger thickness) and (ii) the distance of the beam from the flake truncation. We observe that the peak position is blue-shifting when the beam is at thicker

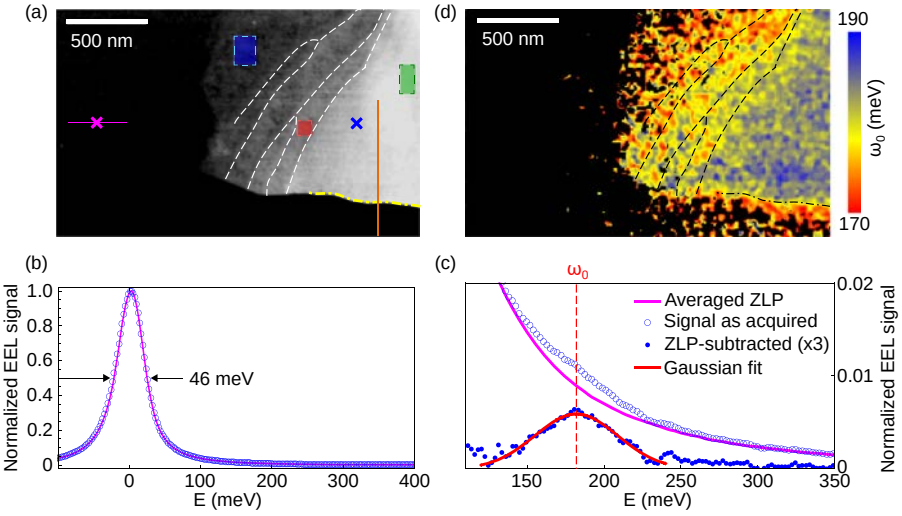

FIGURE 2.1: (a) STEM-HAADF image of the h-BN flake on a TEM membrane. Brighter areas correspond to a larger h-BN thickness, black is the supporting TEM membrane. White dashed lines are guides marking steps on the flake surface, yellow dash-dotted line marks the flake edge. Blue, red, and green rectangles denote the area from which the spectra in Fig. 2.6(b) were collected. The orange line shows where the data for Fig. 2.7(c) were taken from. (b) Typical spectrum extracted for the beam penetrating the h-BN flake [at the position denoted by the blue cross in (a)] with the ZLP being the dominant feature (empty blue points). The magenta line denotes the averaged spectrum measured with the beam far away from the flake [as outlined by the magenta horizontal line in (a)] containing purely the ZLP and losses related to the membrane. (c) Close-up view of the spectra from (b) in the region of phonon losses. Full blue points show the spectrum for the beam going through the flake after subtraction of the ZLP. The red curve is a Gaussian fit to the subtracted spectrum. (d) Map of the peak positions ω_0 retrieved from the fitting. Black color marks regions of insufficient signal level (below 2.5×10^{-4} threshold) or that of irregular fits. Measurements were performed by Prof. Andrey Chuvilin and data were processed by Dr. Alexander Govyadinov in NanoGUNE (San Sebastián).

places of the flake and also when it is scanned across the truncation from outside on top of the sample, which we explain in the following sections.

2.2 Dielectric properties of h-BN and hyperbolic dispersion

We first review the optical properties of h-BN to be later used in the theoretical analysis. Due to the atomic arrangement discussed in the introduction of this chapter, h-BN is an uniaxial dielectric whose bulk optical response (i.e., response of a sufficiently thick layer, typically involving 10 or more h-BN sheets [135]) can be expressed by a dielectric tensor

$$\overleftrightarrow{\varepsilon} = \begin{pmatrix} \varepsilon_R & 0 & 0 \\ 0 & \varepsilon_R & 0 \\ 0 & 0 & \varepsilon_z \end{pmatrix},$$

where ε_R is the ordinary (in-plane) component of the tensor, whereas ε_z is the extraordinary (out-of-plane) component with respect to the h-BN layer stacking arranged as shown in Fig. 2.2(b). We can further assume that both the ordinary and extraordinary components of the dielectric tensor are well described by the Lorentz-Drude model

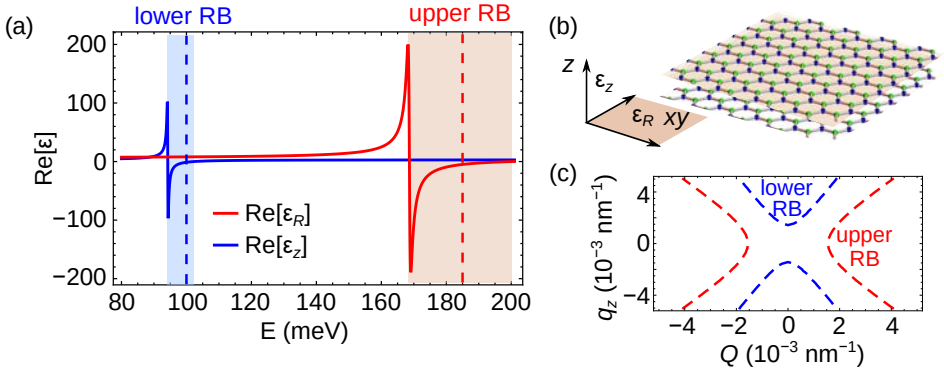

FIGURE 2.2: (a) Real part of the dielectric tensor characterizing the optical response of h-BN, showing lower (light blue) and upper (beige) Reststrahlen bands. (b) Orientation of the dielectric tensor components with respect to stacking of the layers. (c) Hyperbolas characterizing isofrequency surfaces obtained from Eq. (2.2) for energies 100 meV (blue) and 185 meV (red) that are marked by the vertical dashed lines in (a).

$$\varepsilon_{R/z}(\omega) = \varepsilon_{\infty,R/z}\left(1 + \frac{\omega^2_{LO,R/z} - \omega^2_{TO,R/z}}{\omega^2_{TO,R/z} - \omega^2 - i\gamma_{R/z}\omega}\right), \tag{2.1}$$

where $\hbar\omega$ is energy, and the parameters which describe the response of h-BN are shown in Table 2.1. h-BN exhibits two Reststrahlen bands (RBs) when either $\mathrm{Re}[\varepsilon_R]$ or $\mathrm{Re}[\varepsilon_z]$ is negative, as observed in Fig. 2.2(a). In a conventional isotropic material, the appearance of the RB means that the propagation of the electromagnetic waves in the bulk material is forbidden between the TO and LO frequencies, as discussed in Section 1.1.1. However, in this energy range the material can support surface phonon polaritons (coupled excitation of a photon and a surface phonon) if an interface is present [19].

The situation in h-BN is more complex due to the anisotropy. The wavevector components $\mathbf{q} = (q_x, q_y, q_z)$ of the (extraordinary) electromagnetic waves propagating in bulk h-BN need to fulfill the dispersion relationship [136, 137]:

$$\frac{q_z^2}{\varepsilon_R} + \frac{Q^2}{\varepsilon_z} = \frac{\omega^2}{c^2}, \tag{2.2}$$

where the crystal orientation corresponds to the sketch in Fig. 2.2(b), $Q^2 = q_x^2 + q_y^2$, and c is the speed of light. The isofrequency surfaces ($\omega(\mathbf{q}) = \text{const.}$) thus form hyperboloids of either type I in the lower RB ($\mathrm{Re}[\varepsilon_z] < 0 \wedge \mathrm{Re}[\varepsilon_R] > 0$) or type II in the upper RB ($\mathrm{Re}[\varepsilon_z] > 0 \wedge \mathrm{Re}[\varepsilon_R] < 0$) as shown in Fig. 2.2(c) where we plot the solution of Eq. (2.2) for an energy of 100 meV (blue dashed curve) and 185 meV (red dashed curve), which belong to the lower and the upper RB, respectively. The hyperbolic isofrequency surfaces determine the peculiar propagation of waves in bulk h-BN, and also, as we show in the following sections, yields different nature of polaritonic excitations compared to a conventional isotropic material.

TABLE 2.1: Parameters corresponding to the ordinary and extraordinary components of the dielectric tensor characterizing the dielectric response of hexagonal boron nitride (h-BN), according to Ref. [137] :

$\varepsilon_{\infty,R}$	4.9	$\varepsilon_{\infty,z}$	2.95
$\omega_{LO,R}$	$1614\,\mathrm{cm}^{-1}/200.1\,\mathrm{meV}$	$\omega_{LO,z}$	$825\,\mathrm{cm}^{-1}/102.3\,\mathrm{meV}$
$\omega_{TO,R}$	$1360\,\mathrm{cm}^{-1}/168.6\,\mathrm{meV}$	$\omega_{TO,z}$	$760\,\mathrm{cm}^{-1}/94.2\,\mathrm{meV}$
γ_R	$7\,\mathrm{cm}^{-1}/0.87\,\mathrm{meV}$	γ_z	$2\,\mathrm{cm}^{-1}/0.25\,\mathrm{meV}$

2.3 Interaction of an electron beam with a thin h-BN slab

Although the geometry of the investigated sample [see Fig. 2.1(a)] is rather complex, we can argue that for the beam positions further from the flake boundaries, penetrating the material, we might use a simplified description of the beam passing through an infinite free-standing slab to mimic the experimental situation. Furthermore, a thin film of the investigated material is a typical sample for a TEM experiment, and hence, several theoretical works [109–111, 138–140], triggered by the seminal paper by Ritchie [38], were devoted to such calculations. In this section, we derive the EEL probability for an electron moving along the z direction and penetrating an anisotropic h-BN slab of thickness d with boundaries at $|z| = d/2$ with a layer arrangement as sketched in Fig. 2.2(b) (see also the schematics of Fig. 2.3), and analyze the nature of the excitations. We show that the simple dielectric model is suitable to explain the experimentally observed spectral dependence of the EEL spectra on the h-BN flake's thickness [see Fig. 2.1(d)].

To obtain the loss probability, we solve Maxwell's equations to retrieve the induced field arising from the beam-slab interaction. To that end we take advantage of the symmetry in the radial coordinate $R = \sqrt{x^2 + y^2}$ with $R = 0$ the position of the electron trajectory parallel to the z axis, and perform the Fourier transform of the field in this coordinate [138, 139]. The loss probability defined in Section 1.2.2 is then rewritten as:

$$\Gamma(\omega) = \int_0^{Q_c} dQ\, P(Q, \omega), \tag{2.3}$$

where $Q = \sqrt{q_x^2 + q_y^2}$ the wavevector in the perpendicular direction with respect to the electron's trajectory along the z axis, Q_c is the wavevector cutoff and the energy and transverse momentum dependent loss probability, $P(Q, \omega)$, is

$$P(Q, \omega) = \frac{eQ}{2\pi^2 \hbar \omega} \mathrm{Re}\left[\int_{-\infty}^{\infty} dz\, E_z^{ind}(Q, \omega, z) \exp\left(-i\frac{\omega z}{v}\right) \right], \tag{2.4}$$

where e is the elementary charge, v is the speed of the electron, and E_z^{ind} is the z component of the induced field arising in the interaction.

The total electric field $\mathbf{E} = (E_R, E_z)$ produced by the electron inside a uniaxial anisotropic medium can be retrieved as a solution of the Fourier-transformed inhomogeneous wave equation

$$\left(-Q^2 + \frac{\partial^2}{\partial z^2}\right)(E_R, E_z) - \left(iQ, \frac{\partial}{\partial z}\right)\left(iQE_R + \frac{\partial E_z}{\partial z}\right) =$$

$$-\mu_0 i\omega(J_{e,R}, J_{e,z}) - \mu_0\varepsilon_0\omega^2(\varepsilon_R E_R, \varepsilon_z E_z), \tag{2.5}$$

where μ_0 is the vacuum permeability, ε_0 the vacuum permittivity, $J_{e,R}$ and $J_{e,z}$ are the transverse and parallel components of the beam current density. If we combine Eq. (2.5) with the Fourier-transformed Gauss's law,

$$\frac{\partial E_z}{\partial z} = \frac{\rho_F}{\varepsilon_0\varepsilon_z} - \frac{\varepsilon_R}{\varepsilon_z}(iQE_R), \tag{2.6}$$

where

$$\rho_F = \frac{e}{v}\exp\left(\frac{i\omega z}{v}\right) \tag{2.7}$$

is the free charge density $\rho_F(Q, z, \omega)$, we can straightforwardly retrieve a solution for the perpendicular component E_R inside the slab (the electron is moving along the z direction, thus we have $J_R = 0$):

$$E_R(|z| < d/2) = A\exp(\alpha z) + B\exp(-\alpha z) + \frac{iQe}{v\varepsilon_0\varepsilon_z\left(\frac{\omega^2}{v^2} + \alpha^2\right)}\exp\left(i\frac{\omega z}{v}\right), \tag{2.8}$$

where A and B are integration constants and where we define

$$\alpha^2 = \frac{\varepsilon_R}{\varepsilon_z}Q^2 - \frac{\omega^2}{c^2}\varepsilon_R. \tag{2.9}$$

The z component of the field inside the slab can be calculated from Eq. (2.6):

$$\begin{aligned} E_z(|z| < d/2) = &-i\frac{Q\varepsilon_R}{\alpha\varepsilon_z}[A\exp(\alpha z) - B\exp(-\alpha z)] \\ &+ \left(1 - \frac{\varepsilon_R}{\varepsilon_z}\frac{Q^2}{\frac{\omega^2}{v^2} + \alpha^2}\right)\frac{ie}{\varepsilon_0\varepsilon_z\omega}\exp\left(i\frac{\omega z}{v}\right). \end{aligned} \tag{2.10}$$

The field in vacuum outside the slab ($|z| > d/2$), transformed in the (Q, z, ω) domain, is readily obtained by setting $\varepsilon_R = \varepsilon_z = 1$ in Eqs. (2.8) and (2.10):

$$E_{>,R}(z > d/2) = B_>\exp(-\alpha_0 z) + \frac{iQe}{\varepsilon_0 v\left(\frac{\omega^2}{v^2} + \alpha_0^2\right)}\exp\left(i\frac{\omega z}{v}\right), \tag{2.11a}$$

$$E_{>,z}(z > d/2) = i\frac{Q}{\alpha_0}B_> \exp(-\alpha_0 z) + \left(1 - \frac{Q^2}{\frac{\omega^2}{v^2} + \alpha_0^2}\right)\frac{ie}{\varepsilon_0 \omega}\exp\left(i\frac{\omega z}{v}\right), \tag{2.11b}$$

$$E_{<,R}(z < -d/2) = A_< \exp(\alpha_0 z) + \frac{iQe}{\varepsilon_0 v\left(\frac{\omega^2}{v^2} + \alpha_0^2\right)}\exp\left(i\frac{\omega z}{v}\right), \tag{2.11c}$$

$$E_{<,z}(z < -d/2) = -i\frac{Q}{\alpha_0}A_< \exp(\alpha_0 z) + \left(1 - \frac{Q^2}{\frac{\omega^2}{v^2} + \alpha_0^2}\right)\frac{ie}{\varepsilon_0 \omega}\exp\left(i\frac{\omega z}{v}\right), \tag{2.11d}$$

where we required the finiteness of the fields at infinity, and denoted the integration constants as $A_<$ and $B_>$, with

$$\alpha_0^2 = Q^2 - \frac{\omega^2}{c^2}. \tag{2.12}$$

The integration constants $A, B, A_<$ and $B_>$ are retrieved from the boundary conditions for the field components at the interfaces between the slab and vacuum. We require E_R and $\varepsilon_z E_z$ to be continuous so that:

$$\begin{aligned} E_{>,R}(z = d/2) &= E_R(z = d/2), \qquad & E_{>,z}(z = d/2) &= \varepsilon_z E_z(z = d/2), \\ E_{<,R}(z = -d/2) &= E_R(z = -d/2), \qquad & E_{<,z}(z = -d/2) &= \varepsilon_z E_z(z = -d/2). \end{aligned} \tag{2.13}$$

The solutions for E_z will be substituted in Eq. (2.4) and then in Eq. (2.3). We find that the loss probability can be split in different contributions: the bulk loss term Γ_{bulk} (as if the electron were passing through an unbounded environment) and the guided (Γ_{guid}) and the "Begrenzungs" (Γ_{Begr}) loss terms arising from the presence of the slab surfaces:

$$\Gamma_{slab}(\omega) = \Gamma_{bulk}(\omega) + \Gamma_{guid}(\omega) + \Gamma_{Begr}(\omega), \tag{2.14}$$

with

$$\begin{aligned} \Gamma_{bulk}(\omega) &= \int_0^{Q_c} dQ\, P_{bulk}(Q, \omega) \\ &= -\frac{d\, e^2}{2\pi^2 \hbar \omega^2 \varepsilon_0} Im\left[\int_0^{Q_c} dQ\, \frac{Q}{\varepsilon_z}\left(1 - \frac{\varepsilon_R}{\varepsilon_z}\frac{Q^2}{\frac{\omega^2}{v^2} + \frac{\varepsilon_R}{\varepsilon_z}Q^2 - \frac{\omega^2}{c^2}\varepsilon_R}\right)\right] \end{aligned} \tag{2.15a}$$

$$= -\frac{de^2}{4\pi^2\hbar v^2\varepsilon_0}\,\mathrm{Im}\left[\frac{c^2-v^2\varepsilon_R}{c^2\varepsilon_R}\,\ln\left(\frac{Q_c^2v^2c^2\varepsilon_R}{\omega^2\varepsilon_z(c^2-v^2\varepsilon_R)}+1\right)\right], \tag{2.15b}$$

and the sum of the guided and the Begrenzung contributions:

$$\Gamma_{guid}(\omega)+\Gamma_{Begr}(\omega) = \int_0^{Q_c} dQ\,\left[P_{guid}(Q,\omega)+P_{Begr}(Q,\omega)\right] \tag{2.16a}$$

$$= \frac{v}{2\pi^2\varepsilon_0\hbar\omega}\mathrm{Im}\left[\int_0^{Q_c} dQ\,\frac{\varepsilon_R Q^2}{\varepsilon_z\alpha}\left(\frac{A\sinh\left(\frac{d}{2}\left(\alpha-\frac{i\omega}{v}\right)\right)}{\alpha v-i\omega}-\frac{B\sinh\left(\frac{d}{2}\left(\alpha+\frac{i\omega}{v}\right)\right)}{\alpha v+i\omega}\right)\right.$$

$$\left.-\frac{Q^2A_<\exp\left(\frac{d}{2}\left(-\alpha_0+\frac{i\omega}{v}\right)\right)}{\alpha_0(\alpha_0 v-i\omega)}+\frac{Q^2B_>\exp\left(\frac{d}{2}\left(\alpha_0-\frac{i\omega}{v}\right)\right)}{\alpha_0(\alpha_0 v+i\omega)}\right]. \tag{2.16b}$$

The explicit expressions can be obtained after evaluating the coefficients using Eqs. (2.13) (see Appendix A.1 for the complete expressions in the non-retarded approximation).

2.3.1 Slab modes

We concentrate now on the maxima of the EEL $(Q-\omega)$ dependent probabilities, which arise as the poles of the loss functions in Eq. (2.15a) and Eq. (2.16b). We first note that the poles of $P_{bulk}(Q,\omega)$ in Eq. (2.15a) yield the bulk dispersion relation [Eq. (2.2)] with $q_z=\omega/v$ matching the wavevector provided by the fast electron in the z direction. We can similarly analyze poles of $P_{guid/Begr}$. The Begrenzungs term is responsible for the compensation of the bulk losses and therefore needs to have the same denominator as that in Eq. (2.15a). As the slab gets thinner, the Begrenzungs contribution, Γ_{Begr}, tends to cancel the bulk contribution Γ_{bulk}.

On the other hand, the poles corresponding to the guided loss P_{guid} are given by the following transcendental equations:

$$\frac{\alpha}{\varepsilon_R\alpha_0}\coth(\alpha d)+1=0, \tag{2.17a}$$

$$\frac{\alpha}{\varepsilon_R\alpha_0}\tanh(\alpha d)+1=0. \tag{2.17b}$$

By performing mode analysis [141, 142] we find that Eq. (2.17a) corresponds to the dispersion of p-polarized charge-symmetric slab modes (with respect to $z=0$) and Eq. (2.17b) to charge-antisymmetric modes, which propagate along the slab surfaces. In the quasistatic limit ($c\to\infty$), the dispersion of these modes can be expressed by one single equation [68]

$$Qd = \mathrm{Re}\left\{ i\sqrt{\frac{\varepsilon_z}{\varepsilon_R}}\left(\pi n + 2\,\mathrm{atan}\left[\frac{i}{\sqrt{\varepsilon_R\varepsilon_z}}\right]\right)\right\}, \tag{2.18}$$

where $n = 0, 1, 2, ...$ is the mode order. In the case of h-BN, we have symmetric and antisymmetric modes for n even and odd, respectively. We note that this condition arises also from the denominator of Eq. (A.3) in Appendix A.

In Fig. 2.3 we plot the non-retarded (Q, ω)-dependent loss probability, i.e. the sum of the integrands in Eq. (A.1) and Eq. (A.3) in Appendix A, in the upper RB for (a) an anisotropic slab of hBN characterized by the dielectric tensor parameters from Table 2.1, and (b) a hypothetical isotropic slab with $\overleftrightarrow{\varepsilon} = \mathrm{diag}(\varepsilon_R, \varepsilon_R, \varepsilon_R)$, respectively. The expressions for the isotropic non-retarded loss probability can be further simplified to a more compact form (discussed in Chapter 3). On top of the color maps we plot the dispersion curves (dashed lines) given by Eq. (2.18), which trace well the maxima of the (Q, ω)-dependent loss probability. However, $P(Q, \omega)$ also includes the efficiency of the coupling between the different modes and the fast electron as given by the color scale.

The dispersion of the slab modes in Eq. (2.17) [or Eq. (2.18)] is illustrative for identifying the fundamental difference in the properties of the modes excitable by the electron beam in a hyperbolic material compared to the isotropic case. As in the upper RB of h-BN $\mathrm{Im}[\alpha] \gg \mathrm{Re}[\alpha] \approx 0$ and $\mathrm{Re}[\varepsilon_R] < 0 \wedge \mathrm{Im}[\varepsilon_R] \approx 0$ holds (considering higher wavevectors), the solution of Eq. (2.17) yields multiple dispersion branches below $\omega_{LO,R}$ that are assigned to hyperbolic phonon polariton (HPhP) modes marked as M_n (with $n = 0, ...4$) [68, 69]. These modes are denoted as "guided" HPhPs, because they are analogous to dielectric waveguide modes. The fact that $\mathrm{Im}[\alpha] \gg \mathrm{Re}[\alpha]$ also means that these modes correspond to oscillatory field solutions inside the slab. The oscillatory character of the field is illustrated in Fig. 2.3(c,e), where we plot the components of the induced field $\mathrm{Re}[E_{z,ind}]$ and $\mathrm{Re}[E_{R,ind}]$, respectively, in the $z - Q$ space at energy $\hbar\omega = 175$ meV. As we can observe, the mode order n denotes the number of nodes in the radial field component inside the slab [see Fig. 2.3(e)], analogous to the waveguide notation.

On the contrary, in the hypothetic isotropic slab we have $\mathrm{Re}[\alpha] \gg \mathrm{Im}[\alpha] \approx 0$ for higher wavevectors and energies inside the RB. Hence, the solutions of Eq. (2.17) result only in two branches assigned to the charge symmetric and antisymmetric coupled-surface mode, respectively [see Fig. 2.3(b)]. These modes originate from hybridization of two surface modes described in Section 1.1.2 and give rise to a field which is exponentially decaying from the slab boundary towards its center and outside the slab as observed in Figs. 2.3(d,f) which show the field at 175 meV (symmetric branch) and 197 meV (antisymmetric branch), respectively.

As we mentioned, the color maps in Fig. 2.3(a,b) can be understood as dispersions of the slab modes (either HPhP modes or coupled-surface modes) including the efficiency of the mode coupling with the field of the fast electron. One

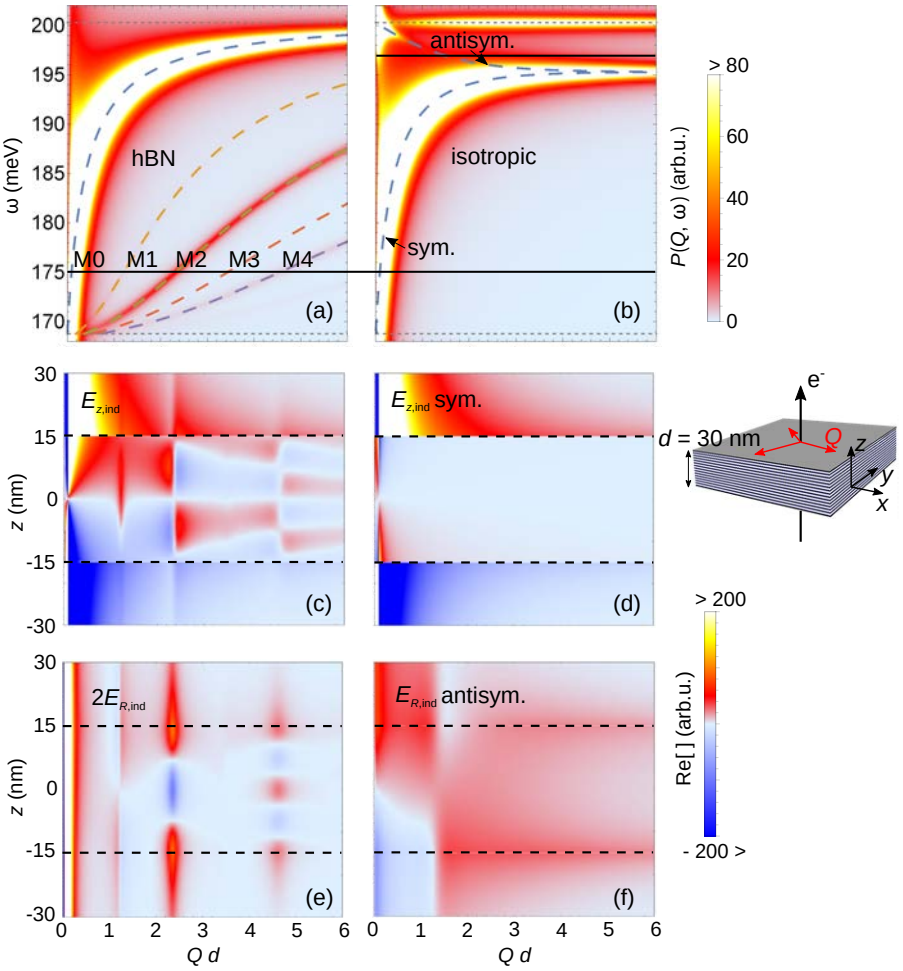

FIGURE 2.3: (a,b) (Q, ω)-dependent non-retarded loss probability [integrands of Eqs. (A.1) and (A.3)] (colour density plots) with dispersion curves [Eq. (2.18)] calculated for (a) an anisotropic h-BN slab (see the schematics) characterized by ε_R and ε_z, and (b) an isotropic slab with $\varepsilon = \varepsilon_R$. The thickness is $d = 30$ nm in both cases. The electron speed is $v = 0.446c$ (energy 60 keV). The horizontal dashed lines denote the RB boundaries. (c) $E_{z,ind}(Q)$ calculated at energy 175 meV for a h-BN slab, and (d) an isotropic slab. Lowest row: (e) the radial component of the induced field at 175 meV for the h-BN slab and (f) at 197 meV to show the antisymmetric-mode field of the isotropic slab. The induced electric field in (c-f) is obtained from the retarded analytic calculation by subtracting the field of the electron in vacuum in Eqs. (2.8), (2.10) and (2.11). Dashed black horizontal lines denote the slab boundaries.

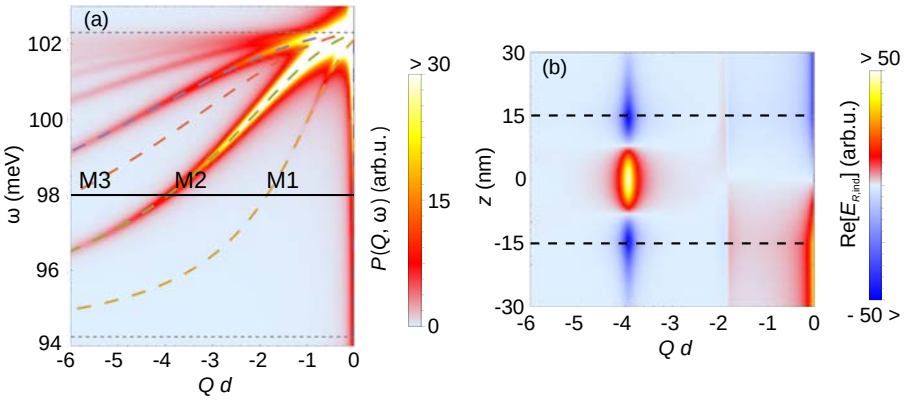

FIGURE 2.4: (a) (Q, ω)-dependent retarded loss probability with dispersion curves (2.17) calculated for an anisotropic h-BN slab with the parameters as in Fig. 2.3. (b) Radial component of the retarded induced field Re $\left[E_{R,ind}(Q)\right]$ at energy 98 meV. Horizontal dashed black lines indicate the slab boundaries.

can observe that (i) the intensity of $P(Q, \omega)$ (the excitation probability) decreases for increasing Q, which we focus on later, and (ii) the even modes are excited dominantly, as their field symmetry matches better with the fast electron's field. In Fig. 2.3(c,d) we indeed observe mostly the field corresponding to the charge-symmetric modes. The higher excitation probability of the charge symmetric modes in thin slabs is also reflected in the isotropic case, where the symmetric coupled-surface mode is dominant [compare the intensity of the branches in Fig. 2.3(b)]. Furthermore, for high momenta, the field appears more within the volume of the h-BN slab, which determines volume-like character of the modes, whereas in the isotropic polaritonic slab, the field is mostly localized at the slab surfaces, with the surface phonon being the limiting case for $Q \to \infty$.

Similarly, we can analyze the dispersion in the lower RB between $\omega_{TO,z}$ and $\omega_{LO,z}$ (see Fig. 2.2). The guided HPhP modes in this energy region exhibit negative dispersion which yields a negative phase velocity $\boldsymbol{v}_p = \omega/\mathbf{q}$, as proven by time-domain near-field interferometry [69].[1] In Fig. 2.4(a), where we show the modes' dispersion, we thus denote $Q \to -\sqrt{q_x^2 + q_y^2}$. We plot the retarded probability $P(Q, \omega)$ together with the solutions of Eqs. (2.17) (dashed curves). Importantly, if we consider retardation, the fundamental M0 mode is not supported and we note that it was identified incorrectly in several near-field studies of h-BN phononic modes [69, 143]. Hence, only the modes with $n > 0$ are excitable. The symmetry of the odd and even modes is equivalent to the corresponding modes in the upper RB. Again, the electron beam excites the charge symmetric (even)

[1] The group velocity $\boldsymbol{v}_g = \partial\omega/\partial\mathbf{q}$ which determines the energy flow and wave propagation from the source stays positive.

modes dominantly, which makes the mode "M2" the first significantly contributing guided mode if we consider higher |Q|, as one can observe in the plot of the radial component of the induced field in Fig. 2.4(b).

2.3.2 Electron energy loss spectra

From the above analysis, we have found that the fast electrons naturally launch hyperbolic phonon polariton modes propagating in h-BN slabs. The excitation of these modes should be also reflected in the integrated EEL probability [Eq. (2.14)], which is the quantity to be compared with experimentally measured spectra (as with those in Fig. 2.1). The integration over the perpendicular momenta according to Eq. (2.3) can be performed analytically only for the bulk term. The guided and Begrenzungs loss terms have to be integrated numerically. We also note that the classical dielectric formalism is valid if the cutoff momentum is much smaller than the inverse of the distances between atoms, therefore it is reasonable to integrate only up to $Q_c \approx 1\text{Å}^{-1}$ [106, 138].

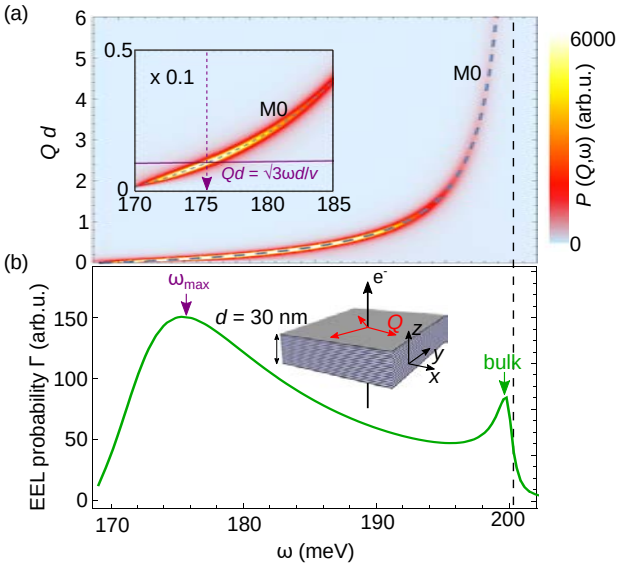

FIGURE 2.5: (a) (Q, ω)-dependent non-retarded loss probability evaluated for the same parameters as in Fig. 2.3(a) (d = 30 nm, $v = 0.446c$) but plotted on unsaturated color scale. The dominantly excited M0 mode is traced by the dashed blue line. (b) The loss probability obtained according to Eq. (2.3) by integrating $P(Q, \omega)$ from (a) over Q up to $Q_c = 0.1$ a.u. The inset of (a) shows that the position of the peak arising in the excitation of the M0 mode is found approximately from matching the mode dispersion $Q(\omega)$ with the condition $Q(\omega_{max}) = \sqrt{3}\omega_{max}/v$.

In Fig. 2.5 we illustrate how $P(Q,\omega)$ is related to the integrated EEL probability. We evaluate $P(Q,\omega)$ in (a) for the same parameters as in Fig. 2.3(a), but now we plot the values on unsaturated color scale to emphasize that the fundamental M0 mode is excited much more efficiently than the higher-order modes. The spectrum in Fig. 2.5(b) obtained after integration of $P(Q,\omega)$ from (a) over Q [see Eq. (2.3)] exhibits two peaks: (i) the broad peak around 175 meV which originates from the M0 mode as we will discuss in the following, and (ii) the narrow peak close to $\omega_{LO,R}$ which arises from the bulk loss term. The latter peak would be present also if the electron were moving in unbounded h-BN.

In Fig. 2.6(a) we perform the integration of the (Q,ω)-dependent loss probability, as illustrated in Fig. 2.5, and obtain the theoretical EEL spectra for slabs of varying thickness (full lines) in both RBs. We also plot the bulk contribution from Eq. (2.15) with dashed lines, which corresponds to the loss experienced by the electron passing a distance d in an unbounded h-BN crystal. We can observe that the thicker the slab is, the more the bulk loss contributes to the resulting spectrum in the upper RB. For thinner slabs, the bulk contribution is reduced at the expense of the activation of the guided-mode loss. Interestingly, for the chosen parameters, the bulk loss does not contribute in the lower RB (for $\omega_{TO,z} < \omega < \omega_{LO,z}$), as the condition given by the bulk dispersion [Eq. (2.2)] with $q_z = \omega/v$ is not fulfilled for $v = 0.446\,c$ (only slower electrons would excite the bulk mode in the lower RB). In this spectral region, the electron can thus couple only to the guided modes.

Apart from the bulk loss peaks, other spectral features emerge from the guided loss term Γ_{guid} in both RBs. To better understand this contribution, it is necessary to analyze Eq. (2.16b). If we consider a thin slab limit ($\omega d/v \approx 0$), we find out that for a given frequency ω, the most probable momentum transferred from the fast electron (to the polariton) is $Q_{max} = \sqrt{3}\omega/v$ as demonstrated in Appendix A.1.2 [138]. This finding explains why the higher order HPhP modes are not excited very efficiently as they favor higher momenta and thus not couple so well to the fast electron. Hence, we can assume that in the upper RB this momentum is transferred to the M0 mode, and obtain the approximate position of the guided-loss peak ω_{max} for $\omega_{TO,R} < \omega < \omega_{LO,R}$:

$$\sqrt{3}\frac{\omega_{max} d}{v} = \mathrm{Re}\left\{ 2i\sqrt{\frac{\varepsilon_z(\omega_{max})}{\varepsilon_R(\omega_{max})}}\,\mathrm{atan}\left[\frac{i}{\sqrt{\varepsilon_R(\omega_{max})\varepsilon_z(\omega_{max})}}\right]\right\}. \tag{2.19}$$

In the inset of Fig. 2.5(a) we show the graphical solution of the above condition. The obtained ω_{max} indeed matches very well with the peak position in the spectrum of Fig. 2.5(b). The condition for the peak position in Eq. (2.19) also explains the continuous shift of the broad guided-mode loss peak to higher energies in the upper RB with increasing slab thickness. In the lower RB we observe only one peak close to the energy $\omega_{LO,z}$ for the selected slab thicknesses. This peak can be attributed to the excitation of an assembly of modes that appear at this energy

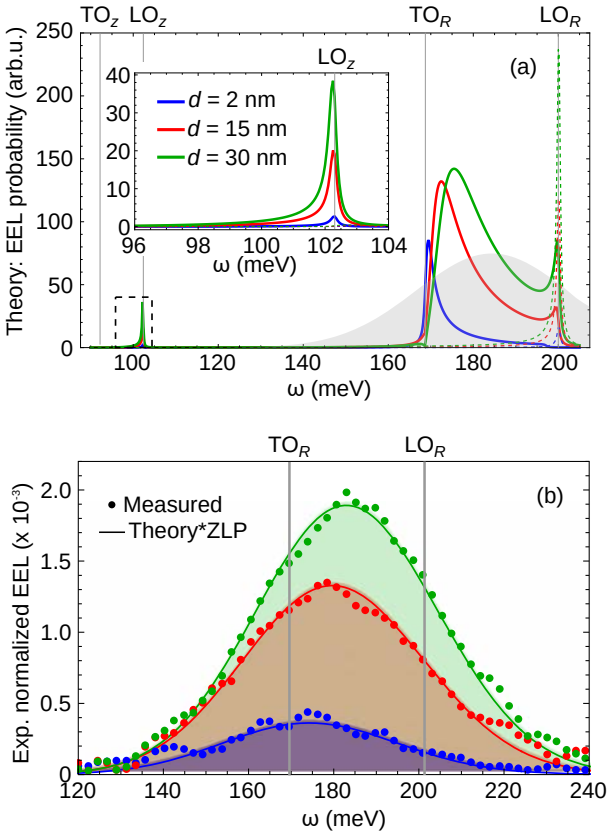

FIGURE 2.6: (a) EEL spectra calculated for a 60-keV electron passing through an infinite h-BN slab of varying thickness d = 2/15/30 nm (blue/red/green) and cutoff $Q_c = 0.08\,(\text{a.u.}) = 0.15\ \text{Å}^{-1}$. Inset: zoom of the spectra in the lower Reststrahlen band. Dashed lines show the contribution of the bulk loss [Eq. (2.15)] to the total energy loss [Eq. (2.3), full lines]. (b) Processed experimental spectra (dots) in the upper Reststrahlen band compared with theoretically calculated spectra (full lines) convolved with a Gaussian function of 46 meV FWHM [shown as the gray overlay in (a)] and denoted as "ZLP".

for small $|Q|$ [see Fig. 2.4(a)] and match with the condition $Q_{max} = \sqrt{3}\omega/v$.

We can now address our initial goal and compare the calculated spectra with the measurement on the h-BN flake on the terraces of varying thickness. We average the background-free spectra (after ZLP subtraction) measured at each region marked by the colored rectangles in Fig. 2.1(a) with approximate thicknesses 2/15/30 nm and plot the results in Fig. 2.6(b) as dots. The finite resolution of the instrument hides the narrow spectral features predicted theoretically and enables us to observe only one peak in the upper RB. It also prevents us to reliably identify any vibrational signal in the lower RB. To mimic the finite experimental resolution, we convolve the theoretical spectra with a Gaussian function of full width at half maximum (FWHM) of 46 meV [shown as the shaded gray line in Fig. 2.6(a)], which approximates the instrumental point spread function [see Fig. 2.1(b)]. Although the finer spectral features could not be resolved, the resulting convolved spectra plotted by solid lines in Fig. 2.6(b) are in excellent qualitative and quantitative agreement with the measured peak, which corroborates our modeling. Furthermore, we note that all theoretically predicted spectral features from Fig. 2.6(a) were resolved in several experiments performed with the STEM-EELS systems featuring ≈ 10 meV energy resolution [144, 145].

2.4 Hyperbolic surface modes at a truncation of h-BN slab

In this section we focus on the explanation of the spectral variations when the electron beam is scanned across an abrupt truncation of the h-BN flake. In particular, we analyze a spectral linescan over the region where the flake has an approximately constant thickness, highlighted by the orange line in Fig. 2.1(a). Motivated by the experimental observation, we aim at clarifying why the peak position significantly blue-shifts when the beam is scanned across the truncation [denoted by the yellow dashed-dotted line in Fig. 2.1(a)] from vacuum (penetrating only the TEM membrane) towards h-BN. In the following, we analyze only the spectral region of the upper RB ($\omega_{TO,R} < \omega < \omega_{LO,R}$).

In the theoretical model, we approximate the realistic geometrical arrangement by a semi-infinite slab of thickness $d = 30$ nm with a truncation at $x = 0$ as sketched in the inset of Fig. 2.7(a). As it is not possible to obtain an analytical solution for such an arrangement, we perform numerical simulations in a solver of Maxwell's equations implemented in the commercial finite-element-method software Comsol Multiphysics (see more details in Appendix B). Due to the translational invariance of the truncated slab along the y axis, we utilize a 2D simulation domain, where we allow propagation of electromagnetic waves in the y direction by setting the out-of-plane wavevector q_y. We thus obtain a solution for the electric field in the $(x, q_y, z; \omega)$ space and the $q_y - \omega$ dependent probability $\Pi(x, q_y; \omega)$. The electron beam (propagating parallel to the z axis) is

considered as a surface current proportional to $\exp(i\omega z/v)\exp(iq_y y)$, which means that to obtain the EEL probability for a localized electron beam, we need to integrate the numerical calculations for a sufficiently large range of q_y^c:

$$\begin{aligned}\Gamma_{\text{trunc. slab}}(\omega, x) &= \int_0^{q_{y,c}} dq_y \Pi(x, q_y; \omega) \\ &= \frac{e}{\pi^2 \hbar \omega} \int_0^{q_{y,c}} dq_y \int_{-z_{max}}^{z_{max}} dz \, \mathrm{Re}\left[E_z(x, q_y, z; \omega) \exp\left(-\frac{i\omega z}{v}\right)\right],\end{aligned} \tag{2.20}$$

where z_{max} is the size of the simulation domain along the z axis. We note that instead of the integration we perform a summation of spectra calculated numerically for a discrete set of q_y.

The resulting energy- and position-dependent spectra in Fig. 2.7(a) exhibit several interesting features. When the beam is further inside the slab ($x < 0$), it excites the guided slab modes with the M0 mode being dominant, as discussed in the previous section. The guided modes in h-BN can propagate several μm before

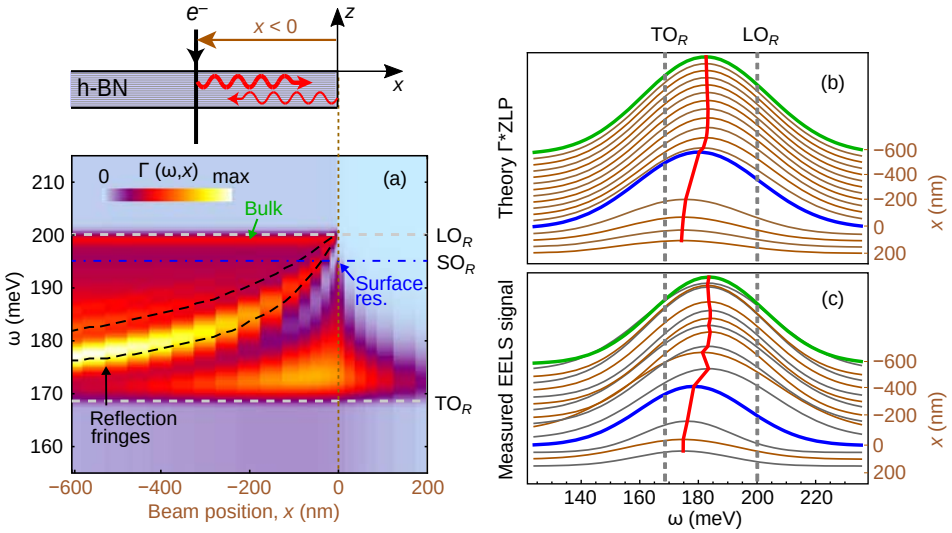

FIGURE 2.7: (a) Numerically calculated EEL spectra for a 60-keV electron passing at different positions x close to a truncation of 30-nm h-BN slab as sketched in the inset. The numerically obtained map is overlaid by analytically calculated peak maxima from the polariton reflection model [Eq. (2.21)]. (b) Spectra from (a) after convolution with a 46-meV Gaussian function on the same energy scale as the experimental results in (c). The red curves trace the positions of the peak maxima.

they are damped, and thus we can observe peaks resulting from a constructive interference of the guided waves propagating towards the slab truncation and those that are reflected back. The energy of the peak shifts depending on the distance of the electron beam to the truncation. In the spatially-resolved spectra we can observe fringes formed by the spectral maxima, similar to those observed in the near-field optical experiments [68, 134, 146]. By applying a phenomenological model for the wave reflection which consists of contributions from a freely propagating polaritonic wave $P(Q,\omega)$ and from a reflected wave proportional to $P(Q,\omega)(\cos(2Q|x|)+\phi_r)$ one gets the following expression for the loss probability:[2]

$$\Gamma_{\text{trunc. slab}}(\omega, x<0) \sim \int_0^{Q_c} dQ\, P(Q,\omega)\,[1+\cos(2Q|x|+\phi_r)]\,, \tag{2.21}$$

where $P(Q,\omega) = P_{\text{bulk}}(Q,\omega) + P_{\text{guid}}(Q,\omega) + P_{\text{Begr}}(Q,\omega)$ is the analytically retrieved result for the infinite h-BN slab and ϕ_r is a reflection phase. We show the analytically obtained peak maxima corresponding to the constructively interfering waves by black dashed lines in Fig. 2.7(a), reproducing very well the numerically calculated fringes if we set $\phi_r = \pi/2$ in the analytical model. The closer the beam is positioned to the truncation, the shorter polariton wavelengths (higher momenta) fulfill the condition for the constructive interference, which causes the shift of the spectral peaks (those traced by the black dashed lines) to higher energies [compare with the dispersion of the M0 mode in Fig. 2.3(a)].

Furthermore, we observe the bulk loss contribution at $\omega_{LO,R}$, which disappears suddenly when the beam is at $x = 0$, and for impact parameters $0 > x \gtrapprox -200$ nm a broad peak at lower energies. From our model, we can find that this peak around 175 meV originates from a contribution of a volume guided mode propagating in the negative x direction without experiencing any reflection. However, there might be also a contribution of a surface mode guided along the edge, which we analyze in the following discussion.

Interestingly, in addition to the broad peak around 175 meV a sharp peak appears at 195 meV [see also Fig. 2.9(a)] if we position the beam very close to the truncation ($|x| \lesssim 2$ nm). To explore the nature of the excitation at the slab truncation, we analyze the numerically calculated probability $\Pi(x, q_y; \omega)$ [see Eq. (2.20)], which represents a pseudo-dispersion of the excited modes coupled to the electron beam excitation. In Fig. 2.8 we plot $\Pi(x, q_y; \omega)$ for several beam positions x. When the beam is passing through h-BN far away from the truncation ($x = -1000$ nm), we can match the calculated maxima of $\Pi(x, q_y; \omega)$ with the dispersions of the even slab guided modes, as if they were the ones excited in the infinite slab. We superimpose the green dashed line tracing the dispersion of the dominant M0 mode (Eq. (2.18) for $n = 0$). The higher-order guided modes are also slightly visible in the plots.

[2] A similar model was applied in Ref. [93], where reflection of the surface plasmon polaritons at a truncated metallic waveguide was investigated.

However, a mode with a different dispersion is excited when the beam approaches the truncation and also, when the beam is outside, not penetrating the slab ($x > 0$). The dispersion of the so far unknown mode approaches the limiting energy 195 meV for short-wavelength excitations ($q_y \to \infty$). We find that this energy limit agrees with the asymptotic behavior of the $q_y - \omega$ relationship of the launched hyperbolic surface phonon polaritons at an infinite interface between h-BN and vacuum (i.e. if we consider $d \to \infty$, see Appendix A.2.1) in the same crystal orientation with respect to the beam trajectory:

$$q_y \approx \frac{\omega}{v}\sqrt{\frac{\varepsilon_R \varepsilon_z - 1}{1 - \varepsilon_R^2}} \tag{2.22}$$

$$\Rightarrow \omega_{SO,R}(q_y \to \infty) = \sqrt{\frac{\omega_{LO,R}^2 \varepsilon_{\infty,R} + \omega_{TO,R}^2}{\varepsilon_{\infty,R} + 1}} = 195\ \text{meV}. \tag{2.23}$$

Hence, we identify this excitation, which is excited only when the beam is close to the edge, as the fundamental surface hyperbolic mode which is guided by the slab

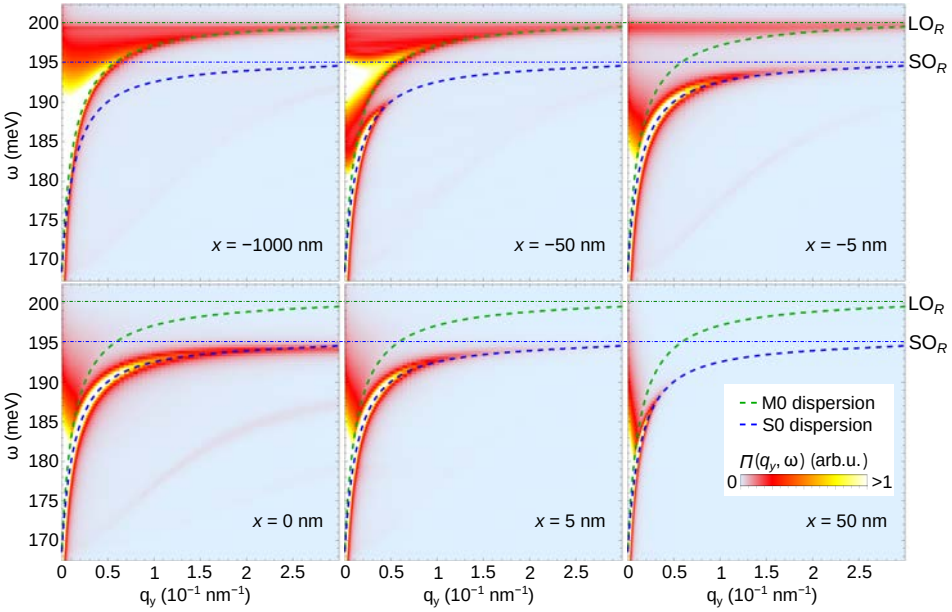

FIGURE 2.8: Simulated loss probability $\Pi(q_y; \omega)$ as defined in Eq. (2.20) for the beam positions x denoted in the figures. Dashed curves trace the dispersion of the guided M0 mode (Eq. (2.18) for $l = 0$) and the surface S0 mode [Eq. (2.24)], respectively.

boundaries along the yz surface. This mode can be understood as 2D analogue of the M0 mode and here we denote it as "S0". We can find an approximate $q_y - \omega$ relationship describing the S0 mode in the upper RB:

$$q_y(\omega_{TO,R} < \omega < \omega_{LO,R}) \approx \frac{1}{d}\mathrm{Re}\left[\frac{\varepsilon_R\varepsilon_z - 1}{1 - \varepsilon_R^2}\right], \tag{2.24}$$

which we plot with a blue dashed line in Fig. 2.8 matching very well the numerically calculated maxima.

In Fig. 2.9(a) we compare the spectra calculated for the beam at the truncation ($x = 0$, blue curve), just outside ($x = 5$ nm, violet curve) and a situation as if the beam were passing through an infinite slab (green dashed curve), which agrees well with the simulated result from Comsol [solid green curve in Fig. 2.9(b)]. Importantly, the peak from the guided surface mode appears at lower energy compared to the bulk guided mode as we can anticipate from the different dispersion of these modes and thus a different energy value for the optimal coupling to the field of the electron beam. These modes were also identified in near-field optical experiments where variations in periodicity of the interference fringes corresponding to the guided volume and surface waves were detected [147]. Analogous surface hyperbolic modes can be observed also in the VIS range e.g. in topological insulator materials, such as Bi_2Se_3, which was examined by means of EELS in

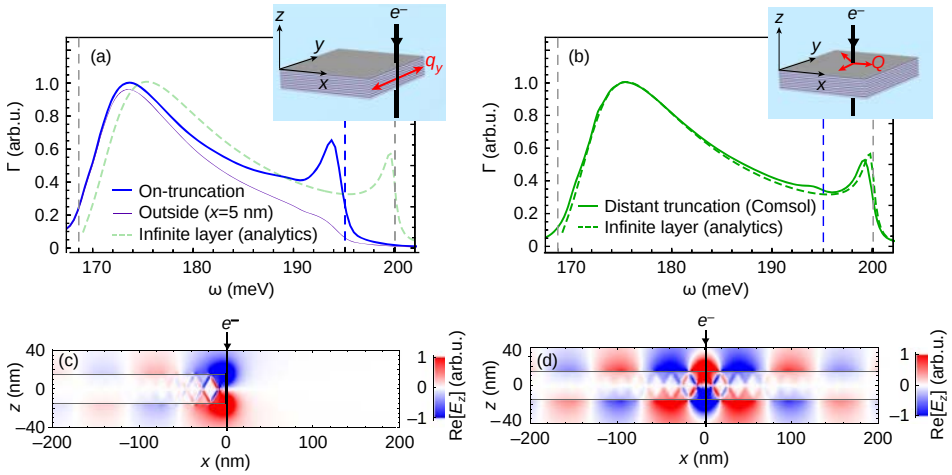

FIGURE 2.9: (a) Comparison of spectra from Fig. 2.7 for $x = 0$ (blue line) and $x = 5$ (violet line) together with the analytical calculation for an infinite slab (green dashed line). (b) Comparison of the analytical result for the infinite slab and numerical calculation in Comsol (dashed vs. solid line). (c,d) Field profiles $\mathrm{Re}[E_z(\omega_{SO,R})]$ for the beam at the truncation of the finite slab ($x = 0$) and for the beam penetrating an infinite slab, respectively.

Ref. [148].

We also analyze the localization of the surface guided mode at the truncation by plotting the distribution of the total field, $\mathrm{Re}[E_z(\omega_{SO,R})]$ for the electron trajectory at $x = 0$ [Fig. 2.9(c)] and for the beam passing through the infinite slab [Fig. 2.9(d)]. The beam penetrating the infinite slab excites only the volume guided modes, whose superposition creates the "zig-zag" pattern for $|z| < d/2$. Outside the slab ($|z| > d/2$), we find the field oscillations that correspond to the dominantly excited M0-HPhP mode. On the other hand, when the beam is at the slab truncation, it launches both the volume guided modes propagating in the negative x direction as well as the surface guided modes propagating at $x = 0$ along the y direction, responsible for the intense field localization at the corners of the truncation.

The overall spectral change when the beam is scanned across the truncation after convolution with the 46-meV Gaussian function again agrees very well with the experimental observation [Fig. 2.7(b) vs. (c)]. The main reason for the redshift of the convolved peak position for the beam outside the h-BN slab ($x > 0$) is the disappearance of both the bulk and the high-Q surface excitations (sharp peaks at $\omega_{LO,R}$ and ω_{SO_R}, respectively). As these peaks originate from the high-momentum excitations in the sample, they are highly localized and, therefore, are less accessible by aloof beams. However, the excitation of surface guided HPhPs with lower momenta is possible even with the electron beam relatively far outside the slab truncation, which is related to the typical decay length $\approx v/\omega$ of the electron's near field. The excitation of MIR PhP by the electron beam is therefore accessible even for $x \sim 10^2$ nm, in agreement with both the simulated and experimental result. In Chapter 3 we discuss the aspect of the spatial extent of the EEL signal in more detail, considering an isotropic truncated slab.

2.5 Summary

We have thoroughly analyzed how fast electron beams couple to HPhPs in h-BN and identified the modes excited in both infinite and truncated thin slabs. By employing classical electrodynamics, we found that modes guided in the slab volume, analogous to the modes in dielectric waveguides, as well as the modes guided along the surface at a slab truncation can be probed by fast electrons.

Our work can contribute to interpretation of spatially-resolved vibrational EELS measurements in a conventional scattering geometry and suggests that with improved spectral resolution, EELS is a promising technique for probing the intriguing (hyperbolic) phonon polaritons at the nanoscale, complementary to near-field optical methods such as SNOM.

Chapter 3

Vibrational electron energy loss spectroscopy near truncations and junctions of dielectric slabs

Sub-Ångstrom spatial resolution is nowadays routinely achieved with well-defined electron probes in STEM imaging [7] as well as in core-loss EELS [12]. However, if one filters the EEL signal at low energies in a conventional scattering geometry, it is possible to acquire information from an area significantly beyond the beam focus. Unless direct impact scattering takes place (when the beam can interact with both optical and acoustic lattice vibrations [62, 118, 145]), most of the EEL vibrational signal arises purely from the excitation of optical phonons. Optical phonons can couple to the electron beam tens or hundreds of nanometers away from the sample, due to the spatial decay of the electron's field [in the IR typically tens or hundreds of nanometers [10, 60, 63], see Eq. (1.24)]. If all electrons are collected (the electrons scattered at small angles are not filtered out [59, 145]), most of the EEL signal is coming from the rather long-range electromagnetic interaction [59, 149], which is even more pronounced when the beam interacts with samples supporting collective polaritonic excitations. This we demonstrated in Chapter 2, where we showed a slow spatial intensity decay of polaritonic losses as a function of the electron beam distance to a truncated h-BN slab together with the dependence of the loss peak energy on the beam position with respect to the truncation.

In this chapter, we further develop our understanding of EEL spectra close to truncated slabs and slab junctions, now considering isotropic materials. We particularly focus on a truncated thin slab of silica (SiO_2), which supports both polaritonic and non-polaritonic optical phonon excitations in the region between 90 and 160 meV. Then we analyze the EEL spectra at a silica-silicon slab junction as shown in Fig. 3.1(a). Such geometrical arrangements are very common in experimental situations and represent benchmarks to test the spatial dependence of

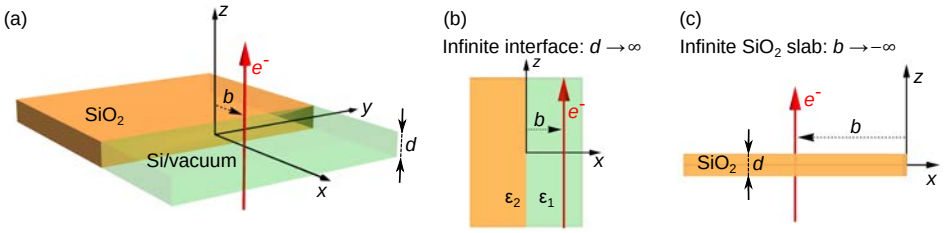

FIGURE 3.1: (a) Schematics of the considered geometry. The sample is a slab of thickness d, infinite in the xy plane with a sharp interface in the plane $x = 0$. We consider either a slab with a silica-silicon interface or a semi-infinite silica slab surrounded by vacuum. A 60-keV electron ($v = 0.446c$) is moving in the positive z direction at a distance b from the silica-silicon or silica-vacuum interface at $x = 0$. Negative values of b stand for the beam inside silica. Limiting cases of (b) an infinite interface geometry and (c) an infinite silica slab.

energy-filtered EELS. We identify different types of losses arising for both sample geometries and discuss the signal decay as a function of the beam distance to the slab truncation. Moreover, for the silica-silicon junction, we demonstrate an excellent agreement between the simulated spectra and experimental data from Ref. [63].

3.1 Analytical solutions of limiting cases

We first present analytical models to describe electron energy losses at an infinite interface and at an extended thin slab, to understand the results from numerical simulations. For our geometry of interest, sketched in Fig. 3.1(a), we will thus start from the solutions of the response of an infinite interface [Fig. 3.1(b)] [108, 150] and an infinite silica slab [Fig. 3.1(c)] [38, 109, 138, 151], with the electron beam traveling parallel and perpendicular to the interfaces, respectively.

3.1.1 Infinite interface geometry

We start with a limiting case of an electron moving parallel to an infinite interface between two media, as sketched in Fig. 3.1(b), which can describe well the experimental situations of a beam positioned close to the interface and/or large slab thicknesses d. For a beam moving at speed v in a medium characterized by a local dielectric function $\varepsilon_1(\omega)$ passing the distance d at an impact parameter b from a neighboring medium characterized by a dielectric function $\varepsilon_2(\omega)$, the EEL probability $\Gamma_{\text{interface}}$ including retardation effects (see also Appendix A.2.2) can be expressed as [150]:

$$\Gamma_{\text{interface}} = \frac{de^2}{2\pi^2\varepsilon_0\hbar v^2}\int_0^{q_y^c} dq_y \,\text{Im}\left\{\underbrace{-\frac{1-\varepsilon_1\beta^2}{\varepsilon_1\alpha_1}}_{\text{bulk}} + e^{-2\alpha_1|b|} \times \left(\underbrace{\frac{1-\varepsilon_1\beta^2}{\varepsilon_1\alpha_1}}_{\text{Begr.}} \underbrace{-\frac{2}{\varepsilon_1\alpha_2+\varepsilon_2\alpha_1}+\frac{2\beta^2}{\alpha_1+\alpha_2}}_{\text{interface}}\right)\right\}, \tag{3.1}$$

where $\beta = v/c$, c is the speed of light in vacuum, $\hbar\omega$ energy and

$$\alpha_n = \sqrt{(\omega/v)^2 + q_y^2 - \varepsilon_n\omega^2/c^2} \tag{3.2}$$

with $n = \{1, 2\}$. The integration above is performed up to the cutoff q_y^c to prevent divergence of the integral for the wavevector component $q_y \to \infty$.[1]

The non-retarded version of Eq. (3.1), $\Gamma^{\text{NR}}_{\text{interface}}$ is obtained by letting $c \to \infty$:

$$\Gamma^{\text{NR}}_{\text{interface}} = \frac{2de^2}{4\pi^2\varepsilon_0\hbar v^2}\text{Im}\left\{\underbrace{-\frac{\ln(2q_{y,c}v/\omega)}{\varepsilon_1}}_{\text{bulk}} + K_0\left(\frac{2\omega b}{v}\right)\left(\underbrace{\frac{1}{\varepsilon_1}}_{\text{Begr.}}\underbrace{-\frac{2}{\varepsilon_1+\varepsilon_2}}_{\text{interface}}\right)\right\}. \tag{3.3}$$

The bulk losses were integrated up to the momentum cutoff, assuming $q_y^c \gg \omega/v$, whereas the integrals of the remaining loss terms were carried out up to $q_y^c \to \infty$. We also implicitly consider $q_x^c \to \infty$. We again note that the classical description using the local dielectric function is valid only for small scattering angles, where the $q_{x,y}$ wavenumbers are smaller than the inverse of the atomic distances of the materials [138], which is in principle not fully fulfilled for both $\Gamma^{\text{NR}}_{\text{interface}}$ and $\Gamma_{\text{interface}}$. Nevertheless, we analyse here the EELS of optical phonons whose dominant contribution is at low momenta, thus justifying the expressions above. Only if one aims at properly describing momentum-filtered experiments or the interaction with acoustic phonons, it would be crucial to consider the dispersion of the sample's response and the full description of the phononic density of states [59, 118, 145, 149, 152].

We discuss now the different loss contributions in Eqs. (3.1) and (3.3). We denote the bulk loss as if the electron were travelling across an infinite medium characterized by $\varepsilon_1(\omega)$. Notice that the (non-retarded) bulk loss function $\text{Im}[-1/\varepsilon_1]$

[1] See Ref. [150] for expressions taking into account a circular collection aperture.

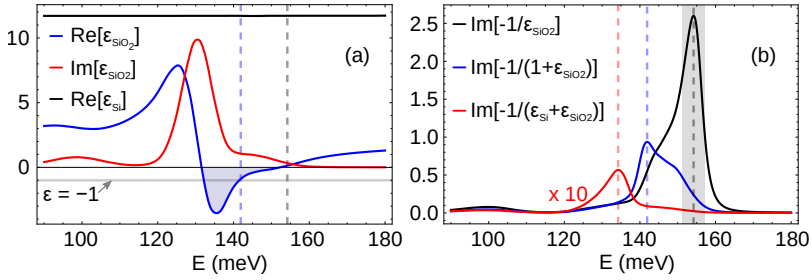

FIGURE 3.2: (a) Real and imaginary part of the dielectric function of silica ε_{SiO_2} together with the real part of the dielectric function of silicon (the imaginary part is four orders of magnitude smaller and thus negligible). (b) Bulk loss function of silica $\mathrm{Im}[-1/\varepsilon_{SiO_2}]$ (black) with peak energy at 154 meV, the silica-vacuum interface loss function $\mathrm{Im}[-1/(\varepsilon_{SiO_2}+1)]$ peaking at 142 meV (blue) and the much weaker silica-silicon interface loss function $\mathrm{Im}[-1/(\varepsilon_{SiO_2}+\varepsilon_{Si})]$ with a maximum at 134 meV (red). Vertical dashed lines mark the corresponding positions of the loss peaks. The gray shaded area in (b) emphasizes the region of bulk losses in SiO_2.

has a pole, if $\varepsilon_1(\omega_b) = 0$. This condition is satisfied for silica in the IR, as observed in Fig. 3.2(a) where $\mathrm{Re}[\varepsilon_{SiO_2}]$ (blue line) is plotted with dielectric data obtained from Ref. [153]. For energies above 132 meV, silica exhibits a Si-O-Si asymmetric stretching mode with a large effective charge (dipole strength), which yields a negative real part of the dielectric response in the blue region, where it enables excitation of surface phonon polaritons, as in polar crystals [19, 62] (see also Section 1.1.2). $\mathrm{Re}[\varepsilon_{SiO_2}]$ is negative almost up to the bulk mode energy $\hbar\omega_{SiO_2,b} = 154$ meV, where we observe an intense peak in the non-retarded bulk loss function $\mathrm{Im}[-1/\varepsilon_{SiO_2}]$, shown by the black curve in Fig. 3.2(b). Another spectral feature appears due to the Si-O-Si symmetric stretch at about 100 meV. However, the corresponding effective charge is relatively small and there is no pole of ε_{SiO_2} around this region ($\mathrm{Re}[\varepsilon_{SiO_2}] > 0$). The symmetric stretching mode thus contributes only weakly to the bulk loss and does not promote polaritonic excitations.

The interface loss function $\Gamma_{\text{interface}}$ also contains the so-called "Begrenzungseffekt" contribution, which is responsible for a reduction of the bulk losses. It has the same functional dependence as the bulk loss except for the negative sign and the prefactor that increases for small impact parameters b. Therefore, for a close approach of the electron to the interface, this contribution almost perfectly compensates for the bulk loss. The "pure" interface losses will become dominant in such situation. In the non-retarded case, the pole of the interface loss function $\mathrm{Im}[-1/(\varepsilon_1+\varepsilon_2)]$ would occur at an energy where $\varepsilon_1(\omega_s)+\varepsilon_2(\omega_s) = 0$. As $\mathrm{Re}[\varepsilon_{SiO_2}] < 0$ and $|\mathrm{Re}[\varepsilon_{SiO_2}]| > \mathrm{Re}[\varepsilon_{Vac}] = 1$, this condition is approximately fulfilled for the silica-vacuum interface (blue curve in Fig. 3.2(b) peaking at

$\hbar\omega_{SiO_2/Vac,s} = 142$ meV) corresponding to the excitation of surface phonons. On the contrary, the silica-silicon interface loss function $\mathrm{Im}[-1/(\varepsilon_{Si} + \varepsilon_{SiO_2})]$ exhibits only a weak non-resonant peak at 134 meV (red curve in Fig. 3.2(b) multiplied by factor of 10) because of the large and almost constant real value of the dielectric function of silicon in the spectral region of interest (plotted by the black line in Fig. 3.2(a), data taken from Ref. [154]). As we have $|\mathrm{Re}[\varepsilon_{SiO_2}]| < \mathrm{Re}[\varepsilon_{Si}] \sim 11.7$, no surface phonon excitation is supported at the silica-silicon interface.

3.1.2 Infinite slab geometry

If we place the beam far from the interface at $x = 0$ in Fig. 3.1(a), i.e. $b \to \pm\infty$, the geometrical arrangement will be well described as if the beam were passing through an infinite slab in the xy plane. Due to the possibility of exciting surface phonon polaritons at the silica-vacuum interface, we are particularly interested in such a calculation for the infinite silica slab as sketched in Fig. 3.1(c). In the non-retarded approximation, the slab loss probability can be expressed in a compact form (the retarded expressions see Section 2.3 and Refs. [109, 138]) as:

$$\begin{aligned}\Gamma_{\mathrm{slab}}^{\mathrm{NR}} &= \underbrace{\frac{de^2}{4\pi^2\varepsilon_0\hbar v^2}\,\mathrm{Im}\left\{-\frac{1}{\varepsilon_{SiO_2}}\right\}\ln\left(\frac{Q_c^2v^2+\omega^2}{\omega^2}\right)}_{\text{bulk}} \\ &+ \underbrace{\frac{e^2v^2}{\varepsilon_0\pi^2\hbar}\int_0^{Q_c} dQ\,\mathrm{Im}\left\{\frac{Q^2(\varepsilon_{SiO_2}-1)^2}{(Q^2v^2+\omega^2)^2\varepsilon_{SiO_2}} \times \left[\underbrace{\frac{\sin^2\left(\frac{\omega d}{v}\right)}{\varepsilon_{SiO_2}+\tanh(dQ)}}_{\text{sym.}} + \underbrace{\frac{\cos^2\left(\frac{\omega d}{v}\right)}{\varepsilon_{SiO_2}+\coth(dQ)}}_{\text{antisym.}}\right]\right\}}_{\text{Begr.+coupled surf.}},\end{aligned} \tag{3.4}$$

where Q is the wavevector perpendicular to the electron's trajectory and Q_c is the wavevector cutoff. Eq. (3.4) is a special case of Eqs. (A.1) and (A.3) for an isotropic slab ($\varepsilon_R = \varepsilon_z = \varepsilon_{SiO_2}$). Unfortunately, for the complex dielectric function ε_{SiO_2} and an arbitrary slab thickness, it is not possible to solve the integral in Eq. (3.4) in closed form and the integration has to be performed numerically.

The loss probability in Eq. (3.4) again contains several loss channels: the bulk loss probability, which would correspond to the losses of the beam in an infinite medium (but now integrated over the perpendicular momentum to consider the cylindrical symmetry), and the remaining loss term arising due to the presence of the top and bottom slab surfaces. The latter will have strong effects on the resulting spectra especially in the case of polaritonic materials. For thin slabs, the bulk loss will be reduced by the negative Begrenzungs contribution, similar to

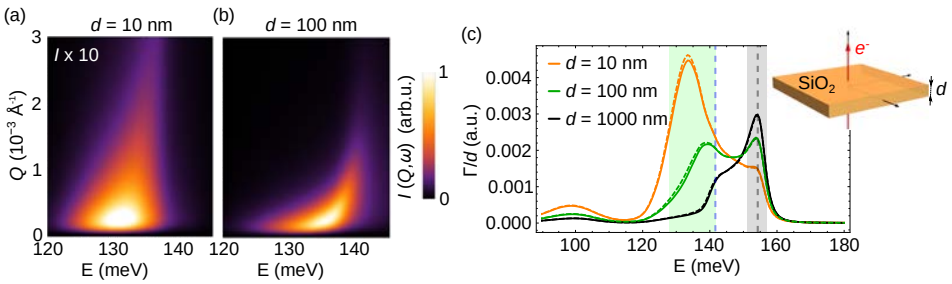

FIGURE 3.3: (a,b) Integrands of Eq. (3.4) evaluated for a 60-keV electron beam passing through an infinite silica slab of thicknesses 10 nm and 100 nm, respectively. For better visualization, the magnitude of (a) is multiplied by 10. (c) Non-retarded [full lines, according to Eq. (3.4)] and retarded (dashed lines) EEL probability normalized by the slab thickness, evaluated for $d = 10/100/1000$ nm. The momentum cutoff used in the calculation is $Q_c = 0.27\,\text{Å}^{-1}$.

what was observed for the case of the h-BN slab, and importantly, the upper and bottom surfaces become electromagnetically coupled, giving rise to symmetric and antisymmetric coupled surface modes as demonstrated in Fig. 2.3(b,d,f) of Chapter 2 [141].

We again note that the integrand of Eq. (3.4) can be understood as a dispersion of these modes, taking into account the coupling with the field of the fast electron [60]. In particular, the fast electron excites efficiently the charge-symmetric coupled surface modes [64, 110, 127, 155], whose (electron-excitation) weighted dispersion can be observed in Fig. 3.3(a,b). To see the dependence on the slab thickness, we evaluate the integrand of Eq. (3.4) for a silica slab of thickness $d = 10$ nm and $d = 100$ nm, respectively. Notice that the optimum of the coupling between the fast electron and the slab modes produces a spectral peak at higher energies for the thicker slab, which is consistent with the analysis performed in Section 2.3 for the anisotropic slab made of h-BN. The surface coupling can be neglected for thick slabs ($d \gtrsim 300$ nm for 60-keV electrons and silica), where the electron would excite independent surface phonon polaritons (yielding the loss peak approximately at an energy given by the condition $\varepsilon_{SiO_2} + 1 = 0$) at the top and bottom slab surfaces. However, the surface loss for very thick slabs is overwhelmed by the bulk loss in such situation.

The calculated loss probability spectra for a silica slab with different thicknesses are depicted in Fig. 3.3(c). We compare the non-retarded calculation using Eq. (3.4) (solid lines) with the fully retarded solution (dashed lines; almost coinciding with the solid lines) for 60-keV electron beam excitation. The retardation effects in this case introduce only a negligible red-shift, as expected, and a slight broadening of the peaks. In the calculated spectra, we observe three peaks: (i) a weak peak close to 100 meV coming from the excitation of the symmetric stretch of silica, (ii) the peaks in the light-green area which can be assigned to the

coupled-surface, polaritonic type of loss and finally, (iii) the bulk loss contribution close to $\hbar\omega_{SiO_2,b} = 154$ meV (light gray area).

The slab thickness determines the relative intensity of the bulk and coupled-surface losses, as well as the spectral position of the loss peak due to the symmetric coupled-surface mode [60], which we could anticipate from Fig. 3.3(a,b). The peak energy $\hbar\omega_M$ corresponding to the coupled-surface losses can be found analytically by performing a similar analysis as in Appendix A.1.2 for thin slabs of isotropic materials with small damping ($\mathrm{Im}[\varepsilon] \approx 0$) [138]:

$$\sqrt{3}\omega_{max} d = v \ln[(\varepsilon(\omega_M) - 1)/(\varepsilon(\omega_M) + 1)], \tag{3.5}$$

which, however, holds only approximately for thin silica slabs, as $\mathrm{Im}\left[\varepsilon_{SiO_2}\right]$ is not negligible. The thicker the slab is, the closer the peak appears to the silica-vacuum surface phonon energy at 142 meV (for $d = 1000$ nm hidden in the "shoulder" of the bulk loss). If the imaginary part (damping) of ε_{SiO_2} were smaller, we would observe two separate peaks below the bulk loss energy. The first peak corresponds to the charge-symmetric slab mode, and another peak at the silica-vacuum surface phonon energy ($\varepsilon_{SiO_2} + 1 = 0$ at 142 meV)[138] (see the pseudo-dispersion in Fig. 2.3(b) evaluated for a hypothetic material with much smaller damping). On the other hand, the weak non-polaritonic loss at 99 meV, which does not experience any substantial influence of the slab surface coupling, remains at the same spectral position for all slab thicknesses.

3.2 Electron energy loss in a truncated silica slab and silica-silicon junction

We address now a situation highly interesting in experiments: a truncated silica slab and a slab with a silica-silicon junction. We employ the same type of numerical EELS calculations developed in Comsol Multiphysics as in Section 2.4 (see also Appendix B). We consider the 2D geometry sketched in Fig. 3.4 and focus on the spectral region that corresponds to the asymmetric Si-O-Si stretch, where we can expect a polaritonic behavior of silica.

3.2.1 Modes interpretation

The calculated momentum-resolved spectra $\Pi(x, q_y; \omega)$ for the slab thickness $d = 100$ nm are shown in the color plots of Fig. 3.4, and can be understood as pseudo-dispersion relationships which account for the coupling with the field of the fast electron, similarly to the expressions in the integrals of Eq. (3.1) and Eq. (3.4) [the latter evaluated in Fig. 3.3(a,b)]. The green dashed line in Fig. 3.4 shows the maxima extracted from Fig. 3.3(b), tracing the dispersion of the charge-symmetric coupled-surface mode. The blue and light red lines trace the maxima

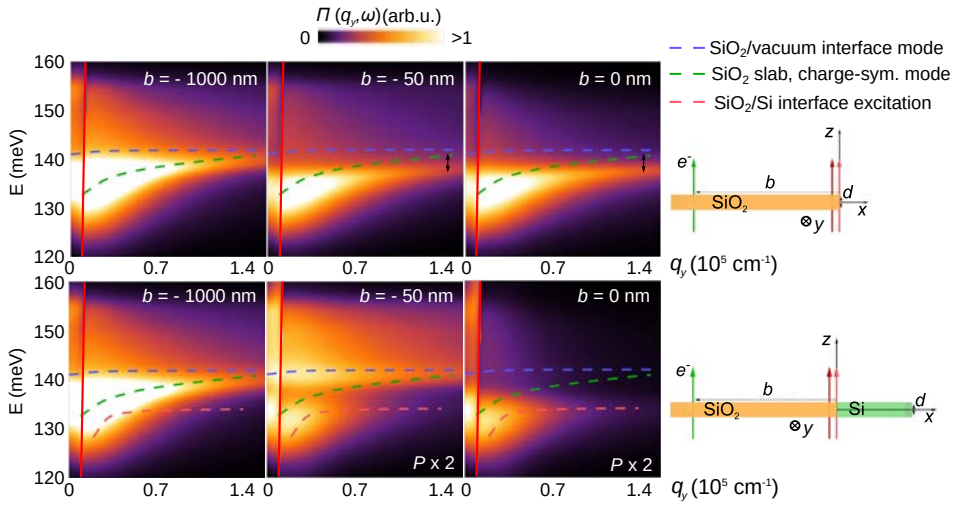

FIGURE 3.4: Numerically calculated momentum-resolved EEL probability $\Pi(q_y, \omega)$ for a truncated silica slab (upper row) and a silica-silicon junction (lower row) for two impact parameters of the beam passing through silica ($b = -1000$ nm and -50 nm, respectively) and another impact parameter at the slab truncation or junction ($b = 0$ nm). The slab thickness is $d = 100$ nm. The intensity of the last two plots for the silica-silicon junction is multiplied by a factor of 2. The dashed curves are analytically calculated maxima of momentum-dependent loss probabilities for the infinite silica slab (green), infinite silica-vacuum interface (blue) and infinite silica-silicon interface (red). Solid straight red lines denote the threshold for radiation losses.

of the momentum-dependent retarded loss in the integrand of Eq. (3.1) at an infinite silica-vacuum and a silica-silicon interface, respectively.

From the plots for impact parameter $b = -1000$ nm, it is clearly noticeable that this situation is analogue to the infinite silica slab limit as the numerical result nicely matches the symmetric coupled-surface mode dispersion (green dashed curve). A smaller contribution of the bulk loss appears at higher energies around 155 meV, which becomes the dominant loss channel for higher momenta ($q_y \gtrsim 0.01\,\text{Å}^{-1}$; not shown in the plots).

For smaller impact parameters ($|b| \lesssim 100$ nm; with b negative), the results differ from the infinite silica slab limit (central and right-hand columns). For the silica truncated slab, we observe an intense excitation of a mode with a different dispersion. We assign this excitation to a coupled edge mode, with limiting energy $\hbar\omega_{SiO_2,edge} = 140$ meV for $q_y \to \infty$, which is slightly lower than the silica-vacuum interface loss limit $\hbar\omega_{SiO_2/Vac,s}$ (see the small black arrows denoting the mismatch). We note that the coupled edge dispersion cannot be reproduced analytically [73].

On the other hand, the momentum-resolved probability when the electron beam is at the silica-silicon junction ($b = 0$ nm, bottom plot) resembles the dispersion of the silica-silicon infinite interface (marked by the dashed light red curve). Compared to the vacuum-surrounded silica truncated slab, the coupled edge modes cannot be excited in the SiO_2/Si junction due to the high refractive index of silicon present at one of the interfaces. If the beam is slightly moved from the interface towards the silica ($b = -50$ nm, bottom plot), we observe both the interface loss and also an additional loss contribution around 140 meV. In this case, the beam excites the coupled surface modes across the silica slab that are influenced by the presence of silicon and can get reflected at the interface. In particular, when the beam is very close to the junction, the constructive interference of the reflected waves and those propagating towards the interface (with short-wavelength polaritons dominantly involved) determines the position of the spectral maximum. Therefore, the coupled-surface loss appears close to the silica surface phonon energy at 142 meV, which is the large-wavevector limit of the surface phonon polariton dispersion denoted by the blue dashed line.

3.2.2 Electron energy loss spectra

We focus in this section on conventional energy-dependent EELS in both truncated slabs structures. We perform numerical calculations in a 3D geometry, but as pointed out in Section 2.4, the results can be reproduced also from 2D calculations according to Eq. (2.20). We note that the finite size of the mesh elements in the numerical simulation acts as an effective momentum cutoff and thus naturally eliminates the divergence of the losses for high momenta. The average cutoff in the performed 3D simulations is $\sim 0.2\,\text{Å}^{-1}$.

The spectra calculated for a varying impact parameter both from the silica-vacuum and from the silica-silicon junction are plotted in Fig. 3.5(a) and (b), respectively. The spectral sets exhibit two common features: the bulk loss peak around 154 meV (gray region) and the coupled-surface loss (green region) appear when the beam is inside silica, as derived from Eq. (3.4). As the beam is getting closer to the interface, we observe a weakening of the coupled-surface loss peak and a slight continuous shift of its energy towards the silica surface phonon energy at $\hbar\omega_{SiO_2/Vac,s} = 142$ meV (denoted by the blue dashed line), which is related to the momentum dependence discussed above.

The spectral features appearing in the red region correspond to a strong silica polaritonic coupled-edge mode in Fig. 3.5(a) and to a weaker non-resonant silica-silicon junction excitation in Fig. 3.5(b), respectively (as revealed also in the momentum-resolved spectra of Fig. 3.4). The spectral shape and peak position of the latter contribution can be described by the silicon-silica interface loss function $\text{Im}\left\{-1/(\varepsilon_{SiO_2} + \varepsilon_{Si})\right\}$. We have also found that when the beam goes through silicon, a relatively strong positive background is produced in the spectra. As silicon has a large refractive index, this introduces a contribution of radiation losses to the total energy loss (see also Eq. (1.35) and related discussion). Radiation losses

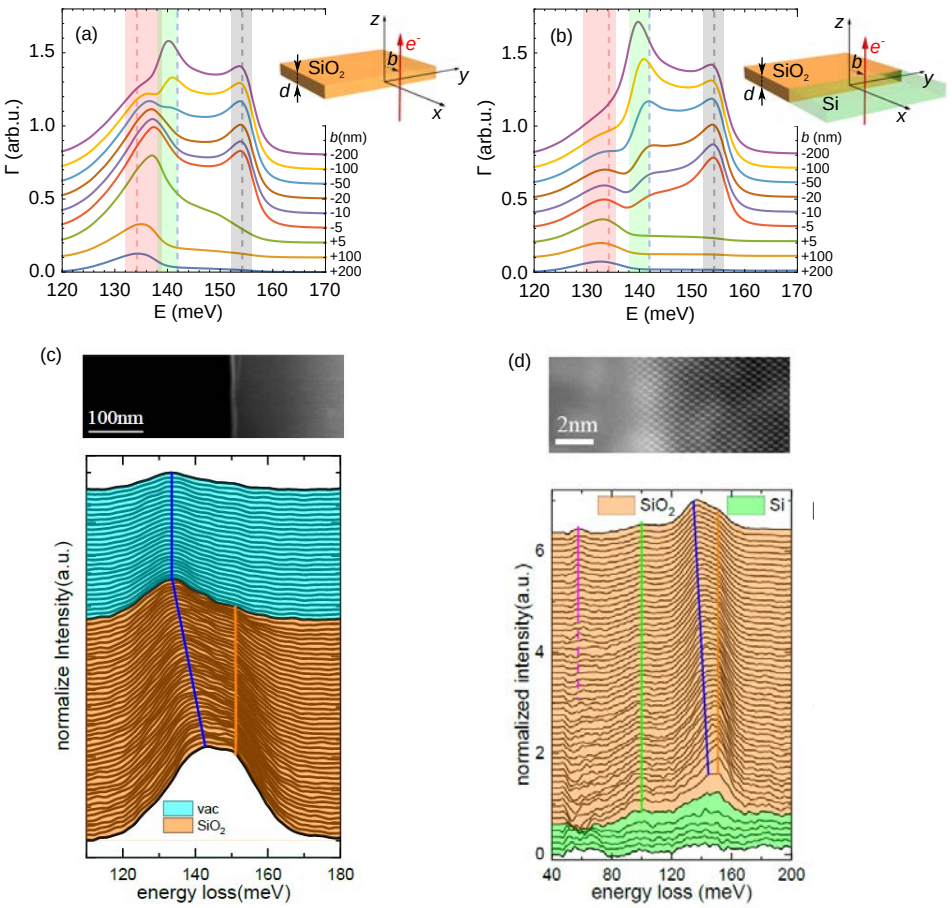

FIGURE 3.5: Numerically calculated EEL spectra for an electron beam probing (a) a truncated silica slab and (b) a silica-silicon junction at varying impact parameter b as displayed in the insets. b is negative, when the beam is inside silica and positive when it is placed either in vacuum or in silicon. The slab thickness is in both cases d = 100 nm. Spectra are vertically shifted by a constant value for clarity. Plots (c,d) are reproduced with permission from Ref. [65] by Li et al., and show experimental measurements of EEL for a truncated silica slab (c) and a silica-silicon junction (d) with a slab thickness ~ 80 nm. The spectra were recorded with 4.7-nm step (c) and 0.78-nm step (d), respectively. Orange spectra are for the beam penetrating silica, cyan for the beam outside the slab and light green spectra for the beam passing through silicon.

appear above the light lines in Fig. 3.4 and become the dominant loss channel when the beam goes through silicon (b > 0).

A recent work by Li at al. [65] shows experimental data corresponding to the

cases of our consideration: we reproduce the plots in Fig. 3.5(c,d). Both the line-scan across the silica truncation (c) and the junction between silica and silicon (d), recorded with spectral resolution ~ 8 meV and a slab thickness ~ 80 nm, show excellent correspondence with our calculations in (a) and (b), respectively.

3.3 Spatial variation of electron energy loss intensity

We complete our analysis by addressing the spatial variation of EEL intensity at the energies of the different excitations identified in the previous sections.

The impact parameter dependence of the EEL signal filtered at the energies of the loss peaks of the coupled-edge, coupled-surface, and bulk losses are plotted in Fig. 3.6(a) for the silica truncated slab and in Fig. 3.6(b) for the silica-silicon

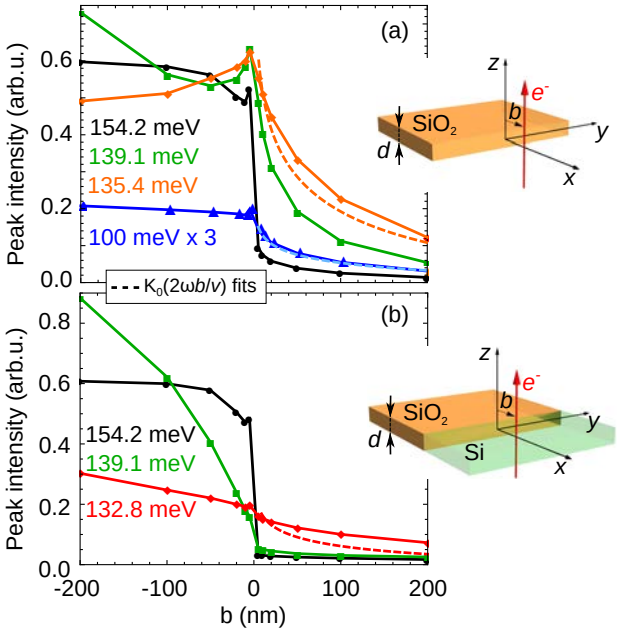

FIGURE 3.6: Extracted EEL intensities at fixed energies are plotted in (a) for the truncated silica slab and in (b) for the silica-silicon junction. The energies correspond to the silica bulk loss peak (black), the coupled-surface loss for an infinite 100-nm thick silica slab (green), the silica edge excitation [orange points in (a)], non-polaritonic Si-O-Si symmetric stretch signal (blue in (a), multiplied by 3). The spatial dependence of the silicon-silica junction excitation intensity is plotted in (b) (red). Dashed curves are fits of the decay for $b > 0$, using $K_0(2\omega b/v)$ at 100 meV (light blue), at coupled-edge loss energy (orange) and junction excitation energy (red).

slab junction. We further add the intensity of the non-polaritonic contribution at 100 meV in (a). Due to the large damping present in the material response, it is not straightforward to separate the contributions from the different loss channels, as they spectrally overlap and are rather blurred (see, e.g., Fig. 3.4). However, the signal decays shown in Fig. 3.6(a,b) provide a valuable insight.

Outside the truncated silica slab ($b > 0$ nm), we observe that the coupled edge excitation is dominant [orange points in Fig. 3.6(a)]. A smaller portion of the signal at the coupled-surface loss (green) and at the bulk loss (black) arises mostly due to the spectral overlap. As the beam is scanned across the truncation ($b \leqslant 0$ nm), we observe an immediate increase in the signal at the bulk loss energy, which eventually becomes constant. We note that in the case of no spectral overlap, the bulk signal would exhibit a step-like profile close to the interface. The coupled-surface loss probability also increases when the beam is scanned into the material (negative x direction) and, at larger distances from the truncation, similarly to the bulk loss, becomes constant (not shown in the plot). We note that the large damping of silica hides clear spectral signatures of interference of the coupled-surface waves propagating towards and backwards from the interface at $x = 0$ [60], and the energy-filtered intensity is thus increasing smoothly. The edge mode excitation probability shows a maximum for the beam positioned exactly at the edge ($b = 0$, orange line) and smoothly decreases with the beam distance from the truncation at both sides with different decay.

We also plot the signal filtered-out at 100 meV in Fig. 3.6(a) (blue points). The spectral overlap with other loss channels in this region is not that pronounced and we can thus study the spatial dependence of this non-polaritonic contribution. When the beam is scanned into the silica, the intensity of the 100-meV loss slightly increases and quickly saturates, similar to the bulk loss. As the influence of coupling of the silica edges and surfaces can be neglected at this energy (the excitation has non-polaritonic character), the signal drop for the beam outside the slab approximately follows the infinite-interface decay. Indeed, a fit by the $K_0(2\omega b/v)$ dependence [see Eq. (3.3)] reasonably traces the result of the numerical simulation (blue dashed curve), except for the singular behavior close to $b = 0$. We emphasize that the functional dependence of the signal decay strongly depends on the particular type of excitation and the corresponding induced EM field distribution. In summary, the signal decay from polaritonic materials can be approximated by the K_0 dependence either for an infinite interface ($d \to \infty$) or for very small impact parameters ($b \ll d$) in the cases when retardation effects can be neglected. As we demonstrate here, K_0 fits the decay from thin truncated slabs only if the excitation is not polaritonic, however, it is not appropriate for modeling the decay when the coupled-edge modes are involved [see the orange points vs. the dashed orange curve in Fig. 3.6(a)]. In such a case, the signal decay has to be retrieved numerically.

The spatial dependence of the energy-filtered signal changes substantially when the beam is scanned across the silica-silicon junction, as shown in Fig. 3.6(b). Due to the non-resonant character of the excitation at the silica-silicon

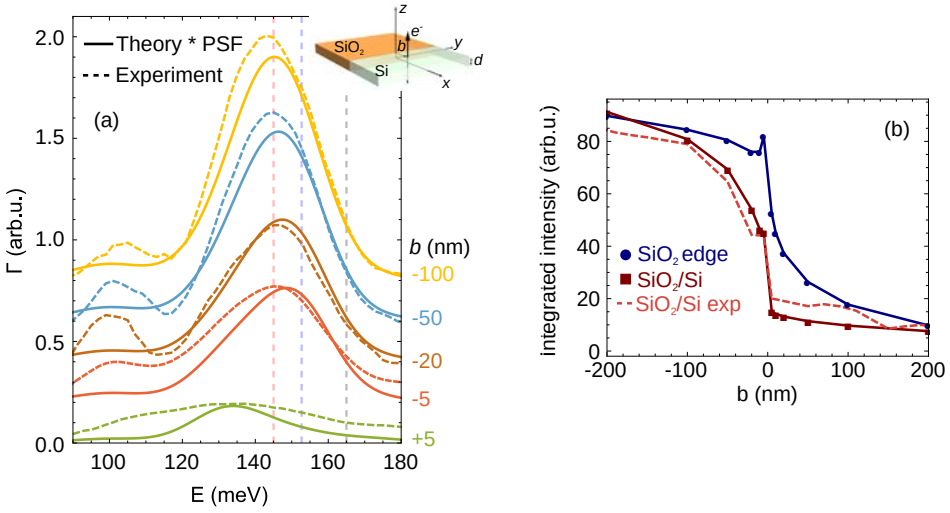

FIGURE 3.7: (a) Numerically calculated EEL spectra from Fig. 3.5(b) after convolution with a point spread function (PSF) represented by a Gaussian function of FWHM 20 meV mimicking the finite experimental resolution (full lines) and experimentally measured spectra (dashed lines, taken from Ref. [63]). The impact parameters as denoted next to the plot. The spectra are vertically shifted for clarity. Graph (b) depicts the total intensity integrated over an energy window of 120-160 meV for the silica edge (dark blue) and silica-silicon slab junction (dark red). Symbols represent the calculated data, lines are guides to the eye. The dashed line shows the experimental result for the silica-silicon junction integrated over a 120-180 meV energy window.

interface at 132.8 meV, we observe only a tiny peak at the junction ($b = 0$). The "interface" signal for $b > 0$ comes mostly from radiation (Čerenkov type of losses in silicon which arise due to its high refractive index), and therefore slowly decreases with the distance of the beam to the interface (red curve). In this case, retardation effects (i.e. the constant radiation contribution) make the fitting of the signal decay by the K_0 dependence (red dashed curve) not suitable. On the contrary, we get an immediate decrease in the bulk and the coupled-surface loss signal when the beam crosses the interface towards silicon (black and green lines, respectively). Importantly, the smaller spectral overlap of the loss channels and the suppression of the coupled edge excitation because of the presence of silicon makes it possible to obtain nanometer spatial resolution by filtering the signal at the bulk loss or coupled-surface loss energies.

Finally, in Fig. 3.7(a) we show a direct comparison of the experimental spectra from Ref. [63] (dashed curves) obtained for the same geometrical arrangement as that considered in the calculations, and the numerically calculated spectra convolved with a point spread function (PSF) to simulate the experimental resolution

(solid curves). We approximate the PSF by a Gaussian function with full width at half maximum (FWHM) of 20 meV. Unfortunately, such resolution smears out the finer spectral structure shown in Fig. 3.5(a,b) and only two main peaks can be observed. We obtain very good agreement between the theory and experiment in the spectral positions and relative intensities of the peaks above 130 meV. When the beam is passing through silicon, the experimental spectra are noisier and we observe that the calculated spectra are narrower than the experimental ones. We observe that all theoretical spectra underestimate the strength of the 100-meV Si-O-Si symmetric stretch. These discrepancies can be caused by the experimental noise, differences in the sample geometry, including possible mixing of material layers or impurities, and the finite size of the probe. However, as we have shown in Fig. 3.5(c,d), the recent experimental EEL study reaching a spectral resolution of ~ 8 meV [65] demonstrates very clearly the predicted finer spectral details. One might expect further advances in vibrational EELS analysis along these lines in near future with the constantly improving experimental capabilities [156].

Due to the limited experimental resolution and noise, energy-filtered maps (or linescans) are often acquired not by selecting a discrete energy, but rather by integrating over a wider energy window. Hence, in Fig. 3.7(b) we compare the calculated EEL intensity integrated over the energy window 120-160 meV. The integrated spectral signal corresponding to the truncated silica slab peaks at $b = 0$ and then slowly decays for $b > 0$ (dark blue curve). The integrated signal for the silica-silicon junction (dark red curve) exhibits a nearly step-like profile very close to the interface ($|b| < 5$ nm) with a smooth increase when the beam is placed into the silica ($b \leqslant -5$ nm) and a positive radiation background for $b > 0$.

The calculations predict that it would be possible to use either the energy-filtered signal or the integrated signal (the energy-filtered signal in larger energy range) to distinguish the edge boundary with nanometric precision. However, we expect that the peak at the boundary of the truncated silica slab ($b = 0$) will be smeared out in experiments, since it arises from a perfectly abrupt interface considered in the theoretical simulations, and also neglects the finite convergence angle of the beam. Hence, in such an arrangement, the nature of the electron-sample interaction will make it experimentally difficult to distinguish the material boundary directly from the energy-filtered maps and thus, a correlation with high-resolution imaging capabilities will be needed [10].

On the other hand, the interface between silica and silicon can be well distinguished by filtering the loss at energies of either bulk or coupled-surface losses, as they are strongly suppressed close to the junction. As these losses are prevailing in the overall spectral response, the sudden drop of intensity is also observed in the integrated signal. This is indeed confirmed by comparing the theoretical prediction with the experimentally measured data for the same geometrical arrangement [63], where the spectral intensity was integrated over 120-180 meV energy window. The experimental result [pink dashed curve in Fig. 3.7(b)] reasonably well matches the theoretical prediction (dark red points). The step-like

profile is still present for $|b| < 5$ nm and thus we can conclude that the dielectric screening by silicon helps to distinguish the interface directly from the EELS linescan. It was shown recently that truly atomic resolution in vibrational EELS can be achieved if the impact scattering and excitation of acoustic modes is taking place [125]. However, these excitations cannot be described by the classical dielectric theory, and proper ab-initio modeling needs to be involved.

3.4 Summary

We have thoroughly analyzed the spatial dependence of EEL spectra for two relevant geometrical arrangements: the truncated slab of silica and the slab with an interface of silica and silicon, representing typical configurations for TEM specimens. We have observed a large contribution to EEL spectra from the optical phonon polariton modes supported by silica, whose excitation probability is strongly influenced by the electron beam position. The different spatial decay of the polaritonic signal compared to the non-polaritonic contribution has been demonstrated and clarified, and the possibility to distinguish the material interface at high spatial resolution from the energy-filtered linescans has been discussed. Although we studied specific material systems, our findings can be generalized and serve as a guide for interpretation and analysis of experimental data in spatially-resolved vibrational EELS of common geometries.

Furthermore, thin oxide layers grown on silicon substrates [157] are of high interest in the semiconductor industry and in particular, amorphous silica is often exploited as an insulating material in electronic nanodevices due to its high dielectric strength [158, 159]. Spatial characterization of the vibrational response of these morphologies together with high-resolution imaging using STEM-EELS could help, e.g., to better understand heat dissipation in such nanostructures.

Chapter 4

Thermal effects in the interaction of a focused electron beam with matter

Recent instrumental improvements have shown that it is nowadays possible to detect very low-loss vibrational excitations with a nanometer- or even atomic-focused electron beam [10, 62]. Importantly, the energies of the vibrations are comparable to k_BT (with k_B being the Boltzmann's constant and T temperature), and thus thermal effects start to be important with the possibility of inducing temperature-stimulated energy loss and gain contributions to the interaction of an electron beam and a sample, analogous to the appearance of Stokes and anti-Stokes peaks in Raman scattering [110, 160]. The energy gain peaks were first predicted and observed in high-resolution (HR)-EELS with micrometer-sized electron beams used in reflection geometry [161, 162]. However, recent experiments [61, 163, 164] have demonstrated that the effects of temperature are now detectable in vibrational spectra in STEM-EELS, which can be used for temperature measurements with nanoscale spatial resolution.

We have previously discussed that a substantial amount of EEL signal is formed by electrons that have not lost nor gained (nearly) any energy. These electrons contribute to an intense zero-loss peak (see Fig. 1.6 and Fig. 2.1), which we now denote, in the context of this chapter, as a quasi-elastic peak (QEP) to emphasize that it can contain ultra-low energy losses and gains. The QEP is typically removed during post-processing of measured spectra and only peaks at non-zero energies are analyzed. However, it has been observed that the intensity and width of the QEP significantly varies with sample temperature both in HR-EELS [165–167] and STEM-EELS [163] (see Fig. 4.1(a) and (b), respectively), whereas the behavior of the QEP in the latter technique has not been theoretically addressed and fully understood yet. In this chapter we show how the complete EEL and electron energy gain (EEG) spectra, including the QEP, change when we consider the temperature variations in a sample. To that end, we employ an analytical modeling of electron energy loss and gain probability dependent on

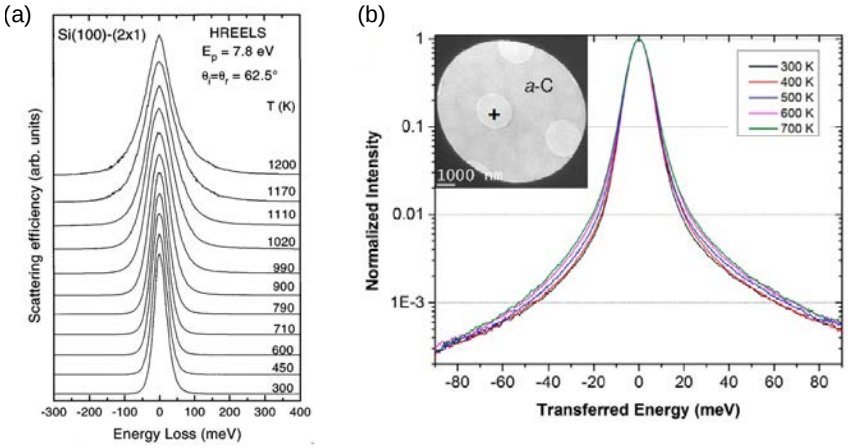

FIGURE 4.1: (a) Temperature dependence of the QEP peak in HREELS experiment recorded in specular reflection geometry with equal incident and reflection angles ($\theta_i = \theta_r = 62.5°$) for a primary beam of energy $E_p = 7.8$ eV impinging at Si surface. The broadening is caused by changes in excitation occupation statistics as well as by intrinsic phase changes in the material. Reprinted with permission from Ref. [165]. ©1996 by the American Physical Society. (b) Temperature-induced broadening of the QEP in STEM-EELS experiment for an electron beam interacting with a membrane made of amorphous carbon. Reprinted with permission from Ref. [163]. ©2018 American Chemical Society.

temperature and on the beam position. We also show experimental evidence of the predicted behavior.

4.1 Temperature-dependent electron energy loss and gain

To describe the temperature-dependent spectra including the energy loss and gain events we adapt the theoretical description developed in Refs. [110, 160]. We express the probability $\Gamma(\omega, T)$ of losing or gaining energy $\hbar\omega$ per unit energy arising from the interaction of an electron beam with a sample in thermal equilibrium at temperature T as

$$\Gamma(\omega,T) \approx P_0 \sum_i \{\delta(\omega)\,[1-2A_i(\omega_i)n(\omega_i,T)] + A_i\,[\delta(\omega-\omega_i)\,(n(\omega_i,T)+1) + \delta(\omega+\omega_i)n(\omega_i,T)]\}, \quad (4.1)$$

where only the 0th and the 1st order terms of the perturbative expansion are taken into account (as in Section 1.2.3), $\hbar\omega_i$ are the energies of the excitations in the sample, $\delta(x)$ is the Dirac delta function, and A_i are amplitudes of the excitations. P_0 is a normalization factor ensuring that

$$\int_{-\infty}^{\infty} d\omega\, \Gamma(\omega, T = 0) = \int_{-\infty}^{\infty} d\omega\, \Gamma(\omega, T \neq 0) = 1 \tag{4.2}$$

holds, and

$$n(\omega, T) = \frac{1}{e^{\hbar\omega/(k_B T)} - 1} \tag{4.3}$$

is the Bose-Einstein distribution introducing thermal occupation statistics valid for phonons. If we further consider an electron beam with a trajectory $\mathbf{r}_b$ in aloof geometry (not penetrating the sample placed at $\mathbf{r}_s$, thus interacting only with optical excitations), the terms $A_i\delta(\omega \pm \omega_i)$ can be replaced by the classical loss probability Γ_{cl} [introduced in Section 1.2, calculated e.g. from Eq. (1.28)], which depends on the sample geometry and its position with respect to the beam.

We can observe that Eq. (4.1) contains a delta-like zero loss line at energy $\hbar\omega = 0$ which is reduced at the expense of the discrete single-loss and gain lines at energies $\hbar\omega_i$ and $-\hbar\omega_i$, respectively, whose intensity ratio is

$$\frac{I_{gain}(\omega_i)}{I_{loss}(\omega_i)} = \frac{n(\omega_i, T)}{n(\omega_i, T) + 1} = e^{-\hbar\omega_i/(k_B T)}. \tag{4.4}$$

At zero temperature, only the loss event stimulated by the field of the electron beam appears (as assumed in preceding chapters of this thesis).

In reality, a broadening of the spectral features can be observed due to the finite lifetime of the excitations and also due to the point spread function $PSF(\omega)$ of the instrument. The PSF reveals the influence of aberrations in the electron optics and the finite energy monochromation width. Therefore, if there is no sample present in the microscope, we can express the "pure" temperature-independent zero-loss/gain peak as the $PSF(\omega)$. If we take all these considerations into account, Eq. (4.1) becomes

$$\begin{aligned}\Gamma(\omega, T, \mathbf{r}_s, \mathbf{r}_b) \approx \underbrace{P_0\, PSF(\omega)\left(1 - 2\int_0^{\infty} d\omega\, \Gamma_{cl}(\omega, \mathbf{r}_s, \mathbf{r}_b) n(\omega, T)\right)}_{\text{zero-loss/gain peak}} \\ + P_0\, PSF(\omega) * \Gamma_T(\Gamma_{cl}, T),\end{aligned} \tag{4.5}$$

where $*$ stands for the convolution and where we define

$$\Gamma_T(\Gamma_{cl}, T) = \Gamma_{cl}(|\omega|, \mathbf{r}_s, \mathbf{r}_b)\, n(|\omega|, T)|_{\omega<0} + \Gamma_{cl}(\omega, \mathbf{r}_s, \mathbf{r}_b)\,(n(\omega, T)+1)|_{\omega>0}. \quad (4.6)$$

The spectrum in Eq. (4.5) consists of the zero-loss peak, which is reduced at higher sample temperatures [upper line of Eq. (4.5)], energy gains and energy losses [lower line of Eq. (4.5)], which can also have non-zero values at very low energies and together with the zero-loss/gain distribution contribute to the overall shape of the QEP. The gain spectrum is the mirrored loss spectrum with respect to $\hbar\omega = 0$ obeying the intensity ratio in Eq. (4.4). We note that the effect of temperature appears explicitly in the Bose-Einstein distribution terms, but in real systems, the finite temperature can also affect intrinsic energies of excitations and their lifetimes. Such temperature dependence can be included "ad hoc" by adjusting the material response in the classical probability Γ_{cl}, or studied ab initio. The influence of the temperature on energies of the excitations was addressed in the context of EELS, e.g., in Ref. [61] where shifts of energies of h-BN phonons were described, or in Refs. [168, 169] where spatially-resolved temperature mapping was obtained from shifts of plasmon energies.

To study the significance of the changes in loss and gain probability caused by the finite sample temperature, we model the spectrum in a simple geometrical

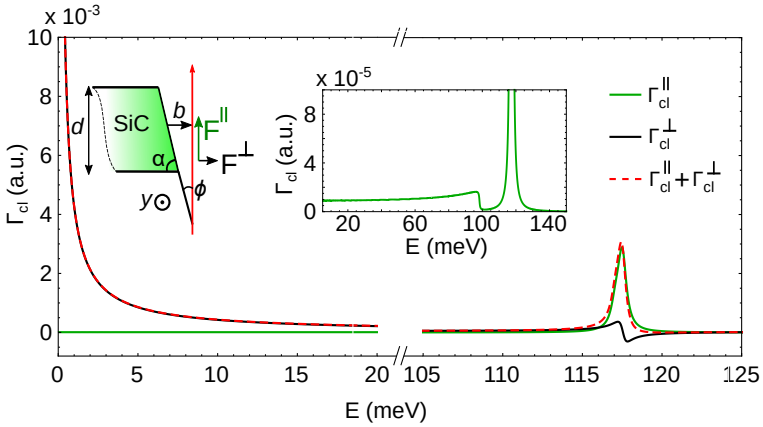

FIGURE 4.2: Classical loss probability calculated for a 60-keV electron beam moving in vacuum along an interface with SiC under a small tilt angle $\phi = 0.02$ rad. We consider that the distance traveled along the interface (thickness of SiC slab) is $d = 500$ nm and that the average distance of the beam from SiC is $b = 10$ nm (see the inset schematics). The total loss probability [Eq. (4.7)] (red dashed line) is split in the parallel, Eq. (4.8) (green line), and the perpendicular, Eq. (4.9) (black line), contribution, respectively. The inset shows close-up view of the parallel contribution showing small constant radiation background at low energies.

arrangement: an electron beam moving close to a truncation of a thick slab of SiC. We assume that the slab thickness d is large enough so that we can neglect the coupling between the slab surfaces (as discussed in the previous chapters) and the influence of edge modes, and we approximate this geometrical arrangement as if the electron were moving in vacuum close to an infinite interface at an impact parameter b. For an electron trajectory perfectly parallel to the interface, we can directly utilize the results from Section 3.1.1 to describe the spectra. However, we now analyze also the effect of a tilt of the electron beam with respect to the interface by an angle ϕ (see the schematics of Fig. 4.2). If we consider a very small tilt angle, $\phi \sim 0$, so that it causes only a small perturbation of the induced field compared to the case when $\phi = 0$, we can write the classical loss probability as:

$$\Gamma_{cl}(\omega, b) = \Gamma_{cl}^{\parallel}(\omega, b) + \Gamma_{cl}^{\perp}(\omega, b) \tag{4.7}$$

where the terms $\Gamma_{cl}^{\parallel}(\omega, b)$ and $\Gamma_{cl}^{\perp}(\omega, b)$ arise due to the induced field (producing the force acting against the electron) parallel and perpendicular to the slightly tilted trajectory. These contributions can be expressed as [170]:

$$\Gamma_{cl}^{\parallel}(\omega, b) \approx \frac{2d(1-|\phi|)}{\pi v^2} \int_0^\infty dq_y e^{-2\nu_1 b} \mathrm{Im}\left[\Sigma(q_y, \omega)\right], \tag{4.8}$$

$$\Gamma_{cl}^{\perp}(\omega, b) \approx \frac{2d|\phi|}{\pi v \omega} \int_0^\infty dq_y e^{-2\nu_1 b} \nu_1 \mathrm{Re}\left[\Sigma(q_y, \omega)\right], \tag{4.9}$$

where v is the speed of the electron, $\hbar q_y$ is the momentum perpendicular to the electron trajectory and parallel to the interface, and we define

$$\Sigma = \frac{1}{\nu_1(\nu_1 + \nu_2)} \left[\frac{2\nu_1^2(\varepsilon_2 - 1)}{\nu_2 + \varepsilon_2 \nu_1} - \left(1 - \frac{v^2}{c^2}\right)(\nu_1 - \nu_2) \right], \tag{4.10}$$

where c is the speed of light in vacuum, $\nu_{1/2} = \sqrt{(\omega/v)^2 + q_y^2 - \varepsilon_{1/2}\omega^2/c^2}$, $\varepsilon_1 = 1$ and ε_2 is the local dielectric function of the sample. In the following modeling, we consider silicon carbide as the sample material, i.e., $\varepsilon_2 = \varepsilon_{SiC}$. We approximate the low-energy response of SiC by the Lorentz-Drude model [see Eq. (1.11)] with high-energy dielectric response $\varepsilon_\infty = 6.7$, transverse optical phonon energy $\hbar\omega_{TO} = 98$ meV, longitudinal optical phonon at $\hbar\omega_{LO} = 120$ meV and damping $\hbar\gamma = 0.59$ meV [171].

In Fig. 4.2 we show the classical loss probability [Eq. (4.7)] (red dashed line) consisting of $\Gamma_{cl}^{\parallel}(\omega, b)$ and $\Gamma_{cl}^{\perp}(\omega, b)$, evaluated for an impact parameter $b = 10$ nm, sample thickness of $d = 500$ nm, and a 60-keV electron beam, with a small tilt angle $\phi = 0.02$ rad. The contribution arising from the parallel force $\Gamma_{cl}^{\parallel}$ (green line) features a peak close to 120 meV originating from the excitation of the surface phonon polariton of SiC [67] [see also the analysis of Fig. 1.1(e)] and a small

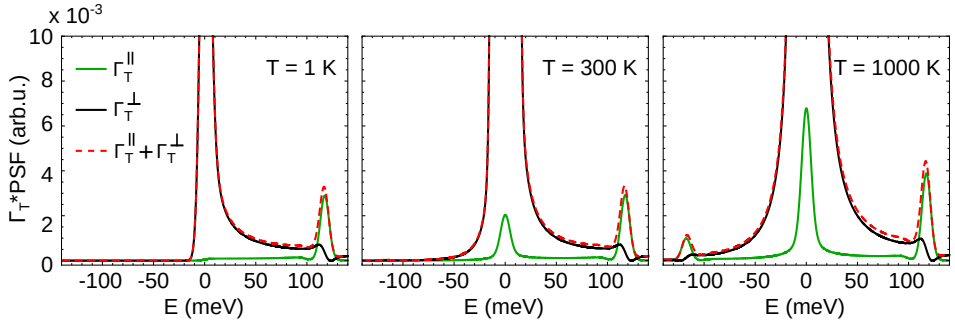

FIGURE 4.3: Temperature-enhanced loss probability Γ_T [as from Eq. (4.6)] convolved with a point spread function represented by a Gaussian with FWHM 10 meV. We split the contributions to the loss probability as in Fig. 4.2 and consider the same parameters for the calculation. Γ_T is evaluated for three different temperatures as denoted in the graphs: 1 K, 300 K and 1000 K, respectively.

contribution of radiation-type of losses, which gives rise to a similar spectral feature and constant background below 100 meV (see the inset of Fig. 4.2), similar to what we observed in Fig. 1.4(b) in the bulk loss corresponding to the beam moving in SiC. Importantly, in the very low-energy region, the loss probability from Eq. (4.9) due to the perpendicular induced field is clearly dominant (black line; compare with the summed probability plotted by the dashed red line). This contribution can be understood from a quasi-static picture of an electron attracted by a polarized medium, causing an additional small deflection of the beam. At very low energies, we thus have

$$\Gamma_{cl}(\omega \to 0, b) \approx \Gamma_{cl}^{\perp}(\omega \to 0, b) \approx \frac{|\phi| d}{\pi v b} \frac{\mathrm{Re}[\varepsilon_2(0)] - 1}{\mathrm{Re}[\varepsilon_2(0)] + 1} \frac{1}{\omega}. \tag{4.11}$$

The importance of the perpendicular contribution is even more pronounced when we consider the "thermally-enhanced" spectra. In Fig. 4.3 we plot Γ_T [Eq. (4.6)] convolved with a PSF modeled by a Gaussian function with 10-meV FWHM for temperatures of 1 K, 300 K and 1000 K. We split the contributions from the parallel ($\Gamma_T^{\parallel}$) and perpendicular ($\Gamma_T^{\perp}$) forces as in Fig. 4.2. We note that the divergence of the loss function close to zero in Eq. (4.11) for $\omega \to 0$ is washed out due to the discrete convolution with the point spread function (effectively replacing the finite detectable energy transfer and the wavevector cutoff). The perpendicular contribution then forms a peak around $E = 0$ whose intensity is increasing with temperature (black line; cropped in the plot to make also $\Gamma_T^{\parallel}$ visible). Furthermore, for temperature $T = 1000$ K, the gain peak close to $E = -120$ meV starts to be clearly visible, although still less intense than the loss peak according to Eq. (4.4). The spectral feature around zero coming from the parallel contribution (green line) is the radiation background (see the inset of

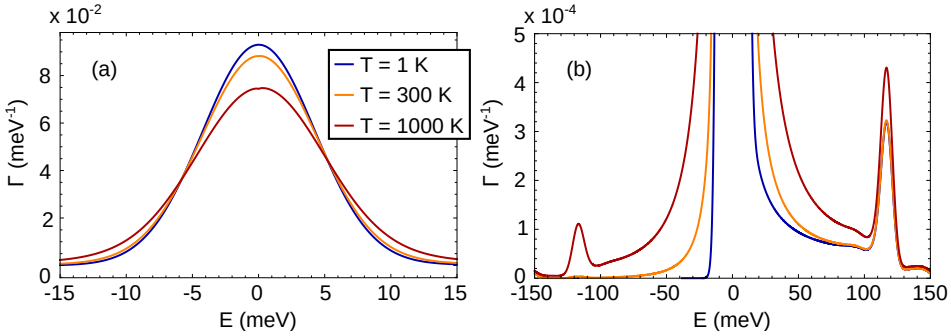

FIGURE 4.4: The complete temperature-dependent loss probability $\Gamma(\omega, T)$ [as from Eq. (4.5)]. We consider the same parameters as in Fig. 4.2 and the point spread function is represented by a Gaussian with FWHM 10 meV. The spectra are evaluated for three sample temperatures: 1 K (blue line), 300 K (orange line) and 1000 K (red line), respectively. The graph (a) shows the region around zero and the broadening of the quasi-elastic peak. (b) focuses on the loss and gain peaks corresponding to the surface phonon polariton in SiC.

Fig. 4.2) enhanced by the thermal occupation statistics.

We have now all the ingredients for the theoretical "reconstruction" of the complete temperature- (and spatially-) dependent EEL/EEG spectrum. We consider the probability Γ_T from Fig. 4.3 and plug it in Eq. (4.5), again assuming the PSF to be a Gaussian function with FWHM 10 meV. We plot the evaluated spectra in the region around zero in Fig. 4.4(a), where we observe a noticeable variation of the QEP. The peak gets broader and significantly decreases in intensity with increased temperature which is mostly due to the contribution of $\Gamma_T^{\perp}$. Fig. 4.4(b) displays the spectra over a broader energy region covering the loss and gain peaks arising from the excitation of the surface phonons in SiC. Similarly to Fig. 4.3, we observe that at very low temperature, the gain side of the spectrum goes quickly to zero whereas at high temperatures, the gain peaks are clearly visible. However, we note that the observed change will depend on the geometrical parameters of the beam-sample interaction [see Eq. (4.11)]. For beam trajectories far from the sample no significant changes in the QEP should be observed.

4.2 Experimental evidence of changes in the quasi-elastic peak

To verify the theoretical predictions, an experimental test is performed in a monochromated aberration-corrected STEM-EELS system by Dr. Juan Carlos Idrobo and Dr. Jordan Hachtel at Oak Ridge National Laboratory. In the experimental arrangement schematically depicted in Fig. 4.5(a), a focused electron beam is

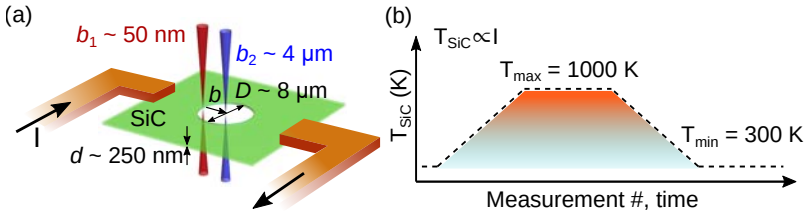

FIGURE 4.5: (a) Schematics of the performed experiment. The electron beam is passing through a 8-µm hole in a 250-nm thick slab made of SiC, which is heated by an external current source. The beam is positioned at an impact parameter b measured from the edge of the hole. (b) Heating scheme applied while EEL/EEG spectra are being recorded.

passing through a 8-µm hole in a membrane made of silicon carbide of thickness $d = 250$ nm supported by silicon nitride, which is integrated in a heating device. The heating device is calibrated to control the temperature of the membrane by an applied electric current at 5% precision. In Fig. 4.5(b) we show a graph of the target temperature set on the heating device while acquiring spectra: the membrane is linearly heated from 300 K to 1000 K, then the temperature is kept at 1000 K and finally, the membrane is cooled down back to 300 K. Each of these steps takes approximately 10 s. Afterwards, the temperature is kept at 300 K for another ~ 15 s. EEL spectra are recorded simultaneously while applying the temperature changes.

The details of aligned spectra in the region of the QEP for a beam position very close to the edge of the hole (at distance $b_1 \lesssim 50$ nm) are plotted in Fig. 4.6(a). We observe a clear weakening of the peak intensity with increasing temperature and vice versa. To better quantify the observed effect, in Fig. 4.6(b,c) we plot the full width at half maximum (FWHM) and the maximum of the intensity, respectively, extracted from fitting a Gaussian function to the measured QEP from Fig. 4.6(a) in the region from -9 meV to 9 meV. We observe that with increasing temperature, the FWHM increases from $\approx$ 12.5 meV to 14 meV, in a way which is complementary to the intensity decrease. The temperature dependence of both the FWHM and intensity approximately follows the applied heating-constant-cooling scheme and one can observe that the process is reversible. The same experiment is repeated with the beam placed approximately in the center of the hole, at position $b_2 \approx 4$ µm. The recorded QEP in Fig. 4.6(d) and the extracted FWHM and intensity in Fig. 4.6(e,f) also exhibit changes which follow the applied temperature cycle. However, these changes are less pronounced than for the beam at position b_1, thus giving an evidence that the distance of the beam from the heated membrane strongly influences the observed effect.

For the close approach of the beam to the edge at impact parameter b_1, we can also observe intense peaks corresponding to surface phonon excitation in SiC, as

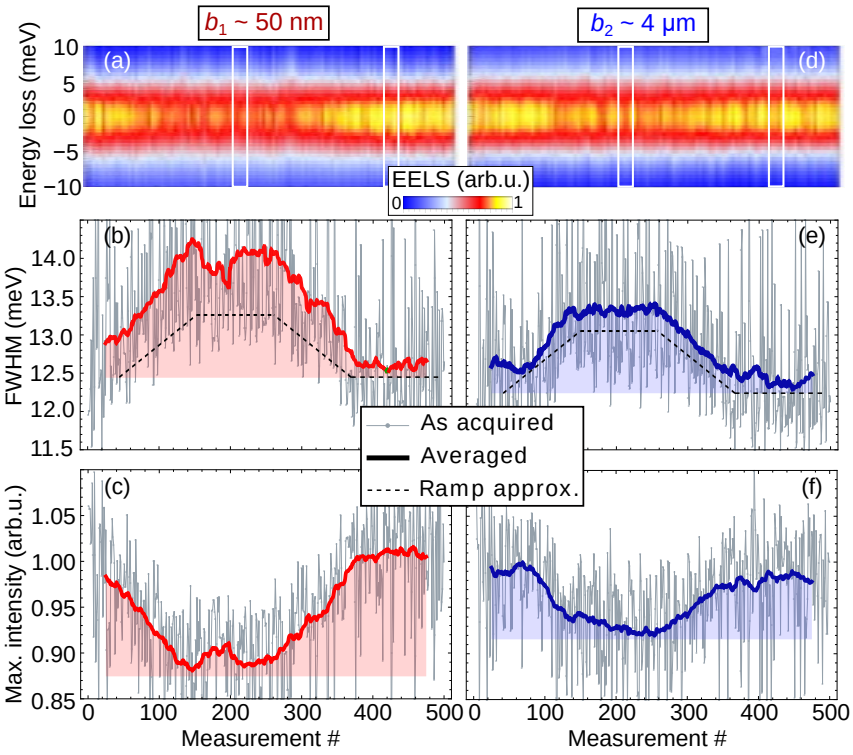

FIGURE 4.6: (a) Recorded QEP with the beam placed at a distance $b_1 \approx 50$ nm from the hole edge. (b,c) Extracted FWHM and intensity of the QEP recorded at the beam position b_1 (see Fig. 4.5). (d,e,f) similar to (a,b,c), obtained with the electron beam positioned approximately in the center of the hole (at distance b_2 from the edge). In plots (b,c) and (e,f) the signal is plotted as acquired (thin gray lines) and averaged over 50 neighboring measurements (thick lines). The heating-constant temperature-cooling cycle is schematically depicted by black dashed lines, with minimum and maximum temperature of 300 K and 1000 K, respectively. All measurements are performed by Dr. Jordan Hachtel and Dr. Juan Carlos Idrobo at Oak Ridge National Laboratory, USA.

shown in Fig. 4.7. The experimental spectra are obtained by averaging 20 measurements at 1000 K and 300 K (red and orange dots, respectively) denoted by the white frames in Fig. 4.6(a) and (d). At 300 K we can observe only a single loss peak around 115 meV whereas at 1000 K a gain peak at $E \sim -112$ meV is visible as well. Theoretically predicted spectra plotted by solid lines reproduce the experimental results reasonably well. However, the calculation for high temperature overestimates the strength of the gain and loss peaks, and does not reproduce the small energy red-shift and broadening of the peaks. Such behavior is most-likely

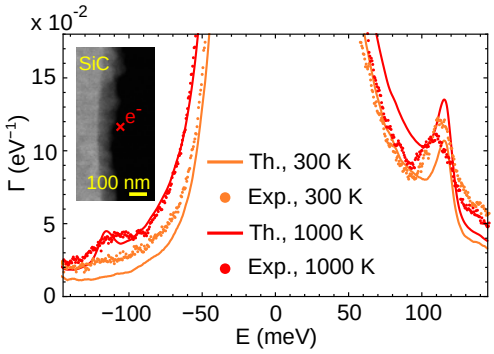

FIGURE 4.7: Comparison of calculated EEL probability [Eq. (4.5)] for the beam positioned at the impact parameter b_1 (see the micrograph in the inset) with experimental data at temperature 300 K and 1000 K (orange and red dots, respectively). In the calculations (orange and red solid lines), we consider approximate geometric parameters of the experiment and the experimentally measured PSF. The plots are focused on gain/loss peaks arising from the excitation of optical phonons at the SiC surface.

caused by structural changes of SiC lattice with temperature and/or increased phonon scattering [164]. As we discussed, these intrinsic changes of material properties could be effectively introduced in our approach by considering a temperature dependent $\varepsilon_{SiC}(\omega, T)$.

We note that for the beam positioned at b_2, no phonon loss/gain peaks are visible neither in calculated nor in measured spectra (not shown). Our calculations also predict that we should not observe any change in the QEP which is in the contradiction with the results presented in Fig. 4.6(d,e,f). To better visualize theoretically predicted and experimentally observed changes of the QEP with temperature, we normalize the theoretical and experimental spectra (divide them by their maximal values) as obtained for the hot (1000 K) and cooled (300 K) sample and subtract them. The resulting curves are plotted in Fig. 4.8(a) for the beam positions close to the sample ($b_1 \leqslant 50$ nm) and in Fig. 4.8(b) for the beam at b_2. The theoretical predictions show that at b_2 there is almost no difference in the QEP obtained at 1000 K and 300 K [dashed blue line in Fig. 4.8(b)] which fails to reproduce the experimental data (blue points). At b_1, the predicted change in the QEP is already observable [dashed red line in Fig. 4.8(a)]. However, compared to the measured data (red dots), the theoretical prediction yields a smaller difference. We can thus argue that there is an additional distortion and deflection of the electron beam when the heating device is on due to an external current loop, causing a modification of the PSF of the STEM-EELS system. According to our theoretical prediction, the entire change with temperature observed in the spectra recorded at b_2 [Fig. 4.6(d)] should correspond to the fact that $PSF = PSF(\omega, I)$, where I is the applied current in the device. If we take this assumption into account, the

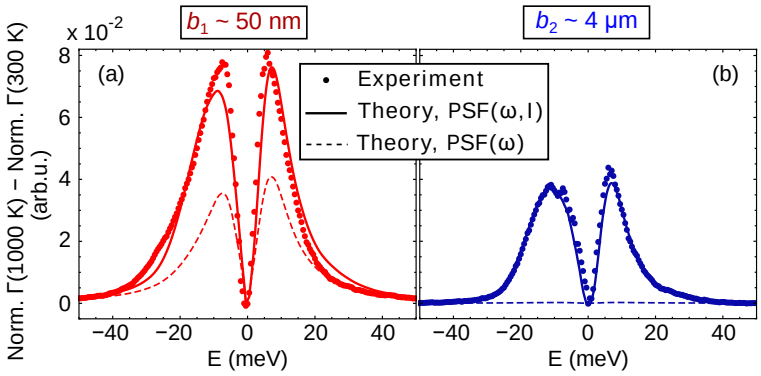

FIGURE 4.8: Difference of the normalized QEP obtained at 1000 K and 300 K after the holder was cooled down for the beam positions b_1 (a) and b_2 (b), respectively. The experimental data points (dots) are averaged over 20 measurements denoted by white frames in Figs. 4.6(a,d). Theoretical predictions taking into account the change of the PSF with increasing current in the heating device, i.e. PSF $=$ PSF(ω, I), are plotted by solid lines. Results where the change of the PSF with the applied current is not considered, i.e. PSF $=$ PSF(ω) are plotted by dashed lines.

theoretical prediction for the beam at b_1 [solid red line in Fig. 4.8(a)] reproduces more satisfactorily the measured data.

4.3 Summary

In this chapter we showed how temperature-dependent EEL/EEG spectra can be theoretically modeled. We demonstrated significant variations of the QEP with temperature for an electron beam positioned very close to a sample. We also designed an experiment employing a cycle of in-situ heating of the sample to corroborate the theoretical model. However, further experimental tests, which would eliminate the influence of the external current applied during heating of the sample should be performed. We suggest that the changes in the QEP arise mostly due to small deflections of an electron beam, which seems to be confirmed by experimental results in Ref. [172]. The presented analysis might be important for setting the fundamental energy resolution limits of the technique and for further understanding and analyzing of the complete EEL and EEG spectra.

Chapter 5

Molecular spectroscopy with an electron beam

Spectroscopic information on vibrational and electronic excitations in organic materials and molecules is of utmost importance in many research fields as it allows for characterizing material properties and identifying chemical compounds. Although excellent spectral resolution can be achieved by using conventional far-field optical spectroscopies [14, 173], diffraction limits the spatial resolution of acquired spectra. Furthermore, small molecular amounts are often undetectable because of strong background signal arising due to the large illuminated area. These drawbacks can be overcome by using optical nanoantennas [20] to localize light below the diffraction limit. Such approach is exploited in the so-called tip-enhanced or surface-enhanced spectroscopies, where either a sharp tip [174–178] or a free-standing nanoantenna [28, 179–182], respectively, plays the role of a near-field probe strongly localizing light at its apex, as sketched in Fig. 5.1(a, b). The resonant electromagnetic modes of the antenna can be either detuned with respect to the energies of molecular excitations, or matched to achieve resonant coupling with the molecular samples.

As an electron beam represents a localized near-field probe (see Section 1.2.1), it could be readily used for spectrosopic probing of molecular samples with high spatial resolution [schematically depicted in Fig. 5.1(c)]. However, there have been several major drawbacks of using fast electrons to investigate the response of molecular samples: (i) spectral resolution has not been good enough until recently to resolve molecular vibrations nor excitons, (ii) molecules are often destroyed when they are in close proximity to the electron beam due to various mechanisms including radiolysis, knock-on displacement, heating or charging [183, 184]. However, several experimental works [55, 58, 66, 84, 184] have shown that vibrational EEL spectra of highly sensitive organic samples can be obtained with state-of-art instruments [10, 53] when the mechanism of the long-range electromagnetic interaction of the beam and the sample is conveniently exploited. As we demonstrated in previous chapters, vibrational EEL spectra can be acquired even with the electron beam in aloof geometry relatively far from the sample, but still with spatial resolution below the diffraction limit.

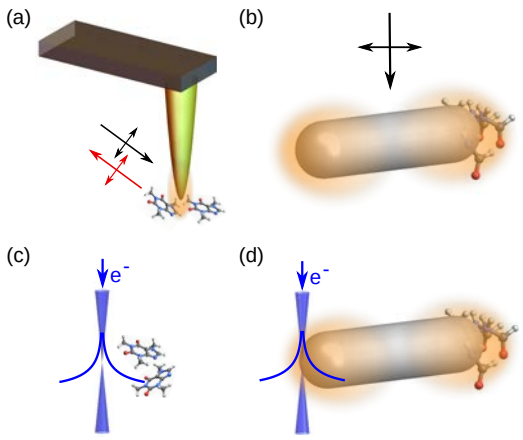

FIGURE 5.1: (a) Schematics of tip-enhanced optical spectroscopy: a sharp tip (optical antenna) focuses light at sub-wavelength scale and scatters enhanced molecular signal in the far field. (b) Principle of surface-enhanced optical spectroscopy: a free-standing optical nanoantenna interacts with molecules located in areas of electromagnetic field enhancement. (c) A focused electron beam directly probing a molecular sample in the near-field. (d) Proposed concept of surface-enhanced EELS: the electron beam interacts with the molecules via the optical nanoantenna.

In this chapter we first discuss aloof sensing of highly sensitive water molecules with a "bare" electron beam, as sketched in Fig. 5.1(c) and show how the spatial distribution of molecules and the geometry of the sample influences EEL spectra. In the following part we transfer the principle of surface-enhanced optical spectroscopy [depicted in Fig. 5.1(b)] to EELS and study the interaction of an antenna-molecule system with an electron beam, as sketched in Fig. 5.1(d), instead of using an optical plane wave. We theoretically describe the interaction of the localized electron beam with molecule-covered nanoantennas and show differences of EEL spectra with those acquired for optical plane-wave excitation. In particular, we focus on plasmonic and infrared phononic antennas covered by molecular layers, exhibiting either an excitonic or vibrational response and explore different aspects of surface-enhanced EELS. We demonstrate how the coupling of antennas and molecules enables to probe molecular samples remotely and how the signal can be enhanced. Furthermore, we show the possibility to probe strongly-coupled antenna-molecule systems and control the coupling strength with the fast electrons.

5.1 Shape effects of molecular samples in vibrational electron energy loss spectroscopy

Probing molecules with an electron beam in a natural environment and preventing their immediate damage is definitely a challenging task, especially when molecular samples are in liquid or gas state. High vacuum in the column of the electron microscope does not provide favorable conditions and hence, specialized experimental techniques need to be employed. One option is to introduce liquid or gas cells encapsulating such samples. In Ref. [66], liquid cells with small amounts of water are formed by using thin h-BN sheets supported by holey carbon membranes. Although water molecules are quickly destroyed when the beam is going through water nanobubbles, high-quality vibrational spectra can be recorded in aloof geometry, with the beam gradually approaching the bubble, as shown by the white arrow in Fig. 5.2(a). Interestingly, the impact-parameter dependent EEL response shown in Fig. 5.2(b) exhibits a pronounced shift of the peak maxima from $\sim$ 360 meV to $\sim$ 400 meV when the beam gets close to the bubble. For the beam going trough encapsulated water, the maximum is still observed close to 400 meV, but the peak is lower in intensity as some of the molecules get destroyed, and also due to the effect of the finite sample thickness (some of the electrons do not penetrate the sample or can be highly scattered).

To theoretically explain the peak shift observed in Fig. 5.2(b), we combine information on the geometry, and the expected composition of the sample (closely related to the vibrational response). First, we assume that the vibrations of water molecules can be probed. Bulk water has several vibrational bands, but in the analyzed spectral region, there is an O-H stretching band close to 420 meV [185, 186], which can be slightly modified in the present configuration due to a possible interaction of the water molecules with the surrounding h-BN layers. However, there can be also a contribution to EEL spectra from adsorbates on carbon, possibly C-H groups, which exhibit stretching modes between 350 and 380 meV [185]. The influence of the carbon adsorbates was confirmed by an additional measurement when the holey carbon membrane was measured far from the water bubbles: in such an arrangement, only a small peak centered around 355 meV was observed. It is thus possible that the spectra in Fig. 5.2(b) show overlapping loss peaks arising from the excitation of C-H and O-H vibrations. To verify this hypothesis, we suggest a simple model sketched in Fig. 5.2(d): we approximate the holey carbon membrane as a truncated slab and the (otherwise irregular) water bubble by a sphere with isotropic optical response. We neglect the presence of h-BN as it contributes to the vibrational spectra at much lower energies (see Chapter 2). We now try to find an analytical fit to the signal decay for $b > 0$ filtered at 360 meV [solid red line in Fig. 5.2(c)] and 400 meV [solid blue line in Fig. 5.2(c)], considering the geometry and the vibrational response of the carbon membrane and the water bubble, respectively.

Following the results of Section 3.3, we can model the decrease of the EEL intensity corresponding to a non-polaritonic excitation, such as the C-H vibrational

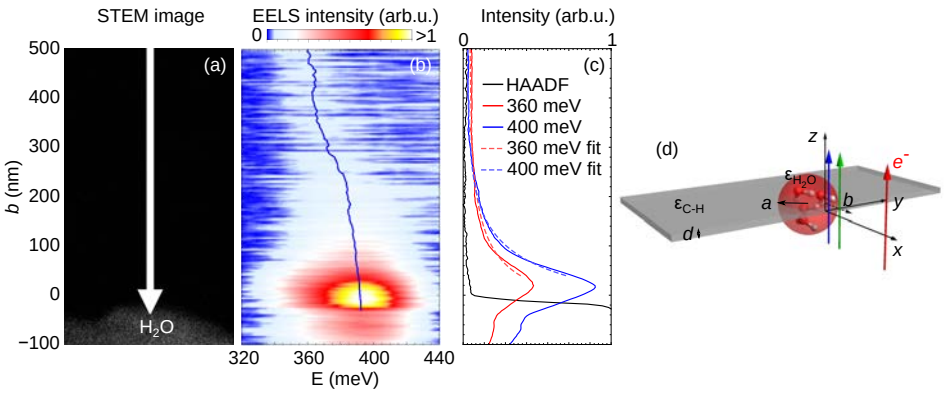

FIGURE 5.2: (a) STEM image of a water nanobubble encapsulated in h-BN. (b) EEL spectra recorded for a beam approaching the bubble in the direction of the white arrow denoted in (a). Blue curve traces averaged peak maxima.(c) Extracted HAADF profile (black) showing the sample boundary and energy-filtered EEL intensity at 360 meV (solid red line) and 400 meV (solid blue line), respectively. Dashed lines correspond to fits using the analytical modeling described in the main text. Graphs (a–c) are aligned with respect to the y axis showing the beam position (the impact parameter b measured from the boundary of the nanobubble). (d) A simplified model of the experimental geometry: encapsulated water represented as a small sphere and holey carbon layer approximated by a thin truncated slab. Experiments were performed by Dr. J. Jokisaari, Dr. J. Hachtel and colleagues at University of Illinois in Chicago and Oak Ridge National Laboratory in the U.S.

stretch, in the truncated slab as

$$I_{C-H}(b) \propto K_0\left(\frac{\omega_{C-H} b}{v}\right), \tag{5.1}$$

where $K_m(x)$ is the modified Bessel function of the second kind of order m, b is the distance from the truncation and the electron's speed is $v = 0.446c$ given by the experimental acceleration voltage of 60 kV. The spatial dependence of the signal coming from the interaction of the aloof beam and a sphere is obtained in Refs. [112, 113, 187], and is presented in Appendix A.3. For simplicity, we will consider only the non-retarded dipole limit [see Eq. (A.45)], which approximates the decay of the EEL intensity from the nanobubble as

$$I_{O-H} \propto K_0^2\left(\frac{\omega_{O-H}(x_b + b)}{v}\right) + K_1^2\left(\frac{\omega_{O-H}(x_b + b)}{v}\right), \tag{5.2}$$

where x_b is the position of the sample dipole (approximately at the center of the mass of the bubble) and b is the distance of the electron beam from the outer boundary of the corresponding sphere.

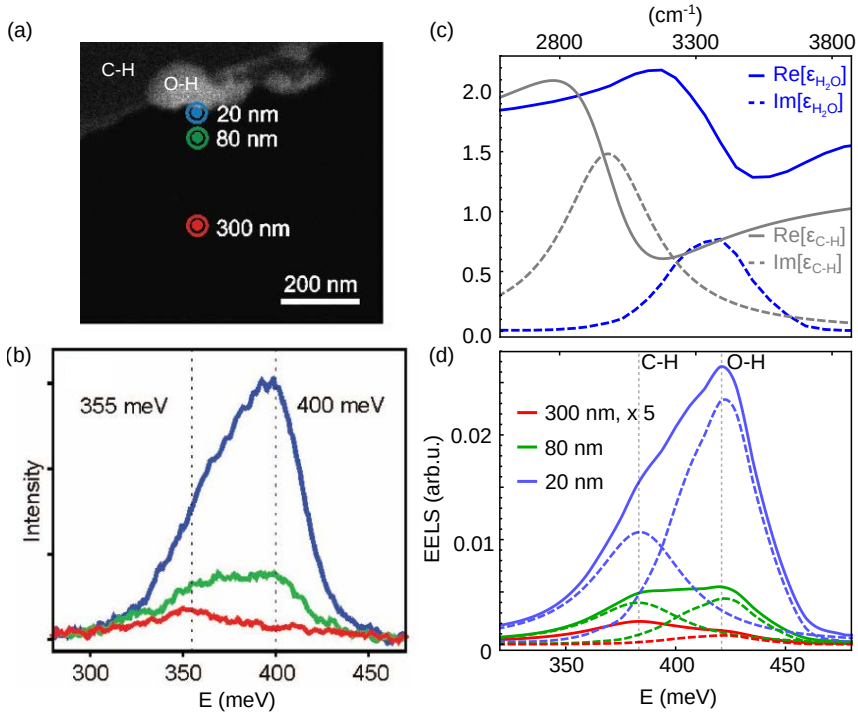

FIGURE 5.3: (a) Beam positions for long-acquisition measurements. (b) Acquired spectra with the colour coding defined in (a). (c) Model dielectric functions assigned to the amorphous carbon substrate (gray lines) and bulk water (blue lines). (d) Contributions to the total EEL probability $\Gamma(\omega, b)$ (solid lines) given by (i) a truncated carbon slab $\Gamma_{\text{slab}}(\omega, b)$ with a peak at 380 meV and (ii) a water sphere $\Gamma_{\text{sphere}}(\omega, b)$ peaking at 420 meV (both marked with dashed lines). Impact parameters b of 20 nm, 80 nm and 300 nm are considered as displayed in the inset; the intensities of the spectra for $b = 300$ nm are multiplied by 5 for clarity. Experimental data in (a,b) were obtained by Dr. J. Jokisaari, Dr. J. Hachtel and colleagues at Oak Ridge National Laboratory in the U.S.

Neglecting the overlap between the vibrational signal of C-H and O-H groups, we can use Eq. (5.1) and Eq. (5.2) to model the intensity of the energy-filtered signal at 360 meV and 400 meV, respectively. The experimental result shown by the solid lines in Fig. 5.2(c) can be for $b > 0$ nicely fit by the analytical functions (dashed lines). From the fitting, we find $x_b \simeq 7$ nm.

For further verification of the different decay lengths of the vibrational EEL signals from the C-H and O-H stretching bands, another nanobubble was examined by Dr. J. Hachtel at Oak Ridge National Laboratory, U.S. at three impact parameters as shown in Fig. 5.3(a). The spectra collected with higher acquisition times are plotted in Fig. 5.3(b), and clearly exhibit the same qualitative behavior

as the spectra in Fig. 5.2(b). The vibrational signal coming from the C-H stretch is dominant for larger impact parameters and on the contrary, the O-H stretch prevails when the beam is close to the water molecules due to the functional dependence of the respective decay of the interactions [Eq. (5.1) vs. Eq. (5.2)].

We now attempt to model the complete spectra using Eq. (3.1) to approximate the energy loss due to the excitation of the C-H stretch with the assumption that the loss occurs when the electron passes by the slab (the molecular layer) of thickness d. Eq. (6.10) is used to calculate the contribution of the water sphere. We characterize the dielectric function of encapsulated water ε_{H_2O} with experimental data from bulk samples following Ref. [188] [see blue curves in Fig. 5.3(c)], whereas to describe the dielectric response corresponding to the C-H stretching we use the model function

$$\varepsilon_{\text{mol}} = \varepsilon_{\infty,s} + \frac{f_s \omega_s^2}{\omega_s^2 - \omega^2 - i\gamma_s \omega}. \tag{5.3}$$

We find that a dielectric background $\varepsilon_{\infty,s} = 1.3$, an oscillator strength $f_s = 0.2$, a vibration energy $\omega_s = 370$ meV and an oscillator damping $\gamma_s = 50$ meV phenomenologically reproduce the observed spectral features. We further consider the radius of the sphere $a = 40$ nm and the molecular layer with thickness 3.2 nm. However, there is a quantitative discrepancy of the peak positions. The energy loss spectrum corresponding to the bubble, calculated with the dielectric function of bulk water, peaks at $\sim$ 420 meV, whereas the experimental spectrum peaks at 400 meV. This difference may arise due to nanoconfinement of the water molecules or due to the interaction with the h-BN encapsulating layers, which could change the chemistry and introduce changes in the vibrational modes. To decipher such effects, a systematic study for different volumes of encapsulated liquid, possibly combined with ab initio modeling would be required. Also, by tilting the electron beam, one could analyze if the molecules are randomly oriented (as assumed in the model) or if they are arranged preferentially in some direction which could be modelled by introducing anisotropy in the response of the molecular sample [189].

5.2 Surface-enhanced EELS

We now turn our attention to the concept of surface-enhanced EELS, which we schematically depicted in Fig. 5.1(d).

5.2.1 Principle of surface-enhanced EELS

We begin our study by describing the general features appearing in EELS of a plasmonic rod, acting as a nanoantenna, interacting with molecules. The considered model system is sketched in Fig. 5.4(a). It consists of a plasmonic antenna fully or partially covered by a molecular layer (sample), which is a system typically studied in optical and infrared spectroscopy. We choose a simple and highly tunable antenna shape: a silver nanorod of variable length L and with rounded tips or radius $R = 20$ nm. The molecular layer thickness is $t = 5$ nm. We consider the coupling of the 60-keV electron beam with the longitudinal antenna modes [45, 46, 48, 190, 191], whose energy can be tuned by varying the antenna length to match the energy of the molecular excitons (relatively short plasmonic antennas) or molecular vibrations (relatively long plasmonic antennas) of the layer. For simplicity, the dielectric response of the plasmonic antenna is approximated by the Drude model [Eq. (1.7)] considering the following parameters for silver: $\varepsilon(\infty) = 3.3$, $\omega_p = 9.3$ eV and $\gamma = 22$ meV [192]. The dielectric response of the molecular sample is modeled by the Lorentz-Drude dielectric function [see Eq. (5.3)]. Electron energy loss probability spectra are calculated numerically within the framework of classical dielectric theory [15] as introduced in Section 1.2.2.

To better understand the EEL spectra of the antenna-molecule system, we first analyze the interaction of the bare antenna with the probing electron beam. To that end, we calculate EEL spectra in Fig. 5.4(b) at the different positions marked by crosses in the inset. When the beam is close to the tip of the antenna (black and blue cross) a single peak at energy $\omega_0 = 1.93$ eV with a full width at half maximum (FWHM) of 187 meV can be observed [black and blue spectra in Fig. 5.4(b)]. The peak disappears when the beam is placed closer to the center of the antenna, at $x_b = 0$ nm (red spectrum). To understand the excitation at ω_0, we plot the total near field (external field of the electron plus the induced field) associated with different beam positions in Figs. 5.4(c). When the beam is placed at the antenna apex [upper panel of Fig. 5.4(c)], we observe a near-field pattern corresponding to the dipolar plasmonic mode induced at the nanorod. On the contrary, when the e-beam is placed near the center of the rod [lower panel of Fig. 5.4(c)], it does not excite the dipolar antenna resonance, and the near-field distribution is thus dominated by the external field of the electron [46, 190, 193]. The low excitation efficiency of the latter case can be explained by the negligible near-field magnitude of the dipolar mode near the rod center.

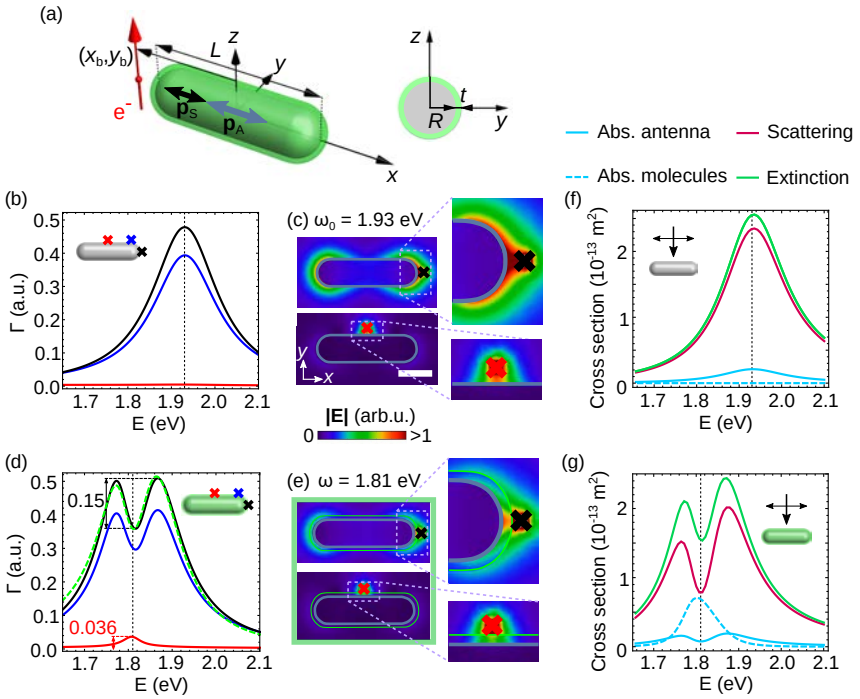

FIGURE 5.4: (a) Schematic of the modelled system: a silver rod of length L and radius R = 20 nm covered with an excitonic layer of thickness t = 5 nm probed by an electron beam with impact parameter (x_b, y_b). (b) EEL spectra of the bare silver antenna of length L = 145 nm. Black, blue and red spectra are obtained for the beam passing at $(L/2 + 10\ \text{nm}, 0)$, $(L/2 - R, R + 10\ \text{nm})$ and $(0, R + 10\ \text{nm})$, respectively. (d) Spectra for the same beam positions as in (b), but for the rod fully covered by an excitonic layer as shown in the inset. The green dashed curve is the coupled-dipole fit using Eq. (5.12). The fitting parameters are: $F_A = 2.51 \times 10^9$ a.u., $\Omega_A = 1.84$ eV, $\kappa_A = 169$ meV, $F_S = 1.18 \times 10^6$ a.u., $\Omega_S = 1.804$ eV, $\kappa_S = 53$ meV, $x_A = 83$ nm, $x_S = 48$ nm, $x_{SA} = 79$ nm. We further denote the spectral contrast, defined as the dip depth or peak height. In (c,e), we plot on the same scale the total electric field amplitude $|\mathbf{E}|$ in the plane $z = 0$ for the bare rod and the covered rod, respectively. Blue and red crosses mark the electron beam position. The scale bar is 50 nm. The rod and the layer boundaries are marked by grey and green lines, respectively. (f,g) Calculated cross sections (absorption in the antenna and molecular layer are solid and dashed light blue spectra, respectively, scattering is plotted by a purple line and extinction by a green line) for a plane wave polarized along the long antenna axis for the uncovered (f) and the covered (g) antenna as displayed in the insets.

Next we cover the rod by an excitonic molecular layer, which is modeled by the following parameters: $\varepsilon_{\infty,s} = 1.69$, $\omega_s = 1.8$ eV, $\gamma_s = 50$ meV and $f_s = 0.02$ [substituted in Eq. (5.3)] mimicking the case of J-aggregates in solution [194–196].

Analogously to the case of the bare antenna, we show EEL spectra in Fig. 5.4(d) for different e-beam positions. When the beam is positioned close to the antenna apex, we efficiently excite the antenna mode and the resulting EEL spectrum exhibits the response of the coupled antenna-molecule system (black, blue). We recognize the coupling signature in the form of a typical Fano-like feature (dip) [28, 197], which reveals the coherent interaction between the antenna and the molecular sample. Moreover, the antenna resonance is slightly red-shifted due to the dielectric screening by the molecular layer ($\varepsilon_{\infty,S}$). The field plot at energy $\omega = 1.81$ eV [upper panel of Fig. 5.4(e)] shows the dipolar near-field pattern surrounding the antenna, revealing the regions of intense field where the electromagnetic coupling between antenna and molecular layer takes place via their near field [175].

When the beam is positioned closer to the antenna center, the dipolar plasmon is not efficiently excited and we thus probe the decoupled excitonic sample. The excitonic response appears in the form of a small narrow peak in the spectrum [red curve in Fig. 5.4(d)]. By defining the spectral contrast as the depth of the dip of the coupled system and as the height of the spectral peak of the uncoupled exciton [marked by black and red vertical arrows in Fig. 5.4(d)], we can estimate the antenna-induced enhancement of the exciton's spectral feature compared to the bare exciton spectrum. From the black and red spectra in Fig. 5.4(d) we find that the contrast is enhanced, without further optimization, more than four times with respect to the uncoupled system.

To better understand the underlying physics and to explain the numerically calculated spectral shapes, we develop an analytical model of the response of the coupled system, described as a combination of two electromagnetically coupled dipoles representing the antenna $\mathbf{p}_A$ and the sample $\mathbf{p}_S$, respectively, excited by the external field of the aloof electron beam [see schematics in Fig. 5.4(a)].

The antenna (A) and the excitonic sample (S) dipoles are situated at positions $(x_{A(S)}, 0, 0)$ and for simplicity, we consider the electron beam passing at the origin, i.e. $x_b = y_b = 0$. The dipoles are characterized by means of their polarizability tensor, $\overleftrightarrow{\alpha}_{A(S)}$. The dipole moment induced by the external field $\mathbf{E}^{\mathrm{tot},A(S)}$ at the dipole position is then $\mathbf{p}_{A(S)} = \overleftrightarrow{\alpha}_{A(S)}\mathbf{E}^{\mathrm{tot},A(S)}$ for the antenna and the sample, respectively. In the considered geometrical arrangement, the antenna is preferentially polarized along the x direction. We therefore consider that the antenna polarizability tensor has a single nonzero component: $\alpha_{A,xx} = \alpha_A$ and assume the sample polarizability α_S to be isotropic. The polarizabilities have Lorentzian line shape: $\alpha_{A(S)} = F_{A(S)}\Omega^2_{A(S)}/(\Omega^2_{A(S)} - \omega^2 - i\kappa_{A(S)}\omega)$ with $\Omega_{A(S)}$ being the resonance frequency, $\kappa_{A(S)}$ the damping parameter and $F_{A(S)}$ the oscillator strength associated with the uncoupled antenna (sample). Due to the symmetry [see Fig. 5.4(a)], the dipole moments can be expressed as $\mathbf{p}_A = (p_{x,A}, 0, 0)$ and $\mathbf{p}_S = (p_{x,S}, 0, p_{z,S})$.

The field driving each dipole is the sum of the field of the electron beam and the field produced by the other dipole [181] $\mathbf{E}^{\mathrm{tot},A(S)} = \mathbf{E}^{A(S)} + \mathbf{E}^{SA(AS)}$, where the

field of the moving electron at the dipoles' positions is [compare with Eq. (1.24)] [15]

$$\mathbf{E}^{A(S)}(x_{A(S)},0,\omega)=\left(-\frac{2\omega}{v^2\gamma_L}K_1\left(\frac{\omega x_{A(S)}}{v\gamma_L}\right),0,\frac{i2\omega}{v^2\gamma_L^2}K_0\left(\frac{\omega x_{A(S)}}{v\gamma_L}\right)\right). \tag{5.4}$$

The interaction field coming from the other dipole (sample acting on the antenna and reversely) in the considered symmetry retains only the x component and can be expressed as

$$\mathbf{E}^{SA(AS)}=(p_x^{S(A)}G,0,0), \tag{5.5}$$

where

$$G=\frac{2\exp\left(i\omega x_{SA}/c\right)}{x_{SA}^2}\left(\frac{1}{x_{SA}}-\frac{i\omega}{c}\right) \tag{5.6}$$

is the xx component of the Green's dyadic, simplified for the particular geometrical arrangement [1]. x_{SA} is an effective distance between the dipoles and for perfect point-like particles, it is $x_{SA}=|x_A-x_S|$. We recast the expression for the x component of the dipole moments:

$$p_x^{A(S)}=\alpha_{A(S)}\left(E_x^{A(S)}+p_x^{S(A)}G\right). \tag{5.7}$$

Eq. (5.7) represents a self-consistent system of equations, which yields the solution:

$$p_x^{A(S)}=\alpha_{A(S)}\frac{E_x^{A(S)}+\alpha_{S(A)}GE_x^{S(A)}}{1-\alpha_A\alpha_SG^2}. \tag{5.8}$$

The equation above involves an infinite number of scattering events between the antenna and the sample. Furthermore, the sample can show a z component of the dipole moment $p_z^S=\alpha_SE_z^S$, which is not influenced by the antenna. Nevertheless, this contribution can be neglected for small F_S ($F_S\ll F_A$).

The electron energy loss probability arising in the excitation of a dipole by the field of the electron beam $\mathbf{E}_{el}$ is expressed as [45, 198]:

$$\Gamma(\omega)=\frac{1}{\pi}\mathrm{Im}\left[\mathbf{p}(\mathbf{r},\omega)\cdot\mathbf{E}_{el}^*(\mathbf{r},\omega)\right], \tag{5.9}$$

which in the case of our interest becomes

$$\Gamma(\omega)=\frac{1}{\pi}\mathrm{Im}\left[p_x^AE_x^{A,*}\right]+\frac{1}{\pi}\mathrm{Im}\left[p_x^SE_x^{S,*}+p_z^SE_z^{S,*}\right]$$

$$
\begin{aligned}
&= \frac{1}{\pi}\mathrm{Im}\left[\frac{\alpha_A \left(E_x^A\right)^2}{1-\alpha_A\alpha_S G^2}\right] + \frac{1}{\pi}\mathrm{Im}\left[\frac{2\alpha_A G \alpha_S E_x^A E_x^S}{1-\alpha_A\alpha_S G^2}\right] \\
&+ \frac{1}{\pi}\mathrm{Im}\left[\frac{\alpha_S \left(E_x^S\right)^2}{1-\alpha_A\alpha_S G^2} + \alpha_S |E_z^S|^2\right] \\
&= \Gamma_A + \Gamma_{AS} + \Gamma_S.
\end{aligned} \tag{5.10}
$$

The loss probability strongly depends on the external electric field produced by the electron at the antenna and the sample positions, respectively, which influences the relative strength of the terms Γ_A, Γ_{AS} and Γ_S. The latter two terms are negligible when the sample is either far from the electron probe or weakly polarizable compared to the antenna. The spectral shape is then properly described by Γ_A:

$$
\Gamma_{x_A<x_S} \approx \Gamma_A = \frac{1}{\pi}\mathrm{Im}\left[\frac{\alpha_A \left(E_x^A\right)^2}{1-\alpha_A\alpha_S G^2}\right]. \tag{5.11}
$$

On the other hand, for a strongly excited sample, we get to the expression:

$$
\Gamma \approx \Gamma_A + \Gamma_{AS} = \frac{1}{\pi}\mathrm{Im}\left[\frac{\alpha_A \left(E_x^A\right)^2}{1-\alpha_A\alpha_S G^2}\right] + \frac{1}{\pi}\mathrm{Im}\left[\frac{2\alpha_A G \alpha_S E_x^A E_x^S}{1-\alpha_A\alpha_S G^2}\right], \tag{5.12}
$$

where we assumed the antenna polarizability α_A to be much larger than the sample polarizability α_S, and omitted Γ_S in Eq. (5.10). Fitting of the coupled dipole model in Eq. (5.12) to the numerical result for a situation with the beam position close to the tip (black) plotted with a green dashed line in Fig. 5.4(d) yields excellent agreement (the green dashed line vs. the black line).

We note that the loss probability as given by Eq. (5.12), except for prefactors, formally provides the same spectral shape as the optical extinction of the coupled system [175, 182]. Importantly, we find that the expression for Γ in Eq. (5.12) contains two contributions to the EEL signal represented by the terms Γ_A and Γ_{AS}. $\Gamma_A \propto \left(E_x^A\right)^2$ arises from the effective polarizability of the antenna that is modified by the presence of the molecular sample and is usually the dominant contribution. On the other hand, $\Gamma_{AS} \propto E_x^A E_x^S$, represents the losses in the sample (the antenna) due to the field generated by the other polarized element, i.e. the antenna (the sample), and is small compared to Γ_A when $2\alpha_S G E_x^S < E_x^A$. However, when the electron beam excites the sample with high efficiency (e.g. when it is close to the sample, $E_x^S \gg E_x^A$), the indirect term Γ_{AS} becomes important and leads to asymmetries in the EEL spectra beyond the Fano-like model, standardly assumed for interpretation of the optical extinction. Indeed, calculations of optical spectra for the same antenna-layer system in Fig. 5.4(g) exhibit an asymmetry compared to an almost symmetric Fano-like dip in the EEL spectra for the coupled system in Fig. 5.4(d), although the peak positions in the spectra for the bare

antenna appear at nearly identical energies [compare Fig. 5.4(f) and (b)]. The asymmetric dip observed in the optical spectra is a signature of the detuning of the uncoupled antenna plasmon with respect to the excitonic transition, which is actually confirmed by checking the obtained fit parameters for the antenna and the sample resonances. We find a significant blueshift of 36 meV (detuning) between the antenna and the sample peak positions $\Omega_{A(S)}$. The general spectral shape of EEL probability [Eq. (5.12)] can thus produce a symmetric feature for a detuned system and vice versa.

5.2.2 Coupling to higher-order plasmonic modes

An important advantage of fast electrons in EELS is their ability to probe "dark" plasmonic modes, which do not efficiently radiate into the far field. These modes are thus hardly detectable by far-field optical spectroscopy in conventional experimental arrangements, but become accessible by localized probes as in EELS experiments [42, 44, 47, 50, 199]. The damping of dark modes is mainly caused by the intrinsic absorption of the material (ohmic losses), with radiation losses largely suppressed. The reduced losses of dark modes thus facilitate reaching the strong coupling regime, where the rate of the molecule-antenna interaction needs to be faster than the loss rate of excitons and plasmons in the system [200]. Moreover, the coupling strength typically increases when the plasmonic near field is more confined (the latter corresponding to a decrease of the effective mode volume)[201], a situation more likely to occur for dark modes. Strong coupling has recently attained a large interest, e.g. because of the possibility to modify chemical reactivity of molecules [78, 202, 203] or for quantum information processing [204]. Strong coupling phenomena have been studied by optically exciting plasmons and excitons e.g. in quantum dots [205–209], transition metal dichalcogenide monolayers [210, 211], or in organic dyes forming J-aggregates [196, 212–216], as the ones considered in our model system. In the following we thus study the coupling of dark antenna modes and molecular excitons with an electron-beam.

We performed calculations similar to those in Fig. 5.4 for a longer antenna of length $L = 340$ nm, which exhibits the second order mode (first dark one) tuned with respect to the energy of the excitonic transition. In Fig. 5.5(a) we show spectra obtained for three different positions (marked by crosses in the inset) of the electron beam along the antenna. The dark mode is excited when the beam is positioned either close to the antenna center or close to the antenna tips (red and black spectra, respectively). Note that the loss peak with a FWHM of 63 meV is much narrower than the loss peak associated to the first dipolar mode in Fig. 5.4(b), which, as mentioned above, is due to the suppression of radiation losses (reduced damping). The near-field plots for each beam position at $\omega_0 = 1.89$ eV [Fig. 5.5(b)] confirm the excitation of the second order antenna mode (three bright spots corresponding to the localized plasmonic mode). This mode is not excited when the beam is positioned at one of the two nodes (dark

areas). Subsequently the excitation probability is close to zero [blue curve in Fig. 5.5(a)] at the position marked with the blue cross.

The coupling of the dark plasmon mode and the excitonic layer covering the plasmonic rod is demonstrated in the spectra of Fig. 5.5(c), which are calculated for the same beam positions as in Fig. 5.5(a). The coupling signatures emerge for the beam positions where it efficiently excites the plasmonic mode, i.e. close to the antenna center or at the apexes (red and black spectra, respectively). On the contrary, when the beam is placed at the node, we probe the uncoupled exciton (blue spectrum), analogously to the centered e-beam in the dipolar plasmonic antenna [red curve in Fig. 5.4(a)]. The field patterns at $\omega = 1.81$ eV for the covered antenna [Fig. 5.5(d)] show similar features as those in Fig. 5.5(b) for the corresponding beam positions, although less intense due to the field screening by the

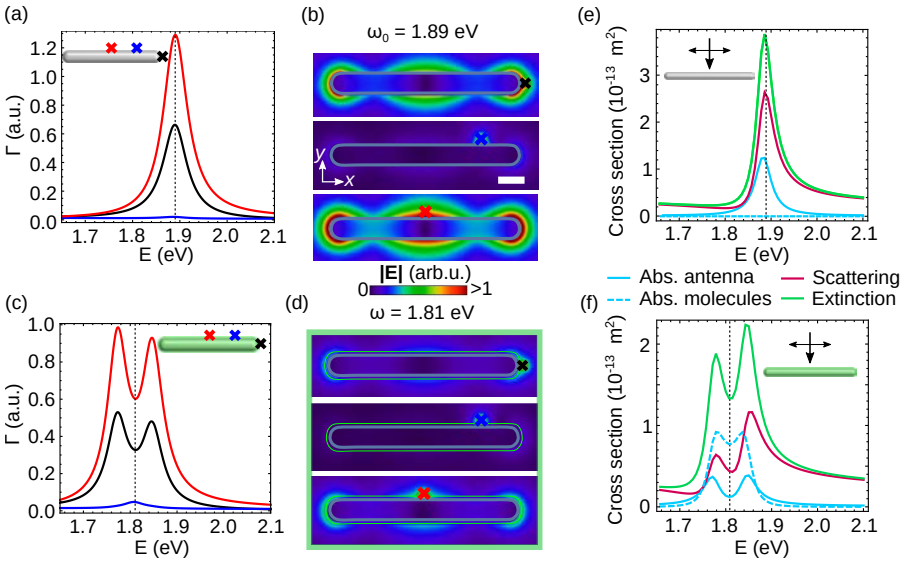

FIGURE 5.5: (a) EEL spectra of a bare silver antenna of length $L = 340$ nm for an electron beam passing at $(L/2 + 10\,\text{nm}, 0)$ (black), $(L/4, R + 10\,\text{nm})$ (blue) and $(0, R + 10\,\text{nm})$ (red). (c) Spectra at the same beam positions for the rod covered by an excitonic layer (see the inset). In (b,d) we plot the total electric field magnitude $|\mathbf{E}|$ in the plane $z = 0$ for the bare rod and the covered rod, respectively, for the beam positions marked by the coloured crosses. The scale bar is 50 nm. The rod and the layer boundaries are marked by grey and green lines, respectively. (e,f) Calculated cross sections (absorption in the antenna and molecular layer plotted by solid and dashed light blue lines, respectively, scattering by purple line and extinction by green line) for an incident optical plane wave polarized along the long antenna axis for the uncovered (e) and the covered (f) antenna as displayed in the insets.

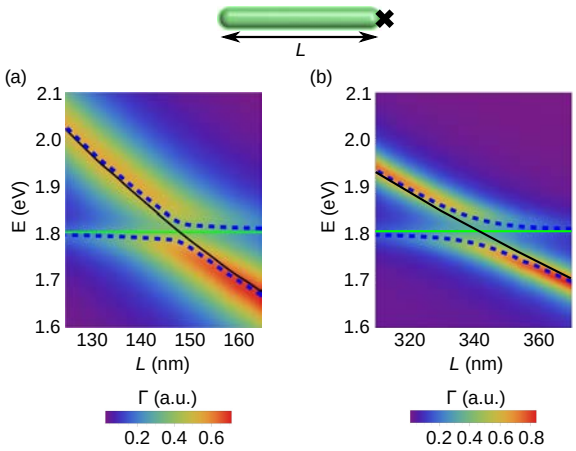

FIGURE 5.6: EEL spectra calculated for rods with varying lengths supporting (a) the first order (bright) dipolar mode and (b) the second order (dark) mode excitation. The beam is placed at $(L/2 + 10\ \text{nm}, 0)$ as sketched in the schematic. The blue dashed lines correspond to the solutions of the coupled oscillator fit obtained as described in the text.

molecular layer. These near-field maps reveal the areas of maximum field enhancement, where the most effective coupling with the sample takes place. The spectra for the beam at the antenna center and apexes [red and black curves in Fig. 5.5(c)] therefore show the response of the coupled system.

Interestingly, the coupling between the dark antenna mode and the molecular exciton seems to be more pronounced than for the bright dipolar mode. Furthermore, all optical spectra including the absorption calculated inside the molecular layer [see dashed light blue line in Fig. 5.5(f)] exhibit two local maxima [compare with Fig. 5.4(g)], which might be a signature that we reach strong coupling regime when two hybridized plasmon-exciton polaritonic modes are created [194, 217, 218]. We perform a quantitative analysis of the coupling in both cases and calculate a set of energy loss spectra for varying antenna lengths around the first order (dipolar) and the second order (first dark) antenna modes. The results are shown in Fig. 5.6 (a) and (b), respectively. As the antenna resonance is detuned with respect to the exciton, we observe in both Figs. 5.6(a) and (b) two peaks which change intensity and energy position. For highly detuned antennas, the peaks correspond to the uncoupled exciton and plasmon excitations (their energy positions are traced by green and black solid lines), respectively. When the plasmon resonances approach the exciton (around $L = 150$ nm and 340 nm), one can observe a typical anti-crossing of the two peaks [194], which is a manifestation of coupling, either weak or strong.

To determine the coupling regime, we use the coupled dipole model introduced in the previous section to obtain the energies of the two new eigenmodes

of the coupled system arising from the interaction. We first calculate the spectra for the uncoupled antenna covered by the non-resonant dielectric layer and the excitonic shell corresponding to each antenna length, and fit them separately to obtain the oscillator parameters for the uncoupled antenna and sample. With the fixed oscillator parameters, we fit the spectra calculated for the coupled antenna-molecule system by Eq. (5.12) with x_{SA} as a free parameter. The coupling gives rise to two new eigenmodes, whose energies are split according to [204, 216]:

$$\omega_{\pm} = \mathrm{Re}\left[\frac{\Omega_A + \Omega_S}{2} \pm \frac{1}{2}\sqrt{4|g|^2 + \left[(\Omega_A - \Omega_S) + \frac{i\,(\kappa_S - \kappa_A)}{2}\right]^2}\right], \tag{5.13}$$

where g is the interaction coupling strength between the oscillators, which in general depends on the oscillator strengths, the damping in the system and the effective volume of the plasmonic mode. For the particular parameters used in our coupled dipole model, we find an approximate expression which holds for small oscillators' damping and close-to-zero detuning ($\Omega_A \cong \Omega_S \cong \Omega_0$): $g \sim \Omega_0\sqrt{F_A F_S}/x_{SA}^3$. The strong coupling is reached, when the energy difference in Eq. (5.13) is larger than the width of the hybridized modes (the total damping of the system), i.e. if $|g|/|\gamma_A + \gamma_S'| > 0.25$ holds [204]. The mode energies obtained from this simple model, traced in Fig. 5.6 by blue dashed curves, closely correspond to the peak maxima retrieved numerically.

For the dipolar antenna mode and zero detuning, we obtain a coupling strength $2g_1 = 72$ meV and a value of $|g_1|/|\kappa_A + \kappa_S| = 0.16 < 0.25$ (weak coupling). However, for the first dark antenna mode, the strong coupling criterion is just above the threshold, as $|g_2|/|\gamma_A + \gamma_S'| = 0.26 > 0.25$. Although the coupling strength $2g_2 = 52$ meV for the dark antenna mode is smaller than for the bright dipolar mode, the smaller damping of the dark mode is crucial to achieve the strong coupling regime [compare FWHM in Figs. 5.5(a) vs. 5.4(b)].

5.2.3 Surface-enhanced vibrational spectroscopy with fast electrons

The concept to study the coupling of molecules with antennas in EELS is general and does not apply only to plasmon-exciton systems. Plasmonic antennas can exhibit resonances in widely different spectral ranges, including the mid-infrared spectral range (50 to 500 meV) where molecular vibrations occur. Both mid-infrared plasmons and molecular vibrations can be well accessed by recently developed EELS instrumentation [10, 53]. Most interesting, the mid-infrared spectral range also hosts phonon polaritons in polar crystals (e.g. SiC, MgO, quartz) [19] and van der Waals materials (e.g. h-BN) [68, 69, 137]. Recent experimental studies demonstrate that SiC and h-BN phonon polariton resonators (in the following referred to as IR-phononic antennas) exhibit mid-infrared resonances of quality factors much higher than that of plasmonic antennas [19, 72,

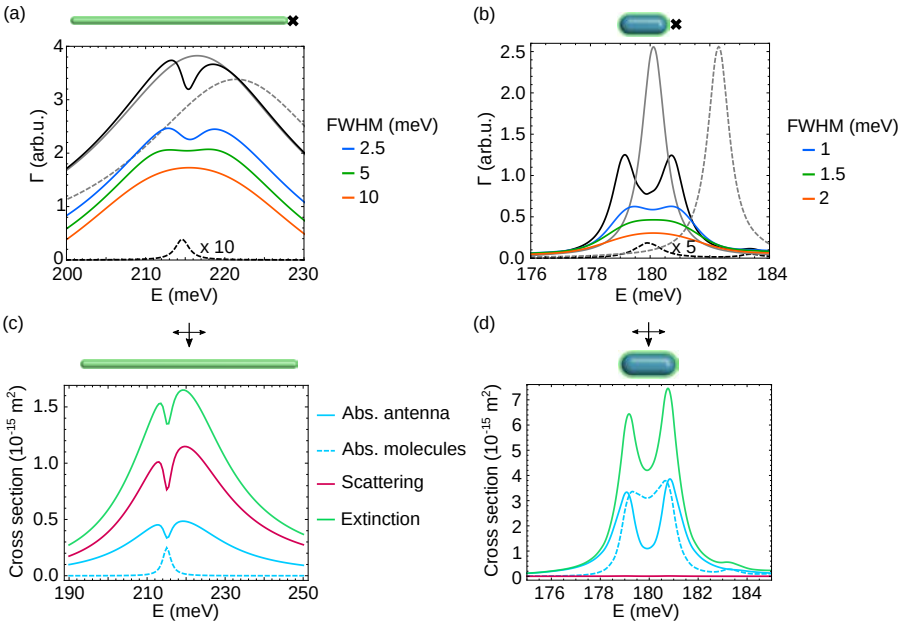

FIGURE 5.7: (a) EELS of a silver wire with length L = 1910 nm covered by a PMMA layer, excited by an electron beam passing at $(L/2+10\text{ nm}, 0)$. The simulated spectrum (black) is convolved with Gaussian functions of FWHM 2.5 meV, 5 meV and 10 meV (green/red/blue). (b) A h-BN antenna of length L = 102 nm covered by a layer of CBP molecules is probed by an electron beam passing at position $(L/2+10\text{ nm}, 0)$. The calculated EEL spectrum (black) is convolved with Gaussian functions of FWHM 1 meV, 1.5 meV and 2 meV (green/red/blue). The calculated spectra are expressed in atomic units (a.u.), the convolved spectra are scaled and vertically shifted for better readability. (c) Optical spectra calculated for the same silver wire as in (a) covered by a PMMA layer (absorption in the antenna and in the molecular layer are plotted by light blue solid and dashed lines, respectively, scattering by purple line and extinction by green line). (d) Similar to (c) calculated for the same h-BN antenna as in (b) covered by the CBP layer.

131, 137, 219], which can be accessed by EELS as well [62, 155]. The coupling of molecules and well-defined phononic antennas has been only very recently demonstrated by infrared far-field spectroscopy of h-BN ribbons covered by molecules, reaching even the strong coupling limit [72]. In the following, we thus explore the potential of surface-enhanced EELS of molecular vibrations in the IR spectral range employing plasmonic and phononic antennas.

We first study the EEL spectra of a long silver wire (exhibiting mid-IR plasmon resonances) covered by a thin poly(methyl methacrylate) (PMMA) layer.

PMMA exhibits a rich infrared absorption spectrum, but we focus on the interaction of the plasmons with the carbonyl (C=O bond) stretching mode. The carbonyl stretching vibration is well characterized by a Lorentz oscillator [according to Eq. (5.3)] with $\varepsilon_{\infty,s} = 2.12$, $\omega_s = 214.4$ meV, $\gamma_s = 2$ meV and $f_s = 0.0136$, and produces the weak peak in the EEL spectrum calculated only for the PMMA layer [black dashed line in Fig. 5.7(a)].

If we tune the antenna to interact with the continuous PMMA layer and find its optimal length to be $L = 1910$ nm. The spectrum for the bare antenna is plotted in Fig. 5.7(a) with a grey dashed line. The spectrum of the antenna covered with a dielectric layer characterized by $\varepsilon_s = \varepsilon_{\infty,s} = 2.12$ is shown as a gray solid line. When the molecular layer is placed on top of the antenna, one can clearly observe a Fano-like vibrational feature in the IR EEL spectrum (solid black curve), similar to surface-enhanced IR absorption (SEIRA) spectra plotted in Fig. 5.7(c). However, the experimental detection of vibrational fingerprints in EELS is still very challenging because of the limited spectral resolution caused by the finite width of the zero-loss peak [10]. We thus consider the finite experimental energy resolution, by convolving the calculated spectra with a Gaussian function whose FWHM corresponds to the instrumental resolution. In Fig. 5.7(a) we compare calculated EEL spectrum for the coupled system (black curve, zero-loss peak width is zero) with those where a convolution was applied to mimic the finite energy resolution (i.e. the finite width of the zero-loss peak). The colored spectra display the results for zero-loss peak widths of 2.5 meV, 5 meV, and 10 meV. Our results show that (in the absence of experimental noise) a spectral resolution of at least 5 meV or better is required to resolve the spectral features associated with the molecular vibrations.

In Fig. 5.7(b) we study surface-enhanced EELS based on IR-phononic antennas. We consider a similar system as in Ref. [72]: a h-BN rod, with the dielectric properties described by Eq. (2.1) with the parameters in Table 2.1, covered by a layer of 4,4'-bis(N-carbazolyl)-1,1'-biphenyl (CBP) molecules. The CBP molecules are characterized by their experimental dielectric response [220], giving rise to an intense vibration at 180 meV [see EEL spectrum for the uncoupled CBP shell shown by the black dashed curve in Fig. 5.7(b)]. The h-BN antenna of length $L = 102$ nm supports a dipolar localized phonon polariton mode in the upper Reststrahlen band,[1] which produces a narrow EEL peak [grey dashed curve in Fig. 5.7(b)], shifted to lower energies when the antenna is covered by a non-resonant dielectric layer (mimicking the molecular layer without absorption resonance) with $\varepsilon_s = \varepsilon_{\infty,s} = 2.8$ (grey continuous curve). The EEL spectrum of the antenna covered by the molecules (black curve) shows a pronounced peak splitting. We find that the system is strongly coupled as absorption spectra both

[1] We note that in the studied case, the anisotropy and complex hyperbolic nature of h-BN phonon polaritons [60, 131] does not significantly influence the coupling. The spectral response is thus nearly identical as for an isotropic antenna with $\overleftrightarrow{\varepsilon} = (\varepsilon_R, \varepsilon_R, \varepsilon_R)$.

in the antenna and in the molecular layer plotted in Fig. 5.7(d) exhibit two maxima, which is a signature of the presence of two new distinct hybrid plasmon-exciton polariton modes. By comparing the solid black spectra in Fig. 5.7(a) and (b), we can immediately identify the difference between the weak perturbation of the plasmonic antenna response and the emergence of the two hybridized modes, when the CBP molecules are coupled with the h-BN antenna. However, the convolution of the spectrum for the strongly coupled system in Fig. 5.7(b) predicts that an instrumental resolution of at least 1 meV is required to resolve both peaks. Although such resolution is challenging even for state-of-the art EELS instruments, we envision that emerging technical developments could allow for experimental observation of this effect in the near future.

5.2.4 EEL Signal decay

The coupling of molecular excitations with plasmonic antennas enables to acquire information on the molecules through the plasmonic field. However, this field significantly extends away from the particle boundaries [see e.g. Fig. 5.4(c)], which implies that the spatial resolution in plasmon-enhanced EELS should be reduced compared to EELS of bare molecular samples. To explore this aspect, we performed EELS calculations for molecule-covered plasmonic and IR-phononic antennas for various beam positions in aloof geometry, i.e. when the beam passes the molecule-covered antenna at an impact parameter $b > 0$ nm where $b = 0$ defines the antenna boundary (see schematics on the top of Fig. 5.8).

We first analyze the EEL spectra as a function of distance b for a plasmonic antenna in the visible spectral range. To that end, we choose the same system parameters as in Fig. 5.4(d). We find that the electron energy loss probability [solid lines in Fig. 5.8(a)] for distances up to $b = 30$ nm is still larger than in the case of the bare excitonic shell (dashed lines; the bare excitonic EEL spectra are zoomed in Fig. 5.8(b) for better visibility). For a quantitative analysis, we extract the spectral contrast [defined as the difference between local maximum and minimum in the spectral region of the Fano feature, as marked in Fig. 5.4(d)] from the EEL spectra in Fig. 5.8(a) and plot it as a function of the distance b in Fig. 5.8(c) (black dots). We find that the spectral contrast of the coupled system decays less quickly with b than that of the bare excitonic shell [defined as the peak height in Fig. 5.8(b); shown by red squares in Fig. 5.8(c)]. Furthermore, the coupling of the molecular excitons to the plasmon yields a more than five-fold contrast enhancement.

We performed the same analysis for the long PMMA-covered silver wire at mid-infrared energies [same as in Fig. 5.7(a)]. The results are shown in Figs. 5.8(d-f). The solid curves in Fig. 5.8(d) display the EEL spectra of the PMMA-covered wire, while the dashed curves in Fig. 5.8(d,e) show the EEL spectra of the bare PMMA shell. The spectral contrast in Fig. 5.8(f) is more than ten times larger when the PMMA vibrations are coupled to the plasmons in the wires (black dots vs. red squares, respectively). Importantly, the decay of the spectral contrast is

much less pronounced for the PMMA shell coupled to the antenna fields (black dots) compared to the pure PMMA shell (red squares), allowing for detection of the PMMA vibrational EEL signal at much larger impact parameters, which could help to reduce electron beam induced sample damage.

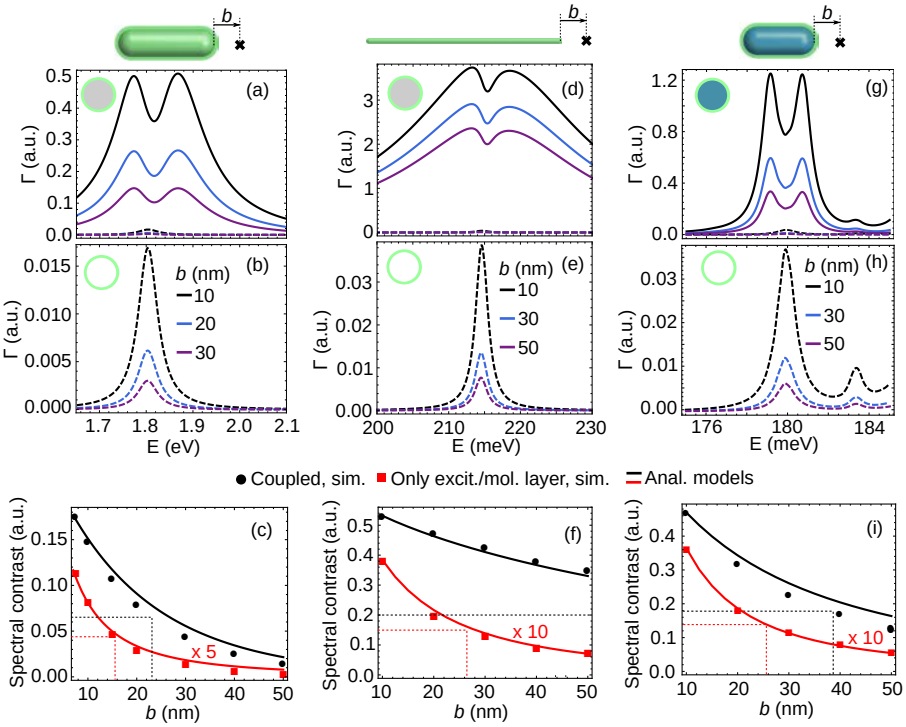

FIGURE 5.8: (a,b) Full lines: EEL probability calculation for a silver rod ($L = 145$ nm) covered by an excitonic layer and for impact parameters $(L/2 + b, 0)$, where the distance of the electron beam from the particle boundary b is 10 nm (black), 20 nm (blue) and 30 nm (purple). Dashed lines: calculation without the silver wire, zoomed in (b). (c) EELS spectral contrast for the coupled scenario (black) or for the molecular response (red, multiplied by a factor of 5) as a function of b. (d,e) Analogous calculations for the silver wire ($L = 1910$ nm) covered by a PMMA layer and for b 10 nm (black), 30 nm (blue) and 50 nm (purple). (f) Analogous to (c), evaluated for the IR wire. The molecular peak height is multiplied by a factor 10. (g,h) Analogous calculation for a h-BN phononic antenna with CBP molecules. Full lines are for the coupled system (antenna's length is $L = 102$ nm), the dashed lines are for uncoupled CBP shell. The impact parameters are the same as in (d,e). (i) Analogous to (c,f), evaluated for the coupled h-BN antenna - CBP molecular shell. The dashed lines in (c,f,i) mark the values of b where the spectral contrast drops to $1/e$ of its maximal value. The solid lines are analytical fits derived from the model introduced in the text.

Finally, we present in Fig. 5.8(g) the calculated EEL spectra of an IR-phononic h-BN antenna covered by the CBP molecular layer [same as in Fig. 5.7(b)]. All spectra calculated for the coupled system (solid lines) exhibit a clear peak splitting and higher loss probability than for the uncoupled CBP shell [dashed lines in Figs. 5.8(g,h)]. The spectral contrast for the coupled scenario is also more than ten times higher and slightly slower decaying than if one probes the uncoupled CBP shell, as shown in the comparison in Fig. 5.8(i).

We now compare and analytically model the spatial decay of the spectral contrast plotted in Figs. 5.8(c,f,i) both in the uncoupled and coupled scenarios. The uncoupled molecular shell is excited only in a small volume close to the beam,

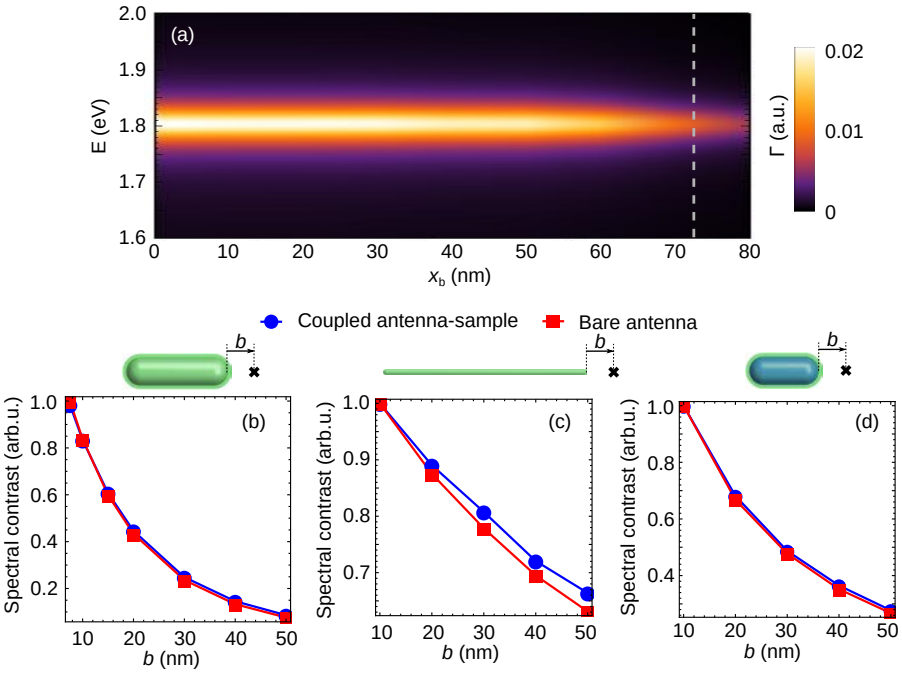

FIGURE 5.9: (a) Spectral linescan along the excitonic shell surrounding a rod with length L = 145 nm [only the excitonic material is present in the calculation as in Fig. 5.8(b)] and the beam at $(x_b, R + 10\,\text{nm})$. A single peak at the excitonic transition is observed and its intensity "saturates" for a beam position approximately 20 nm from the shell tip whose position is denoted by the dashed vertical line. (b,c,d) Functional decay dependence of the dip depth in the EEL spectra for the coupled system (blue) and the peak height of the uncoupled antennas (red). (b) is calculated for the same system as in Fig. 5.8(a), (c) corresponds to Fig. 5.8(d) and (d) to Fig. 5.8(g). Points are calculated data and curves are a guide to the eyes. The slight differences are coming mainly from the direct sample excitations. The calculated data are divided by maximal values.

which we demonstrate by calculating the EEL probability for the beam scanned along the excitonic shell in Fig. 5.9(a) (with no antenna present), which shows that only a certain "effective" volume of the shell is excited. Hence, the uncoupled shell can be replaced by an effective point dipole. In such a case, from Eq. (5.10), and setting $\alpha_A = 0$ [138], the peak height follows:

$$I_{dipole,S}(b) \propto \frac{1}{\gamma_L^2} K_0^2\left(\frac{\omega(b + b_{dip,S})}{v\gamma_L}\right) + K_1^2\left(\frac{\omega(b + b_{dip,S})}{v\gamma_L}\right), \tag{5.14}$$

with the beam passing at $(L/2 + b, 0)$ and the dipole being located at the effective distance $(L/2 - b_{dip,S}, 0)$, which approximately corresponds to the center of mass of the excited sample volume. We also note that the above equation [Eq. (5.14)] is the retarded version of Eq. (5.2). We found $b_{dip,ex} = 8$ nm for the excitonic sample, $b_{dip,PMMA} = 20$ nm for the PMMA sample and $b_{dip,CBP} = 15$ nm for the CBP molecules to reproduce the bare sample decay [red curves in Fig. 5.8(c,f,i)]. The PMMA and CBP dipoles are placed further due to the larger shell volume excited in the IR.

Next we describe the decay of the spectral contrast in the coupled case. In Fig. 5.9(b,c,d) we show that it approximately follows the signal decay of the bare antenna and hence, we model the latter case. The antennas are preferentially polarized along the x direction (see Eq. (5.10) for $\alpha_S = 0$), which retains only the second term of Eq. (5.14). The contrast decay for the short antennas can be then expressed as:

$$I_{dipole,A}(b) \propto K_1^2\left(\frac{\omega(b + L/2)}{v\gamma_L}\right), \tag{5.15}$$

where we considered the dipole placed at the antenna's center of mass. The long IR antenna is described by a line charge distribution [221], which can be approximated for the dipolar plasmon as $\sigma(x) = \sigma_0 x$ for $-L/2 < x < L/2$ and $\sigma(x) = 0$ otherwise. In the non-retarded approximation, we obtain the following expression for the intensity of the antenna peak as a function of the beam position [222, 223]:

$$I_A(b) \propto \left|\int_0^L dx'\,(x' - L/2) K_0\left(\frac{\omega(x' + b)}{v}\right)\right|^2. \tag{5.16}$$

The corresponding expression for the analytical decay shown by the red curves in Fig. 5.8(c,f,i) is in excellent agreement with the data points (red squares) obtained from the numerical simulations. Note that the signal decay length depends inversely on the energy of the excitations, which is a consequence of the spatial decay of the electromagnetic field of the electron beam [see Eq. (5.4)]. The

decay length is thus larger for molecular vibrations [Fig. 5.8(f,i)] compared to visible excitons [Fig. 5.8(c)].

We next compare the contrast decay for the molecules coupled with the antennas. As pointed out above, we find that the decay length is larger than without the antenna for each case [compare black and red dots in Fig. 5.8(c,f,i)]. Furthermore, we find significant differences in the decay considering the IR plasmonic and phononic antennas. As the spatial dependence of the spectral contrast for the coupled antenna-molecule system [black dots in Fig. 5.8(c,f,i)] closely follows the strength of the bare antenna excitation as a function of b [as demonstrated in Fig. 5.9(b,c,d)], we can explain the results of our simulations by modeling the contrast decay of the corresponding uncovered antennas. The short plasmonic and phononic antennas can be replaced by point dipoles, positioned at the center of mass of the antennas and polarized along the x direction [see Eq. (5.15)]. The modeled decay is then plotted by black curves in Fig. 5.8(c) and (i), reasonably reproducing the simulated results. However, the charge induced in the long IR plasmonic antenna is better described by considering a finite surface charge distribution of the plasmonic excitation [221], which yields the EEL intensity decay [see Eq. (5.16)] plotted by the black line in Fig. 5.8(f), which is in nice agreement with the numerically calculated points.

By comparing the black curves in Figs. 5.8(f,i), we can conclude, that the near-field of the IR plasmonic antenna is spatially much more extended (less confined). This occurs due to the fact that the plasmon polariton wavelength is much larger than the phonon polariton wavelength, even though both IR antennas exhibit the fundamental resonance at similar energies. We thus emphasize that the nature of the polaritonic excitation as well as the particular charge distribution and shape of the antenna strongly influence the observed spectral contrast decay [224].

5.2.5 Ultra-remote sensing in EELS

An interesting aspect of the use of plasmonic and IR-phononic antennas and nanostructures in EELS is the possibility to probe molecular excitations remotely, that is, in aloof geometry but with enhanced sensitivity. We explore this possibility for probing excitons in smaller amounts of molecules covering plasmonic antennas. To that end, we study a plasmonic silver rod with an excitonic molecular cap placed at only one of the antenna apexes [see schematic in Fig. 5.10(a)]. To match the energy of the dipolar plasmon with the exciton of the molecular capping layer (characterized by the same parameters as previously), we consider a silver rod of length $L = 155$ nm.

In Fig. 5.10(a) we show the calculated spectra at different beam positions along the antenna, as marked by the crosses in the schematic. When the beam is close to the antenna apexes, we excite the dipolar plasmon resonance around 1.8 eV. Interestingly, the spectra exhibit the Fano-like feature arising due to the plasmon-exciton coupling at both apexes, even when the electron beam passes close to the uncovered rod apex. For comparison, we show in Fig. 5.10(b) the spectra for the

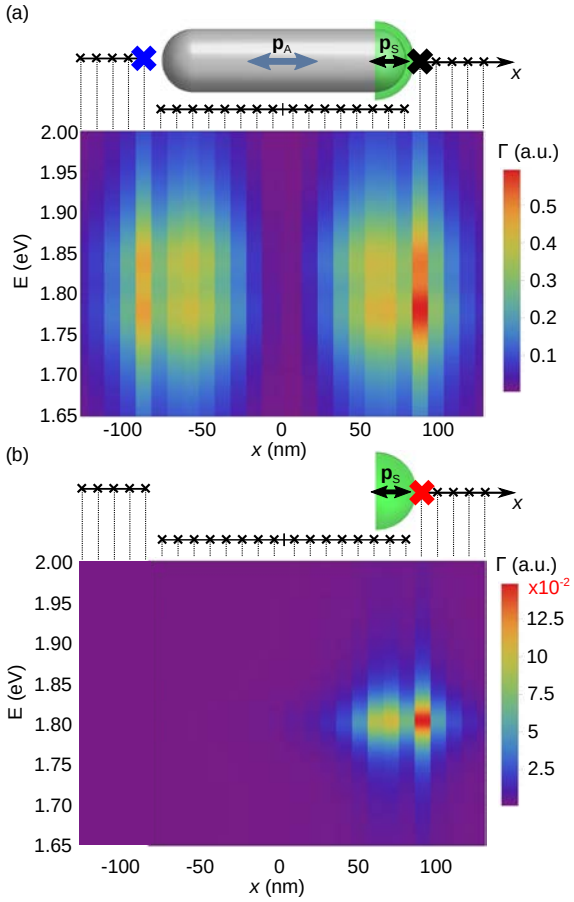

FIGURE 5.10: (a) EELS scan along a silver antenna of length L = 155 nm with an excitonic cap placed as shown in the schematic. (b) The same calculation as in (a) but without the antenna. Notice much lower values of the EELS intensity.

situation when only the molecular cap is present, exhibiting an excitonic peak only for the beam positions close to the cap.

Most importantly, the Fano feature in the spectra calculated for the antenna-cap system is also present when the beam is probing the uncovered rod extremity [$x < 0$ nm, Fig. 5.10(a)], i.e. at rather large distances from the excitonic cap. In comparison, the EEL spectra of the bare molecular cap at positons $x < 0$ nm are more than a factor of 10^2 smaller [Fig. 5.10(b)] and thus undetectable. The plasmonic (or in general polaritonic) field thus represents a unique means for ultra-distant remote sensing with EELS.

To discuss more quantitatively the spectral contrast enhancement obtained

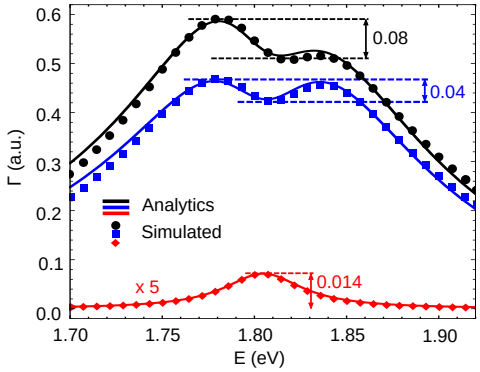

FIGURE 5.11: Spectra for the beam positions denoted by the coloured crosses in the schematic of Fig. 5.10 $(L/2+10\,\text{nm}, 0)$ in black, $(-L/2-10\,\text{nm}, 0)$ in blue and $(L/2+10\,\text{nm}, 0)$ in red (calculated without the antenna, multiplied by 5). The points represent numerically calculated data, the continuous lines are obtained from fitting of the analytical model of the coupled dipoles as depicted in the schematic of Fig. 5.10(a). The response of the bare excitonic cap (red) was fitted to Eq. (5.10) considering $\alpha_A = 0$. The fitted parameters are: $F_A = 3.32 \times 10^9$ a.u., $\Omega_A = 1.817$ eV, $\kappa_A = 175$ meV, $F_S = 98561$ a.u., $\Omega_S = 1.805$ eV, $\kappa_S = 52$ meV, $x_A = 87/90$ nm, $x_{SA} = 63/61$ nm in the black/blue spectrum and $x_S = 20$ nm in the black spectrum.

with the plasmonic antenna, we plot in Fig. 5.11 the EEL spectra for beam positions at the antenna apexes [positions marked by coloured crosses in the schematics of Fig. 5.10(a,b)]. For a beam position close to the cap, we observe that the EEL contrast is more than five times larger when the cap is placed onto the plasmonic antenna (compare black and red spectral points in Fig. 5.11). However, as discussed above, the excitonic fingerprint is also clearly visible in the spectrum when the electron beam passes close to the uncovered apex (blue points), whereas the uncoupled excitonic cap is undetectable for the same beam position.

We also observe a slight variation in the spectral shape of the Fano-like coupling feature [compare the black and blue spectra in Fig. 5.11]. When the beam is close to the molecular cap, it efficiently excites both the antenna and the molecular sample and the calculated spectra can be nicely fitted by the coupled dipole model in Eq. (5.12) (black curve, see the figure caption for the fitting parameters). On the other hand, for the beam placed at the uncovered antenna tip, we excite mainly the plasmon and the direct excitation of the molecular cap is negligible [blue curve obtained with Eq. (5.11)].

5.3 Summary

In the first part of this chapter we showed local spectroscopy of water molecules with a localized electron beam. From the knowledge of the sample geometry provided by HAADF images we suggested a simple analytical model to describe the spatial decay of the vibrational EEL signal. The vibrational peaks corresponding to water encapsulated in a small area exhibited much faster decay than the signal from molecules adsorbed on the extended supporting carbon layer. We anticipate that follow-up experiments accompanied by more sophisticated modeling combining classical electromagnetic response theory with ab initio modeling could be capable of determining nanoconfinement effects or orientation of molecules in future.

In the main part of this chapter, we studied the electromagnetic coupling in a molecule-plasmonic antenna system probed by an electron beam and described the physics involved in this localized e-probing. We demonstrated that EEL spectra of the molecule-antenna coupled system can exhibit Fano-like or strong coupling features, similar to the ones observed in far-field optical and infrared spectroscopy. Surface-enhanced EELS offers the advantage of acquiring spectral information with nanoscale spatial resolution, and importantly, of controlling the antenna-molecule coupling on demand. The implementation of this electron beam probing thus opens possibilities to explore fundamental aspects of Fano-like or strong coupling of polaritons with excitons or vibrations. Together with high-resolution imaging, we find that STEM-EELS is capable of providing detailed spectral and structural information on a complex interacting system.

Furthermore, the studied coupling mechanism offers significant enhancement of the signal from molecules and brings the possibility of fully remote sensing, which is important especially for sensitive organic specimens. The plasmon-field mediated energy loss signal could be then used for studying the composition of cell membranes and their active sites, for instance. The coupling phenomena could also appear naturally in the exploration of catalytic reactions on metallic surfaces or small amounts of organic molecules, where both the signal enhancement and the remote sensing capability could be crucial. Considering the ongoing instrumental developments, EELS in STEM shows the potential to become a powerful tool for fundamental studies of molecules that are naturally or intentionally located on nanostructures supporting localized plasmon or phonon polaritons. Surface-enhanced EELS might also open the door to novel STEM-EELS applications such as remote- and thus damage-free- sensing of excitonic and vibrational excitations in molecules, quantum dots or 2D materials.

Chapter 6

Probing the electromagnetic response of dielectric antennas by vortex electron beams

Nanoparticles made of materials with high refractive index have recently attracted large interest in the field of nanoscale optics as an alternative to their metallic counterparts for applications in the control and engineering of light at the nanoscale [225, 226]. As discussed in Chapter 5, metallic nanoparticles support resonant LSP modes [20], which enable to strongly localize light in the form of EM near field around the nanoparticle, or vice versa, to scatter EM radiation from the near field to the far field. A similar effect can be obtained by exciting resonant EM Mie modes in high-refractive-index nanoparticles, such as those made of transition metal dichalcogenides [227], silicon [228], or other semiconductors [229, 230]. Importantly, the EM modes of these so-called dielectric nanoantennas are less lossy than the LSP modes, which suffer from heat dissipation [229, 231]. Another advantage of the dielectric antennas is that they exhibit modes of both electric and magnetic nature [228, 232–235], and thus can be used to create electric and magnetic near-field "hot spots" at the nanoscale [236]. Hence, dielectric antennas represent a suitable platform for enhancing emission from electric [237–239] and also magnetic [240, 241] emitters. Other applications involve the enhancement of circular dichroism in chiral molecules [242, 243], surface-enhanced Raman scattering [244], achieving strong coupling of the EM modes with solid state excitations in matter [245], or employing the dielectric antennas as building blocks of metasurfaces and metamaterials [246–248].

The dielectric nanoantennas' modes have been mostly studied by far-field spectroscopic methods [228, 234]. However, as many functionalities rely on the EM field localized close to the nanoparticles, it is desirable to characterize the antennas also in the near field. Several studies have employed near-field probes such as sharp tips in near-field optical microscopy or focused electron beams in cathodoluminescence (CL) measurements for nanoscale excitation of the resonant modes in silicon nanoparticles, where the spectral response was obtained in the

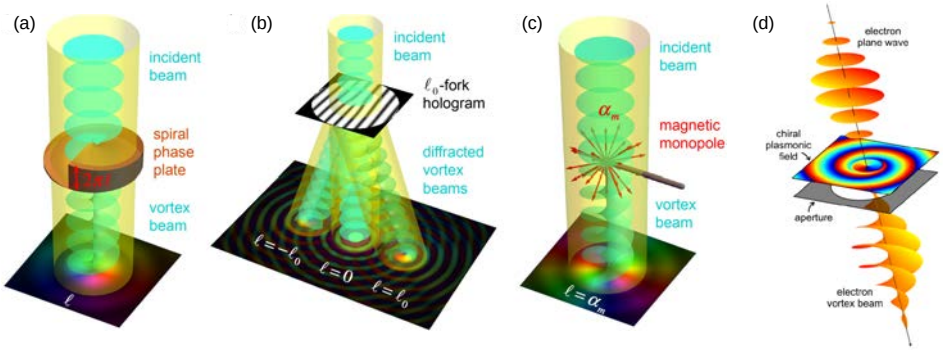

FIGURE 6.1: Different means of generation of VEBs: (a) by transmission through a phase plate, (b) after diffraction on a specially designed aperture, (c) due to the interaction with a magnetic monopole-like field, or (d) in the interaction with a chiral plasmonic field. Plots (a-c) are reprinted from Ref. [273] with permission from Elsevier, (d) is reprinted from Ref. [271].

far-field [236, 249–255].

An alternative technique for acquiring truly near-field spectral information on the dielectric nanoparticles could be EELS performed with a focused fast electron beam in STEM, which was confirmed in a very recent study [256]. Interestingly, besides using conventional electron beams in STEM, recent efforts [79, 80, 257–259] have led to generation of vortex electron beams (VEBs) carrying orbital angular momentum (OAM), which provide the possibility of direct interaction of the beam with excitations of both electric and magnetic nature. The introduction of VEBs in the electron microscopy opened a pathway to probing magnetic fields [260, 261], magnetic transitions in bulk materials [262–265] and chirality of crystals [266]. It was also theoretically suggested that EELS with VEBs might be used to probe photonic nanoantennas and help to separate the contribution from the electric and magnetic modes [267], selectively excite modes with certain symmetry [268, 269] or to locally investigate dichroic response of chiral plasmonic nanostructures [269, 270]. The chiral EM fields could be also exploited for creating an electron vortex out of a non-vortex beam [94, 270–272].

Here we suggest that STEM-EELS with either a conventional or a vortex beam might be a suitable technique for spectral near-field mapping of the EM modes supported by dielectric antennas. We employ a classical description of EEL with a focused electron beam and perform fully retarded calculations to retrieve the electric field arising in the electron-sample interaction, considering beams with zero and non-zero OAM. We study single and dimer antennas of different shapes, in particular spheres and cylinders, made of silicon. We show that we can distinguish modes of electric and magnetic nature by either tuning the excitation parameters or by comparing the spectra acquired with either a non-vortex or a vortex beam, each preferentially coupling to different modes. In the last part of

this chapter we explore dichroic EEL signals when the VEB interacts with chiral nanostructures.

6.1 Theoretical framework for vortex-electron energy loss spectroscopy at optical frequencies

We first introduce a theoretical approach for calculating the interaction between VEBs and arbitrarily shaped nanostructures in the framework of classical electrodynamics. We show how a VEB can be approximated by an effective electric and magnetic charge moving along optical axis, which enables us to calculate the induced electric and magnetic field arising from the interaction of the beam with the sample. Then we evaluate the energy loss experienced by the VEB, in analogy with the classical formalism used for EELS with conventional electron beams [15].

The wavefunction of a vortex electron ,ψ_l, can be described in the non-relativistic approximation[1] as a solution of the Schrödinger equation for a free-space moving electron with a non-vanishing angular momentum $l\hbar$, where l is the angular momentum quantum number and $\hbar$ is the reduced Planck constant. In cylindrical coordinates (R, ϕ, z), one of the simplest solution takes the form of a Bessel beam [257, 273, 276]

$$\psi_l(R, \phi, z) = N_l J_l(QR) \exp(il\phi) \exp(iq_z z), \tag{6.1}$$

where Q and q_z are the radial and perpendicular wavevectors of the electron moving along the z axis, respectively. The Bessel function $J_l(QR)$ governs the radial shape of the beam (as we can observe in the upper row of Fig. 6.2) and N_l is a normalization factor. The helical form of the wavefront, and thus the angular momentum, are captured through the exponential term $\exp(il\phi)$ and determine the phase variation in the transverse plane (see the lower row of Fig. 6.2). In the classical approximation, we can describe the vortex electron beam by the current density

$$\mathbf{j}_l(\mathbf{r}, t) \simeq -\frac{e\hbar}{m_e}\left(\mathbf{e}_\phi \frac{l}{R} + \mathbf{e}_z q_z\right) J^2_{|l|}(QR) N_l^2 \, \delta\left(z_e(t) - z\right), \tag{6.2}$$

where e is the elementary charge and m_e the mass of the electron positioned at $\mathbf{r}_e(t) = \mathbf{e}_z z_e(t) = \mathbf{e}_z v t$ ($\boldsymbol{e}_z$ is the unit vector in the z direction), and we consider the beam moving with velocity $\mathbf{v} = (0, 0, v)$. Importantly, the azimuthal component $\mathbf{j}_{l,\phi} = \mathbf{e}_\phi(\mathbf{j}_l \cdot \mathbf{e}_\phi)$ yields a magnetic dipole density associated to the current loop in a fixed z plane [277]:

$$\mathbf{m}(z, t) = \frac{1}{2}\frac{\int dS' \, \mathbf{r}' \times \mathbf{j}_{l,\phi}(\mathbf{r}', t)}{\int dS' \, |\psi_l|^2} = -\mathbf{e}_z \mu_B l \delta(z_e(t) - z), \tag{6.3}$$

[1] For discussion of the relativistic solutions, see Refs. [274, 275].

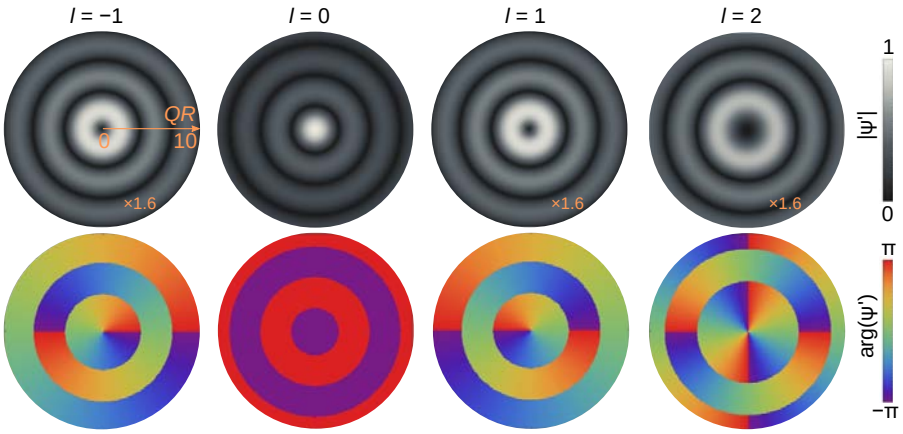

FIGURE 6.2: Intensity (upper row, scaling denoted in the plots) and phase (lower row) of the function $\psi' = J_l(QR)\exp(il\phi)$ governing the transverse behavior of a beam given by Eq. (6.1) in polar coordinates (R, ϕ) (the spatial scaling is the same in all plots). Columns correspond to different OAM values l as denoted on top of the plots.

where $\mu_B = e\hbar/(2m_e)$ is the Bohr magneton and where we integrated over the surface of the fixed z plane.

For implementation of the current as a source in analytical calculations and also in numerical solvers of the Maxwell's equations, we thus replace the azimuthal electric current component in Eq. (6.2) by an effective magnetic dipole current density in the z direction (in the following denoted as the magnetic current), which in the frequency domain reads:

$$\mathbf{J}_m(z,\omega) = -i\omega\tilde{\mathbf{m}}(z,\omega) = \mathbf{e}_z \frac{i\omega\mu_B l}{v} \exp\left(\frac{i\omega z}{v}\right). \tag{6.4}$$

Similarly, neglecting the transverse profile of the beam in Eq. (6.2), we can approximate the z component of the electric current density in the frequency domain as

$$\mathbf{J}_e(z,\omega) = -\mathbf{e}_z\, e \exp\left(\frac{i\omega z}{v}\right), \tag{6.5}$$

which together with the magnetic current from Eq. (6.4) acts as an external source inducing the electromagnetic response of the sample as schematically depicted in Fig. 6.3.

We now modify the classical dielectric theory of EELS, which assumes that the energy loss of the electron beam can be obtained by evaluating the work performed by the induced EM field [15] (see Section 1.2.2), and introduce electric and magnetic loss channels [267]:

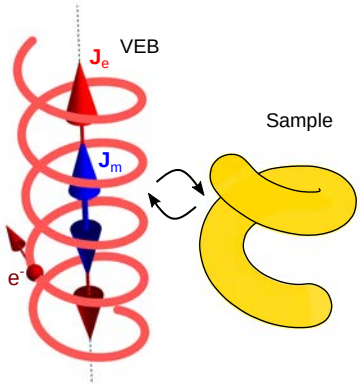

FIGURE 6.3: VEB represented as a classical spiralling electric current that can be replaced by a superposition of linear electric and magnetic currents interacting with their surroundings.

$$\Delta E_e = -\frac{1}{\pi}\int_0^\infty d\omega \int_{-\infty}^{\infty} dz\, \mathrm{Re}\left[E_z^{ind}(\mathbf{r}_e(t),\omega)J_{e,z}^*(z,\omega)\right] = \int_0^\infty d\omega\, \hbar\omega\Gamma_e(\omega), \tag{6.6}$$

$$\Delta E_m = -\frac{1}{\pi}\int_0^\infty d\omega \int_{-\infty}^{\infty} dz\, \mathrm{Re}\left[B_z^{ind}(\mathbf{r}_e(t),\omega)J_{m,z}^*(z,\omega)\right] = \int_0^\infty d\omega\, \hbar\omega\Gamma_m(\omega), \tag{6.7}$$

where E_z^{ind} and B_z^{ind} are the z components of the induced electric and the magnetic field, respectively, coming from the interaction of the VEB and the sample. The total energy loss is then the sum of these two contributions: $\Delta E = \Delta E_e + \Delta E_m$. In the expressions above, we have also defined the electric and magnetic loss probabilities Γ_e and Γ_m, respectively, which contribute to the total loss probability $\Gamma(\omega) = \Gamma_e(\omega) + \Gamma_m(\omega)$, the quantity which corresponds to the measured loss spectrum if a well-focused VEB is employed. By inserting the current densities from Eq. (6.5) and Eq. (6.4) into Eq. (6.6) and Eq. (6.7), respectively, the probabilities can be expressed as:

$$\begin{aligned}\Gamma_e &= \Gamma_{e,\mathbf{J}_e} + \Gamma_{e,\mathbf{J}_m} \\ &= \frac{e}{\pi\hbar\omega}\int_{-\infty}^{\infty} dz\, \mathrm{Re}\left[\left(E_{z,\mathbf{J}_e}^{ind}(\mathbf{r}_e(t),\omega) + E_{z,\mathbf{J}_m}^{ind}(\mathbf{r}_e(t),\omega)\right)\exp\left(-\frac{i\omega z}{v}\right)\right], \\ \Gamma_m &= \Gamma_{m,\mathbf{J}_m} + \Gamma_{m,\mathbf{J}_e}\end{aligned} \tag{6.8}$$

$$= -\frac{\mu_B l}{\pi\hbar v}\int_{-\infty}^{\infty} dz\, \mathrm{Im}\left[\left(B^{ind}_{z,\mathbf{J}_m}(\mathbf{r}_e(t),\omega) + B^{ind}_{z,\mathbf{J}_e}(\mathbf{r}_e(t),\omega)\right)\exp\left(-\frac{i\omega z}{v}\right)\right], \quad (6.9)$$

where we consider that the induced electric field can arise both due to the electric and the magnetic current ($E^{ind}_{z,\mathbf{J}_e}$ and $E^{ind}_{z,\mathbf{J}_m}$), yielding the corresponding loss probability channel $\Gamma_{e,\mathbf{J}_e}$ and $\Gamma_{e,\mathbf{J}_m}$, respectively. Similarly, the induced magnetic field is also originated from the interaction with both current sources ($B^{ind}_{z,\mathbf{J}_e}$ and $B^{ind}_{z,\mathbf{J}_m}$), giving rise to the loss channels $\Gamma_{m,\mathbf{J}_e}$ and $\Gamma_{m,\mathbf{J}_m}$. The electric loss probability channel $\Gamma_{e,\mathbf{J}_e}$ in Eq. (6.8) corresponds to the conventional EEL spectrum (considering a beam with $l = 0$, see Section 1.2.2). We note that our approach does not rigorously take into account transfer to different vortex states (characterized by $l_{final} \neq l_{initial}$). We assume that the strength of the magnetically-mediated interactions is simply proportional to the OAM of the beam as expressed in Eq. (6.9).

To obtain the loss probabilities [Eqs. (6.8) and (6.9)], we have to solve for the induced fields, which can be accomplished either analytically in simple cases, or numerically in more complex geometries. In the following, we discuss analytical results for a single spherical sample and an infinite cylindrical wire and also numerical solutions for spherical dimers and chirally arranged cylinders, respectively (for details on numerical implementation, see Appendix B).

6.2 Spectroscopy of localized modes in spherical dielectric antennas

6.2.1 Single spherical nanoparticle

We first consider the canonical example of a single spherical nanoparticle. Due to the symmetry of the beam-particle geometry, the terms $\Gamma^{sph}_{e,\mathbf{J}_m}$ and $\Gamma^{sph}_{m,\mathbf{J}_e}$ cancel each other and do not contribute to the overall loss probability. We thus evaluate only the terms $\Gamma^{sph}_{e,\mathbf{J}_e}$ and $\Gamma^{sph}_{m,\mathbf{J}_m}$. The fully-retarded solution of the induced electric field coming from the excitation by the electric current and the corresponding EEL probability was obtained by García de Abajo in Ref. [112]:

$$\Gamma^{sph}_e \to \Gamma^{sph}_{e,\mathbf{J}_e} = \frac{e^2}{4\pi\varepsilon_0 c\hbar\omega}\sum_{n=1}^{\infty}\sum_{m=-n}^{n} K^2_m\left(\frac{\omega b}{v\gamma_L}\right)\left[C^M_{n,m}\mathrm{Im}[t^M_n] + C^E_{n,m}\mathrm{Im}[t^E_n]\right], \quad (6.10)$$

where the summation is performed over multipoles $\{n, m\}$, $K_m(x)$ is the modified Bessel function of the second kind of order m, $\gamma_L = 1/\sqrt{1 - v^2/c^2}$ is the Lorentz contraction factor, b is the distance of the beam from the center of the sphere, the coefficients $C^{E/M}_{n,m}$ take into account coupling with the excitation field of the fast electrons (see the expressions in Appendix A.3). We use superscripts M/E to

denote the coefficients related to the excitation of the magnetic/electric modes. Eq. (6.10) also includes the Mie coefficients:

$$t_n^M = (-i)\frac{-j_n(q_0a)[k_{in}aj_n(q_{in}a)]' + j_n(q_{in}a)[q_0aj_n(q_0a)]'}{h_n^{(1)}(q_0a)[k_{in}aj_n(q_{in}a)]' - j_n(q_{in}a)[q_0ah_n^{(1)}(q_0a)]'}, \tag{6.11}$$

$$t_n^E = (-i)\frac{-j_n(q_0a)[q_{in}aj_n(q_{in}a)]' + \varepsilon j_n(q_{in}a)[q_0aj_n(q_0a)]'}{h_n^{(1)}(q_0a)[q_{in}aj_n(q_{in}a)]' - \varepsilon j_n(q_{in}a)[q_0ah_n^{(1)}(q_0a)]'}, \tag{6.12}$$

where $q_0 = \omega/c$ is the magnitude of the wave vector in vacuum, $q_{in} = \sqrt{\varepsilon}\omega/c$ the wave vector inside the sphere characterized by relative dielectric function ε, and a is radius of the sphere. $j_n(x)$ and $h_n^{(1)}(x)$ are the spherical Bessel and Hankel functions of the first kind, respectively. The derivatives in Eq. (6.11) and Eq. (6.12) are performed with respect to the functions' arguments.

If we consider the excitation of the sphere by the magnetic current, the corresponding loss probability Γ_m^{sph} can be readily obtained if we utilize the invariance of Maxwell's equations under the transformation

$$\mathbf{E} \to -\frac{Z}{\mu_0}\mathbf{B}, \quad \mathbf{B} \to \frac{\mu_0}{Z}\mathbf{E}, \quad \mathbf{J}_e \to \frac{\mathbf{J}_m}{c}, \tag{6.13}$$

where $Z = \sqrt{\mu_0/(\varepsilon_0\varepsilon)}$ with the vacuum permeability μ_0, the vacuum permittivity ε_0 and the relative permittivity of a medium where the field is evaluated ε (we consider a non-magnetic medium with relative permeability $\mu = 1$). The magnetic-current-mediated loss probability is then

$$\begin{aligned}\Gamma_m^{sph} &\to \Gamma_{m,\mathbf{J}_m}^{sph} \\ &= \left(\frac{\mu_B l}{v}\right)^2 \frac{\mu_0\omega}{4\pi\hbar c}\sum_{n=1}^{\infty}\sum_{m=-n}^{n} K_m^2\left(\frac{\omega b}{v\gamma}\right)\left[C_{n,m}^M \mathrm{Im}[t_n^E] + C_{n,m}^E \mathrm{Im}[t_n^M]\right].\end{aligned} \tag{6.14}$$

We now explore whether we can distinguish modes of electric and magnetic nature excited in silicon nanoparticles with help of the VEB-EEL spectra. In Fig. 6.4(a,b) we calculate the spectral contributions Γ_e^{sph} and Γ_m^{sph}, respectively, for a single silicon nanosphere with radius $a = 150$ nm, an impact parameter $b = 157.5$ nm [as denoted in the inset of Fig. 6.4(b)] and considering a 100 keV beam ($v = 0.548c$) with $l = +100$.[2]

[2]For a lossless dielectric material (such that $\mathrm{Im}[\varepsilon] = 0$) the excited modes can decay only radiatively [278]. Hence, in such a case, the EEL probability is equal to the probability of photon emission, the CL probability. In our work we consider a realistic dielectric function with a small nonzero damping, so the equality between EEL and CL probability is only approximate.

To understand the origin of the resulting spectral features, we split the spectra (solid lines) in contributions of different multipoles n of electric (E_n) or magnetic (M_n) modes (dashed lines), i.e., the spectra before summation over n. In the considered spectral range, the probability Γ_e^{sph} [solid red line in Fig. 6.4(a)] exhibits four well visible peaks, which arise due to the excitation of a magnetic

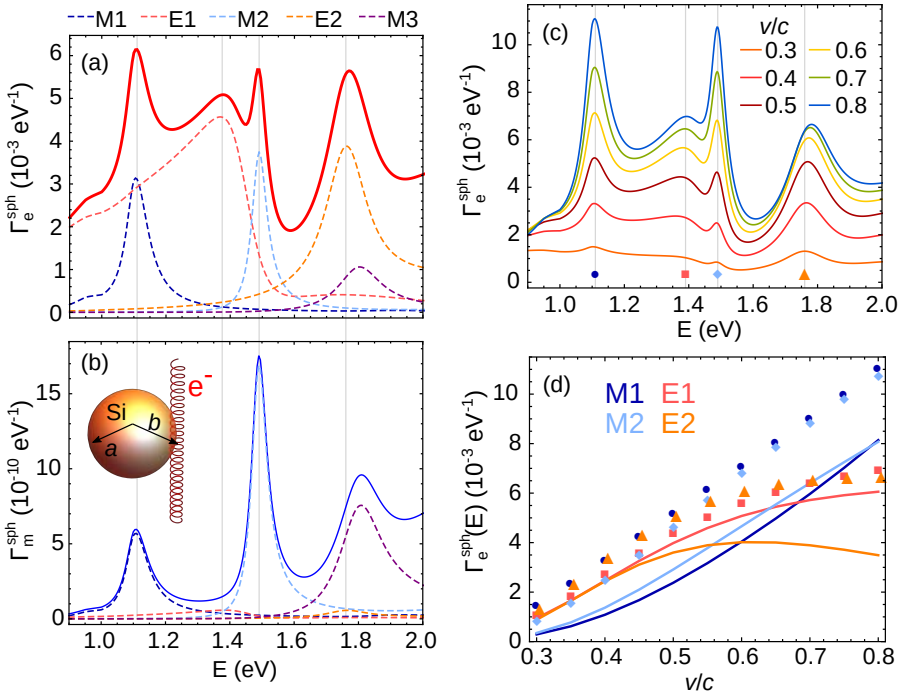

FIGURE 6.4: (a) EEL probability from Eq. (6.10) (solid red line) evaluated for an electron of energy 100 keV ($v = 0.548c$) interacting with a silicon sphere of radius $a = 150$ nm and at an impact parameter $b = 157.5$ nm (see the inset of (b) for the geometrical arrangement). The dielectric function of amorphous silicon is taken from Ref. [154]. (b) Magnetic-current mediated loss probability from Eq. (6.14) for the same parameters as in (a) and considering OAM $l = 100$ (solid blue line). Contributions to the loss probabilities from different modes are split in (a,b): magnetic dipole (M1, dark blue dashed line), electric dipole (E1, light red dashed line), magnetic quadrupole (M2, light blue dashed line), electric quadrupole (E2, orange dashed line), and magnetic octupole (M3, purple dashed line). Notice the different intensity scale of (b). (c) The same as (a) but evaluated for varying electron's velocity v. (d) Intensities of the peaks from (c) [symbols, the color-coding corresponds to (a,b)] together with the intensities extracted from the separated spectra corresponding to the different modes [solid lines, with the spectral contributions for each mode obtained as shown in (a,b)].

dipolar mode (M1, dark blue dashed line), electric dipole (E1, light red dashed line), magnetic quadrupole (M2, light blue dashed line) and electric quadrupole (E2, orange dashed line), whose energy nearly coincides with the magnetic octupole (M3, purple dashed line). On the other hand, due to the interchange of the coupling coefficients [compare Eq. (6.10) vs. Eq. (6.14)], only the excitation of magnetic modes (M1, M2 and M3) is visible in the probability Γ_m^{sph} [solid blue line in Fig. 6.4(b)]. The coupling of the magnetic part of the current with the electric modes is negligible and produces only a small contribution [see dashed light red and orange lines in Fig. 6.4(b) close to zero].

As we discussed, in an experimental measurement one would obtain the total loss probability $\Gamma^{sph} = \Gamma_e^{sph} + \Gamma_m^{sph}$, and in order to separate the loss probability components Γ_e^{sph} and Γ_m^{sph}, two measurements would need to be performed: one with a beam having $l \neq 0$ and another with a beam with $l = 0$. After subtraction of these two spectra, one would obtain Γ_m^{sph}, which shows clearly only the peaks corresponding to the magnetic modes. Unfortunately, we see that even for relatively large OAM, the "magnetic" part of the loss probability Γ_m^{sph} is six orders of magnitude smaller than Γ_e^{sph}, which is not detectable with currently achievable signal-to-noise ratio in STEM-EELS experiments.

In addition to varying the OAM of the VEB, there is an additional degree of freedom which might be used to assign the spectral peaks to the modes as either electric or magnetic: the electron's speed v which governs the strength of the coupling coefficients $C_{n,m}^{E/M}$ (related to the EM field of the beam). In Fig. 6.4(c) we evaluate Γ_e^{sph} for varying v and $l = 0$ (conventional electron beam). We can observe that the intensity ratio of the four visible peaks changes significantly. With increasing accelerating voltage (electron's speed), the coupling of the beam with the magnetic modes is much more efficient and the intensity corresponding to the excitation of the M1 and M2 modes grows significantly faster than the peak assigned to the E1 mode which starts saturating for larger speeds ($v > 0.7c$). This trend is confirmed in Fig. 6.4(d) where we plot the intensities of the peaks extracted from spectra in Fig. 6.4(c) at the energies corresponding to the M1 (dark blue points), E1 (light red squares), M2 (light blue diamonds), and E2 (orange triangles) modes, depending on the electron's speed. We plot the peak intensities as if the modes were excited independently (solid lines with the same color coding corresponding to the different modes), thus eliminating the influence of the spectral overlap of the excited modes [see Fig. 6.4(a) showing that, e.g., E1 contributes significantly even at the energy of the M1 peak]. This trend is similar also for higher-order modes and we suggest that obtaining the EEL spectra at several acceleration voltages might serve for a relatively straightforward classification of the modes.

6.2.2 Dimer of spherical nanoparticles

Dimers made of two (identical) particles separated by a small gap are also of high interest as they can provide a significant enhancement of the field in the gap or yield directional scattering [229, 236, 279, 280]. In Fig. 6.5 we thus study VEB-EELS for a pair of spheres (each of them is the same as the sphere from Fig. 6.4) separated by a gap $g = 15$ nm. It has been shown that in such a system, the modes of individual particles hybridize and form bonding and antibonding modes of the dimer [234]. In Fig. 6.5(a,b) we analyze how the hybridized modes contribute to the spectra for different beam positions.

In Fig. 6.5(a) we consider a 100-keV electron beam with $\ell = 100$ passing through the middle of the gap and calculate the EEL probability. We note that if the beam is positioned at either axis of symmetry of the dimer, the "crossed" loss probability components Γ_{e,J_m} and Γ_{m,J_e} cancel each other and we can again assign $\Gamma_e \to \Gamma_{e,J_e}$ and $\Gamma_m \to \Gamma_{m,J_m}$. Due to the interchange of electric and magnetic components of the field produced by the electric and the magnetic part of VEB current, each current component couples to different modes of the dimer. Each current component excites better the modes that possess the same field symmetry as the field produced by the respective current component. Γ_e [solid red line

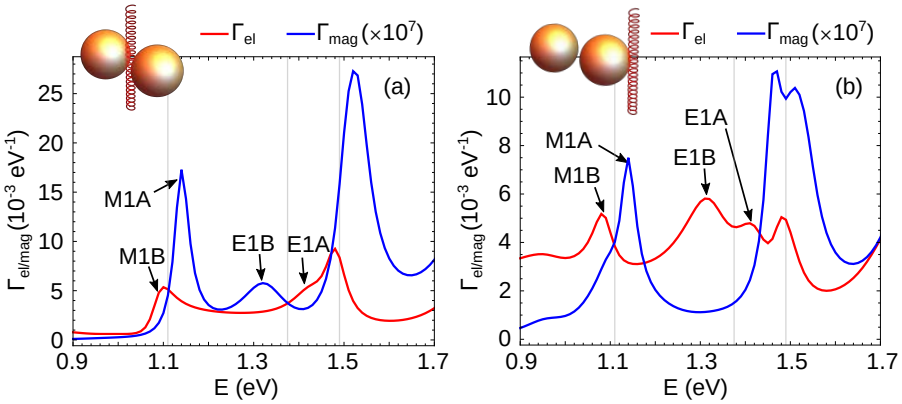

FIGURE 6.5: Numerically calculated electric-current and magnetic-current-mediated EEL probability (solid red and blue lines, Eq. (6.8) and Eq. (6.9), respectively) for a 100-keV electron beam with OAM $\ell = 100$ exciting a spherical dimer. Each sphere of radius $a = 150$ nm is made of silicon (dielectric response is taken from Ref. [154]). The gap between the spheres is $g = 15$ nm and the beam is passing either (a) through the middle of the gap or (b) by side of one of the spheres at the axis of the dimer, 7.5 nm from its surface. We also denote the peaks corresponding to the hybridized dipolar modes in a dimer: bonding and antibodingmagnetic dipole (M1B and M1A), and bonding and antibodingelectric dipole (E1B and E1A). Gray vertical lines denote spectral positions of the modes M1, E1 and M2 in EEL calculated for a single sphere (see Fig. 6.4).

in Fig. 6.5(a)] shows that the conventional beam can excite the magnetic dipolar bonding mode (M1B), the electric antibonding mode (E1A), and the bonding magnetic quadrupolar mode yielding a peak close to 1.5 eV. On the other hand, the magnetic part of the current couples to the magnetic dipolar anti-bonding mode (M1A), the electric dipolar bonding mode (E1B) and the anti-bonding magnetic quadrupolar mode (see the peak above 1.5 eV), which appears in Γ_m [solid blue line in Fig. 6.5(a)]. The energy splitting of the bonding and antibonding modes is apparent when the peak positions are compared to the spectral positions of the modes excited in the individual sphere (plotted by vertical gray lines).

When the beam is moved to the side of one of the spheres along the dimer axis [see the schematics of Fig. 6.5(b)], the electric component of the current can couple with the M1B mode, E1A mode and also E1B mode [solid red line in Fig. 6.5(b)], whereas the magnetic current component in this configuration couples only weakly to the E1B mode, so that this mode is not visible in the corresponding spectrum [solid blue line in Fig. 6.5(b)]. On the other hand, Γ_m shows a spectral feature arising from the excitation of both M1A and M1B. Interestingly, M1A is dominant with respect to M1B, whose excitation gives rise to a small shoulder below 1.1 eV.

Considering the set of hybridized dipolar modes, the conventional EELS with a $l = 0$ beam cannot excite the M1A mode, which is visible only in the loss probability Γ_m arising from the magnetic part of the current of a vortex beam. However, we note that this component is still six orders of magnitude smaller than the electric contribution for the OAM $l = 100$, and thus it would be difficult to isolate.

6.3 Photonic density of states in an infinite cylinder

Long dielectric cylindrical wires have been shown to exhibit equally interesting optical behaviour as small particles [237, 281–285]. Theoretical analysis of the interaction of fast electrons with such dielectric cylindrical waveguides suggested applications in single-photon sources [286]. Here we study the EEL probability of a VEB exciting an infinite cylindrical wire of radius R_0. We consider a geometrical arrangement as sketched in Fig. 6.6: an electron beam moving at speed v parallel to the axis of the wire at distance $b > R_0$ from the center of the cylinder. For this geometry, the retarded analytical solution of the EEL probability was presented e.g. in Ref. [116] (see Appendix A.4), which we modify to take into account the contribution to the loss experienced by the magnetic component of the current using the transformation in Eqs. (6.13). We can write these two parts of the overall loss probability of the VEB per unit length as:

$$\frac{d\Gamma_e}{dz} = \frac{d\Gamma_{e\mathbf{J}_e}}{dz}$$

$$= \frac{e^2}{2\pi^2\hbar\omega^2\varepsilon_0} \underbrace{\sum_{m=0}^{\infty} \mathrm{Re}\left\{(2-\delta_{m0})K_m(\Omega_o b)(q_z^2-q_0^2)b_e(q_z,\omega)\right\}|_{q_z=\frac{\omega}{v}}}_{\gamma_e(q_z,\omega)}, \tag{6.15}$$

$$\frac{d\Gamma_m}{dz} = \frac{d\Gamma_{m,J_m}}{dz}$$
$$= \frac{\mu_B^2 l^2 \mu_0}{2\pi^2 v^2 \hbar} \underbrace{\sum_{m=0}^{\infty} \mathrm{Re}\left\{(2-\delta_{m0})K_m(\Omega_o b)(q_z^2-q_0^2)d_m(q_z,\omega)\right\}|_{q_z=\frac{\omega}{v}}}_{\gamma_m(q_z,\omega)}, \tag{6.16}$$

where m denotes different azimuthal modes, δ_{m0} is the Kronecker delta, q_z stands for the wavevector along the axis of the cylinder which has to match the wavevector component imposed by the fast electron $q_z = \omega/v$. The dimensionless coefficients $b_e(q_z,\omega)$ and $d_m(q_z,\omega)$ are defined in Eq. (A.67) in Appendix A.4. We also define

$$\Omega_o = \sqrt{q_z^2 - q_0^2}. \tag{6.17}$$

The denominators of the coefficients b_m and d_m yield the dispersion of all the modes supported by the cylinder:

$$\begin{aligned}
&\frac{q_0^2 q_z^2 m^2}{R_0^2 \Omega_o^4 \Omega_i^2} K_m(\Omega_o R_0)^2 I_m(\Omega_i R_0)^2 (\varepsilon-1)^2 \\
&+ \left[\frac{\Omega_i}{\Omega_o} I_m(\Omega_i R_0) K_m'(\Omega_o R_0) - K_m(\Omega_o R_0) I_m'(\Omega_i R_0)\right] \\
&\times \left[\varepsilon K_m(\Omega_o R_0) I_m'(\Omega_i R_0) - \frac{\Omega_i}{\Omega_o} I_m(\Omega_i R_0) K_m'(\Omega_o R_0)\right] = 0,
\end{aligned} \tag{6.18}$$

where $I_m(x)$ and $K_m(x)$ are the modified Bessel functions of the first and the second kind, respectively, of order m, and

$$\Omega_i = \sqrt{q_z^2 - q_{in}^2}, \tag{6.19}$$

where $q_{in} = \sqrt{\varepsilon} q_0$.
In Fig. 6.6(a,b) we plot the (q_z,ω)-dependent loss probabilities γ_e and γ_m as defined in Eq. (6.15) and Eq. (6.16), respectively, for geometrical parameters $R_0 = 150$ nm and $b = 160$ nm. On top of the density plots we show dispersion curves corresponding to the guided EM modes (leaky modes above the light line given by $q_z = \omega/c$ are not shown as they are not excitable by the parallel beam)

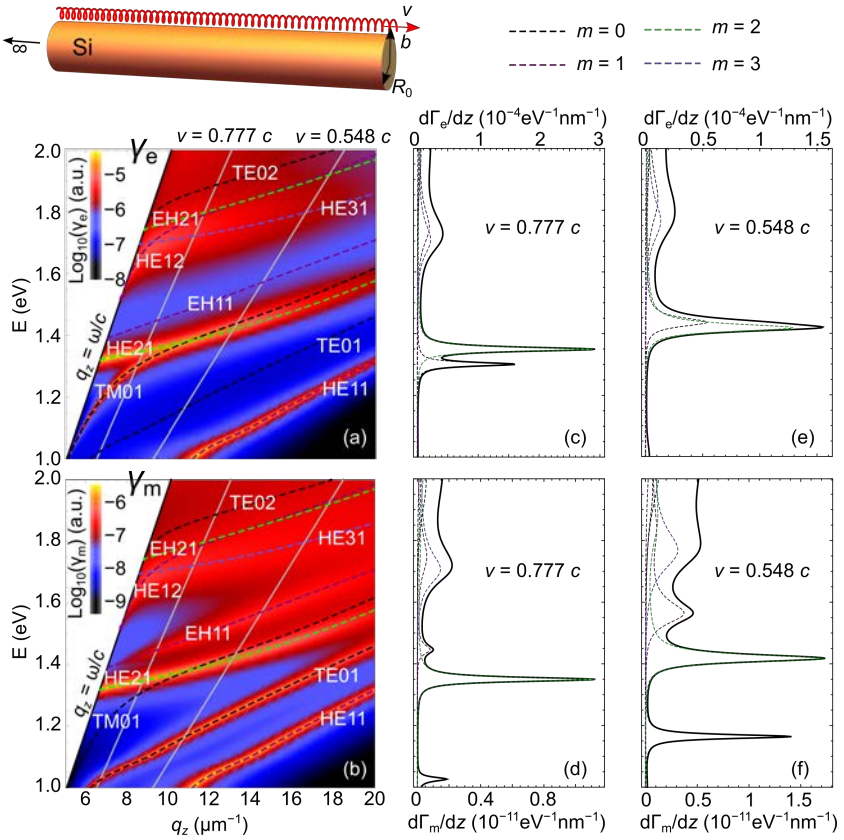

FIGURE 6.6: EEL probability calculations for an electron beam moving parallel to the axis of an infinite silicon cylinder along the z direction (see the schematics) with speed v. The radius of the cylinder is $R_0 = 150$ nm and the beam distance from the center of the cylinder is $b = 160$ nm. (a,b) Electric- and magnetic-current mediated (q_z, ω)-dependent loss probabilities γ_e from Eq. (6.15) and γ_m from (6.16) (evaluated for $l = 100$) in logarithmic color scale. Dashed lines overlaying the density plot correspond to dispersions of different azimuthal modes m from Eq. (6.18) (color coding shown in the legend). Solid gray lines show the wavevectors provided by the electron beam, $q_z = \omega/v$ for velocities $v = 0.777c$ (300-keV beam) and $v = 0.548c$ (100-keV beam). (c,d) Loss probabilities per unit trajectory corresponding to the electric current component [Eq. (6.15)] and to the magnetic current component [Eq. (6.16)] calculated for a 300-keV beam (solid black line). The dashed lines show contributions of different azimuthal components m to the spectra. (e,f) the same as (c,d) but for a 100-keV beam. For plots (a,b) we considered only the first four azimuthal modes in the summation. The total probabilities in (c-f) were calculated with $m = 0, 1, ..., 6$.

supported by the infinite cylinder obtained as solutions of Eq. (6.18) for the different orders m denoting the modes' azimuthal symmetry. We consider only the first four azimuthal numbers $m = \{0, 1, 2, 3\}$, but as higher-order modes are much more damped, we capture all the dominant spectral features. We can observe that some of the modes (denoted by using the standard notation from waveguide theory, see e.g. Refs. [287, 288]) are visible only in the electrical contribution to the spectra, γ_e [Fig. 6.6(a)] or, vice versa, in the magnetic contribution, γ_m [Fig. 6.6(b)]. We can conclude that due to the symmetry of the EM field produced by the current components, transverse electric modes (TE01, TE01,...) are excitable only by the magnetic current and on the contrary, transverse magnetic modes (TM01, TM02,...) couple only to the electric current component.

From the (q_z, ω)-dependent plots in Fig. 6.6(a,b) we can readily obtain the EEL spectra by setting $q_z = \omega/v$ [see the gray lines in Fig. 6.6(a,b)], which corresponds to the wavevector provided by the electron moving along the z direction. In Fig. 6.6(c,d) we plot $d\Gamma_{e,\mathbf{J}_e}/dz$ [Eq. (6.15)] and $d\Gamma_{m,\mathbf{J}_m}/dz$ [Eq. (6.16)], respectively, evaluated for a 300-keV electron beam ($v = 0.777c$). The total probabilities (solid black lines) are split in contributions of the different azimuthal modes $m = 0, 1, 2, 3$ denoted by the colored dashed lines. We observe that the hybrid HE21 mode produces the dominant spectral feature in both cases. On the other hand, the peak corresponding to the excitation of the TM01 mode is present only in the spectrum of Fig. 6.6(c), and the peak arising from the excitation of the TE01 mode appears only in Fig. 6.6(d).

The hybrid EH11 is also dominantly excitable by the magnetic current, and has only a negligible contribution in the electric-current-mediated spectrum, as confirmed in the field plots in Fig. 6.7 where we show the out-of-plane field components for the excitation by VEB with $l = 1$, induced by the electric current (upper row) and the magnetic current (lower row) component. We observe that at 1.45 eV where the EH11 mode appears, the typical field pattern corresponding to this mode is visible only in the plot $\mathrm{Re}[H_z]$ whereas the field pattern in $\mathrm{Re}[E_z]$ is overwhelmed by the overlap with the HE21 mode. Also, by comparing the upper row with the lower row, we find the symmetry between the fields according to Eq. (6.13).

By changing the acceleration voltage to 100 kV, we obtain the spectra in Fig. 6.6(e,f) where the same modes give rise to peaks at slightly different energies due to the change of the energy-momentum matching (higher q_z is provided at a fixed energy compared to the faster 300-keV electron).

Importantly, the EEL probability in geometries possessing translational invariance, such as in the current situation of the beam moving parallel to an infinite cylinder, can be related to the photonic local density of states (LDOS). More precisely the EEL signal obtained with a non-vortex beam in Eq. (6.15) is proportional to the Fourier component (with $q_z = \omega/v$) of the electric LDOS projected in the direction of the electron's trajectory $\rho_{e,\hat{z}}$ [289]:

$$\frac{d\Gamma_{el}(b, \omega)}{dz} \propto \frac{\rho_{e,\hat{z}}(b, q_z, \omega)}{\omega}. \tag{6.20}$$

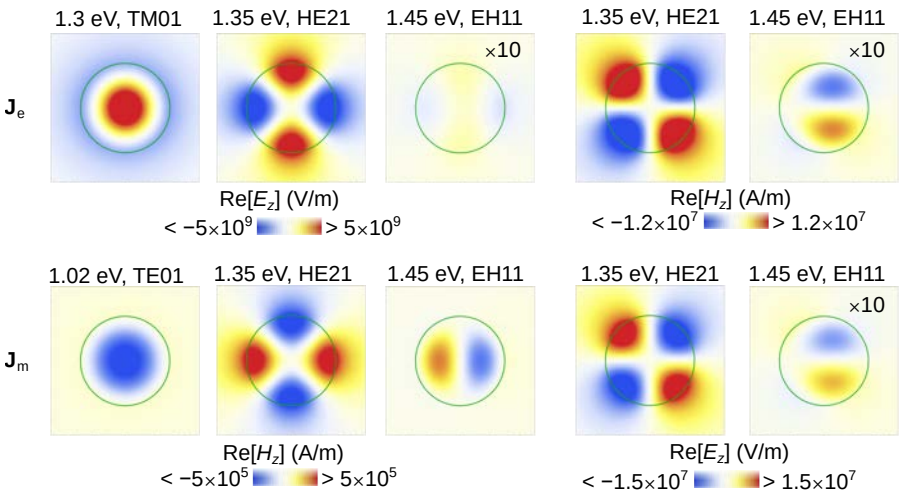

FIGURE 6.7: Real parts of out-of-plane electric and magnetic field extracted at fixed energies (as denoted above the plots) in the excitation of a dielectric cylinder with the same parameters as in Fig. 6.6 by a 300-keV VEB ($v = 0.777c$) with $l = 1$. We split the field induced in the interaction with the electric current component (upper row) and the magnetic current component (lower row). The green circles denote the boundaries of the cylinder with radius $R = 150$ nm.

The analogous proportionality holds between the magnetic-current-mediated loss $d\Gamma_m/dz$ in Eq. (6.16) and the magnetic LDOS $\rho_{e,\hat{z}}$:

$$\frac{d\Gamma_m(b,\omega)}{dz} \propto \frac{\rho_{m,\hat{z}}(b,q_z,\omega)}{\omega}, \tag{6.21}$$

and hence, our results might be used in the context of the interaction of magnetic emitters with such structures. Our results are consistent with the findings in Ref. [290] where the coupling of modes to differently oriented electric dipoles was linked to the excitation by electric/magnetic current components.

6.4 Dichroic spectroscopy with vortex electron beams

Until now, we have considered geometrical arrangements yielding zero or negligible dichroic signal, i.e. no difference in VEB-EEL spectra obtained with a beam featuring positive OAM ($l > 0$, Γ_{l+}) and negative OAM ($l < 0$, Γ_{l-}). Now we focus on a situation where a dichroic signal emerges. First we analyze the canonical case of a small dipolar particle with a combined electro-magnetic polarizability to understand the origin of the dichroism in VEB-EELS. Afterwards, we

focus on extended chirally-arranged particles (i.e., a system not possessing mirror symmetry) [291], and we show that a strong dichroic contribution can arise in spatially-resolved VEB-EELS.

6.4.1 Probing a small chiral particle

Before we proceed with the calculations of VEB-EEL spectra within the classical formalism for extended nanostructures, we show an analysis of the emergence of the dichroic signal in the interaction of the VEB with a small chiral particle, which can be e.g. a chiral molecule. The EM response of the chiral particle can be described by the combined electro-magnetic dipole polarizability $\boldsymbol{\alpha}$, which is a 6×6 tensor [270, 292]:

$$\boldsymbol{\alpha} = \begin{bmatrix} \alpha_{EE}\mathbf{I} & \alpha_{EM}\mathbf{I} \\ -\alpha_{EM}\mathbf{I} & \alpha_{MM}\mathbf{I} \end{bmatrix}, \tag{6.22}$$

where we assumed isotropic polarizabilities: electric-electric α_{EE}, magnetic-magnetic α_{MM}, and mixed electric-magnetic term α_{EM}. $\mathbf{I}$ is the 3×3 unit matrix. The EEL probability for a VEB interacting with the chiral particle can be then expressed as[3]

$$\Gamma(\omega) = \frac{1}{\pi}\mathrm{Im}\left[\begin{bmatrix}\mathbf{E}^*_{VEB}(\mathbf{r}_{dip},\omega) & \mathbf{B}^*_{VEB}(\mathbf{r}_{dip},\omega)\end{bmatrix} \cdot \boldsymbol{\alpha} \cdot \begin{bmatrix}\mathbf{E}_{VEB}(\mathbf{r}_{dip},\omega) \\ \mathbf{B}_{VEB}(\mathbf{r}_{dip},\omega)\end{bmatrix}\right], \tag{6.23}$$

where $\mathbf{r}_{dip}$ is the position of the dipolar particle, $\mathbf{E}_{VEB} = \mathbf{E}_e + \mathbf{E}_m$ is the electric field produced by the VEB with contributions from the electric current component ($\mathbf{E}_e$) and the magnetic current component ($\mathbf{E}_m$). Analogously, we can split the magnetic field of the VEB as $\mathbf{B}_{VEB} = \mathbf{B}_e + \mathbf{B}_m$. The field components [fulfilling the relationships in Eq. (6.13)] are:

$$\mathbf{E}_e(\mathbf{r},\omega) = \frac{2e\omega\, e^{i\omega z/v}}{4\pi\varepsilon_0\gamma_L v^2}\left[-K_1\left(\frac{\omega|\mathbf{R}-\mathbf{R}_b|}{\gamma_L v}\right)\frac{\mathbf{R}-\mathbf{R}_b}{|\mathbf{R}-\mathbf{R}_b|} + \frac{i}{\gamma_L}K_0\left(\frac{\omega|\mathbf{R}-\mathbf{R}_b|}{\gamma_L v}\right)\hat{\mathbf{z}}\right], \tag{6.24a}$$

$$\mathbf{B}_e(\mathbf{r},\omega) = \frac{2e\omega\, e^{i\omega z/v}}{4\pi\varepsilon_0\gamma_L v c^2}\left[-K_1\left(\frac{\omega|\mathbf{R}-\mathbf{R}_b|}{\gamma_L v}\right)\hat{\boldsymbol{\varphi}}\right], \tag{6.24b}$$

$$\mathbf{E}_m(\mathbf{r},\omega) = -\mathbf{B}_e(\mathbf{r},\omega)\frac{e_m}{e}, \tag{6.24c}$$

$$\mathbf{B}_m(\mathbf{r},\omega) = \mathbf{E}_e(\mathbf{r},\omega)\frac{e_m}{ec^2}, \tag{6.24d}$$

[3] In Chapter 5 we used a special case of this formula for $\alpha_{EM} = 0$, $\alpha_{MM} = 0$ and the excitation field of a conventional electron beam with $l = 0$, see Eq. (5.9).

where $\hat{\boldsymbol{\varphi}}$ is the azimuthal unit vector, $\hat{\mathbf{z}}$ is the unit vector along the z axis, $\mathbf{R}_b = (x_b, y_b)$ is the position of the electron beam traveling parallel to the z axis in the transverse plane, and we defined an effective magnetic charge

$$e_m = \frac{i\omega\mu_B l}{v}. \tag{6.25}$$

After some algebra we can rewrite Eq. (6.23) as

$$\begin{aligned}\Gamma(\omega) = \frac{1}{\pi}\Big\{&\mathrm{Im}\left[\alpha_{EE}\right]|\mathbf{E}_{VEB}(\mathbf{r}_{dip},\omega)|^2 + \mathrm{Im}\left[\alpha_{MM}\right]|\mathbf{B}_{VEB}(\mathbf{r}_{dip},\omega)|^2 \\ &-2\mathrm{Im}\left[\alpha_{EM}\right]\mathrm{Im}\left[\mathbf{E}^*_{VEB}(\mathbf{r}_{dip},\omega)\cdot\mathbf{B}_{VEB}(\mathbf{r}_{dip},\omega)\right]\Big\}.\end{aligned} \tag{6.26}$$

We can find that the last term in the curly brackets, proportional to the "crossed" electric-magnetic polarizability term and to the chirality of the probing field [292], is responsible for the non-zero difference between the spectra obtained for positive and negative OAM, i.e. the dichroic signal. After substitution of the EM field of the VEB, we can write this difference as

$$\Gamma_{l+} - \Gamma_{l-} = -\mathrm{Im}[\alpha_{EM}]\frac{4\omega\mu_B l}{evc^2}\left(|\mathbf{E}_e(\mathbf{r}_{dip},\omega)|^2 + |\mathbf{E}_m(\mathbf{r}_{dip},\omega)|^2\right). \tag{6.27}$$

The proportionality of the dichroic signal to $-\mathrm{Im}[\alpha_{EM}]$ holds also for optical circular dichroism (CD) [292]. However, compared to optical spectroscopy with circularly-polarized light, the local excitation by a focused VEB makes it possible to probe chiral properties of nanostructures with high spatial resolution, which is reflected in the fast decay of the signal strength with increasing distance of the beam from the particle (molecule).

6.4.2 Dichroic VEB-EELS of a chirally-arranged nanorod dimer

Now we focus on extended particles in a chiral arrangement, which we model numerically within the classical formalism described in Section 6.1. Before we start with calculations for a system with particles made of silicon, we analyze a more canonical case with a simpler modal structure. We adopt the geometry studied in Refs. [293, 294] and consider two vertically displaced gold rods that are rotated by 90° and stacked at their corners as shown in Fig. 6.8(a). As discussed in Ref. [293], such a system can be described as two coupled harmonic oscillators driven orthogonally, representing electric dipolar modes excitable in the rods.

Interestingly, this system can be understood as a plasmonic analogue of the Born-Kuhn model of optical activity in chiral media [295, 296]. The coupled rods in such an arrangement can mimic the behavior of a simple chiral molecule, and in the interaction with a circularly polarized plane wave, the overall response

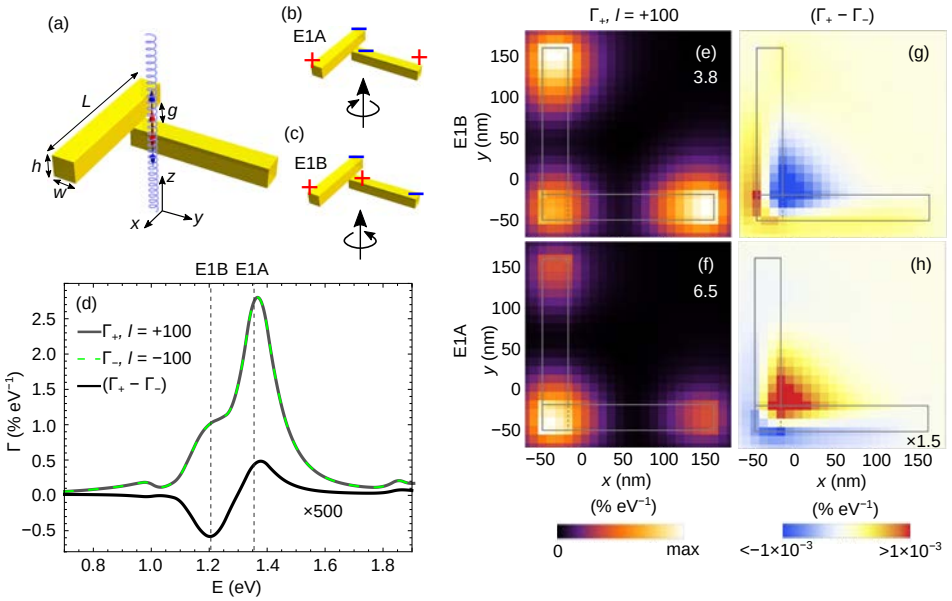

FIGURE 6.8: (a) Schematics of a plasmonic analogue of the Born-Kuhn model: two gold rods of length $L = 200$ nm, height $h = 30$ nm and width $w = 30$ nm ($h = w$), vertically displaced by 60 nm so that the gap between the rods is $g = 40$ nm. The dielectric response of gold is taken from Ref. [154]. We consider the excitation by an electron beam moving at speed $v = 0.5c$ along the z axis (stacking direction of the rods). (b) Schematic representation of the excitation of the dipole anti-bonding mode (E1A) with LCP light. (c) The electric bonding mode excited by RCP light. (d) VEB-EEL spectra $\Gamma = \Gamma_e + \Gamma_m$ calculated for a beam with $l = 100$ (Γ_+, solid gray line) and $l = -100$ (Γ_-, dashed green line). The beam is placed as shown in (a) at distance 10 nm from each rod [position $x = y = 0$ in maps (e-h)]. The difference $\Gamma_+ - \Gamma_-$ is plotted by the solid black line and multiplied by a factor of 500. (e,f) Maps of $\Gamma_+ = \Gamma_e + \Gamma_m$ as defined in Eq. (6.8) and (6.9), calculated for different (x, y) positions of the beam, at energies of (e) E1B, and (f) E1A as denoted by the vertical dashed lines in (d). Maxima of the color scale are denoted in each plot. (g,h) Energy-filtered maps of dichroic EEL signal $\Gamma_+ - \Gamma_-$ at the energy corresponding to (g) E1B and (h) E1A. The values plotted in (h) are multiplied by 1.5. The gray lines in (e-h) denote boundaries of the rods.

of the structure can be described with an effective electric and electro-magnetic polarizability [293]. As we showed in the previous section, the electro-magnetic polarizability term is responsible for the dichroic response to the excitation by a VEB and thus, we should expect the emergence of dichroism also in VEB-EEL spectra. However, the finite spatial extent of the structure might produce a non-trivial spatial dependence of the dichroic signal.

We consider similar parameters as in Ref. [293] with the gold rods of length

$L = 200$ nm, height and width $h = w = 30$ nm, with the vertical spacing $g = 40$ nm between them, as plotted in Fig. 6.8(a). The response of gold is characterized by experimental values from Ref. [154]. In Fig. 6.8(d) we plot the calculated VEB-EEL spectra for the excitation with a VEB moving at speed $v = 0.5c$ and placed as depicted in the schematics of (a), at position $x = y = 0$. In the calculations, we set $l = +100$ (Γ_+, gray solid line) or $l = -100$ (Γ_-, green dashed line). Both spectra exhibit a dominant peak at 1.35 eV corresponding to the excitation of the dipolar anti-bonding mode [denoted as E1A, see the schematics showing the symmetry of the corresponding oscillating charges in Fig. 6.8(b)] and a smaller peak at 1.2 eV, which originates from the excitation of the dipolar bonding arrangement [E1B, see Fig. 6.8(c)]. We can assign the peaks to the corresponding modes by either checking the induced field, or by analyzing the energy-filtered maps of the overall EEL signal in Fig. 6.8(e,f). Both maps exhibit three intense spots corresponding to areas where the dipolar modes can be efficiently excited in both rods, i.e. close to the rod tips [compare with results in Fig. 5.4(b,c)]. However, in the anti-bonding scenario [Fig. 6.8(f)], we observe higher absolute intensity, which is dominant close to the stacking point of the rods, and which appears due to the constructive addition of the z component of the field induced in both rods along the electron's trajectory.

Importantly, there is a small difference between the spectra Γ_+ and Γ_-, i.e. the dichroic signal, which is plotted by the black solid line in Fig. 6.8(d). Its spectral behavior shows that the VEB with $l > 0$ in the considered geometry preferentially excites the E1A mode whereas $l < 0$ couples better with the E1B mode, which produces a bisignate shape of the dichroic spectrum. The same spectral dependence can be observed in the difference between spectra acquired by exciting the structure with left-handed circularly polarized (LCP) and right-handed circularly polarized (RCP) light (see the schematics of Fig. 6.8(b,c), respectively). This can be understood by considering the rotation of the field vector components in space and time. However, compared to the interaction with an extended plane wave, the excitation of the rods with the VEB produces a complex spatial dependence of the dichroic EEL signal on the beam position. We show the theoretically predicted VEB-EEL dichroic maps in Fig. 6.8(g,h). The strongest dichroic response arises for the beam close to the stacking point of the rods, where the strongest interference and the phase difference between the fields induced at each of the rods appears.

Although the dichroic signal is two to three orders of magnitude weaker than the overall spectra, we believe that it might be experimentally detectable (with a preliminary evidence in Ref. [272]). We note that our approach assuming an infinitely focused VEB presumably underestimates the intensity of the dichroic signal. By taking into account an overlap of a realistic beam profile with the electromagnetic field in the structure (e.g., as in Refs. [269, 270]), one might expect a higher contribution of the dichroic signal to the overall loss probability, with a qualitatively similar spatial dependence.

Next we consider two dielectric cylindrical rods made of silicon arranged in

the same way, but supporting a more complex system of magnetic and electric modes. We set the length of each rod $L = 800$ nm, radius $R_0 = 80$ nm and vertical spacing between the rods $g = 30$ nm as shown in the inset of Fig. 6.9(a), and take the dielectric response of silicon from Ref. [154]. We calculate EEL spectra for the excitation by a VEB with energy 100 keV and OAM $l = \pm 100$ at different beam positions. The spectra in Fig. 6.9(a) are obtained for the beam placed in the corner between the rods, 10 nm from their boundaries, whereas in Fig. 6.9(b) the beam

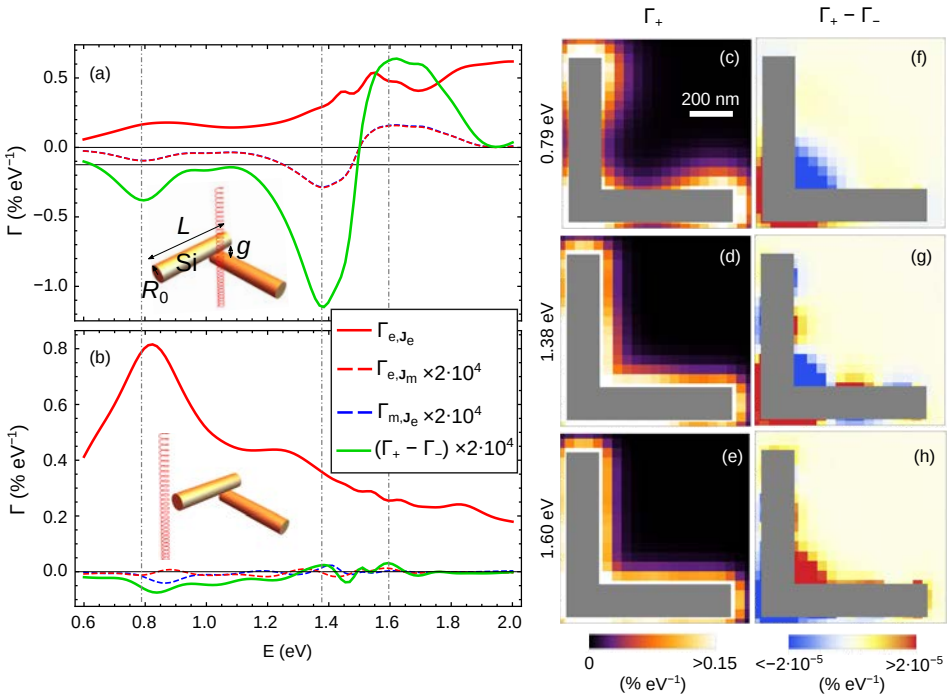

FIGURE 6.9: (a,b) VEB-EEL spectra calculated for chirally-arranged silicon rods with parameters $R_0 = 80$ nm, $L = 800$ nm, $g = 30$ nm [see the inset of (a)]. The dielectric response of silicon is taken from Ref. [154]. We consider the excitation by a 100 keV VEB with $l = +100$ and split the spectral contributions according to Eqs. (6.8) and (6.9): Γ_{e,J_e} (solid red line), Γ_{e,J_m} (dashed red line), and Γ_{m,J_e} (dashed blue line). We omit the Γ_{m,J_m} term. The green line shows VEB-EEL dichroism obtained as a difference between spectra calculated for $l = +100$ and $l = -100$. In (a) the beam is positioned according to the inset 10 nm from the surface of the rods, whereas in (b) the beam is placed 10 nm from the tip of one of the rods as depicted. (c-e) Energy-filtered maps of the total EEL for $l = +100$, and (f-h) the dichroic signal at energies marked on the left of each row. The selected energies correspond to positions of the peaks in the dichroic signal in (a). The spatial scaling is the same in all maps and the cross-section of the cylinders is plotted as gray rectangles.

is 10 nm from the tip of one of the rods (see the corresponding insets). We split the relevant spectral components as in Eqs. (6.8) and (6.9): the purely electric loss probability term $\Gamma_{e,\mathbf{J}_e}$ (solid red line), and the "crossed" electric-magnetic terms $\Gamma_{e,\mathbf{J}_m}$ (dashed red line) and $\Gamma_{m,\mathbf{J}_e}$ (dashed blue line). We do not plot the purely magnetic term $\Gamma_{m,\mathbf{J}_m}$, which is much weaker.

The modes of a sufficiently long finite silicon cylinder can be understood as standing waves along the long axis of the cylinder, formed by the different modes of an infinite cylinder that we analyzed in Section 6.3 [283, 297]. The first dominant peak in $\Gamma_{e,\mathbf{J}_e}$ close to 0.8 eV in Fig. 6.9(a,b) originates mostly from the bonding arrangement of two dipolar modes [as can be seen from the energy-filtered map in Fig. 6.9(c)] with TM01 transverse modal profile, which in this geometry couples well to the EM field of the electric current component. The second-order mode with TM01 modal profile appears around 1.3 eV [the corresponding peak is visible in Fig. 6.9(b)], but it already overlaps with an admixture of higher-order electric and magnetic modes at higher energies. Hence, the energy-filtered maps at energies 1.38 eV [Fig. 6.9(d)] and also 1.6 eV [Fig. 6.9(e)] show nearly homogeneous intensity for all beam positions close to the rod surfaces.

The spatially-resolved spectral behavior of the "crossed" loss terms $\Gamma_{e,\mathbf{J}_m}$ and $\Gamma_{m,\mathbf{J}_e}$ [dashed lines in Fig. 6.9(a,b)] and the resulting dichroic signal [$\Gamma_+ - \Gamma_-$, plotted by the solid green lines in Fig. 6.9(a,b) and in the energy-filtered maps (f-h)] shows some similarities with the previously analyzed case of two metallic rods. The high intensity of the dichroic signal is achieved close to the corner formed by the rods. The dichroic VEB-EEL spectra also flip sign depending on the structure of the local phase and the nature of the induced field along the z axis. The sign change of the dichroic signal appears in the region between 1.4 eV and 1.6 eV, where hybridized modes with TE polarization, i.e. coupled magnetic dipoles and higher-order modes polarized along the long axes of the rods, can be excited. These modes couple preferentially to the EM field of the magnetic current component, which changes its sign depending on $\mathfrak{l}$ [see Eq. (6.24)], and explains the observation. However, we note that the interpretation of spatially-resolved dichroic VEB-EELS in a general case can be rather complicated, and will require further theoretical analysis.

6.5 Summary

In this chapter we set a classical theoretical framework suitable for a qualitative modeling of vortex electron energy loss spectroscopy at optical frequencies. We calculated VEB-EEL spectra for dielectric nanostructures such as spherical particles and cylindrical wires made of silicon, possessing resonant optical modes of both electric and magnetic nature. We showed that to distinguish these modes, either EELS with a conventional beam, or with a VEB can be employed. Although our calculations predict that by using the vortex beams we achieve only a very small enhancement of the purely magnetic signal, the VEBs might be promising in probing the dichroic response of chiral structures at the nanoscale.

Conclusions and outlook

In this thesis, we theoretically described how focused electron beams interact with low-energy excitations that are of high interest in the field of nanophotonics. In particular we were dealing with optical phonons, molecular vibrations, plasmons, excitons, and optical resonant cavity modes. We used classical electrodynamics to evaluate energy loss experienced by the fast electrons due to the interaction with the aforementioned excitations, and calculated spatially-resolved electron energy loss spectra in different situations. We now summarize our findings together with some of the possible future directions:

- In Chapters 2 and 3 we described phononic excitations in infinite and truncated thin slabs. We showed that a focused electron beam, which represents a near-field probe, can couple to low-loss phonon polaritons in such nanostructures. Hence, by measuring electron energy loss spectra by state-of-the-art STEM-EELS, one can acquire spectral information on the polaritonic excitations with high spatial resolution. Furthermore, it is possible to link the spatially-resolved EEL spectra with high-resolution images, which could be used, e.g., to investigate influence of atomic- or nanoscale structural defects and inhomogeneities on the polaritonic excitations as well as on high-momenta phonons, which might be theoretically described by combining classical and quantum modeling.

- In Chapter 4 we discussed how finite temperature affects measured spectra. We showed that at elevated temperatures, one can expect emergence of both energy loss and gain peaks arising from the phononic excitations, as well as changes in the quasi-elastic peak that corresponds to electrons that have not experienced (nearly) any energy gain or loss. Importantly, it is possible to use the spectral information to extract temperature with high spatial resolution, which might find interesting applications in studying phase changes of materials or thermal conductivity at nanoscale.

- In Chapter 5 we explored different options of probing molecular excitations by fast electrons. First we presented a combined theoretical-experimental study showing that even molecules highly sensitive to radiation damage can be studied by STEM-EELS with an electron beam in aloof geometry. Then we proposed the concept of "surface-enhanced EELS" exploiting electromagnetic coupling between plasmonic antennas and molecular samples, which could enhance sensitivity of the technique to small molecular

amounts. We also expect that the coupling phenomena might appear naturally in various experiments, such as in-situ studies of catalytic reactions on metallic surfaces. In such applications, the signal enhancement could be also an important factor. From a theoretical perspective, we suggest that developing a combination of ab initio and classical models to calculate EEL spectra might be crucial to describe situations when small molecular amounts are probed, or when the molecular sample is strongly influenced by its environment (such as encapsulated water molecules that we were dealing with in this chapter).

- Chapter 6 was focused on high-refractive-index nanoparticles that support optical resonant modes of both magnetic and electric nature. We modified the classical formalism to calculate EEL spectra to explore whether vortex electron beams could be used for preferential excitation of magnetic modes. However, we found the contribution of the purely magnetic interaction to be really small. On the other hand, vortex beams are promising in probing chiral nanostructures at the nanoscale, which we demonstrated by calculating spatial variations of dichroic EEL signal.

Fast-electron spectroscopy offers many exciting possibilities for future research, and we believe that the topics discussed in this thesis can contribute to some of these emerging new directions.

Appendix A

Supplementary calculations

This appendix provides supplementary calculations related to the derivation of EEL probabilities in different geometrical arrangements, presented thorough this thesis. First we show non-retarded expressions for the loss probability of an electron passing through a uniaxial slab in Section A.1. In Section A.2 we derive both non-retarded and retarded solutions for a beam moving parallel to an infinite interface, considering anisotropy in one of the media. Section A.3 contains the coupling coefficients to evaluate the loss probability for a beam passing close to a dielectric sphere and finally, in Section A.4 we present a solution for a beam traveling parallel to the axis of an infinite cylindrical wire.

A.1 Electron passing through a uniaxial slab

A.1.1 Non-retarded approximation

If we consider an electron beam moving along the z axis and penetrating an isotropic slab of thickness d with dielectric properties defined in Section 2.2, we can express the non-retarded bulk loss probability Γ^{NR}_{bulk} (limit of Eq. (2.15) for $c \to \infty$) as:

$$\Gamma^{NR}_{bulk}(\omega) = \int_0^{Q_c} dQ\, P^{NR}_{bulk}(Q,\omega) = \int_0^{Q_c} dQ \frac{e^2 Q d}{2\pi^2 \hbar \varepsilon_0} Im\left[\frac{-1}{\varepsilon_z \omega^2 + \varepsilon_R^2 v^2}\right] \tag{A.1}$$

$$= \frac{e^2 d}{4\pi^2 \hbar \varepsilon_0 v^2} Im\left[\frac{-1}{\varepsilon_R}\right] \ln\left(1 + \frac{\varepsilon_R Q_c^2 v^2}{\varepsilon_z \omega^2}\right), \tag{A.2}$$

where e is the elementary charge, v is the speed of the electron, ε_0 is the vacuum permittivity, $Q = \sqrt{q_x^2 + q_y^2}$ is the wavevector in the perpendicular direction with respect to the electron's trajectory, Q_c is the cutoff value (maximal allowed perpendicular wavevector transfer) and ω is the frequency.

The non-retarded guided plus the Begrenzungs contribution (limit of Eq. (2.16) for $c \to \infty$) is:

$$\Gamma^{NR}_{guid+Begr}(\omega) = \int_0^{Q_c} dQ \, \frac{e^2 Q}{2\pi^2 \hbar \varepsilon_0}$$
$$\mathrm{Im}\left\{ \left[a_3(Q,\omega) \frac{e^{-d/2(Q-i\omega/\nu)}}{Q\nu - i\omega} + b_1(Q,\omega) \frac{e^{-d/2(Q+i\omega/\nu)}}{Q\nu + i\omega} \right.\right.$$
$$\left.\left. + 2\sqrt{\varepsilon_z} \left(\frac{a_2(Q,\omega) \sin\left[\frac{d\omega}{2\nu} + \frac{idQ}{2}\sqrt{\frac{\varepsilon_R}{\varepsilon_z}} \right]}{\omega\sqrt{\varepsilon_z} + iQ\nu\sqrt{\varepsilon_R}} + \frac{b_2(Q,\omega) \sin\left[\frac{d\omega}{2\nu} - \frac{idQ}{2}\sqrt{\frac{\varepsilon_R}{\varepsilon_z}} \right]}{\omega\sqrt{\varepsilon_z} - iQ\nu\sqrt{\varepsilon_R}} \right) \right] \right\}, \tag{A.3}$$

where the coefficients are:

$$a_3(Q,\omega) = \frac{t_c e^{\frac{dQ}{2} - \frac{i\omega d}{2\nu}}}{Q\left(1 - r_p^2 e^{-2Qd\sqrt{\frac{\varepsilon_R}{\varepsilon_z}}}\right)} \left[\sqrt{\varepsilon_R \varepsilon_z}\, HQ \left(1 - r_p e^{-2Qd\sqrt{\frac{\varepsilon_R}{\varepsilon_z}}} - 2t_c \right.\right.$$
$$\left.\left. \times e^{-Qd\sqrt{\frac{\varepsilon_R}{\varepsilon_z}} + \frac{i\omega d}{\nu}} \right) + \left(1 + r_p e^{-2Qd\sqrt{\frac{\varepsilon_R}{\varepsilon_z}}} - 2t_c\sqrt{\varepsilon_R\varepsilon_z} e^{-Qd\sqrt{\frac{\varepsilon_R}{\varepsilon_z}} + \frac{i\omega d}{\nu}} \right) G \right], \tag{A.4a}$$

$$b_1(Q,\omega) = \frac{t_c e^{\frac{dQ}{2} + \frac{i\omega d}{2\nu}}}{Q\left(1 - r_p^2 e^{-2Qd\sqrt{\frac{\varepsilon_R}{\varepsilon_z}}}\right)} \left[\sqrt{\varepsilon_R \varepsilon_z}\, HQ \left(1 - r_p e^{-2Qd\sqrt{\frac{\varepsilon_R}{\varepsilon_z}}} - 2t_c \right.\right.$$
$$\left.\left. \times e^{-Qd\sqrt{\frac{\varepsilon_R}{\varepsilon_z}} - \frac{i\omega d}{\nu}} \right) + \left(1 + r_p e^{-2Qd\sqrt{\frac{\varepsilon_R}{\varepsilon_z}}} - 2t_c\sqrt{\varepsilon_R\varepsilon_z} e^{-Qd\sqrt{\frac{\varepsilon_R}{\varepsilon_z}} - \frac{i\omega d}{\nu}} \right) G \right], \tag{A.4b}$$

$$a_2(Q,\omega) = \frac{t_c e^{\frac{dQ}{2}\sqrt{\frac{\varepsilon_R}{\varepsilon_z}} - \frac{i\omega d}{2\nu}}}{Q\left(1 - r_p^2 e^{-2Qd\sqrt{\frac{\varepsilon_R}{\varepsilon_z}}}\right)} \left[HQ \left(r_p e^{-2Qd\sqrt{\frac{\varepsilon_R}{\varepsilon_z}}} + e^{-Qd\sqrt{\frac{\varepsilon_R}{\varepsilon_z}} + \frac{i\omega d}{\nu}} \right) \right.$$
$$\left. + \left(e^{-Qd\sqrt{\frac{\varepsilon_R}{\varepsilon_z}} + \frac{i\omega d}{\nu}} - r_p e^{-2Qd\sqrt{\frac{\varepsilon_R}{\varepsilon_z}}} \right) G \right], \tag{A.4c}$$

$$b_2(Q,\omega) = \frac{t_c e^{\frac{dQ}{2}\sqrt{\frac{\varepsilon_R}{\varepsilon_z}} - \frac{i\omega d}{2\nu}}}{Q\left(1 - r_p^2 e^{-2Qd\sqrt{\frac{\varepsilon_R}{\varepsilon_z}}}\right)} \left[(G - HQ)\, e^{-Qd\sqrt{\frac{\varepsilon_R}{\varepsilon_z}}} - (G + HQ) \right.$$
$$\left. \times r_p e^{-2Qd\sqrt{\frac{\varepsilon_R}{\varepsilon_z}} + \frac{id\omega}{\nu}} \right], \tag{A.4d}$$

and where we defined

$$H = v\left(\frac{1}{\omega^2+Q^2v^2}-\frac{1}{\omega^2\varepsilon_z+Q^2v^2\varepsilon_R}\right), \tag{A.5a}$$

$$G = i\omega\left(\frac{1}{\omega^2+Q^2v^2}-\frac{\varepsilon_z}{\omega^2\varepsilon_z+Q^2v^2\varepsilon_R}\right), \tag{A.5b}$$

$$r_p = \frac{\sqrt{\varepsilon_R\varepsilon_z}-1}{\sqrt{\varepsilon_R\varepsilon_z}+1}, \tag{A.5c}$$

$$t_c = \frac{1}{\sqrt{\varepsilon_R\varepsilon_z}+1}. \tag{A.5d}$$

A.1.2 Thin film limit

If we now consider the limiting case of very thin slab, so that $\omega d/v \approx 0$, we find that we can neglect the contribution of the bulk and the Begrenzungs term. The $(Q-\omega)$ dependent guided loss term is then written as

$$P_{guid}(Q,\omega) \approx \frac{e}{\pi^2\hbar v}\frac{Q^2v^2}{(Q^2v^2+\omega^2)^2} \times \mathrm{Im}\left[\frac{\sqrt{\varepsilon_R\varepsilon_z}\left(1-r_p e^{-2\sqrt{\frac{\varepsilon_R}{\varepsilon_z}}Qd}-2t_c e^{-\sqrt{\frac{\varepsilon_R}{\varepsilon_z}}Qd}\right)}{\left(1+\sqrt{\varepsilon_R\varepsilon_z}\right)\left(1-r_p^2 e^{-2\sqrt{\frac{\varepsilon_R}{\varepsilon_z}}Qd}\right)}\right]. \tag{A.6}$$

By further noticing that for large $|\varepsilon_R|$ or $|\varepsilon_z|$ (which is valid in the RBs), we have $r_p \approx \sqrt{\varepsilon_R\varepsilon_z}/(1+\sqrt{\varepsilon_R\varepsilon_z}) \sim 1$ and $t_c \sim 0$, which yields

$$P^{NR}_{guid}(Q,\omega) \approx \frac{e}{\pi^2\hbar v}\frac{Q^2v^2}{(Q^2v^2+\omega^2)^2}\mathrm{Im}\left[R_p\right], \tag{A.7}$$

where R_p is the (quasistatic) reflection coefficient from an anisotropic slab [68]

$$R_p = \frac{r_p\left(1-e^{-2Qd\sqrt{\frac{\varepsilon_R}{\varepsilon_z}}}\right)}{1-r_p^2 e^{-2Qd\sqrt{\frac{\varepsilon_R}{\varepsilon_z}}}}. \tag{A.8}$$

The poles of the reflection coefficient results in the quasistatic dispersion of the guided modes as shown in Eq. (2.18).

For thin samples and relatively low momenta, we have $Qd \ll 1$ which means that the leading term in the Taylor expansion of the numerator of Eq. (A.8) is

$2Qdr_p\sqrt{\varepsilon_R/\varepsilon_z} \propto Q$. We can then pull the factor Q out of R_p and define the function $F(Q,\omega)$

$$F(Q,\omega) = \frac{e}{\pi^2\hbar v}\frac{Q^3v^2}{(Q^2v^+\omega^2)^2}, \tag{A.9}$$

yielding

$$P^{NR}_{guid} \approx F(Q,\omega)\mathrm{Im}\left[Q^{-1}R_p(Q,\omega)\right]. \tag{A.10}$$

To evaluate Γ_{guid}, one can formally employ the pole approximation:

$$\Gamma_{guid} = \int dQ P^{NR}_{guid}(Q,\omega) = 2\pi i\sum_n \mathrm{Res}\left[P^{NR}_{guid}(Q,\omega)\right]_{Q=Q_n(\omega)}, \tag{A.11}$$

where $Q = Q_n(\omega)$ represents the dispersion of the guided mode given by Eq. (2.18) (with n being the mode index). By plugging Eq. (A.10) into Eq. (A.11), the residue is then directly proportional to $F(Q_n(\omega),\omega)$ (for each fixed frequency ω). Since $\max[F(Q,\omega)]$ occurs when $Q = Q_{max}(\omega) = \sqrt{3}\omega/v$, the peak position will arise for

$$\frac{\sqrt{3}\omega_{max}}{v} = Q_n(\omega_{max}), \tag{A.12}$$

as demonstrated in the inset of Fig. 2.5(a).

A.2 Electron passing parallel to an infinite interface

A.2.1 Non-retarded solution for (anisotropic) interface

If we adapt the geometrical arrangement of Fig. 1.5(a) with an electron moving in a medium characterized by dielectric function ε_1 along the z axis parallel to an interface with medium characterized by ε_2, due to the symmetry it is advantageous to rewrite the electron energy loss probability from Eq. (1.28) in terms of the Fourier-transformed field in (q_y, q_z) coordinates (with q_y and q_z the wavevector components in the y and z directions, respectively). We will now consider the non-retarded approximation (the speed of light $c \to \infty$), where we obtain the loss probability per unit trajectory in the terms of the electrostatic potential Φ[1]:

$$\frac{d\Gamma(\omega)}{dz} = \frac{2e}{(2\pi)^3\hbar\omega}\int_{-\infty}^{\infty} dq_z \int_{-\infty}^{\infty} dq_y \, \mathrm{Im}\left\{q_z \Phi_1^{\mathrm{ind}}(b, q_y, q_z, \omega)\exp\left[i(q_z z - \omega z/v)\right]\right\}, \tag{A.13}$$

where Φ_1^{ind} is the induced potential in the medium where the electron is moving at speed v, evaluated at the position of the electron along the x axis, $x_b = b$.

Now we need to solve for the induced electrostatic potential. If we consider a general case of the potential in an unbounded anisotropic medium in a presence of a localized charge source (as the electron beam), the potential is obtained from the transformed Poisson's equation:[2]

$$\mathrm{FT}\left\{\nabla\cdot\left[\overleftrightarrow{\varepsilon}\nabla\Phi(\mathbf{r},t)\right]\right\} = \frac{e}{\varepsilon_0}\mathrm{FT}\{\delta\left[\mathbf{r}-\mathbf{r}_b(t)\right]\} \tag{A.15a}$$

$$\varepsilon_x\frac{d^2\Phi}{dx^2} - (\varepsilon_y q_y^2 + \varepsilon_z q_z^2)\Phi = \frac{2\pi e}{\varepsilon_0 v}\delta\left(q_z - \frac{\omega}{v}\right)\delta(x-b), \tag{A.15b}$$

where ε_0 is the vacuum permitivity, and the anisotropic medium is characterized by a dielectric tensor $\overleftrightarrow{\varepsilon} = \mathrm{diag}(\varepsilon_x, \varepsilon_y, \varepsilon_z)$. To account for the material interface present at $x = 0$, we rewrite Eq. (A.15b) separately for two half-spaces ($\Phi(x >$

[1] The electrostatic potential is defined as $\mathbf{E} = -\nabla\Phi$.

[2] The Fourier transform of the potential and the moving charge is:

$$\Phi(\mathbf{r},t) = \frac{1}{(2\pi)^3}\iint dq_z dq_y \int d\omega\ \Phi(x, q_y, q_z, \omega)\exp\left[i(q_z z + q_y y - \omega t)\right], \tag{A.14a}$$

$$e\delta(x-b)\delta(y)\delta(z-vt) = \frac{1}{(2\pi)^3}\iint dq_z dq_y \int d\omega \frac{2\pi e}{v}\delta\left(q_z - \frac{\omega}{v}\right)\delta(x-b). \tag{A.14b}$$

$0) = \Phi_1$ and $\Phi(x < 0) = \Phi_2$) and assume that the electron is moving in the isotropic medium ε_1 parallel to the anisotropic material $\overleftrightarrow{\varepsilon_2} = \mathrm{diag}(\varepsilon_x, \varepsilon_y, \varepsilon_z)$:

$$\frac{d^2\Phi_1}{dx^2} - (q_y^2 + q_z^2)\Phi_1 = \frac{2\pi e}{\varepsilon_0\varepsilon_1 v}\delta\left(q_z - \frac{\omega}{v}\right)\delta(x-b), \tag{A.16a}$$

$$\varepsilon_x\frac{d^2\Phi_2}{dx^2} - (\varepsilon_y q_y^2 + \varepsilon_z q_z^2)\Phi_2 = 0. \tag{A.16b}$$

The solutions for the potential in both half-spaces vanishing at infinity are, after applying the boundary condition at the interface ($x = 0$)[3]:

$$\Phi_1 = \frac{\pi e\delta\left(q_z - \frac{\omega}{v}\right)}{\varepsilon_0\varepsilon_1 v\alpha_0}\left[\frac{\varepsilon_x\alpha - \varepsilon_1\alpha_0}{\varepsilon_x\alpha + \varepsilon_1\alpha_0}\exp\left[-\alpha_0(x+b)\right] - \exp(-\alpha_0|x-b|)\right], \tag{A.18a}$$

$$\Phi_2 = \frac{-2\pi e\delta\left(q_z - \frac{\omega}{v}\right)}{\varepsilon_0 v(\varepsilon_x\alpha + \varepsilon_1\alpha_0)}\exp(-\alpha_0 b)\exp(\alpha x), \tag{A.18b}$$

where we denoted

$$\alpha(q_y, q_z) = \sqrt{\frac{\varepsilon_z}{\varepsilon_x}q_z^2 + \frac{\varepsilon_y}{\varepsilon_x}q_y^2}, \qquad \alpha_0(q_y, q_z) = \sqrt{q_z^2 + q_y^2}. \tag{A.19}$$

The EEL probability is found by substituting the potential Eq. (A.18a) in Eq. (A.13) and performing the integration over q_z:

$$\frac{d\Gamma(\omega)}{dz} = \frac{2e^2}{(2\pi)^2\hbar v^2\varepsilon_0}\int_0^\infty dq_y\ \mathrm{Im}\left\{-\frac{1}{\varepsilon_1\alpha_0'} + \left[-\frac{2}{\varepsilon_x\alpha' + \varepsilon_1\alpha_0'} + \frac{1}{\varepsilon_1\alpha_0'}\right]\exp(-\alpha_0' 2b)\right\} \tag{A.20}$$

where $\alpha' = \alpha(q_y, \omega/v)$ and $\alpha_0' = \alpha_0(q_y, \omega/v)$.[4]

If both media are isotropic, i.e. we have $\alpha' = \alpha_0'$, the integration in Eq. (A.20) over the q_y wavevector can be carried out analytically [108]:

[3] The boundary conditions require continuity at the interface:

$$\Phi_1(x=0) = \Phi_2(x=0), \qquad \varepsilon_1\frac{d\Phi_1}{dx}\bigg|_{x=0} = \varepsilon_x\frac{d\Phi_2}{dx}\bigg|_{x=0}. \tag{A.17}$$

[4] Similarly, we can arrive to the EEL probability for the electron traveling in the anisotropic medium with the medium 2 being isotropic:

$$\frac{d\Gamma(\omega)}{dz} = \frac{2e^2}{(2\pi)^2\hbar v^2\varepsilon_0}\int_0^\infty dq_y\ \mathrm{Im}\left\{-\frac{1}{\varepsilon_x\alpha'} + \left[-\frac{2}{\varepsilon_x\alpha' + \varepsilon_2\alpha_0'} + \frac{1}{\varepsilon_x\alpha'}\right]\exp\left(-\alpha' 2b\right)\right\}. \tag{A.21}$$

$$\frac{d\Gamma(\omega)}{dz} = \frac{2e^2}{(2\pi)^2\hbar v^2\varepsilon_0}\mathrm{Im}\left\{-\frac{\ln(2q_{y,c}v/\omega)}{\varepsilon_1} + K_0\left(\frac{2\omega b}{v}\right)\left[-\frac{2}{\varepsilon_2+\varepsilon_1}+\frac{1}{\varepsilon_1}\right]\right\}, \tag{A.22}$$

where K_m is the modified Bessel function of the second kind of order m, which is the expression used in Section 3.1.1. The interface contribution (the second term in the curly bracket) was integrated up to $q_y \to \infty$, but we applied the cutoff for the bulk losses $q_{y,c}$ to prevent the divergence for large momenta, and further assuming $q_{y,c} \ll \omega/v$. We note that the scattering in the x direction is implicitly integrated up to infinity.

A.2.2 Retarded solution

We will consider the same geometry as in the previous section, but now we derive the fully retarded solution of the loss probability. We start from the inhomogeneous wave equation for the (total) electric field $\mathbf{E}$:

$$\nabla(\nabla\cdot\mathbf{E}) - \nabla^2\mathbf{E} = -\mu_0\left(\frac{\partial \mathbf{J}_e}{\partial t} + \varepsilon_0 \overleftrightarrow{\varepsilon}\cdot\frac{\partial^2\mathbf{E}}{\partial t^2}\right), \tag{A.23}$$

where μ_0 is the vacuum permeability and $\mathbf{J}_e$ is the electric current density corresponding to the fast electron. The Fourier transformation of the wave equation (A.23) from the (x, y, z, t) domain to the (x, q_y, q_z, ω) domain supplied by the transformed Gauss's law

$$\frac{\partial E_x}{\partial x} = \frac{\rho_F}{\varepsilon_0\varepsilon_x} - \frac{\varepsilon_z}{\varepsilon_x} i q_z E_z - \frac{\varepsilon_y}{\varepsilon_x} i q_y E_y \tag{A.24}$$

yields the equations written for the electric field components:

$$\left(-\frac{\varepsilon_z}{\varepsilon_R}q_z^2 - q_y^2 + \varepsilon_z\frac{\omega^2}{c^2} + \frac{\partial^2}{\partial x^2}\right)E_z = -\mu_0 i\omega\rho_F v + i q_z\frac{\rho_F}{\varepsilon_0\varepsilon_R}, \tag{A.25a}$$

$$\left(-q_z^2 - q_y^2 + \varepsilon_R\frac{\omega^2}{c^2} + \frac{\partial^2}{\partial x^2}\right)E_y + q_z q_y E_z\left(1-\frac{\varepsilon_z}{\varepsilon_R}\right) = i q_y\frac{\rho_F}{\varepsilon_0\varepsilon_R}, \tag{A.25b}$$

$$\left(-q_z^2 - q_y^2 + \varepsilon_R\frac{\omega^2}{c^2} + \frac{\partial^2}{\partial x^2}\right)E_x - \frac{\partial}{\partial x}\left(i q_z E_z\left(1-\frac{\varepsilon_z}{\varepsilon_R}\right) + \frac{\rho_F}{\varepsilon_0\varepsilon_R}\right) = 0, \tag{A.25c}$$

where we assumed the symmetry $\varepsilon_x = \varepsilon_y = \varepsilon_R$. $c = 1/\sqrt{\mu_0\varepsilon_0}$ is the speed of light and $\rho_F = \mathbf{J}_e/v$ is the free charge density, which is expressed for the moving electron (the source) as:

$$\rho_F = -2\pi e\delta(x-b)\delta(\omega - q_z v). \tag{A.26}$$

We now consider the electron moving in an isotropic medium characterized by ε_1 parallel to the anisotropic neighboring medium and solve the set of Eqs. (A.25) separately in both media (requiring finiteness at infinity):

$$E_{z1} = A_1 \exp(-x\alpha_{el}) + \frac{\pi i e \delta(\omega - q_z v)}{\alpha_{el}} \left(-\mu_0 \omega v + \frac{q_z}{\varepsilon_0 \varepsilon_1} \right) \exp\left(-\alpha_{el}|x-b|\right), \tag{A.27a}$$

$$E_{y1} = B_1 \exp(-x\alpha_{el}) + \frac{\pi i e \delta(\omega - q_z v)}{\alpha_0} \frac{q_y}{\varepsilon_0 \varepsilon_1} \exp\left(-\alpha_{el}|x-b|\right), \tag{A.27b}$$

$$E_{x1} = C_1 \exp(-x\alpha_{el}) - \operatorname{sgn}(x-b) \frac{\pi e \delta(\omega - q_z v)}{\varepsilon_0 \varepsilon_1} \exp(-\alpha_{el}|x-b|) \tag{A.27c}$$

$$E_{z2} = A_2 \exp(x\alpha_{2,A}), \tag{A.27d}$$

$$E_{y2} = B_2 \exp(x\alpha_{2,B}) + \frac{q_z q_y A_2 \exp(x\alpha_{2,A}) \left(\frac{\varepsilon_\parallel}{\varepsilon_\perp} - 1 \right)}{\alpha_{2,A}^2 - \alpha_{2,B}^2}, \tag{A.27e}$$

$$E_{x2} = C_2 \exp(x\alpha_{2,B}) - \frac{i\alpha_{2,A} q_z A_2 \exp(x\alpha_{2,A}) \left(\frac{\varepsilon_\parallel}{\varepsilon_\perp} - 1 \right)}{\alpha_{2,A}^2 - \alpha_{2,B}^2}, \tag{A.27f}$$

where we denoted

$$\alpha_{el}^2 = q_z^2 + q_y^2 - \varepsilon_1 \frac{\omega^2}{c^2}, \tag{A.28a}$$

$$\alpha_{2,A}^2 = \frac{\varepsilon_z}{\varepsilon_R} q_z^2 + q_y^2 - \varepsilon_z \frac{\omega^2}{c^2}, \tag{A.28b}$$

$$\alpha_{2,B}^2 = q_z^2 + q_y^2 - \varepsilon_R \frac{\omega^2}{c^2}. \tag{A.28c}$$

To find the unknown coefficients, we use the boundary conditions at the interface

$$E_{x1}(x=0) = \varepsilon_R E_{x2}(x=0), \tag{A.29a}$$

$$E_{z1}(x=0) = E_{z2}(x=0), \tag{A.29b}$$

$$E_{y1}(x=0) = E_{y2}(x=0), \tag{A.29c}$$

$$B_{x1}(x=0) = B_{x2}(x=0), \tag{A.29d}$$

$$B_{y1}(x=0) = B_{y2}(x=0), \tag{A.29e}$$

$$B_{z1}(x=0) = B_{z2}(x=0), \tag{A.29f}$$

where the magnetic field is

$$B_z = -\frac{i}{\omega}\left(iq_y E_x - \frac{\partial E_y}{\partial x}\right), \tag{A.30a}$$

$$B_y = -\frac{i}{\omega}\left(\frac{\partial E_z}{\partial x} - iq_z E_x\right), \tag{A.30b}$$

$$B_x = \frac{1}{\omega}\left(q_z E_y - q_y E_z\right), \tag{A.30c}$$

which provides six equations with one of them being redundant. However, the Gauss's law (A.24) yields another independent equation:

$$E_{y2} = \frac{i}{q_y}\frac{\partial E_{x2}}{\partial x} - \frac{q_z}{q_y}\frac{\varepsilon_z}{\varepsilon_R}E_{z2}. \tag{A.31}$$

After solving the system of Eqs. A.29 and (A.31), the loss probability can be obtained by substituting $E_{z1}(x = b)$ in Eq. (1.28) (with use of the Fourier transform in the (y, z) coordinates).

A.2.3 Coefficients in the isotropic case

As an example, we present here the coefficients for the simplest case, when the electron is moving in vacuum, i.e. $\varepsilon_1 = 1$ and when the medium 2 is isotropic, characterized by the dielectric response ε_2, $a_2 = 0$, $\alpha_{2,A} = \alpha_{2,B} = \alpha_2$:

$$A_1 = \frac{iK\left[2q_y^2 q_z(1-\varepsilon_2) + (q_z - \omega v/c^2)\left[(1-\varepsilon_2)(\alpha_2\alpha_{el} + 2q_z^2) - (\alpha_2^2 - \varepsilon_2\alpha_{el}^2)\right]\right]}{\varepsilon_0\alpha_{el}\left(\alpha_{el}+\alpha_2\right)\left(\alpha_2 + \varepsilon_2\alpha_{el}\right)}, \tag{A.32}$$

$$A_2 = \frac{i2K\left[q_z\alpha_2(\alpha_2 + \alpha_{el}) - \omega v/c^2\left[\alpha_{el}\left(\alpha_2 + \varepsilon_2\alpha_{el}\right) + q_z^2(1-\varepsilon_2)\right]\right]}{\varepsilon_0\alpha_{el}\left(\alpha_{el}+\alpha_2\right)\left(\alpha_2 + \varepsilon_2\alpha_{el}\right)}, \tag{A.33}$$

$$B_1 = \frac{-iKq_y\left[-\alpha_{el}\alpha_2 + (\varepsilon_2 - 1)(q_y^2 + q_z^2 - 2\omega v q_z/c^2) + \alpha_2\alpha_{el}\varepsilon_2\right]}{\varepsilon_0\alpha_{el}\left(\alpha_{el}+\alpha_2\right)\left(\alpha_2 + \varepsilon_2\alpha_{el}\right)}, \tag{A.34}$$

$$B_2 = \frac{i2Kq_y\left[\alpha_2\alpha_{el} + \alpha_2^2 + (\varepsilon_2 - 1)\,q_z\omega v/c^2\right]}{\varepsilon_0\alpha_{el}\left(\alpha_{el}+\alpha_2\right)\left(\alpha_2 + \varepsilon_2\alpha_{el}\right)}, \tag{A.35}$$

$$C_1 = \frac{K\left[-\alpha_2\alpha_{el} + \varepsilon_2\left(q_y^2 + \omega^2/c^2 - 2\omega v q_z/c^2\right)\right]}{\varepsilon_0\alpha_{el}\left(\alpha_2 + \varepsilon_2\alpha_{el}\right)}, \tag{A.36}$$

$$C_2 = \frac{2K\left(q_z^2 + q_y^2 - \omega v q_z/c^2\right)}{\varepsilon_0\alpha_{el}\left(\alpha_2 + \varepsilon_2\alpha_{el}\right)}, \tag{A.37}$$

where $K = e\delta(\omega - q_z v)$. The loss probability per unit path is then after substituting Eq. (A.32) in Eq. (A.27a) and subsequently to Eq. (1.28) given by Eq. (3.1).

A.3 Electron interacting with a dielectric sphere

The analytical solution for the geometry in Fig. 1.5(c) – the electron beam passing by a dielectric sphere of radius a in a non-penetrating configuration – was originally obtained in the non-retarded approximation [113, 187], but later derived also including retardation effects in Ref. [112]. The solution exploits the multipole expansion and by matching the field components on the sphere boundary, we can obtain closed expressions for the induced electromagnetic field and also for the loss probability, which can be split in a contribution from the magnetic and the electric modes as shown in Eq. (6.10) with the electric and magnetic Mie coefficients [Eqs. (6.11) and (6.12)].

The coefficients reflecting the coupling of the magnetic and electric modes with the field of the fast electrons $C^{M}_{n,m}$ and $C^{E}_{n,m}$, respectively, are given by:

$$C^{M}_{n,m} = \frac{1}{n(n+1)} \left| \frac{2m\nu}{c} A^{+}_{n,m} \right|^2 \qquad C^{E}_{n,m} = \frac{1}{n(n+1)} \left| \frac{1}{\gamma_L} B_{n,m} \right|^2, \tag{A.38}$$

where (n, m) are mode indices, $\gamma_L = 1/\sqrt{1-\nu^2/c^2}$ is the Lorentz contraction factor, ν is speed of the electron, c is the speed of light in vacuum,

$$B_{n,m} = A^{+}_{n,m+1}\sqrt{(n+m+1)(n-m)} - A^{+}_{n,m-1}\sqrt{(n-m+1)(n+m)} \tag{A.39}$$

and

$$A^{+}_{n,m} = \frac{1}{(\nu/c)^{n+1}} \sum_{j=m}^{n} \sqrt{\frac{2n+1}{4\pi}\frac{(n-m)!}{(n+m)!}} \times \frac{i^{n-j}(2n+1)!!}{\gamma^j 2^j (n-j)![(j-m)/2]![(j+m)/2]!} I^{n,m}_{j,n-j}, \tag{A.40}$$

with a restriction of the summation for even $j+m$ integers, where

$$I^{n,m}_{i_1,i_2} = \int_{-1}^{1} \mu^{i_2}(1-\mu^2)^{\frac{i_1}{2}} P^{m}_{n}(\mu) d\mu, \tag{A.41}$$

with $P^{m}_{n}(x)$ Legendre functions. To evaluate Eq. (A.41) for different n, m, we can utilize recurrence relationships for $I^{l,m}_{i_1,i_2}$ with index $n > m$

$$(n-m)I^{n,m}_{i_1,i_2} = (2n-1)I^{n-1,m}_{i_1,i_2+1} - (n+m-1)I^{n-2,m}_{i_1,i_2}. \tag{A.42}$$

The initial values of the recurrence are

$$I^{m-1,m}_{i_1,i_2} = 0 \tag{A.43a}$$

$$I^{m,m}_{i_1,i_2} = \begin{cases} (-1)^m (2m-1)!! B\left(\frac{i_1+m+2}{2}, \frac{i_2+1}{2}\right), & \text{if } i_2 \text{ is even} \\ 0, & \text{if } i_2 \text{ is odd,} \end{cases} \tag{A.43b}$$

where $B(x,y)$ is the beta function.

In the nonrelativistic limit, when $c \to \infty$, and considering the small sphere limit ($ka \ll 1$) the contribution from the magnetic modes vanishes and the loss probability from Eq. (6.10) can be simplified to [112, 113]

$$\Gamma_{\text{sph,NR}} = \frac{e^2 4a}{4\pi^2 \varepsilon_0 \hbar v^2} \sum_{n=1}^{\infty} \sum_{m=-n}^{n} \left(\frac{\omega a}{v}\right)^{2l} \frac{n}{(n-m)!(n+m)!} \times K_m^2\left(\frac{\omega b}{v}\right) \operatorname{Im}\left\{\frac{\varepsilon - 1}{n\varepsilon + n + 1}\right\}, \tag{A.44}$$

where b is the impact parameter (the closest distance of the beam from the sphere center).

We can also consider the dipolar limit, when we retain only the $n = 1$ mode contribution:

$$\Gamma_{\text{dip}} = \frac{4\omega^2 a^3}{\pi v^4 \gamma^2} \operatorname{Im}\left[\frac{\varepsilon - 1}{\varepsilon + 1}\right] \left[K_1^2\left(\frac{\omega b}{v\gamma}\right) + K_0^2\left(\frac{\omega b}{v\gamma}\right)\right]. \tag{A.45}$$

A.4 Electron interacting with a dielectric cylinder

We adapt the expressions from Ref. [116] for the electromagnetic field expressed in cylindrical coordinates (R, ϕ, z) for an electron beam moving in vacuum, parallel to an infinite dielectric cylinder along the z axis. The cylinder has a radius R_0 and the electron beam is positioned at radial distance $b > R_0$ from the center of the cylinder as shown in Fig. 6.6.

The electric and magnetic field components, produced by the fast electron moving in vacuum, in cylindrical coordinates, and Fourier-transformed in the q_z space are:

$$E_{el,z}(R,\phi,q_z,\omega) = \frac{i\omega e}{v^2\varepsilon_0}(1-v^2/c^2)\delta(\omega/v-q_z) \times \sum_{m=-\infty}^{\infty}\left[K_m(R\Omega)I_m(b\Omega)H(R-b)+K_m(b\Omega)I_m(R\Omega)H(b-R)\right]e^{im\phi}, \quad (A.46)$$

$$E_{el,R}(R,\phi,q_z,\omega) = \frac{\Omega e}{v\varepsilon_0}\delta(\omega/v-q_z) \times \sum_{m=-\infty}^{\infty}\left[K'_m(R\Omega)I_m(b\Omega)H(R-b)+K_m(b\Omega)I'_m(R\Omega)H(b-R)\right]e^{im\phi}, \quad (A.47)$$

$$E_{el,\phi}(R,\phi,q_z,\omega) = \frac{i\omega e}{v\varepsilon_0}\delta(\omega/v-q_z) \times \sum_{m=-\infty}^{\infty}\frac{m}{R}\left[K_m(R\Omega)I_m(b\Omega)H(R-b)+K_m(b\Omega)I_m(R\Omega)H(b-R)\right]e^{im\phi}, \quad (A.48)$$

$$H_{el,z}(R,\phi,q_z,\omega) = 0, \quad (A.49)$$

$$H_{el,R}(R,\phi,q_z,\omega) = -ie\delta(\omega/v-q_z) \times \sum_{m=-\infty}^{\infty}\left[K_m(R\Omega)I_m(b\Omega)H(R-b)+K_m(b\Omega)I_m(R\Omega)H(b-R)\right]e^{im\phi}, \quad (A.50)$$

$$H_{el,\phi}(R,\phi,q_z,\omega) = \Omega e\delta(\omega/v-q_z) \times \sum_{m=-\infty}^{\infty}\left[K'_m(R\Omega)I_m(b\Omega)H(R-b)+K_m(b\Omega)I'_m(R\Omega)H(b-R)\right]e^{im\phi}, \quad (A.51)$$

where e is the elementary charge, c is the speed of light, v is the speed of the electron, ω is the frequency, and ε_0 is the vacuum permittivity. $I_m(x)$ and $K_m(x)$ are the modified Bessel functions of the first and the second kind, respectively, of order m, and $H(x)$ is the Heaviside step function. We also defined

$$\Omega = \omega/v\sqrt{1-v^2/c^2}. \quad (A.52)$$

The components of the induced electric and magnetic field inside the cylinder ($R < R_0$) characterized by a dielectric function ε are:

$$E_{in,z}(R,\phi,q_z,\omega) = \sum_{m=-\infty}^{\infty} -\kappa_i^2 a_m I_m(\kappa_i R) e^{im\phi}, \tag{A.53}$$

$$E_{inR}(R,\phi,q_z,\omega) = \sum_{m=-\infty}^{\infty} \left[iq_z\kappa_i a_m I'_m(\kappa_i R) - \frac{\omega\mu_0 m}{R} c_m I_m(\kappa_i R) \right] e^{im\phi}, \tag{A.54}$$

$$E_{in,\phi}(R,\phi,q_z,\omega) = \sum_{m=-\infty}^{\infty} \left[-\frac{mq_z}{R} a_m I_m(\kappa_i R) - i\omega\mu_0\kappa_i c_m I'_m(\kappa_i R) \right] e^{im\phi}, \tag{A.55}$$

$$H_{in,z}(R,\phi,q_z,\omega) = \sum_{m=-\infty}^{\infty} -\kappa_i^2 c_m I_m(\kappa_i R) e^{im\phi}, \tag{A.56}$$

$$H_{in,R}(R,\phi,q_z,\omega) = \sum_{m=-\infty}^{\infty} \left[\frac{m\omega\varepsilon\varepsilon_0}{R} a_m I_m(\kappa_i R) + iq_z\kappa_i c_m I'_m(\kappa_i R) \right] e^{im\phi}, \tag{A.57}$$

$$H_{in,\phi}(R,\phi,q_z,\omega) = \sum_{m=-\infty}^{\infty} \left[i\omega\varepsilon\varepsilon_0\kappa_i a_m I'_m(\kappa_i R) - \frac{mq_z}{R} c_m I_m(\kappa_i R) \right] e^{im\phi}, \tag{A.58}$$

whereas the induced electric and magnetic field outside the cylinder ($R > R_0$) in vacuum are:

$$E_{out,z}(R,\phi,q_z,\omega) = \sum_{m=-\infty}^{\infty} -\kappa_o^2 b_m K_m(\kappa_o R) e^{im\phi}, \tag{A.59}$$

$$E_{out,R}(R,\phi,q_z,\omega) = \sum_{m=-\infty}^{\infty} \left[iq_z\kappa_o b_m K'_m(\kappa_o R) - \frac{\omega\mu_0 m}{R} d_m K_m(\kappa_o R) \right] e^{im\phi}, \tag{A.60}$$

$$E_{out,\phi}(R,\phi,q_z,\omega) = \sum_{m=-\infty}^{\infty} \left[-\frac{mq_z}{R} b_m K_m(\kappa_o R) - i\omega\mu_0\kappa_o d_m K'_m(\kappa_o R) \right] e^{im\phi}, \tag{A.61}$$

$$H_{out,z}(R,\phi,q_z,\omega) = \sum_{m=-\infty}^{\infty} -\kappa_o^2 d_m K_m(\kappa_o R) e^{im\phi}, \tag{A.62}$$

$$H_{out,R}(R,\phi,q_z,\omega) = \sum_{m=-\infty}^{\infty}\left[\frac{m\omega\varepsilon_0}{R}b_m K_m(\kappa_o R) + iq_z\kappa_o d_m K'_m(\kappa_o R)\right]e^{im\phi}, \tag{A.63}$$

$$H_{out,\phi}(R,\phi,q_z,\omega) = \sum_{m=-\infty}^{\infty}\left[i\omega\varepsilon_0\kappa_o b_m K'_m(\kappa_o R) - \frac{mq_z}{R}d_m K_m(\kappa_o R)\right]e^{im\phi}. \tag{A.64}$$

In the above expressions we assumed only solutions not diverging at $R = 0$ and at infinity, and we also defined

$$\kappa_i = \sqrt{q_z^2 - \varepsilon\frac{\omega^2}{c^2}}, \tag{A.65}$$

$$\kappa_o = \sqrt{q_z^2 - \frac{\omega^2}{c^2}}. \tag{A.66}$$

The unknown coefficients a_m, b_m, c_m and d_m are obtained by imposing boundary conditions at the boundaries of the cylinder:

$$H_{in,z}(R_0,0,q_z,\omega) = H_{out,z}(R_0,0,q_z,\omega), \tag{A.67a}$$

$$E_{in,z}(R_0,0,q_z,\omega) = E_{out,z}(R_0,0,q_z,\omega) + E_{el,z}(R_0,0,q_z,\omega), \tag{A.67b}$$

$$\varepsilon E_{in,R}(R_0,0,q_z,\omega) = E_{out,R}(R_0,0,q_z,\omega) + E_{el,R}(R_0,0,q_z,\omega), \tag{A.67c}$$

$$H_{in,R}(R_0,0,q_z,\omega) = H_{out,R}(R_0,0,q_z,\omega) + H_{el,R}(R_0,0,q_z,\omega). \tag{A.67d}$$

The loss probability per unit trajectory is then given by Eq. (6.15).

Appendix B

Finite element method in electron energy loss calculations

Various numerical methods have been used to numerically solve Maxwell's equations in the interaction of a moving charged particle and arbitrarily shaped geometrical objects (nanoparticles), namely:

- Boundary element method (BEM) [192, 222],
- Discrete dipole approximation (DDA) [45, 51, 198, 298],
- Finite-difference time-domain (FDTD) method [299, 300],
- Finite element method (FEM) in frequency domain [60, 301, 302].

In this thesis we employ a particular implementation of the FEM in the commercial software `Comsol Multiphysics` [303]. Here we briefly describe the main points to perform simulations of EELS for arbitrarily shaped structures within this software.

For all simulations, we utilize the `Radio Frequency toolbox` where we solve the wave equation for the total electric field in the frequency domain. All simulations are performed twice: with $\varepsilon(\mathbf{r}, \omega)$ corresponding to the probed structure and then with $\varepsilon(\mathbf{r}, \omega) = 1$ everywhere, so that only the field of the electron is present, preserving the same discretization (meshing) of the geometrical domains. Afterwards, the loss probability obtained from these two calculations is subtracted to obtain the induced field coming from the interaction of the electron beam with the nanostructure and to correct for the finite length of the electron's trajectory and non-zero values of the fast electron's field at the boundaries of the simulation domain [60, 301, 302]. We perform the calculations either in a 2D or 3D simulation domain, which we describe below separately.

B.1 Simulations in 3D domain

For a general geometrical arrangement not possessing any symmetry, it is necessary to perform calculations in a 3D simulation domain. We perform all 3D calculations of EEL in the Cartesian coordinate system (x, y, z). In Fig. B.1(a) we show an example of geometrical arrangement in a simulation of EEL spectra for an electron beam moving close to a metallic sphere. The simulation domain includes the sphere characterized by a dielectric response $\varepsilon_{\text{sphere}}$, a straight line (highlighted by a dark red line) representing the electron's trajectory, a cube surrounding the sphere characterized by $\varepsilon = 1$ and `Perfectly Matched Layers` (PML) with Cartesian symmetry that help to attenuate the electric field at the boundaries of the simulation domain and prevent unphysical field reflections from the boundaries.

We apply the `Free Tetrahedral` mesh with refined elements in areas of high field concentration and gradients, typically close to the electron's trajectory and close and inside nanostructures. We allow for an increase of the size of the mesh elements towards outer boundaries of the simulation domain. The area of PML is meshed by 5-10 `Swept` layers. The maximal allowed elements' dimensions depend on the simulated energy region and thus on the typical wavelengths involved. We typically use fractions of the typical wavelength for the largest elements.

The current density assigned to the electron beam is implemented as an `Edge Current`:

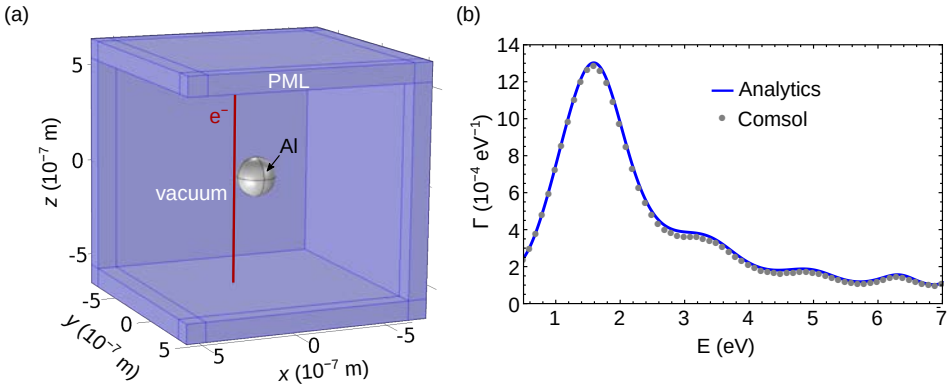

FIGURE B.1: (a) An example of a 3D simulation geometry: Al sphere of radius $a = 100$ nm surrounded by vacuum and excited by an electron beam moving at a distance $b = 120$ nm from the center of the sphere (dark red line). The simulation domain is surrounded by perfectly matched layers (PML). (b) Comparison of analytically and numerically calculated spectra (blue line and gray dots, respectively) for the geometrical arrangement in (a) considering the electron moving at speed $v = 0.5c$. The aluminum sphere is characterized by the Drude model [Eq. (1.7)] with parameters $\hbar\omega_p = 15.1$ eV, $\hbar\gamma = 0.15$ eV and $\varepsilon(\infty) = 1$.

$$I = I_0 \exp(-i\omega z/v), \tag{B.1}$$

where I_0 is magnitude of the current in [A] and v is the electron's speed. The EEL probability is evaluated from 3D calculations according to[1]

$$\Gamma_e(\omega) = \frac{e}{\pi\hbar\omega}\int_{z_{min}}^{z_{max}} dz\, \mathrm{Re}\left[E_z^{ind}(x_b, y_b, z; \omega)\exp\left(\frac{i\omega z}{v}\right)\right] \tag{B.2}$$

directly with this software using an `Edge Probe, Integral` along the electron's trajectory at (x_b, y_b) between the boundaries at z_{min} and z_{max}. In Fig. B.1(b) we show a comparison of numerically and analytically calculated EEL spectra. We considered an Al spherical particle of radius $R = 100$ nm excited by an electron beam moving at an impact parameter $b = 120$ nm [as shown in Fig. B.1(a)] and with speed $v = 0.5c$. We can see that the analytical result (blue line) obtained by using the expressions of Appendix A.3 together with Eq. (6.10) matches the numerically acquired data points (gray dots) very well. The relative error is in this case $< 5\%$ and higher accuracy can be reached when a finer meshing is applied.

Calculations of the energy loss probability corresponding to the magnetic current excitation are performed analogously. The source is implemented as line `Magnetic Current`

$$I_m = I_{m,0}\, i \exp(-i\omega z/v), \tag{B.3}$$

where $I_{m,0}$ is magnitude of the magnetic current in $[V]$. The magnetic loss probability [Eq. (6.9)] is also evaluated using an `Edge Probe, Integral` along the electron's trajectory, with the expression

$$\Gamma_m(\omega) = -\frac{\mu_B l}{\pi\hbar v}\int_{z_{min}}^{z_{max}} dz\, \mathrm{Im}\left[B_z^{ind}(x_b, y_b, z; \omega)\exp\left(\frac{i\omega z}{v}\right)\right]. \tag{B.4}$$

B.2 Simulations in 2D domain

For calculations of EEL in geometries that exhibit translational invariance along one direction, we can employ a 2D simulation domain and solve for the wave equation in (x, y, q_z) space (z being the out-of-plane direction along which the geometry does not change). In the simulation, we vary the out-of-plane wavevector q_z [60] so that we enable propagation of a wave $\mathbf{E}(x, y, z) = \tilde{\mathbf{E}}(x, y)\exp(iq_z z)$.

In 2D calculations, applied e.g. to solve for EEL near the truncated slab (see Section 2.4) or the slab junction (discussed in Section 3.2 and depicted in Fig. B.2), the electron beam parallel to the y axis is implemented as a `Surface Current` (solid red line in Fig. B.2):

$$I_s = I_{0,s}\exp(-i\omega y/v), \tag{B.5}$$

[1] Compare with Eq. (1.28).

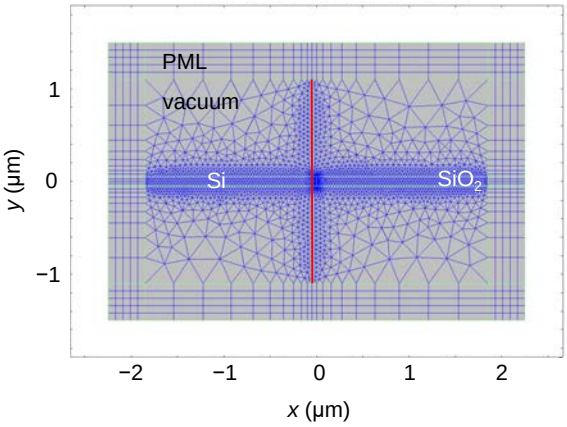

FIGURE B.2: Example of a 2D simulation domain with the meshing applied for calculations of EEL close to a junction of Si and SiO_2 slab which is infinite in the out-of-plane (z) direction. We use a refined meshing inside and close to the surfaces of the slab, close to the junction and along the electron trajectory (highlighted by the red line). Geometrical boundaries are denoted by green lines, whereas boundaries of the mesh elements are in blue.

where $I_{0,s}$ is magnitude of the surface current in [A/m]. The surface current density is also implicitly proportional to $\exp(iq_z z)$. We vary the out of plane wavevector q_z with a discrete step Δq_z over a sufficiently large range so that we mimic the excitation by a focused beam at the z axis and we calculate the EEL probability according to Eq. (2.20).[2]

Calculations in a 2D domain can be also employed in cases where the geometry has a translational symmetry along the electron's trajectory (see e.g. Section 6.3). The out-of-plane wavevector is then fixed to the value of the wavevector provided by the ouf-of-plane current associated with the electron beam, i.e. $q_z = \omega/v$ (the electron's trajectory is parallel to the z axis). The electron beam excitation is implemented as a `Line Current (Out-of-Plane)` I_o in [A] and assigned to the point (x_b, y_b) corresponding to the trajectory.

In Fig. B.3(a) we show an example of a simulation domain used to calculate the interaction of an electron beam moving parallel to the axis of an infinite cylinder. The out-of-plane current is positioned at the red point close to the cylinder's boundary (gray dashed line). Together with the meshing, we plot $\mathrm{Re}[E_z]$ at $E = 1.35$ eV, as numerically calculated for a 300-keV beam passing at $b = 160$ nm from the center of Si cylinder of radius $R_0 = 150$ nm. In Fig. B.3(b) we show a very good agreement between the analytically calculated EEL spectrum (solid

[2]Notice that due to the different coordinate convention used in `Comsol`, we have to exchange the coordinates (x, y, z) by (x, z, y).

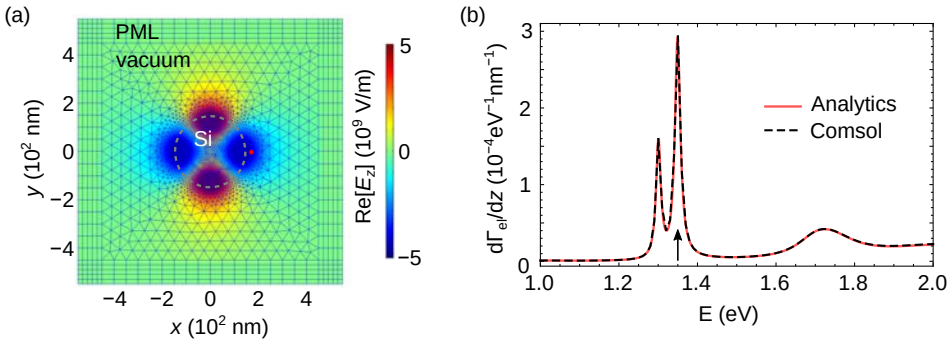

FIGURE B.3: (a) 2D simulation domain applied to calculations of EEL for a 300-keV electron beam positioned at $b = 160$ nm from the center of an infinite cylinder with radius $R_0 = 150$ nm made of silicon (described by dielectric data from Ref. [154]). The position of the beam is denoted by the red dot, whereas the boundary of the cylinder is marked by the gray dashed line. Mesh elements used for the simulation (denoted by blue lines) are overlaid with the density plot of $\mathrm{Re}[E_z]$ calculated at 1.35 eV, which is the energy corresponding to one of the spectral peaks [denoted by the arrow in (b)]. (b) Comparison of analytically calculated spectrum using the results in Appendix A.4 [solid red line; same as in Fig. 6.6(c)] with the numerical simulation (dashed black line).

red line) and the numerical result from `Comsol` (black dashed line) for the geometrical arrangement in Fig. B.3(a) and a 300-keV electron beam.

The meshing strategy in 2D simulations is similar to the 3D case: we refine the mesh in regions where the field varies significantly, as observed in both Fig. B.2 and Fig. B.3(a) (meshing is denser inside nanostructures and along the electron's trajectory). Compared to 3D calculations, we use 2D `Free Triangular` mesh elements in all regions except for PML that are meshed by `Boundary Layers`.

List of publications

Publications discussed in this thesis

1. A. A. Govyadinov*, **A. Konečná***, A. Chuvilin, S. Vélez, I. Dolado, A. Y. Nikitin. S. Lopatin, F. Casanova. L. E. Hueso, J. Aizpurua, and R. Hillenbrand. "Probing low-energy hyperbolic polaritons in van der Walls crystal with an electron microscope". In: *Nat. Commun.* 8.95 (2017). (*contributed equally)

2. **A. Konečná**, K. Venkatraman, K. March, P. A. Crozier, R. Hillenbrand, P. Rez, and J. Aizpurua. "Vibrational electron energy loss spectroscopy in truncated dielectric slabs". In: *Phys. Rev. B* 98 (20 2018), p. 205409.

3. **A. Konečná**, T. Neuman, J. Aizpurua, and R. Hillenbrand. "Surface-Enhanced Molecular Electron Energy Loss Spectroscopy". In: *ACS Nano 12.5* (2018), pp. 4775-4786.

4. J. R. Jokisaari, J. A. Hachtel, X. Hu, A. Mukherjee, C. Wang, **A. Konečná**, T. C. Lovejoy, N. Dellby, J. Aizpurua, O. L. Krivanek, J.-C. Idrobo, and R. F. Klie. "Vibrational Spectroscopy of Water with High Spatial Resolution". In: *Adv. Mater. 30.36* (2018), p. 1802702.

5. **A. Konečná**, M. K. Schmidt, R. Hillenbrand, and J. Aizpurua. "Probing the electromagnetic response of dielectric antennas by vortex electron beams". In preparation.

6. **A. Konečná**, J. A. Hachtel, R. Hillenbrand, J.-C. Idrobo, and J. Aizpurua. "Thermal effects in the near-field interaction of a focused electron beam with matter". In preparation.

Other publications

7. M. J. Lagos, A. Reyes-Coronado, **A. Konečná**, P. M. Echenique, J. Aizpurua, and P. E. Batson. "Attosecond and femtosecond forces exerted on gold nanoparticles induced by swift electrons". In: *Phys. Rev. B* 93 (20 2016), p. 205440.

8. M. Horák, V. Křápek, M. Hrtoň, **A. Konečná**, F. Ligmajer, M. Stöger-Pollach, T. Šamořil, A. Paták, Z. Édes, O. Metelka, J. Babocký, and T. Šikola. "Limits

of Babinet's principle for solid and hollow plasmonic antennas". In: *Sci. Rep.* 9.4004 (2019).

Bibliography

[1] L. Novotny and B. Hecht. *Principles of nano-optics*. New York: Cambridge University Press, 2012.

[2] G. P. Thomson and A. Reid. "Diffraction of Cathode Rays by a Thin Film". In: *Nature* 119.3007 (1927), p. 890. DOI: 10.1038/119890a0.

[3] M. Knoll and E. Ruska. "Das Elektronenmikroskop". In: *Z. Phys.* 78.5 (1932), pp. 318–339. DOI: 10.1007/BF01342199.

[4] E. Ruska. "The development of the electron microscope and of electron microscopy". In: *Rev. Mod. Phys.* 59 (3 1987), pp. 627–638. DOI: 10.1103/RevModPhys.59.627.

[5] D. Shechtman, I. Blech, D. Gratias, and J. W. Cahn. "Metallic Phase with Long-Range Orientational Order and No Translational Symmetry". In: *Phys. Rev. Lett.* 53 (20 1984), pp. 1951–1953. DOI: 10.1103/PhysRevLett.53.1951.

[6] R. Henderson and P. N. T. Unwin. "Three-dimensional model of purple membrane obtained by electron microscopy". In: *Nature* 257.5521 (1975), pp. 28–32. DOI: 10.1038/257028a0.

[7] P. E. Batson, N. Dellby, and O. L. Krivanek. "Sub-ångstrom resolution using aberration corrected electron optics". In: *Nature* 418.6898 (2002), p. 617. DOI: 10.1038/nature00972.

[8] O. L. Krivanek, M. F. Chisholm, V. Nicolosi, T. J. Pennycook, G. J. Corbin, N. Dellby, M. F. Murfitt, C. S. Own, Z. S. Szilagyi, M. P. Oxley, S. T. Pantelides, and S. J. Pennycook. "Atom-by-atom structural and chemical analysis by annular dark-field electron microscopy". In: *Nature* 464.7288 (2010), pp. 571–574. DOI: 10.1038/nature08879.

[9] R. F. Egerton. *Electron Energy-Loss Spectroscopy in the Electron Microscope*. 3rd ed. New York: Springer, 2011.

[10] O. L. Krivanek, T. C. Lovejoy, N. Dellby, T. Aoki, R. W. Carpenter, P. Rez, E. Soignard, J. Zhu, P. E. Batson, M. J. Lagos, R. F. Egerton, and P. A. Crozier. "Vibrational spectroscopy in the electron microscope". In: *Nature* 514 (7521 2014), pp. 209–212. DOI: 10.1038/nature13870.

[11] N. D. Browning, M. F. Chisholm, and S. J. Pennycook. "Atomic-resolution chemical analysis using a scanning transmission electron microscope". In: *Nature* 366 (1993), pp. 143–146. DOI: 10.1038/366143a0.

[12] P. E. Batson. "Simultaneous STEM imaging and electron energy-loss spectroscopy with atomic-column sensitivity". In: *Nature* 366.6457 (1993), pp. 727–728. DOI: 10.1038/366727a0.

[13] D. Kepaptsoglou, T. P. Hardcastle, C. R. Seabourne, U. Bangert, R. Zan, J. A. Amani, H. Hofsäss, R. J. Nicholls, R. M. D. Brydson, A. J. Scott, and Q. M. Ramasse. "Electronic Structure Modification of Ion Implanted Graphene: The Spectroscopic Signatures of p- and n-Type Doping". In: *ACS Nano* 9.11 (2015), pp. 11398–11407. DOI: 10.1021/acsnano.5b05305.

[14] J. M. Hollas. *Modern spectroscopy*. John Wiley & Sons, 2004.

[15] F. J. García de Abajo. "Optical excitations in electron microscopy". In: *Rev. Mod. Phys.* 82 (1 2010), pp. 209–275. DOI: 10.1103/RevModPhys.82.209.

[16] P. N. Prasad. *Nanophotonics*. John Wiley & Sons, 2004.

[17] N. W. Ashcroft and N. D. Mermin. *Solid state physics*. Philadelphia: Saunders College, 1976.

[18] S. A. Maier. *Plasmonics: Fundamentals and Applications*. Springer, 2007.

[19] J. D. Caldwell, L. Lindsay, V. Giannini, I. Vurgaftman, T. L. Reinecke, S. A. Maier, and O. J. Glembocki. "Low-loss, infrared and terahertz nanophotonics using surface phonon polaritons". In: *Nanophotonics* 4.1 (2015), pp. 44–68. DOI: 10.1515/nanoph-2014-0003.

[20] M. Pelton, J. Aizpurua, and G. Bryant. "Metal-nanoparticle plasmonics". In: *Laser Photonics Rev.* 2.3 (2008), pp. 136–159. DOI: 10.1002/lpor.200810003.

[21] A. E. Krasnok, I. S. Maksymov, A. I. Denisyuk, P. A. Belov, A. E. Miroshnichenko, C. R. Simovski, and Y. S. Kivshar. "Optical nanoantennas". In: *Physics-Uspekhi* 56.6 (2013), p. 539. DOI: 10.3367/UFNe.0183.201306a.0561.

[22] T. W. Ebbesen, H. J. Lezec, H. F. Ghaemi, T. Thio, and P. A. Wolff. "Extraordinary optical transmission through sub-wavelength hole arrays". In: *Nature* 391.6668 (1998), pp. 667–669. DOI: 10.1038/35570.

[23] F. Xia, H. Wang, D. Xiao, M. Dubey, and A. Ramasubramaniam. "Two-dimensional material nanophotonics". In: *Nat. Photonics* 8.12 (2014), pp. 899–907. DOI: 10.1038/nphoton.2014.271.

[24] T. Low, A. Chaves, J. D. Caldwell, A. Kumar, N. X. Fang, P. Avouris, T. F. Heinz, F. Guinea, L. Martin-Moreno, and F. Koppens. "Polaritons in layered two-dimensional materials". In: *Nat. Mater.* 16.2 (2017), pp. 182–194. DOI: 10.1038/nmat4792.

[25] F. J. Garcia de Abajo. "Graphene plasmonics: challenges and opportunities". In: *ACS Photonics* 1.3 (2014), pp. 135–152. DOI: 10.1021/ph400147y.

[26] D. R. Smith, J. B. Pendry, and M. C. K. Wiltshire. "Metamaterials and negative refractive index". In: *Science* 305.5685 (2004), pp. 788–792. DOI: 10.1126/science.1096796.

[27] E. Ozbay. "Plasmonics: merging photonics and electronics at nanoscale dimensions". In: *Science* 311.5758 (2006), pp. 189–193. DOI: 10.1126/science.1114849.

[28] F. Neubrech, A. Pucci, T. W. Cornelius, S. Karim, A. García-Etxarri, and J. Aizpurua. "Resonant Plasmonic and Vibrational Coupling in a Tailored Nanoantenna for Infrared Detection". In: *Phys. Rev. Lett.* 101 (15 2008), p. 157403. DOI: 10.1103/PhysRevLett.101.157403.

[29] D. Rodrigo, O. Limaj, D. Janner, D. Etezadi, F. J. García De Abajo, V. Pruneri, and H. Altug. "Mid-infrared plasmonic biosensing with graphene". In: *Science* 349.6244 (2015), pp. 165–168. DOI: 10.1126/science.aab2051.

[30] K. R. Catchpole, and A. Polman. "Plasmonic solar cells". In: *Opt. Express* 16.26 (2008), pp. 21793–21800. DOI: 10.1364/OE.16.021793.

[31] S. Kawata, Y. Inouye, and P. Verma. "Plasmonics for near-field nano-imaging and superlensing". In: *Nat. Photonics* 3.7 (2009), pp. 388–394. DOI: 10.1038/NPHOTON.2009.111.

[32] D. K. Gramotnev and S. I. Bozhevolnyi. "Plasmonics beyond the diffraction limit". In: *Nature photonics* 4.2 (2010), pp. 83–91. DOI: 10.1038/nphoton.2009.282.

[33] H. Heinzelmann and D. W. Pohl. "Scanning near-field optical microscopy". In: *Appl. Phys. A* 59.2 (1994), pp. 89–101. DOI: 10.1007/BF00332200.

[34] C. J. Powell and J. B. Swan. "Origin of the Characteristic Electron Energy Losses in Aluminum". In: *Phys. Rev.* 115 (4 1959), pp. 869–875. DOI: 10.1103/PhysRev.115.869.

[35] C. J. Powell and J. B. Swan. "Origin of the Characteristic Electron Energy Losses in Magnesium". In: *Phys. Rev.* 116 (1 1959), pp. 81–83. DOI: 10.1103/PhysRev.116.81.

[36] D. Bohm and D. Pines. "A Collective Description of Electron Interactions: III. Coulomb Interactions in a Degenerate Electron Gas". In: *Phys. Rev.* 92 (3 1953), pp. 609–625. DOI: 10.1103/PhysRev.92.609.

[37] D. Pines. "Collective Energy Losses in Solids". In: *Rev. Mod. Phys.* 28 (3 1956), pp. 184–198. DOI: 10.1103/RevModPhys.28.184.

[38] R. H. Ritchie. "Plasma Losses by Fast Electrons in Thin Films". In: *Phys. Rev.* 106 (5 1957), pp. 874–881. DOI: 10.1103/PhysRev.106.874.

[39] C. Cherqui, N. Thakkar, G. Li, J. P. Camden, and D. J. Masiello. "Characterizing Localized Surface Plasmons Using Electron Energy Loss Spectroscopy". In: *Annu. Rev. Phys. Chem.* 67.1 (2016), pp. 331–357. DOI: 10.1146/annurev-physchem-040214-121612.

[40] J. Nelayah, M. Kociak, O. Stéphan, F. J. García de Abajo, M. Tencé, L. Henrard, D. Taverna, I. Pastoriza-Santos, L. M. Liz-Marzán, and C. Colliex. "Mapping surface plasmons on a single metallic nanoparticle". In: *Nat. Phys.* 3.5 (2007), pp. 348–353. DOI: 10.1038/nphys575.

[41] F. Ouyang, P. E. Batson, and M. Isaacson. "Quantum size effects in the surface-plasmon excitation of small metallic particles by electron-energy-loss spectroscopy". In: *Phys. Rev. B* 46 (23 1992), pp. 15421–15425. DOI: 10.1103/PhysRevB.46.15421.

[42] A. L. Koh, K. Bao, I. Khan, W. E. Smith, G. Kothleitner, P. Nordlander, S. A. Maier, and D. W. McComb. "Electron Energy-Loss Spectroscopy (EELS) of Surface Plasmons in Single Silver Nanoparticles and Dimers: Influence of Beam Damage and Mapping of Dark Modes". In: *ACS Nano* 3.10 (2009), pp. 3015–3022. DOI: 10.1021/nn900922z.

[43] O. Nicoletti, F. de La Peña, R. K. Leary, D. J. Holland, C. Ducati, and P. A. Midgley. "Three-dimensional imaging of localized surface plasmon resonances of metal nanoparticles". In: *Nature* 502.7469 (2013), pp. 80–84. DOI: 10.1038/nature12469.

[44] F.-P. Schmidt, H. Ditlbacher, U. Hohenester, A. Hohenau, F. Hofer, and J. R. Krenn. "Dark Plasmonic Breathing Modes in Silver Nanodisks". In: *Nano Lett.* 12.11 (2012), pp. 5780–5783. DOI: 10.1021/nl3030938.

[45] N. W. Bigelow, A. Vaschillo, V. Iberi, J. P. Camden, and D. J. Masiello. "Characterization of the Electron- and Photon-Driven Plasmonic Excitations of Metal Nanorods". In: *ACS Nano* 6.8 (2012), pp. 7497–7504. DOI: 10.1021/nn302980u.

[46] M. Bosman, E. Ye, S. Fen Tah, C. A. Nijhuis, J. K. W. Yang, R. Marty, A. Mlayah, A. Arbouet, C. Girard, and M.-Y. Han. "Surface Plasmon Damping Quantified with an Electron Nanoprobe". In: *Sci. Rep.* 3.1312 (2013). DOI: doi:10.1038/srep01312.

[47] M.-W. Chu, V. Myroshnychenko, C. H. Chen, J.-P. Deng, C.-Y. Mou, and F. J. García de Abajo. "Probing Bright and Dark Surface-Plasmon Modes in Individual and Coupled Noble Metal Nanoparticles Using an Electron Beam". In: *Nano Lett.* 9.1 (2009), pp. 399–404. DOI: 10.1021/nl803270x.

[48] I. Alber, W. Sigle, S. Müller, R. Neumann, O. Picht, M. Rauber, P. A. van Aken, and M. E. Toimil-Molares. "Visualization of Multipolar Longitudinal and Transversal Surface Plasmon Modes in Nanowire Dimers". In: *ACS Nano* 5.12 (2011), pp. 9845–9853. DOI: 10.1021/nn2035044.

[49] E. P. Bellido, Y. Zhang, A. Manjavacas, P. Nordlander, and G. A. Botton. "Plasmonic Coupling of Multipolar Edge Modes and the Formation of Gap Modes". In: *ACS Photonics* 4.6 (2017), pp. 1558–1565. DOI: 10.1021/acsphotonics.7b00348.

[50] S. J. Barrow, D. Rossouw, A. M. Funston, G. A. Botton, and P. Mulvaney. "Mapping Bright and Dark Modes in Gold Nanoparticle Chains using Electron Energy Loss Spectroscopy". In: *Nano Lett.* 14.7 (2014), pp. 3799–3808. DOI: 10.1021/nl5009053.

[51] N. W. Bigelow, A. Vaschillo, J. P. Camden, and D. J. Masiello. "Signatures of Fano Interferences in the Electron Energy Loss Spectroscopy and Cathodoluminescence of Symmetry-Broken Nanorod Dimers". In: *ACS Nano* 7.5 (2013), pp. 4511–4519. DOI: 10.1021/nn401161n.

[52] A. B. Yankovich, R. Verre, E. Olsén, A. E. O. Persson, V. Trinh, G. Dovner, M. Käll, and E. Olsson. "Multidimensional Hybridization of Dark Surface Plasmons". In: *ACS Nano* 11.4 (2017), pp. 4265–4274. DOI: 10.1021/acsnano.7b01318.

[53] O. L. Krivanek, T. C. Lovejoy, M. F. Murfitt, G. Skone, P. E. Batson, and N. Dellby. "Towards sub-10 meV energy resolution STEM-EELS". In: *J. Phys. Conf. Ser.* 522.1 (2014), p. 012023. URL: http://stacks.iop.org/1742-6596/522/i=1/a=012023.

[54] S. Lopatin, B. Cheng, W.-T. Liu, M.-L. Tsai, J.-H. He, and A. Chuvilin. "Optimization of monochromated TEM for ultimate resolution imaging and ultrahigh resolution electron energy loss spectroscopy". In: *Ultramicroscopy* 184 (2018), pp. 109–115. DOI: 10.1016/j.ultramic.2017.08.016.

[55] P. Rez, T. Aoki, K. March, D. Gur, O. L. Krivanek, N. Dellby, T. C. Lovejoy, S. G. Wolf, and H. Cohen. "Damage-free vibrational spectroscopy of biological materials in the electron microscope". In: *Nat. Commun.* 7.10945 (2016). DOI: 10.1038/ncomms10945.

[56] G. Radtke, D. Taverna, M. Lazzeri, and E. Balan. "First-Principles Vibrational Electron Energy Loss Spectroscopy of β-Guanine". In: *Phys. Rev. Lett.* 119 (2 2017), p. 027402. DOI: 10.1103/PhysRevLett.119.027402.

[57] P. A. Crozier, T. Aoki, and Q. Liu. "Detection of water and its derivatives on individual nanoparticles using vibrational electron energy-loss spectroscopy". In: *Ultramicroscopy* 169 (2016), pp. 30–36. DOI: 10.1016/j.ultramic.2016.06.008.

[58] D. M. Haiber and P. A. Crozier. "Nanoscale Probing of Local Hydrogen Heterogeneity in Disordered Carbon Nitrides with Vibrational Electron Energy-Loss Spectroscopy". In: *ACS Nano* 12.6 (2018), pp. 5463–5472. DOI: 10.1021/acsnano.8b00884.

[59] C. Dwyer, T. Aoki, P. Rez, S. L. Y. Chang, T. C. Lovejoy, and O. L. Krivanek. "Electron-Beam Mapping of Vibrational Modes with Nanometer Spatial Resolution". In: *Phys. Rev. Lett.* 117 (25 2016), p. 256101. DOI: 10.1103/PhysRevLett.117.256101.

[60] A. A. Govyadinov*, A. Konečná*, A. Chuvilin, S. Vélez, I. Dolado, A. Y. Nikitin, S. Lopatin, F. Casanova, L. E. Hueso, J. Aizpurua, and R. Hillenbrand. "Probing low-energy hyperbolic polaritons in van der Walls crystal with an electron microscope". In: *Nat. Commun.* 8.95 (2017). DOI: 10.1038/s41467-017-00056-y.

[61] J. C. Idrobo, A. R. Lupini, T. Feng, R. R. Unocic, F. S. Walden, D. S. Gardiner, T. C. Lovejoy, N. Dellby, S. T. Pantelides, and O. L. Krivanek. "Temperature Measurement by a Nanoscale Electron Probe Using Energy Gain and Loss Spectroscopy". In: *Phys. Rev. Lett.* 120 (9 2018), p. 095901. DOI: 10.1103/PhysRevLett.120.095901.

[62] M. J. Lagos, A. Trügler, U. Hohenester, and P. E. Batson. "Mapping vibrational surface and bulk modes in a single nanocube". In: *Nature* 543.7646 (2017), pp. 529–532. DOI: 10.1038/nature21699.

[63] K. Venkatraman, P. Rez, K. March, and P. A. Crozier. "The influence of surfaces and interfaces on high spatial resolution vibrational EELS from SiO2". In: *Microscopy* 67 (2018), pp. i14–i23. DOI: 10.1093/jmicro/dfy003.

[64] M. J. Lagos, A. Trügler, V. Amarasinghe, L. C. Feldman, U. Hohenester, and P. E. Batson. "Excitation of long-wavelength surface optical vibrational modes in films, cubes and film/cube composite system using an atom-sized electron beam". In: *Microscopy* 67 (2018), pp. i3–i13. DOI: 10.1093/jmicro/dfx130.

[65] Y.-H. Li, M. Wu, R.-S. Qi, N. Li, Y.-W. Sun, C.-L. Shi, X.-T. Zhu, J.-D. Guo, D.-P. Yu, and P. Gao. "Probing Lattice Vibrations at SiO2/Si Surface and Interface with Nanometer Resolution". In: *Chin. Phys. Lett.* 36.2 (2019), p. 026801. DOI: 10.1088/0256-307x/36/2/026801.

[66] J. R. Jokisaari, J. A. Hachtel, X. Hu, A. Mukherjee, C. Wang, A. Konecna, T. C. Lovejoy, Dellby N., J. Aizpurua, O. L. Krivanek, J.-C. Idrobo, and R. F. Klie. "Vibrational Spectroscopy of Water with High Spatial Resolution". In: *Adv. Mater.* 30 (36 2018), p. 1802702. DOI: 10.1002/adma.201802702.

[67] R. Hillenbrand, T. Taubner, and F. Keilmann. "Phonon-enhanced light-matter interaction at the nanometre scale". In: *Nature* 418.6894 (2002), pp. 159–162. DOI: 10.1038/nature00899.

[68] S. Dai, Z. Fei, Q. Ma, A. S. Rodin, M. Wagner, A. S. McLeod, M. K. Liu, W. Gannett, W. Regan, K. Watanabe, T. Taniguchi, M. Thiemens, G. Dominguez, A. H. Castro Neto, A. Zettl, F. Keilmann, P. Jarillo-Herrero, M. M. Fogler, and D. N. Basov. "Tunable Phonon Polaritons in Atomically Thin van der Waals Crystals of Boron Nitride". In: *Science* 343.6175 (2014), pp. 1125–1129. DOI: 10.1126/science.1246833.

[69] E. Yoxall, M. Schnell, A. Y. Nikitin, O. Txoperena, A. Woessner, M. B. Lundeberg, F. Casanova, L. E. Hueso, F. H. L. Koppens, and R. Hillenbrand. "Direct observation of ultraslow hyperbolic polariton propagation with negative phase velocity". In: *Nat. Photonics* 9 (2015), pp. 674–678. DOI: 10.1038/nphoton.2015.166.

[70] T. Taubner, D. Korobkin, Y. Urzhumov, G. Shvets, and R. Hillenbrand. "Near-field microscopy through a SiC superlens". In: *Science* 313.5793 (2006), pp. 1595–1595. DOI: 10.1126/science.1131025.

[71] A. Y. Nikitin, E. Yoxall, M. Schnell, S. Vélez, I. Dolado, P. Alonso-Gonzalez, F. Casanova, L. E. Hueso, and R. Hillenbrand. "Nanofocusing of Hyperbolic Phonon Polaritons in a Tapered Boron Nitride Slab". In: *ACS Photonics* 3.6 (2016), pp. 924–929. DOI: 10.1021/acsphotonics.6b00186.

[72] M. Autore, P. Li, I. Dolado, F. J. Alfaro-Mozaz, R. Esteban, A. Atxabal, F. Casanova, L. E. Hueso, P. Alonso-González, J. Aizpurua, A. Y. Nikitin, S. Vélez, and R. Hillenbrand. "Boron nitride nanoresonators for phonon-enhanced molecular vibrational spectroscopy at the strong coupling limit". In: *Light Sci. Appl.* 7 (2018), e17172. DOI: 10.1038/lsa.2017.172.

[73] J. Aizpurua, A. Howie, and F. J. García de Abajo. "Valence-electron energy loss near edges, truncated slabs, and junctions". In: *Phys. Rev. B* 60 (15 1999), pp. 11149–11162. DOI: 10.1103/PhysRevB.60.11149.

[74] P. Rez. "Is Localized Infrared Spectroscopy Now Possible in the Electron Microscope?" In: *Microscopy and Microanalysis* 20.3 (2014), pp. 671–677. DOI: 10.1017/S1431927614000129.

[75] F. J. García de Abajo and M. Kociak. "Electron energy-gain spectroscopy". In: *New Journal of Physics* 10.7 (2008), p. 073035. DOI: 10.1088/1367-2630/10/7/073035.

[76] A. Asenjo-Garcia and F. J. García de Abajo. "Plasmon electron energy-gain spectroscopy". In: *New J. Phys.* 15.10 (2013), p. 103021. DOI: 10.1088/1367-2630/15/10/103021.

[77] A. Howie. "Stimulated excitation electron microscopy and spectroscopy". In: *Ultramicroscopy* 151 (2015), pp. 116–121. DOI: 10.1016/j.ultramic.2014.09.006.

[78] R. M. A. Vergauwe, J. George, T. Chervy, J. A. Hutchison, A. Shalabney, V. Y. Torbeev, and T. W. Ebbesen. "Quantum strong coupling with protein vibrational modes". In: *J. Phys. Chem. Lett.* 7.20 (2016), pp. 4159–4164. DOI: 10.1021/acs.jpclett.6b01869.

[79] B. J. McMorran, A. Agrawal, I. M. Anderson, A. A. Herzing, H. J. Lezec, J. J. McClelland, and J. Unguris. "Electron Vortex Beams with High Quanta of Orbital Angular Momentum". In: *Science* 331.6014 (2011), pp. 192–195. DOI: 10.1126/science.1198804.

[80] M. Uchida and A. Tonomura. "Generation of electron beams carrying orbital angular momentum". In: *Nature* 464.7289 (2010), pp. 737–739. DOI: 10.1038/nature08904.

[81] G. Guzzinati, A. Béché, H. Lourenco-Martins, J. Martin, M. Kociak, and J. Verbeeck. "Probing the symmetry of the potential of localized surface plasmon resonances with phase-shaped electron beams". In: *Nat. Commun.* 8.14999 (2017). DOI: 10.1038/ncomms14999.

[82] R. Vincent and J. Silcox. "Dispersion of Radiative Surface Plasmons in Aluminum Films by Electron Scattering". In: *Phys. Rev. Lett.* 31 (25 1973), pp. 1487–1490. DOI: 10.1103/PhysRevLett.31.1487.

[83] F. P. Schmidt, H. Ditlbacher, F. Hofer, J. R. Krenn, and U. Hohenester. "Morphing a plasmonic nanodisk into a nanotriangle". In: *Nano Lett.* 14.8 (2014), pp. 4810–4815. DOI: 10.1021/nl502027r.

[84] J. A. Hachtel, J. Huang, I. Popovs, S. Jansone-Popova, J. K. Keum, J. Jakowski, T. C. Lovejoy, N. Dellby, O. L. Krivanek, and J. C. Idrobo. "Identification of site-specific isotopic labels by vibrational spectroscopy in the electron microscope". In: *Science* 363.6426 (2019), pp. 525–528. DOI: 10.1126/science.aav5845.

[85] J. D. Jackson. *Classical electrodynamics*. 3rd ed. New York: John Wiley & Sons, 1999.

[86] M. Fox. *Optical Properties of Solids*. Oxford: Oxford University Press, 2001.

[87] J. M. Pitarke, V. M. Silkin, E. V. Chulkov, and P. M. Echenique. "Theory of surface plasmons and surface-plasmon polaritons". In: *Rep. Prog. Phys.* 70.1 (2007). DOI: 10.1088/0034-4885/70/1/R01.

[88] A. V. Zayats, I. I. Smolyaninov, and A. A. Maradudin. "Nano-optics of surface plasmon polaritons". In: *Phys. Rep.* 408.3 (2005), pp. 131 –314. DOI: https://doi.org/10.1016/j.physrep.2004.11.001.

[89] H. Ditlbacher, A. Hohenau, D. Wagner, U. Kreibig, M. Rogers, F. Hofer, F. R. Aussenegg, and J. R. Krenn. "Silver Nanowires as Surface Plasmon Resonators". In: *Phys. Rev. Lett.* 95 (25 2005), p. 257403. DOI: 10.1103/PhysRevLett.95.257403.

[90] J. Dorfmüller, R. Vogelgesang, R. T. Weitz, C. Rockstuhl, C. Etrich, T. Pertsch, F. Lederer, and K. Kern. "Fabry-P'erot Resonances in One-Dimensional Plasmonic Nanostructures". In: *Nano Lett.* 9.6 (2009), pp. 2372–2377. DOI: 10.1021/nl900900r.

[91] D. Rossouw, M. Couillard, J. Vickery, E. Kumacheva, and G. A. Botton. "Multipolar Plasmonic Resonances in Silver Nanowire Antennas Imaged with a Subnanometer Electron Probe". In: *Nano Lett.* 11.4 (2011), pp. 1499–1504. DOI: 10.1021/nl200634w.

[92] S. V. Yalunin, B. Schröder, and C. Ropers. "Theory of electron energy loss near plasmonic wires, nanorods, and cones". In: *Phys. Rev. B* 93 (11 2016), p. 115408. DOI: 10.1103/PhysRevB.93.115408.

[93] D. T. Schoen, A. C. Atre, A. Garcáa-Etxarri, J. A. Dionne, and M. L. Brongersma. "Probing Complex Reflection Coefficients in One-Dimensional Surface Plasmon Polariton Waveguides and Cavities Using STEM EELS". In: *Nano Lett.* 15.1 (2015), pp. 120–126. DOI: 10.1021/nl503179j.

[94] W. Cai, R. Sainidou, J. Xu, A. Polman, and F. J. García de Abajo. "Efficient Generation of Propagating Plasmons by Electron Beams". In: *Nano Lett.* 9.3 (2009), pp. 1176–1181. DOI: 10.1021/nl803825n.

[95] H. Wei, D. Pan, S. Zhang, Z. Li, Q. Li, N. Liu, W. Wang, and H. Xu. "Plasmon Waveguiding in Nanowires". In: *Chem. Rev.* 118.6 (2018), pp. 2882–2926. DOI: 10.1021/acs.chemrev.7b00441.

[96] P. B. Johnson and R. W. Christy. "Optical Constants of the Noble Metals". In: *Phys. Rev. B* 6 (12 1972), pp. 4370–4379. DOI: 10.1103/PhysRevB.6.4370.

[97] A. Losquin and M. Kociak. "Link between Cathodoluminescence and Electron Energy Loss Spectroscopy and the Radiative and Full Electromagnetic Local Density of States". In: *ACS Photonics* 2.11 (2015), pp. 1619–1627. DOI: 10.1021/acsphotonics.5b00416.

[98] D. Rossouw and G. A. Botton. "Plasmonic Response of Bent Silver Nanowires for Nanophotonic Subwavelength Waveguiding". In: *Phys. Rev. Lett.* 110 (6 2013), p. 066801. DOI: 10.1103/PhysRevLett.110.066801.

[99] Gustav Mie. "Beiträge zur Optik trüber Medien, speziell kolloidaler Metallösungen". In: *Ann. Phys.* 330.3 (1908), pp. 377–445. DOI: 10.1002/andp.19083300302.

[100] R. Fuchs and K. L. Kliewer. "Optical modes of vibration in an ionic crystal sphere". In: *J. Opt. Soc. Am.* 58.3 (1968), pp. 319–330. DOI: 10.1364/JOSA.58.000319.

[101] C. F. Bohren and D. R. Huffman. *Absorption and Scattering of Light by Small Particles*. New York: John Wiley & Sons, 1983.

[102] S. M. Collins. "Dispersion characteristics of face modes in ionic-crystal and plasmonic-metal nanoparticles". In: *Phys. Rev. B* 97 (24 2018), p. 245422. DOI: 10.1103/PhysRevB.97.245422.

[103] C. Ropers, C. C. Neacsu, T. Elsaesser, M. Albrecht, M. B. Raschke, and C. Lienau. "Grating-Coupling of Surface Plasmons onto Metallic Tips: A Nanoconfined Light Source". In: *Nano Lett.* 7.9 (2007), pp. 2784–2788. DOI: 10.1021/nl071340m.

[104] P. Dvořák, T. Neuman, L. Břínek, T. Šamořil, R. Kalousek, P. Dub, P. Varga, and T. Šikola. "Control and Near-Field Detection of Surface Plasmon Interference Patterns". In: *Nano Lett.* 13.6 (2013), pp. 2558–2563. DOI: 10.1021/nl400644r.

[105] L. Salomon, G. Bassou, H. Aourag, J. P. Dufour, F. de Fornel, F. Carcenac, and A. V. Zayats. "Local excitation of surface plasmon polaritons at discontinuities of a metal film: Theoretical analysis and optical near-field measurements". In: *Phys. Rev. B* 65 (12 2002), p. 125409. DOI: 10.1103/PhysRevB.65.125409.

[106] E. Fermi. "The Ionization Loss of Energy in Gases and in Condensed Materials". In: *Phys. Rev.* 57 (6 1940), pp. 485–493. DOI: 10.1103/PhysRev.57.485.

[107] R. H. Ritchie. "Quantal aspects of the spatial resolution of energy-loss measurements in electron microscopy I. Broad-beam geometry". In: *Philosophical Magazine A* 44.4 (1981), pp. 931–942. DOI: 10.1080/01418618108239558.

[108] R. Garcia-Molina, A. Gras-Marti, A. Howie, and R. H. Ritchie. "Retardation effects in the interaction of charged particle beams with bounded condensed media". In: *J. Phys. C* 18.27 (1985), p. 5335. URL: http://stacks.iop.org/0022-3719/18/i=27/a=019.

[109] E. Kröger. "Transition radiation, Cerenkov radiation and energy losses of relativistic charged particles traversing thin foils at oblique incidence". In: *Z. Phys.* 235.5 (1970), pp. 403–421. DOI: 10.1007/BF01394931.

[110] A. A. Lucas, E. Kartheuser, and R. G. Badro. "Electron-Phonon Interaction in Dielectric Films. Application to Electron Energy Loss and Gain Spectra". In: *Phys. Rev. B* 2 (1970), pp. 2488–2499. DOI: 10.1103/PhysRevB.2.2488.

[111] R. H. Ritchie and H. B. Eldridge. "Optical Emission from Irradiated Foils. I". In: *Phys. Rev.* 126 (6 1962), pp. 1935–1947. DOI: 10.1103/PhysRev.126.1935.

[112] F. J. García de Abajo. "Relativistic energy loss and induced photon emission in the interaction of a dielectric sphere with an external electron beam". In: *Phys. Rev. B* 59 (4 1999), pp. 3095–3107. DOI: 10.1103/PhysRevB.59.3095.

[113] T. L. Ferrell and P. M. Echenique. "Generation of Surface Excitations on Dielectric Spheres by an External Electron Beam". In: *Phys. Rev. Lett.* 55 (14 1985), pp. 1526–1529. DOI: 10.1103/PhysRevLett.55.1526.

[114] N. Zabala, A. G. Pattantyus-Abraham, A. Rivacoba, F. J. García de Abajo, and M. O. Wolf. "Relativistic effects in EELS of nanoporous alumina membranes". In: *Phys. Rev. B* 68 (24 2003), p. 245407. DOI: 10.1103/PhysRevB.68.245407.

[115] J. Aizpurua and A. Rivacoba. "Nonlocal effects in the plasmons of nanowires and nanocavities excited by fast electron beams". In: *Phys. Rev. B* 78 (3 2008), p. 035404. DOI: 10.1103/PhysRevB.78.035404.

[116] C. A. Walsh. "An analytical expression for the energy loss of fast electrons travelling parallel to the axis of a cylindrical interface". In: *Phil. Mag. B* 63.5 (1991), pp. 1063–1078. DOI: 10.1080/13642819108207585.

[117] F. S. Hage, D. M. Kepaptsoglou, Q. M. Ramasse, and L. J. Allen. "Phonon Spectroscopy at Atomic Resolution". In: *Phys. Rev. Lett.* 122 (1 2019), p. 016103. DOI: 10.1103/PhysRevLett.122.016103.

[118] R. J. Nicholls, F. S. Hage, D. G. McCulloch, Q. M. Ramasse, K. Refson, and J. R. Yates. "Theory of momentum-resolved phonon spectroscopy in the electron microscope". In: *Phys. Rev. B* 99 (9 2019), p. 094105. DOI: 10.1103/PhysRevB.99.094105.

[119] J. R. M. Saavedra and F. Javier García de Abajo. "Phonon excitation by electron beams in nanographenes". In: *Phys. Rev. B* 92 (11 2015), p. 115449. DOI: 10.1103/PhysRevB.92.115449.

[120] C. Dwyer. "Localization of high-energy electron scattering from atomic vibrations". In: *Phys. Rev. B* 89 (5 2014), p. 054103. DOI: 10.1103/PhysRevB.89.054103.

[121] P. M. Echenique, F. Flores, and R. H. Ritchie. "Dynamic screening of ions in condensed matter". In: *Solid State Physics*. Vol. 43. 1990, pp. 229–308. DOI: 10.1016/S0081-1947(08)60325-2.

[122] K. Sturm. "Dynamic structure factor: An introduction". In: *Z. Naturforsch. A* 48.1-2 (1993), pp. 233–242.

[123] L. Van Hove. "Correlations in Space and Time and Born Approximation Scattering in Systems of Interacting Particles". In: *Phys. Rev.* 95 (1 1954), pp. 249–262. DOI: 10.1103/PhysRev.95.249.

[124] P. Nozieres and D. Pines. "A dielectric formulation of the many body problem: Application to the free electron gas". In: *Nuovo Cim.* 9.3 (1958), pp. 470–490. DOI: 10.1007/BF02725103.

[125] K. Venkatraman, B. D. A. Levin, K. March, P. Rez, and P. A. Crozier. "Vibrational Spectroscopy at Atomic Resolution with Electron Impact Scattering". In: *arXiv preprint arXiv:1812.08895* (2018). URL: https://arxiv.org/ftp/arxiv/papers/1812/1812.08895.pdf.

[126] O. L. Krivanek, T. C. Lovejoy, N. Dellby, and R.W. Carpenter. "Monochromated STEM with a 30 meV-wide, atom-sized electron probe". In: *Microscopy* 62.1 (2013), pp. 3–21. DOI: 10.1093/jmicro/dfs089.

[127] R. B. Pettit, J. Silcox, and R. Vincent. "Measurement of surface-plasmon dispersion in oxidized aluminum films". In: *Phys. Rev. B* 11 (8 1975), pp. 3116–3123. DOI: 10.1103/PhysRevB.11.3116.

[128] P. Shekhar, M. Malac, V. Gaind, N. Dalili, A. Meldrum, and Z. Jacob. "Momentum-resolved electron energy loss spectroscopy for mapping the photonic density of states". In: *ACS Photonics* 4.4 (2017), pp. 1009–1014. DOI: 10.1021/acsphotonics.7b00103.

[129] Z. Jacob. "Nanophotonics: Hyperbolic phonon-polaritons". In: *Nat. Mater.* 13 (2014), pp. 1081–1083. DOI: 10.1038/nmat4149.

[130] P. Li, M. Lewin, A. V. Kretinin, J. D. Caldwell, K. S. Novoselov, T. Taniguchi, K. Watanabe, F. Gaussmann, and T. Taubner. "Hyperbolic phonon-polaritons in boron nitride for near-field optical imaging and focusing". In: *Nat. Commun.* 6.7507 (2015). DOI: 10.1038/ncomms8507.

[131] F. J. Alfaro-Mozaz, P. Alonso-González, S. Vélez, I. Dolado, M. Autore, S. Mastel, F. Casanova, L. E. Hueso, P. Li, A. Y. Nikitin, and R. Hillenbrand. "Nanoimaging of resonating hyperbolic polaritons in linear boron nitride antennas". In: *Nat. Commun.* 8.15624 (2017). DOI: 10.1038/ncomms15624.

[132] M. Tamagnone, A. Ambrosio, K. Chaudhary, L. A. Jauregui, P. Kim, W. L. Wilson, and F. Capasso. "Ultra-confined mid-infrared resonant phonon polaritons in van der Waals nanostructures". In: *Science Advances* 4.6 (2018), eaat7189. DOI: 10.1126/sciadv.aat7189.

[133] A. Ambrosio, L. A. Jauregui, S. Dai, K. Chaudhary, M. Tamagnone, M. M. Fogler, D. N. Basov, F. Capasso, P. Kim, and W. L. Wilson. "Mechanical Detection and Imaging of Hyperbolic Phonon Polaritons in Hexagonal Boron Nitride". In: *ACS Nano* 11.9 (2017), pp. 8741–8746. DOI: 10.1021/acsnano.7b02323.

[134] A. Ambrosio, M. Tamagnone, K. Chaudhary, L. A. Jauregui, P. Kim, W. L. Wilson, and F. Capasso. "Selective excitation and imaging of ultraslow phonon polaritons in thin hexagonal boron nitride crystals". In: *Light Sci. Appl.* 7.27 (2018). DOI: 10.1038/s41377-018-0039-4.

[135] N. Rivera, T. Christensen, and P. Narang. "Phonon Polaritonics in Two-Dimensional Materials". In: *Nano Lett.* 19.4 (2019), pp. 2653–2660. DOI: 10.1021/acs.nanolett.9b00518.

[136] A. Poddubny, I. Iorsh, and Y. Kivshar. "Hyperbolic metamaterials". In: *Nat. Photonics* 7 (2013), pp. 948–957. DOI: 10.1038/nphoton.2013.243.

[137] J. D. Caldwell, A. V. Kretinin, Y. Chen, V. Giannini, M. M. Fogler, Y. Francescato, C. T. Ellis, J. G. Tischler, C. R. Woods, A. J. Giles, M. Hong, K. Watanabe, T. Taniguchi, S. A. Maier, and K. S. Novoselov. "Sub-diffractional volume-confined polaritons in the natural hyperbolic material hexagonal boron nitride". In: *Nat. Commun.* 5.5221 (2014). DOI: doi:10.1038/ncomms6221.

[138] A. A. Lucas and E. Kartheuser. "Energy-Loss Spectrum of Fast Electrons in a Dielectric Slab. I. Nonretarded Losses and Cherenkov Bulk Loss". In: *Phys. Rev. B* 1 (9 1970), pp. 3588–3598. DOI: 10.1103/PhysRevB.1.3588.

[139] C. H. Chen and J. Silcox. "Calculations of the electron-energy-loss probability in thin uniaxial crystals at oblique incidence". In: *Phys. Rev. B* 20 (1979), pp. 3605–3614. DOI: 10.1103/PhysRevB.20.3605.

[140] J. Heinrichs. "Phonons in Metal Films and Fast-Electron Energy Loss in the Phonon Spectral Range". In: *Phys. Rev. B* 5 (12 1972), pp. 4775–4792. DOI: 10.1103/PhysRevB.5.4775.

[141] K. L. Kliewer and Ronald Fuchs. "Optical Modes of Vibration in an Ionic Crystal Slab Including Retardation. I. Nonradiative Region". In: *Phys. Rev.* 144 (2 1966), pp. 495–503. DOI: 10.1103/PhysRev.144.495.

[142] A. Kumar, T. Low, K. H. Fung, P. Avouris, and N. X. Fang. "Tunable Light-Matter Interaction and the Role of Hyperbolicity in Graphene-hBN System". In: *Nano Lett.* 15.5 (2015), pp. 3172–3180. DOI: 10.1021/acs.nanolett.5b01191.

[143] S. Dai, Q. Ma, T. Andersen, A. S. McLeod, Z. Fei, M. K. Liu, M. Wagner, K. Watanabe, T. Taniguchi, M. Thiemens, F. Keilmann, P. Jarillo-Herrero, M. M. Fogler, and D. N. Basov. "Subdiffractional focusing and guiding of polaritonic rays in a natural hyperbolic material". In: *Nat. Commun.* 6.6963 (2015). DOI: 10.1038/ncomms7963.

[144] P. E. Batson and M. J. Lagos. "Characterization of misfit dislocations in Si quantum well structures enabled by STEM based aberration correction". In: *Ultramicroscopy* 180 (2017), pp. 34–40. DOI: 10.1016/j.ultramic.2017.03.002.

[145] F. S. Hage, R. J. Nicholls, J. R. Yates, Do. G. McCulloch, T. C. Lovejoy, N. Dellby, O. L. Krivanek, K. Refson, and Q. M. Ramasse. "Nanoscale momentum-resolved vibrational spectroscopy". In: *Sci. Adv.* 4.6 (2018), eaar7495. DOI: 10.1126/sciadv.aar7495.

[146] Z. Shi, H. A. Bechtel, S. Berweger, Y. Sun, B. Zeng, C. Jin, H. Chang, M. C. Martin, M. B. Raschke, and F. Wang. "Amplitude- and Phase-Resolved Nanospectral Imaging of Phonon Polaritons in Hexagonal Boron Nitride". In: *ACS Photonics* 2.7 (2015), pp. 790–796. DOI: 10.1021/acsphotonics.5b00007.

[147] P. Li, I. Dolado, F. J. Alfaro-Mozaz, A. Yu. Nikitin, F. Casanova, L. E. Hueso, S. Vélez, and R. Hillenbrand. "Optical Nanoimaging of Hyperbolic Surface Polaritons at the Edges of van der Waals Materials". In: *Nano Lett.* 17.1 (2017), pp. 228–235. DOI: 10.1021/acs.nanolett.6b03920.

[148] N. Talebi, C. Ozsoy-Keskinbora, H. M. Benia, K. Kern, C. T. Koch, and P. A. Van Aken. "Wedge Dyakonov waves and Dyakonov plasmons in topological insulator Bi2Se3 probed by electron beams". In: *ACS nano* 10.7 (2016), pp. 6988–6994. DOI: 10.1021/acsnano.6b02968.

[149] C. Dwyer. "Prospects of spatial resolution in vibrational electron energy loss spectroscopy: Implications of dipolar scattering". In: *Phys. Rev. B* 96 (22 2017), p. 224102. DOI: 10.1103/PhysRevB.96.224102.

[150] P. Moreau, N. Brun, C. A. Walsh, C. Colliex, and A. Howie. "Relativistic effects in electron-energy-loss-spectroscopy observations of the Si/SiO_2 interface plasmon peak". In: *Phys. Rev. B* 56 (11 1997), pp. 6774–6781. DOI: 10.1103/PhysRevB.56.6774.

[151] J. P. R. Bolton and M. Chen. "Electron energy loss in multilayered slabs". In: *Ultramicroscopy* 60.2 (1995), pp. 247–263. DOI: 10.1016/0304-3991(95)00066-0.

[152] U. Hohenester, A. Trügler, P. E. Batson, and M. J. Lagos. "Inelastic vibrational bulk and surface losses of swift electrons in ionic nanostructures". In: *Phys. Rev. B* 97 (16 2018), p. 165418. DOI: 10.1103/PhysRevB.97.165418.

[153] J. Kischkat, S. Peters, B. Gruska, M. Semtsiv, M. Chashnikova, M. Klinkmüller, O. Fedosenko, S. Machulik, A. Aleksandrova, G. Monastyrskyi, Y. Flores, and T. W. Masselink. "Mid-infrared optical properties of thin films of aluminum oxide, titanium dioxide, silicon dioxide, aluminum nitride, and silicon nitride". In: *Appl. Opt.* 51.28 (2012), pp. 6789–6798. DOI: 10.1364/AO.51.006789.

[154] E. D. Palik. *Handbook of optical constants of solids*. Academic Press, 1998.

[155] H. Lourenço-Martins and M. Kociak. "Vibrational Surface Electron-Energy-Loss Spectroscopy Probes Confined Surface-Phonon Modes". In: *Phys. Rev. X* 7 (4 2017), p. 041059. DOI: 10.1103/PhysRevX.7.041059.

[156] T. C. Lovejoy, G. C. Corbin, N. Dellby, M. V. Hoffman, and O. L. Krivanek. "Advances in Ultra-High Energy Resolution STEM-EELS". In: *Microscopy and Microanalysis* 24.S1 (2018), pp. 446–447. DOI: 10.1017/S1431927618002726.

[157] M. Morita, T. Ohmi, E. Hasegawa, M. Kawakami, and M. Ohwada. "Growth of native oxide on a silicon surface". In: *J. Appl. Phys.* 68.3 (1990), pp. 1272–1281.

[158] D. A. Muller, T. Sorsch, S. Moccio, F. H. Baumann, K. Evans-Lutterodt, and G. Timp. "The electronic structure at the atomic scale of ultrathin gate oxides". In: *Nature* 399.6738 (1999), pp. 758–761. DOI: 10.1038/21602.

[159] A. J. Huber, J. Wittborn, and R. Hillenbrand. "Infrared spectroscopic near-field mapping of single nanotransistors". In: *Nanotechnology* 21.23 (2010), p. 235702.

[160] A. A. Lucas and M. Šunjić. "Fast-electron spectroscopy of collective excitations in solids". In: *Prog. Surf. Sci.* 2 (1972), pp. 75–137.

[161] H. Boersch, J. Geiger, and W. Stickel. "Interaction of 25-keV Electrons with Lattice Vibrations in LiF. Experimental Evidence for Surface Modes of Lattice Vibration". In: *Phys. Rev. Lett.* 17 (7 1966), pp. 379–381. DOI: 10.1103/PhysRevLett.17.379.

[162] Ph. Lambin, J. P. Vigneron, and A. A. Lucas. "Electron-energy-loss spectroscopy of multilayered materials: Theoretical aspects and study of interface optical phonons in semiconductor superlattices". In: *Phys. Rev. B* 32 (12 1985), pp. 8203–8215. DOI: 10.1103/PhysRevB.32.8203.

[163] M. J. Lagos and P. E. Batson. "Thermometry with Subnanometer Resolution in the Electron Microscope Using the Principle of Detailed Balancing". In: *Nano Lett.* 18.7 (2018), pp. 4556–4563. DOI: 10.1021/acs.nanolett.8b01791.

[164] X. Yan, C. A. Gadre, S. Dai, K. Yu, and X. Pan. "Investigating Thermal Behavior of Surface Phonon in SiC by in-situ Vibrational Spectroscopy". In: *Microsc. Microanal.* 24.S1 (2018), pp. 416–417. DOI: 10.1017/S143192761800257X.

[165] L. Gavioli, M. G. Betti, and C. Mariani. "Dynamics-Induced Surface Metallization of Si(100)". In: *Phys. Rev. Lett.* 77 (18 1996), pp. 3869–3872. DOI: 10.1103/PhysRevLett.77.3869.

[166] B. N. J. Persson and J. E. Demuth. "High-resolution electron-energy-loss study of the surfaces and energy gaps of cleaved high-temperature superconductors". In: *Phys. Rev. B* 42 (13 1990), pp. 8057–8072. DOI: 10.1103/PhysRevB.42.8057.

[167] A. Kogar, M. S. Rak, S. Vig, A. A. Husain, F. Flicker, Y. I. Joe, L. Venema, G. J. MacDougall, T. C. Chiang, E. Fradkin, J. van Wezel, and P. Abbamonte. "Signatures of exciton condensation in a transition metal dichalcogenide". In: *Science* 358.6368 (2017), pp. 1314–1317. DOI: 10.1126/science.aam6432.

[168] M. Mecklenburg, W. A. Hubbard, E. R. White, R. Dhall, S. B. Cronin, S. Aloni, and B. C. Regan. "Nanoscale temperature mapping in operating microelectronic devices". In: *Science* 347.6222 (2015), pp. 629–632. DOI: 10.1126/science.aaa2433.

[169] X. Hu, P. Yasaei, J. Jokisaari, S. Öğüut, A. Salehi-Khojin, and R. F. Klie. "Mapping Thermal Expansion Coefficients in Freestanding 2D Materials at the Nanometer Scale". In: *Phys. Rev. Lett.* 120 (5 2018), p. 055902. DOI: 10.1103/PhysRevLett.120.055902.

[170] A. Rivacoba and N. Zabala. "Relativistic force between fast electrons and planar targets". In: *New J. Phys.* 16.7 (2014), p. 073048. DOI: 10.1088/1367-2630/16/7/073048.

[171] W. G. Spitzer, D. Kleinman, and D. Walsh. "Infrared Properties of Hexagonal Silicon Carbide". In: *Phys. Rev.* 113 (1 1959), pp. 127–132. DOI: 10.1103/PhysRev.113.127.

[172] P. E. Batson and M.J. Lagos. "Interpretation of meV Resolution Phonon EELS Data". In: *Microsc. Microanal.* 24.S1 (2018), pp. 412–413. DOI: 10.1017/S1431927618002556.

[173] P. J. Hendra and P. M. Stratton. "Laser-Raman spectroscopy". In: *Chem. Rev.* 69.3 (1969), pp. 325–344. DOI: 10.1021/cr60259a003.

[174] R. Zhang, Y. Zhang, Z. C. Dong, S. Jiang, C. Zhang, L. G. Chen, L. Zhang, Y. Liao, J. Aizpurua, Y. Luo, J. L. Yang, and J. G. Hou. "Chemical mapping of a single molecule by plasmon-enhanced Raman scattering". In: *Nature* 498.7452 (2013), pp. 82–86. DOI: 10.1038/nature12151.

[175] P. Alonso-González, P. Albella, M. Schnell, J. Chen, F. Huth, A. García-Etxarri, F. Casanova, F. Golmar, L. Arzubiaga, L. E. Hueso, J. Aizpurua, and R. Hillenbrand. "Resolving the electromagnetic mechanism of surface-enhanced light scattering at single hot spots". In: *Nat. Commun.* 3.684 (2012). DOI: 10.1038/ncomms1674.

[176] F. Huth, A. Govyadinov, S. Amarie, W. Nuansing, F. Keilmann, and R. Hillenbrand. "Nano-FTIR Absorption Spectroscopy of Molecular Fingerprints at 20 nm Spatial Resolution". In: *Nano Lett.* 12.8 (2012), pp. 3973–3978. DOI: 10.1021/nl301159v.

[177] I. Amenabar, S. Poly, W. Nuansing, E. H. Hubrich, A. A. Govyadinov, F. Huth, R. Krutokhvostov, L. Zhang, M. Knez, J. Heberle, A. M. Bittner, and R. Hillenbrand. "Structural analysis and mapping of individual protein complexes by infrared nanospectroscopy". In: *Nat. Commun.* 4.1890 (2013). DOI: 10.1038/ncomms3890.

[178] Y. Zhang, Q.-S. Meng, L. Zhang, Y. Luo, Y.-J. Yu, B. Yang, Y. Zhang, R. Esteban, J. Aizpurua, Y. Luo, J.-L. Yang, Z.-C. Dong, and J. G. Hou. "Sub-nanometre control of the coherent interaction between a single molecule and a plasmonic nanocavity". In: *Nat. Commun.* 8.15225 (2017). DOI: 10.1038/ncomms15225.

[179] P. Hildebrandt and M. Stockburger. "Surface-enhanced resonance Raman spectroscopy of Rhodamine 6G adsorbed on colloidal silver". In: *J. Phys. Chem.* 88.24 (1984), pp. 5935–5944. DOI: 10.1021/j150668a038.

[180] H. Xu, E. J. Bjerneld, M. Käll, and L. Börjesson. "Spectroscopy of Single Hemoglobin Molecules by Surface Enhanced Raman Scattering". In: *Phys. Rev. Lett.* 83 (21 1999), pp. 4357–4360. DOI: 10.1103/PhysRevLett.83.4357.

[181] R. Adato, A. A. Yanik, J. J. Amsden, D. L. Kaplan, F. G. Omenetto, M. K. Hong, S. Erramilli, and H. Altug. "Ultra-sensitive vibrational spectroscopy of protein monolayers with plasmonic nanoantenna arrays". In: *Proc. Natl. Acad. Sci. U.S.A.* 106.46 (2009), pp. 19227–19232. DOI: 10.1073/pnas.0907459106.

[182] T. Neuman, C. Huck, J. Vogt, F. Neubrech, R. Hillenbrand, J. Aizpurua, and A. Pucci. "Importance of Plasmonic Scattering for an Optimal Enhancement of Vibrational Absorption in SEIRA with Linear Metallic Antennas". In: *J. Phys. Chem. C* 119.47 (2015), pp. 26652–26662. DOI: 10.1021/acs.jpcc.5b08344.

[183] R.F. Egerton, P. Li, and M. Malac. "Radiation damage in the TEM and SEM". In: *Micron* 35.6 (2004), pp. 399–409. DOI: 10.1016/j.micron.2004.02.003.

[184] R.F. Egerton. "Scattering delocalization and radiation damage in STEM-EELS". In: *Ultramicroscopy* 180 (2017), pp. 115–124. DOI: 10.1016/j.ultramic.2017.02.007.

[185] B. H. Stuart. *Infrared Spectroscopy: Fundamentals and Applications*. John Wiley & Sons, 2004.

[186] C. Choe, J. Lademann, and M. E. Darvin. "Depth profiles of hydrogen bound water molecule types and their relation to lipid and protein interaction in the human stratum corneum in vivo". In: *Analyst* 141.22 (2016), pp. 6329–6337. DOI: 10.1039/C6AN01717G.

[187] T. L. Ferrell, R. J. Warmack, V. E. Anderson, and P. M. Echenique. "Analytical calculation of stopping power for isolated small spheres". In: *Phys. Rev. B* 35 (14 1987), pp. 7365–7371. DOI: 10.1103/PhysRevB.35.7365.

[188] G. M. Hale and M. R. Querry. "Optical constants of water in the 200-nm to 200-µm wavelength region". In: *Appl. Opt.* 12.3 (1973), pp. 555–563. DOI: 10.1364/AO.12.000555.

[189] L. J. Allen, H. G. Brown, S. D. Findlay, and B. D. Forbes. "A quantum mechanical exploration of phonon energy-loss spectroscopy using electrons in the aloof beam geometry". In: *Microscopy* 67 (2017), pp. i24–i29. DOI: 10.1093/jmicro/dfx038.

[190] G. W. Bryant, F. J. García de Abajo, and J. Aizpurua. "Mapping the Plasmon Resonances of Metallic Nanoantennas". In: *Nano Lett.* 8.2 (2008), pp. 631–636. DOI: 10.1021/nl073042v.

[191] J. Aizpurua, G. W. Bryant, L. J. Richter, F. J. García de Abajo, B. K. Kelley, and T. Mallouk. "Optical properties of coupled metallic nanorods for field-enhanced spectroscopy". In: *Phys. Rev. B* 71 (23 2005), p. 235420. DOI: 10.1103/PhysRevB.71.235420.

[192] U. Hohenester and A. Trügler. "MNPBEM – A Matlab toolbox for the simulation of plasmonic nanoparticles". In: *Comput. Phys. Commun.* 183.2 (2012), pp. 370 –381. DOI: 10.1016/j.cpc.2011.09.009.

[193] S. M. Collins, O. Nicoletti, D. Rossouw, T. Ostasevicius, and P. A. Midgley. "Excitation dependent Fano-like interference effects in plasmonic silver nanorods". In: *Phys. Rev. B* 90 (15 2014), p. 155419. DOI: 10.1103/PhysRevB.90.155419.

[194] T. J. Antosiewicz, S. P. Apell, and T. Shegai. "Plasmon-Exciton Interactions in a Core-Shell Geometry: From Enhanced Absorption to Strong Coupling". In: *ACS Photonics* 1.5 (2014), pp. 454–463. DOI: 10.1021/ph500032d.

[195] A. E. Schlather, N. Large, A. S. Urban, P. Nordlander, and N. J. Halas. "Near-Field Mediated Plexcitonic Coupling and Giant Rabi Splitting in Individual Metallic Dimers". In: *Nano Lett.* 13.7 (2013), pp. 3281–3286. DOI: 10.1021/nl4014887.

[196] N. T. Fofang, T.-H. Park, O. Neumann, N. A. Mirin, P. Nordlander, and N. J. Halas. "Plexcitonic Nanoparticles: Plasmon-Exciton Coupling in Nanoshell-J-Aggregate Complexes". In: *Nano Lett.* 8.10 (2008), pp. 3481–3487. DOI: 10.1021/nl8024278.

[197] V. Giannini, Y. Francescato, H. Amrania, C. C. Phillips, and S. A. Maier. "Fano resonances in nanoscale plasmonic systems: a parameter-free modeling approach". In: *Nano Lett.* 11.7 (2011), pp. 2835–2840. DOI: 10.1021/nl201207n.

[198] L. Henrard and P. Lambin. "Calculation of the energy loss for an electron passing near giant fullerenes". In: *J. Phys. B* 29.21 (1996), pp. 5127–5141. DOI: 10.1088/0953-4075/29/21/024.

[199] B. S. Guiton, V. Iberi, S. Li, D. N. Leonard, C. M. Parish, P. G. Kotula, M. Varela, G. C. Schatz, S. J. Pennycook, and J. P. Camden. "Correlated Optical Measurements and Plasmon Mapping of Silver Nanorods". In: *Nano Lett.* 11.8 (2011), pp. 3482–3488. DOI: 10.1021/nl202027h.

[200] P. Vasa, W. Wang, R. Pomraenke, M. Lammers, M. Maiuri, C. Manzoni, G. Cerullo, and C. Lienau. "Real-time observation of ultrafast Rabi oscillations between excitons and plasmons in metal nanostructures with J-aggregates". In: *Nature Photonics* 7.2 (2013), pp. 128–132. DOI: 10.1038/nphoton.2012.340.

[201] R. Esteban, J. Aizpurua, and G. W. Bryant. "Strong coupling of single emitters interacting with phononic infrared antennae". In: *New J. Phys.* 16.1 (2014), p. 013052. DOI: 10.1088/1367-2630/16/1/013052.

[202] T. W. Ebbesen. "Hybrid Light-Matter States in a Molecular and Material Science Perspective". In: *Acc. Chem. Res.* 49.11 (2016), pp. 2403–2412. DOI: 10.1021/acs.accounts.6b00295.

[203] J. A. Hutchison, T. Schwartz, C. Genet, E. Devaux, and T. W. Ebbesen. "Modifying chemical landscapes by coupling to vacuum fields". In: *Angew. Chem. Int. Ed.* 51.7 (2012), pp. 1592–1596. DOI: 10.1002/anie.201107033.

[204] P. Törmä and W. L. Barnes. "Strong coupling between surface plasmon polaritons and emitters: a review". In: *Rep. Prog. Phys.* 78.1 (2015), p. 013901. DOI: 10.1088/0034-4885/78/1/013901.

[205] R. D. Artuso and G. W. Bryant. "Optical Response of Strongly Coupled Quantum Dot-Metal Nanoparticle Systems: Double Peaked Fano Structure and Bistability". In: *Nano Lett.* 8.7 (2008), pp. 2106–2111. DOI: 10.1021/nl800921z.

[206] D. E. Gómez, K. C. Vernon, P. Mulvaney, and T. J. Davis. "Surface Plasmon Mediated Strong Exciton-Photon Coupling in Semiconductor Nanocrystals". In: *Nano Lett.* 10.1 (2010), pp. 274–278. DOI: 10.1021/nl903455z.

[207] H. Wang, H.-Y. Wang, A. Toma, T. Yano, Q.-D. Chen, H.-L. Xu, H.-B. Sun, and R. P. Zaccaria. "Dynamics of Strong Coupling between CdSe Quantum Dots and Surface Plasmon Polaritons in Subwavelength Hole Array". In: *J. Phys. Chem. Lett.* 7.22 (2016), pp. 4648–4654. DOI: 10.1021/acs.jpclett.6b02059.

[208] J. Wei, N. Jiang, J. Xu, X. Bai, and J. Liu. "Strong coupling between ZnO excitons and localized surface plasmons of silver nanoparticles studied by STEM-EELS". In: *Nano Lett.* 15.9 (2015), pp. 5926–5931. DOI: 10.1021/acs.nanolett.5b02030.

[209] K. Santhosh, O. Bitton, L. Chuntonov, and G. Haran. "Vacuum Rabi splitting in a plasmonic cavity at the single quantum emitter limit". In: *Nat. Commun.* 7.11823 (2016). DOI: 10.1038/ncomms11823.

[210] J. Wen, H. Wang, W. Wang, Z. Deng, C. Zhuang, Y. Zhang, F. Liu, J. She, J. Chen, H. Chen, S. Dens, and N. Xu. "Room-temperature strong light–matter interaction with active control in single plasmonic nanorod coupled with two-dimensional atomic crystals". In: *Nano Lett.* 17.8 (2017), pp. 4689–4697. DOI: 10.1021/acs.nanolett.7b01344.

[211] M. Stührenberg, B. Munkhbat, D. G. Baranov, J. Cuadra, A. B. Yankovich, T. J. Antosiewicz, E. Olsson, and T. Shegai. "Strong Light-Matter Coupling between Plasmons in Individual Gold Bi-pyramids and Excitons in Mono- and Multilayer WSe2". In: *Nano Lett.* 18.9 (2018), pp. 5938–5945. DOI: 10.1021/acs.nanolett.8b02652.

[212] G. A. Wurtz, P. R. Evans, W. Hendren, R. Atkinson, W. Dickson, R. J. Pollard, A. V. Zayats, W. Harrison, and C. Bower. "Molecular Plasmonics with Tunable Exciton–Plasmon Coupling Strength in J-Aggregate Hybridized Au Nanorod Assemblies". In: *Nano Lett.* 7.5 (2007), pp. 1297–1303. DOI: 10.1021/nl070284m.

[213] G. P. Wiederrecht, G. A. Wurtz, and J. Hranisavljevic. "Coherent coupling of molecular excitons to electronic polarizations of noble metal nanoparticles". In: *Nano Lett.* 4.11 (2004), pp. 2121–2125. DOI: 10.1021/nl0488228.

[214] J. Bellessa, C. Bonnand, J. C. Plenet, and J. Mugnier. "Strong Coupling between Surface Plasmons and Excitons in an Organic Semiconductor". In: *Phys. Rev. Lett.* 93 (3 2004), p. 036404. DOI: 10.1103/PhysRevLett.93.036404.

[215] G. Zengin, M. Wersäll, S. Nilsson, T. J. Antosiewicz, M. Käll, and T. Shegai. "Realizing strong light-matter interactions between single-nanoparticle plasmons and molecular excitons at ambient conditions". In: *Phys. Rev. Lett.* 114.15 (2015), p. 157401. DOI: 10.1103/PhysRevLett.114.157401.

[216] D. Melnikau, R. Esteban, D. Savateeva, A. Sánchez-Iglesias, M. Grzelczak, M. K. Schmidt, L. M. Liz-Marzán, J. Aizpurua, and Y. P. Rakovich. "Rabi Splitting in Photoluminescence Spectra of Hybrid Systems of Gold Nanorods and J-Aggregates". In: *J. Phys. Chem. Lett.* 7.2 (2016), pp. 354–362. DOI: 10.1021/acs.jpclett.5b02512.

[217] A. Manjavacas, F. J. García de Abajo, and P. Nordlander. "Quantum Plexcitonics: Strongly Interacting Plasmons and Excitons". In: *Nano Lett.* 11.6 (2011), pp. 2318–2323. DOI: 10.1021/nl200579f.

[218] R. Chikkaraddy, B. de Nijs, F. Benz, S. J. Barrow, O. A. Scherman, E. Rosta, A. Demetriadou, P. Fox, O. Hess, and J. J. Baumberg. "Single-molecule strong coupling at room temperature in plasmonic nanocavities". In: *Nature* 535.7610 (2016), pp. 127–130. DOI: 10.1038/nature17974.

[219] A. M. Poyli, A. Garcia-Etxarri, M. Schnell, R. Hillenbrand, and J. Aizpurua. "Infrared phononic nanoantennas: Localized surface phonon polaritons in SiC disks". In: *Chinese Sci. Bull.* 55.24 (2010), pp. 2625–2628. DOI: 10.1007/s11434-010-4032-4.

[220] T. Glaser, S. Beck, B. Lunkenheimer, D. Donhauser, A. Köhn, M. Kröger, and A. Pucci. "Infrared study of the MoO_3 doping efficiency in 4,4'-bis(N-carbazolyl)-1,1'-biphenyl (CBP)". In: *Org. Electron.* 14.2 (2013), pp. 575 – 583. DOI: https://doi.org/10.1016/j.orgel.2012.11.031.

[221] R. Kalousek, P. Dub, L. Břínek, and T. Šikola. "Response of plasmonic resonant nanorods: an analytical approach to optical antennas". In: *Opt. Express* 20.16 (2012), pp. 17916–17927. DOI: 10.1364/OE.20.017916.

[222] F. J. García de Abajo and A. Howie. "Retarded field calculation of electron energy loss in inhomogeneous dielectrics". In: *Phys. Rev. B* 65 (11 2002), p. 115418. DOI: 10.1103/PhysRevB.65.115418.

[223] G. Boudarham and M. Kociak. "Modal decompositions of the local electromagnetic density of states and spatially resolved electron energy loss probability in terms of geometric modes". In: *Phys. Rev. B* 85 (24 2012), p. 245447. DOI: 10.1103/PhysRevB.85.245447.

[224] H. Cohen, T. Maniv, R. Tenne, Y. Rosenfeld Hacohen, O. Stephan, and C. Colliex. "Near-Field Electron Energy Loss Spectroscopy of Nanoparticles". In: *Phys. Rev. Lett.* 80 (4 1998), pp. 782–785. DOI: 10.1103/PhysRevLett.80.782.

[225] A. I. Kuznetsov, A. E. Miroshnichenko, M. L. Brongersma, Y. S. Kivshar, and B. Luk'yanchuk. "Optically resonant dielectric nanostructures". In: *Science* 354.6314 (2016), aag2472. DOI: 10.1126/science.aag2472.

[226] S. Jahani and Z. Jacob. "All-dielectric metamaterials". In: *Nat. Nanotechnol.* 11.1 (2016), p. 23. DOI: 10.1038/nnano.2015.304.

[227] R. Verre, D. G. Baranov, B. Munkhbat, J. Cuadra, M. Käll, and T. Shegai. "Transition metal dichalcogenide nanodisks as high-index dielectric Mie nanoresonators". In: *arXiv preprint arXiv:1812.04076* (2018). URL: https://arxiv.org/pdf/1812.04076.pdf.

[228] A. B. Evlyukhin, S. M. Novikov, U. Zywietz, R. L. Eriksen, C. Reinhardt, S. I. Bozhevolnyi, and B. N. Chichkov. "Demonstration of magnetic dipole resonances of dielectric nanospheres in the visible region". In: *Nano Lett.* 12.7 (2012), pp. 3749–3755. DOI: 10.1021/nl301594s.

[229] P. Albella, R. Alcaraz de la Osa, F. Moreno, and S. A. Maier. "Electric and Magnetic Field Enhancement with Ultralow Heat Radiation Dielectric Nanoantennas: Considerations for Surface-Enhanced Spectroscopies". In: *ACS Photonics* 1.6 (2014), pp. 524–529. DOI: 10.1021/ph500060s.

[230] J. Cambiasso, G. Grinblat, Y. Li, A. Rakovich, E. Cortés, and S. A. Maier. "Bridging the Gap between Dielectric Nanophotonics and the Visible Regime with Effectively Lossless Gallium Phosphide Antennas". In: *Nano Lett.* 17.2 (2017), pp. 1219–1225. DOI: 10.1021/acs.nanolett.6b05026.

[231] M. Caldarola, P. Albella, E. Cortés, M. Rahmani, T. Roschuk, G. Grinblat, R. F. Oulton, A. V. Bragas, and S. A. Maier. "Non-plasmonic nanoantennas for surface enhanced spectroscopies with ultra-low heat conversion". In: *Nat. Commun.* 6.7915 (2015). DOI: 10.1038/ncomms8915.

[232] A. Garcia-Etxarri, R. Gómez-Medina, L. S. Froufe-Perez, C. López, L. Chantada, F. Scheffold, J. Aizpurua, M. Nieto-Vesperinas, and J. J. Sáenz. "Strong magnetic response of submicron Silicon particles in the infrared". In: *Opt. Express* 19.6 (2011), pp. 4815–4826.

[233] P. Albella, M. A. Poyli, M. K. Schmidt, S. A. Maier, F. Moreno, J. J. Saáenz, and J. Aizpurua. "Low-loss electric and magnetic field-enhanced spectroscopy with subwavelength silicon dimers". In: *J. Phys. Chem. C* 117.26 (2013), pp. 13573–13584. DOI: 10.1021/jp4027018.

[234] U. Zywietz, M. K. Schmidt, A. B. Evlyukhin, C. Reinhardt, J. Aizpurua, and B. N. Chichkov. "Electromagnetic resonances of silicon nanoparticle dimers in the visible". In: *ACS Photonics* 2.7 (2015), pp. 913–920. DOI: 10.1021/acsphotonics.5b00105.

[235] A. E. Krasnok, A. E. Miroshnichenko, P. A. Belov, and Y. S Kivshar. "All-dielectric optical nanoantennas". In: *Opt. Express* 20.18 (2012), pp. 20599–20604. DOI: 10.1364/OE.20.020599.

[236] R. M. Bakker, D. Permyakov, Y. F. Yu, D. Markovich, R. Paniagua-Domínguez, L. Gonzaga, A. Samusev, Y. Kivshar, B. Luk'yanchuk, and A. I. Kuznetsov. "Magnetic and Electric Hotspots with Silicon Nanodimers". In: *Nano Lett.* 15.3 (2015), pp. 2137–2142. DOI: 10.1021/acs.nanolett.5b00128.

[237] A. F. Cihan, A. G. Curto, S. Raza, P. G. Kik, and M. L. Brongersma. "Silicon Mie resonators for highly directional light emission from monolayer MoS 2". In: *Nat. Photonics* 12.5 (2018), pp. 284–290. DOI: 10.1038/s41566-018-0155-y.

[238] R. Regmi, J. Berthelot, P. M. Winkler, M. Mivelle, J. Proust, F. Bedu, I. Ozerov, T. Begou, J. Lumeau, H. Rigneault, M. F. García-Parajó, S. Bidault, J. Wenger, and N. Bonod. "All-Dielectric Silicon Nanogap Antennas To Enhance the Fluorescence of Single Molecules". In: *Nano Lett.* 16.8 (2016), pp. 5143–5151. DOI: 10.1021/acs.nanolett.6b02076.

[239] V. Rutckaia, F. Heyroth, A. Novikov, M. Shaleev, M. Petrov, and J. Schilling. "Quantum Dot Emission Driven by Mie Resonances in Silicon Nanostructures". In: *Nano Lett.* 17.11 (2017), pp. 6886–6892. DOI: 10.1021/acs.nanolett.7b03248.

[240] M. K. Schmidt, R. Esteban, J.J. Sáenz, I. Suárez-Lacalle, S. Mackowski, and J. Aizpurua. "Dielectric antennas-a suitable platform for controlling magnetic dipolar emission". In: *Opt. Express* 20.13 (2012), pp. 13636–13650. DOI: 10.1364/OE.20.013636.

[241] A. Vaskin, S. Mashhadi, M. Steinert, K. E. Chong, D. Keene, S. Nanz, A. Abass, E. Rusak, D.-Y. Choi, I. Fernandez-Corbaton, T. Pertsch, C. Rockstuhl, M. A. Noginov, Y. S. Kivshar, D. N. Neshev, N. Noginova, and I. Staude. "Manipulation of Magnetic Dipole Emission from Eu3+ with Mie-Resonant Dielectric Metasurfaces". In: *Nano Lett.* 19.2 (2019), pp. 1015–1022. DOI: 10.1021/acs.nanolett.8b04268.

[242] A. García-Etxarri and J. A. Dionne. "Surface-enhanced circular dichroism spectroscopy mediated by nonchiral nanoantennas". In: *Phys. Rev. B* 87 (23 2013), p. 235409. DOI: 10.1103/PhysRevB.87.235409.

[243] C.-S. Ho, A. Garcia-Etxarri, Y. Zhao, and J. Dionne. "Enhancing Enantioselective Absorption Using Dielectric Nanospheres". In: *ACS Photonics* 4.2 (2017), pp. 197–203. DOI: 10.1021/acsphotonics.6b00701.

[244] I. Alessandri and J. R. Lombardi. "Enhanced Raman Scattering with Dielectrics". In: *Chem. Rev.* 116.24 (2016), pp. 14921–14981. DOI: 10.1021/acs.chemrev.6b00365.

[245] H. Wang, J. Wen, W. Wang, N. Xu, P. Liu, J. Yan, H. Chen, and S. Deng. "Resonance Coupling in Heterostructures Composed of Silicon Nanosphere and Monolayer WS2: A Magnetic-Dipole-Mediated Energy Transfer Process". In: *ACS Nano* 13.2 (2019), pp. 1739–1750. DOI: 10.1021/acsnano.8b07826.

[246] C. Wu, N. Arju, G. Kelp, J. A. Fan, J. Dominguez, E. Gonzales, E. Tutuc, I. Brener, and G. Shvets. "Spectrally selective chiral silicon metasurfaces based on infrared Fano resonances". In: *Nat. Commun.* 5.3892 (2014). DOI: 10.1038/ncomms4892.

[247] I. Staude and J. Schilling. "Metamaterial-inspired silicon nanophotonics". In: *Nat. Photonics* 11.5 (2017), p. 274. DOI: 10.1038/nphoton.2017.39.

[248] J. Proust, F. Bedu, B. Gallas, I. Ozerov, and N. Bonod. "All-Dielectric Colored Metasurfaces with Silicon Mie Resonators". In: *ACS Nano* 10.8 (2016), pp. 7761–7767. DOI: 10.1021/acsnano.6b03207.

[249] T. G. Habteyes, I. Staude, K. E. Chong, J. Dominguez, M. Decker, A. Miroshnichenko, Y. Kivshar, and I. Brener. "Near-Field Mapping of Optical Modes on All-Dielectric Silicon Nanodisks". In: *ACS Photonics* 1.9 (2014), pp. 794–798. DOI: 10.1021/ph500232u.

[250] A. E. Miroshnichenko, A. B. Evlyukhin, Y. F. Yu, R. M. Bakker, A. Chipouline, A. I. Kuznetsov, B. Luk'yanchuk, B. N. Chichkov, and Y. S. Kivshar. "Nonradiating anapole modes in dielectric nanoparticles". In: *Nat. Commun.* 6.8069 (2015). DOI: 10.1038/ncomms9069.

[251] A. Yu. Frolov, N. Verellen, J. Li, X. Zheng, H. Paddubrouskaya, D. Denkova, M. R. Shcherbakov, G. A. E. Vandenbosch, V. I. Panov, P. Van Dorpe, A. A. Fedyanin, and V. V. Moshchalkov. "Near-Field Mapping of Optical Fabry-Perot Modes in All-Dielectric Nanoantennas". In: *Nano Lett.* 17.12 (2017), pp. 7629–7637. DOI: 10.1021/acs.nanolett.7b03624.

[252] T. Coenen, J. van de Groep, and A. Polman. "Resonant Modes of Single Silicon Nanocavities Excited by Electron Irradiation". In: *ACS Nano* 7.2 (2013), pp. 1689–1698. DOI: 10.1021/nn3056862.

[253] J. van de Groep, T. Coenen, S. A. Mann, and A. Polman. "Direct imaging of hybridized eigenmodes in coupled silicon nanoparticles". In: *Optica* 3.1 (2016), pp. 93–99.

[254] M. A. van de Haar, J. van de Groep, B. J. M. Brenny, and A. Polman. "Controlling magnetic and electric dipole modes in hollow silicon nanocylinders". In: *Opt. Express* 24.3 (2016), pp. 2047–2064. DOI: 10.1364/OE.24.002047.

[255] Y. Fang, R. Verre, L. Shao, P. Nordlander, and M. Käll. "Hot Electron Generation and Cathodoluminescence Nanoscopy of Chiral Split Ring Resonators". In: *Nano Lett.* 16.8 (2016), pp. 5183–5190. DOI: 10.1021/acs.nanolett.6b02154.

[256] Q. Liu, S. C. Quillin, D. J. Masiello, and P. A. Crozier. "Nanoscale probing of resonant photonic modes in dielectric nanoparticles with focused electron beams". In: *Phys. Rev. B* 99 (16 2019), p. 165102. DOI: 10.1103/PhysRevB.99.165102.

[257] K. Y. Bliokh, Y. P. Bliokh, S. Savel'ev, and F. Nori. "Semiclassical Dynamics of Electron Wave Packet States with Phase Vortices". In: *Phys. Rev. Lett.* 99 (19 2007), p. 190404. DOI: 10.1103/PhysRevLett.99.190404.

[258] A. Béché, R. Van Bosem, G. Van Tendeloo, and J. Verbeeck. "Magnetic monopole field exposed by electrons". In: *Nat. Phys.* 10 (2014), pp. 26–29. DOI: 10.1038/nphys2816.

[259] E. Mafakheri, A. H. Tavabi, P.-H. Lu, R. Balboni, F. Venturi, C. Menozzi, G. C. Gazzadi, S. Frabboni, A. Sit, R. E. Dunin-Borkowski, E. Karimi, and V. Grillo. "Realization of electron vortices with large orbital angular momentum using miniature holograms fabricated by electron beam lithography". In: *Appl. Phys. Lett.* 110.9 (2017), p. 093113. DOI: 10.1063/1.4977879.

[260] G. Guzzinati, P. Schattschneider, K. Y. Bliokh, F. Nori, and J. Verbeeck. "Observation of the Larmor and Gouy Rotations with Electron Vortex Beams". In: *Phys. Rev. Lett.* 110 (9 2013), p. 093601. DOI: 10.1103/PhysRevLett.110.093601.

[261] V. Grillo, T. R. Harvey, F. Venturi, J. S. Pierce, R. Balboni, F. Bouchard, G. C. Gazzadi, S. Frabboni, A. H. Tavabi, Z.-A. Li, R. E. Dunin-Borkowski, R. W. Boyd, B. J. McMorran, and E. Karimi. "Observation of nanoscale magnetic fields using twisted electron beams". In: *Nat. Commun.* 8.689 (2017). DOI: 10.1038/s41467-017-00829-5.

[262] J. Verbeeck, H. Tian, and P. Schattschneider. "Production and application of electron vortex beams". In: *Nature* 467.7313 (2010), pp. 301–304. DOI: 10.1038/nature09366.

[263] S. Lloyd, M. Babiker, and J. Yuan. "Quantized Orbital Angular Momentum Transfer and Magnetic Dichroism in the Interaction of Electron Vortices with Matter". In: *Phys. Rev. Lett.* 108 (7 2012), p. 074802. DOI: 10.1103/PhysRevLett.108.074802.

[264] J. Yuan, S. M. Lloyd, and M. Babiker. "Chiral-specific electron-vortex-beam spectroscopy". In: *Phys. Rev. A* 88 (3 2013), p. 031801. DOI: 10.1103/PhysRevA.88.031801.

[265] J. Rusz, J.-C. Idrobo, and L. Wrang. "Vorticity in electron beams: Definition, properties, and its relationship with magnetism". In: *Phys. Rev. B* 94 (14 2016), p. 144430. DOI: 10.1103/PhysRevB.94.144430.

[266] R. Juchtmans, A. Béché, A. Abakumov, M. Batuk, and J. Verbeeck. "Using electron vortex beams to determine chirality of crystals in transmission electron microscopy". In: *Phys. Rev. B* 91 (9 2015), p. 094112. DOI: 10.1103/PhysRevB.91.094112.

[267] Z. Mohammadi, C. P. Van Vlack, S. Hughes, J. Bornemann, and R. Gordon. "Vortex electron energy loss spectroscopy for near-field mapping of magnetic plasmons". In: *Opt. Express* 20.14 (2012), pp. 15024–15034. DOI: 10.1364/OE.20.015024.

[268] D. Ugarte and C. Ducati. "Controlling multipolar surface plasmon excitation through the azimuthal phase structure of electron vortex beams". In: *Phys. Rev. B* 93 (20 2016), p. 205418. DOI: 10.1103/PhysRevB.93.205418.

[269] M. Zanfrognini, E. Rotunno, S. Frabboni, A. Sit, E. Karimi, U. Hohenester, and V. Grillo. "Orbital Angular Momentum and Energy Loss Characterization of Plasmonic Excitations in Metallic Nanostructures in TEM". In: *ACS Photonics* 6.3 (2019), pp. 620–627. DOI: 10.1021/acsphotonics.9b00131.

[270] A. Asenjo-Garcia and F. J. García de Abajo. "Dichroism in the interaction between vortex electron beams, plasmons, and molecules". In: *Phys. Rev. Lett.* 113.6 (2014), p. 066102. DOI: 10.1103/PhysRevLett.113.066102.

[271] G. M. Vanacore, G. Berruto, I. Madan, E. Pomarico, P. Biagioni, R. J. Lamb, D. McGrouther, O. Reinhardt, I. Kaminer, B. Barwick, H. Larocque, V. Grillo, E. Karimi, F. J. García de Abajo, and F. Carbone. "Generation and control of an ultrafast electron vortex beam via chiral plasmonic near-fields". In: *arXiv preprint arXiv:1806.00366* (2018). URL: https://arxiv.org/pdf/1806.00366.pdf.

[272] T. R. Harvey, J. S. Pierce, J. J. Chess, and B. J. McMorran. "Demonstration of electron helical dichroism as a local probe of chirality". In: *arXiv preprint arXiv:1507.01810* (2015). URL: https://arxiv.org/pdf/1507.01810.pdf.

[273] K. Y. Bliokh, I. P. Ivanov, G. Guzzinati, L. Clark, R. Van Boxem, A. Béché, R. Juchtmans, M. A. Alonso, P. Schattschneider, F. Nori, and J. Verbeeck. "Theory and applications of free-electron vortex states". In: *Phys. Rep.* 690 (2017), pp. 1–70. DOI: 10.1016/j.physrep.2017.05.006.

[274] I. Bialynicki-Birula and Z. Bialynicka-Birula. "Relativistic Electron Wave Packets Carrying Angular Momentum". In: *Phys. Rev. Lett.* 118 (11 2017), p. 114801. DOI: 10.1103/PhysRevLett.118.114801.

[275] S. M. Barnett. "Relativistic Electron Vortices". In: *Phys. Rev. Lett.* 118 (11 2017), p. 114802. DOI: 10.1103/PhysRevLett.118.114802.

[276] S. M. Lloyd, M. Babiker, G. Thirunavukkarasu, and J. Yuan. "Electron vortices: Beams with orbital angular momentum". In: *Rev. Mod. Phys.* 89 (3 2017), p. 035004. DOI: 10.1103/RevModPhys.89.035004.

[277] K. Y. Bliokh, P. Schattschneider, J. Verbeeck, and F. Nori. "Electron Vortex Beams in a Magnetic Field: A New Twist on Landau Levels and Aharonov-Bohm States". In: *Phys. Rev. X* 2 (4 2012), p. 041011. DOI: 10.1103/PhysRevX.2.041011.

[278] G. D. Bernasconi, J. Butet, V. Flauraud, D. Alexander, J. Brugger, and O. J. F. Martin. "Where Does Energy Go in Electron Energy Loss Spectroscopy of Nanostructures?" In: *ACS Photonics* 4.1 (2017), pp. 156–164. DOI: 10.1021/acsphotonics.6b00761.

[279] Y. H. Fu, A. I. Kuznetsov, A. E. Miroshnichenko, Y.F. Yu, and B. Luk'yanchuk. "Directional visible light scattering by silicon nanoparticles". In: *Nat. Commun.* 4 (2013), p. 1527. DOI: 10.1038/ncomms2538.

[280] J. Yan, P. Liu, Z. Lin, H. Wang, H. Chen, C. Wang, and G. Yang. "Directional Fano Resonance in a Silicon Nanosphere Dimer". In: *ACS Nano* 9.3 (2015), pp. 2968–2980. DOI: 10.1021/nn507148z.

[281] M. V. Rybin, D. S. Filonov, P. A. Belov, Y. S. Kivshar, and M. F. Limonov. "Switching from visibility to invisibility via Fano resonances: theory and experiment". In: *Sci. Rep.* 5 (2015), p. 8774. DOI: 10.1038/srep08774.

[282] A. L. Holsteen, S. Raza, P. Fan, P. G. Kik, and M. L. Brongersma. "Purcell effect for active tuning of light scattering from semiconductor optical antennas". In: *Science* 358.6369 (2017), pp. 1407–1410. DOI: 10.1126/science.aao5371.

[283] D. J. Traviss, M. K. Schmidt, J. Aizpurua, and O. L. Muskens. "Antenna resonances in low aspect ratio semiconductor nanowires". In: *Opt. Express* 23.17 (2015), pp. 22771–22787. DOI: 10.1364/OE.23.022771.

[284] D. R. Abujetas, R. Paniagua-Domínguez, and J. A. Sánchez-Gil. "Unraveling the Janus Role of Mie Resonances and Leaky/Guided Modes in Semiconductor Nanowire Absorption for Enhanced Light Harvesting". In: *ACS Photonics* 2.7 (2015), pp. 921–929. DOI: 10.1021/acsphotonics.5b00112.

[285] L. Cao, J. S. White, J.-S. Park, J. A. Schuller, B. M. Clemens, and M. L. Brongersma. "Engineering light absorption in semiconductor nanowire devices". In: *Nat. Mater.* 8.8 (2009), pp. 643–647. DOI: 10.1038/nmat2477.

[286] X. Bendaña, A. Polman, and F. J. García de Abajo. "Single-Photon Generation by Electron Beams". In: *Nano Lett.* 11.12 (2011), pp. 5099–5103. DOI: 10.1021/nl1034732.

[287] E. Snitzer. "Cylindrical Dielectric Waveguide Modes". In: *J. Opt. Soc. Am.* 51.5 (1961), pp. 491–498. DOI: 10.1364/JOSA.51.000491.

[288] L. Tong, J. Lou, and E. Mazur. "Single-mode guiding properties of subwavelength-diameter silica and silicon wire waveguides". In: *Opt. Express* 12.6 (2004), pp. 1025–1035. DOI: 10.1364/OPEX.12.001025.

[289] F. J. García de Abajo and M. Kociak. "Probing the Photonic Local Density of States with Electron Energy Loss Spectroscopy". In: *Phys. Rev. Lett.* 100 (10 2008), p. 106804. DOI: 10.1103/PhysRevLett.100.106804.

[290] N. R. Verhart, G. Lepert, A. L. Billing, J. Hwang, and E. A. Hinds. "Single dipole evanescently coupled to a multimode waveguide". In: *Opt. Express* 22.16 (2014), pp. 19633–19640. DOI: 10.1364/OE.22.019633.

[291] M. Schäferling, D. Dregely, M. Hentschel, and H. Giessen. "Tailoring Enhanced Optical Chirality: Design Principles for Chiral Plasmonic Nanostructures". In: *Phys. Rev. X* 2 (3 2012), p. 031010. DOI: 10.1103/PhysRevX.2.031010.

[292] Y. Tang and A. E. Cohen. "Optical Chirality and Its Interaction with Matter". In: *Phys. Rev. Lett.* 104 (16 2010), p. 163901. DOI: 10.1103/PhysRevLett.104.163901.

[293] X. Yin, M. Schäferling, B. Metzger, and H. Giessen. "Interpreting Chiral Nanophotonic Spectra: The Plasmonic Born-Kuhn Model". In: *Nano Lett.* 13.12 (2013), pp. 6238–6243. DOI: 10.1021/nl403705k.

[294] L. Hu, T. Liedl, K. Martens, Z. Wang, and A. O. Govorov. "Long-Range Plasmon-Assisted Chiral Interactions in Nanocrystal Assemblies". In: *ACS Photonics* 6.3 (2019), pp. 749–756. DOI: 10.1021/acsphotonics.8b01676.

[295] M. Born. "Über die natürliche optische Aktivität der Kristalle". In: *Z. Phys.* 8.1 (1922), pp. 390–417. DOI: 10.1007/BF01329609.

[296] Werner Kuhn. "The physical significance of optical rotatory power". In: *Trans. Faraday Soc.* 26 (1930), pp. 293–308. DOI: 10.1039/TF9302600293.

[297] H.-S. Ee, J.-H. Kang, M. L. Brongersma, and M.-K. Seo. "Shape-Dependent Light Scattering Properties of Subwavelength Silicon Nanoblocks". In: *Nano Lett.* 15.3 (2015), pp. 1759–1765. DOI: 10.1021/nl504442v.

[298] N. Geuquet and L. Henrard. "EELS and optical response of a noble metal nanoparticle in the frame of a discrete dipole approximation". In: *Ultramicroscopy* 110.8 (2010). Proc. Enhanced Data Generated by Electrons, pp. 1075 –1080. DOI: https://doi.org/10.1016/j.ultramic.2010.01.013.

[299] Y. Cao, A. Manjavacas, N. Large, and P. Nordlander. "Electron energy-loss spectroscopy calculation in finite-difference time-domain package". In: *ACS Photonics* 2.3 (2015), pp. 369–375. DOI: 10.1021/ph500408e.

[300] P. Das, T. K. Chini, and J. Pond. "Probing Higher Order Surface Plasmon Modes on Individual Truncated Tetrahedral Gold Nanoparticle Using Cathodoluminescence Imaging and Spectroscopy Combined with FDTD Simulations". In: *J. Phys. Chem. C* 116.29 (2012), pp. 15610–15619. DOI: 10.1021/jp3047533.

[301] A. Wiener, H. Duan, M. Bosman, A. P. Horsfield, J. B. Pendry, J. K. W. Yang, S. A. Maier, and A. I. Fernández-Domínguez. "Electron-Energy Loss Study of Nonlocal Effects in Connected Plasmonic Nanoprisms". In: *ACS Nano* 7.7 (2013), pp. 6287–6296. DOI: 10.1021/nn402323t.

[302] S. Raza, N. Stenger, A. Pors, T. Holmgaard, S. Kadkhodazadeh, J. B. Wagner, K. Pedersen, M. Wubs, S. I. Bozhevolnyi, and N. A. Mortensen. "Extremely confined gap surface-plasmon modes excited by electrons". In: *Nat. Commun.* 5.4125 (2014). DOI: 10.1038/ncomms5125.

[303] Comsol Inc. *The Finite Element Method (FEM)*. 2017. URL: https://www.comsol.com/multiphysics/finite-element-method (visited on 02/26/2019).